

**Template - Controlled Synthesis of Magnetic/  
Semiconducting Nanoparticles within Amphiphilic  
Core - Shell Cylindrical Polymer Brushes**

DISSERTATION

zur Erlangung des akademischen Grades eines  
Doktors der Naturwissenschaften (Dr. rer. nat.)

in Fach Chemie der Fakultät für Biologie, Chemie und Geowissenschaften  
der Universität Bayreuth

vorgelegt von

**Mingfu Zhang**

Geboren in Anhui/China

Bayreuth, 2004

Die vorliegende Arbeit wurde in der Zeit von Oktober 2000 bis Oktober 2003 in Bayreuth am Lehrstuhl Makromolekulare Chemie II unter Betreuung von Herrn Prof. Dr. Axel H. E. Müller angefertigt.

Vollständiger Abdruck der von der Fakultät für Biologie, Chemie und Geowissenschaften der Universität Bayreuth zur Erlangung des akademischen Grades eines Doktors der Naturwissenschaften genehmigten Dissertation.

Dissertation eingereicht am:	11.02.2004
Zulassung durch die Promotionskommission:	18.02.2004
Wissenschaftliches Kolloquium:	27.05.2004

Amtierender Dekan: Prof. Dr. O. Meyer

Prüfungsausschuß:

Prof. Dr. A. H. E. Müller (Erstgutachter)

Prof. Dr. G. Krausch (Zweitgutachter)

Prof. Dr. M. Ballauff (Vorsitzender)

Prof. Dr. K. Seifert

Prof. Dr. J. Breu

*To my wife Wen Wu*

*To study without thinking is useless.*

*To think without studying is idle.*

---- Confucius



---

# Table of Contents

<b>1. Introduction</b>	<b>1</b>
<b>1.1 Cylindrical polymer brushes</b>	<b>2</b>
1.1.1 Synthesis of cylindrical polymer brushes	3
1.1.2 Properties of cylindrical polymer brushes in solution and in bulk	5
<b>1.2 Polymer-controlled synthesis of inorganic nanoparticles</b>	<b>7</b>
1.2.1 Metal-containing polymers	7
1.2.2 Nanoparticle formation within polymeric micelles	9
1.2.3 Nanoparticle formation within bulk block copolymer microphases	12
1.2.4 Nanoparticle formation within microporous polymers	13
1.2.5 Nanoparticle formation using single polymer molecules as templates	14
<b>1.3 Magnetic nanoparticles</b>	<b>16</b>
1.3.1 Basics	16
1.3.1.1 Basic definitions	16
1.3.1.2 Type of magnetism	17
1.3.1.3 Hysteresis loop	19
1.3.2 Anisotropy	20
1.3.3 Single domain magnetic nanoparticles	21
1.3.4 Time dependence of magnetization	22
1.3.5 Superparamagnetism	23
1.3.6 Ferrofluids	25
<b>1.4 Semiconductor nanoparticles</b>	<b>27</b>
1.4.1 Bulk semiconductors	27
1.4.2 Nanocrystalline semiconductors	28
<b>1.5 One-dimensional nanostructures</b>	<b>30</b>
<b>1.6 Motivation of this thesis</b>	<b>32</b>
<b>1.7 Structure of this thesis</b>	<b>33</b>

---

<b>2. Methods</b>	<b>41</b>
<b>2.1 Polymerization methods</b>	41
2.1.1 Atom transfer radical polymerization (ATRP)	41
2.1.1.1 Mechanism and kinetics of ATRP	43
2.1.1.2 Monomers	46
2.1.1.3 Initiators	46
2.1.1.4 Catalyst system: transition metals and ligands	47
2.1.1.5 Deactivator	48
2.1.2 Anionic polymerization	50
<b>2.2 Characterization methods</b>	52
2.2.1 Scanning force microscopy (SFM)	52
2.2.2 Transmission electron microscopy (TEM)	54
2.2.3 Light scattering	56
2.2.3.1 Static light scattering (SLS)	57
2.2.3.2 Dynamic light scattering (DLS)	59
2.2.4 Superconducting quantum interference device (SQUID) magnetometer	62
2.2.4.1 The Josephson junction	62
2.2.4.2 SQUID magnetometer	63
2.2.5 Mössbauer spectroscopy	64
2.2.6 Commonly used methods	68
<b>3. Amphiphilic cylindrical brushes with poly(acrylic acid) core and poly(<i>n</i>-butyl acrylate) shell and narrow length distribution</b>	<b>73</b>
<b>3.1 Introduction</b>	74
<b>3.2 Experimental part</b>	77
3.2.1 Materials	77
3.2.2 Synthesis of poly(2-hydroxyethyl methacrylate)	77
3.2.3 Preparation of poly(2-(2-bromoisobutyryloxy)ethyl methacrylate)	79
3.2.4 Typical ATRP procedure for the synthesis of polymer brushes	79
3.2.5 Hydrolysis of the poly( <i>t</i> -butyl acrylate) blocks	80
3.2.6 Analysis	80

---

<b>3.3 Results and discussion</b>	82
3.3.1 Synthesis of poly(2-hydroxyethyl methacrylate)	82
3.3.2 Synthesis of poly(2-(2-bromoisobutyryloxy)ethyl methacrylate)	84
3.3.3 Synthesis of cylindrical brushes with poly( <i>t</i> -butyl acrylate) core and poly( <i>n</i> -butyl acrylate) shell	88
3.3.4 Formation of amphiphilic cylindrical brushes with poly(acrylic acid) core and poly( <i>n</i> -butyl acrylate) shell	95
3.3.5 Scanning force microscopy characterization of cylindrical brushes	97
3.3.6 Synthesis of other polymer brushes and investigation of solution properties	101
<b>3.4 Conclusions</b>	108
<b>4. Polychelates of amphiphilic core-shell cylindrical polymer brushes with iron cations</b>	<b>113</b>
<b>4.1 Introduction</b>	114
<b>4.2 Experimental section</b>	116
4.2.1 Materials	116
4.2.2 Polymer characterization	116
4.2.3 Preparation and characterization of polychelates	116
4.2.4 In situ laser-induced formation of $\alpha$ -Fe <sub>2</sub> O <sub>3</sub> from Fe <sup>3+</sup> ions in the polychelates	117
<b>4.3 Results and discussion</b>	118
4.3.1 Synthesis and characterization of amphiphilic polymer brushes	118
4.3.2 Formation and characterization of polychelates of amphiphilic polymer brushes and iron cations	120
4.3.3 In situ laser-induced formation of $\alpha$ -Fe <sub>2</sub> O <sub>3</sub> from Fe <sup>3+</sup> ions in the polychelates	127
<b>4.4 Conclusions</b>	131

---

<b>5. Superparamagnetic hybrid nanocylinders</b>	<b>135</b>
<b>5.1 Introduction</b>	136
<b>5.2 Experimental section</b>	139
5.2.1 Polymer synthesis	139
5.2.2 Magnetic nanoparticle formation within the polymer brushes	140
5.2.3 Characterization	144
<b>5.3 Results and discussion</b>	146
5.3.1 Synthesis and characterization of magnetic nanocylinders	146
5.3.2 Magnetic properties of the hybrid nanocylinders	157
<b>5.4 Conclusions</b>	163
<b>6. Template-controlled synthesis of wire-like cadmium sulfide nanoparticle assembly within amphiphilic core-shell cylindrical polymer brushes</b>	<b>167</b>
<b>6.1 Introduction</b>	168
<b>6.2 Experimental section</b>	171
<b>6.3 Results and discussion</b>	173
<b>6.4 Conclusions</b>	183
<b>7. Summary/Zusammenfassung</b>	<b>187</b>
<b>8. List of publications</b>	<b>191</b>

## Chapter 1 Introduction

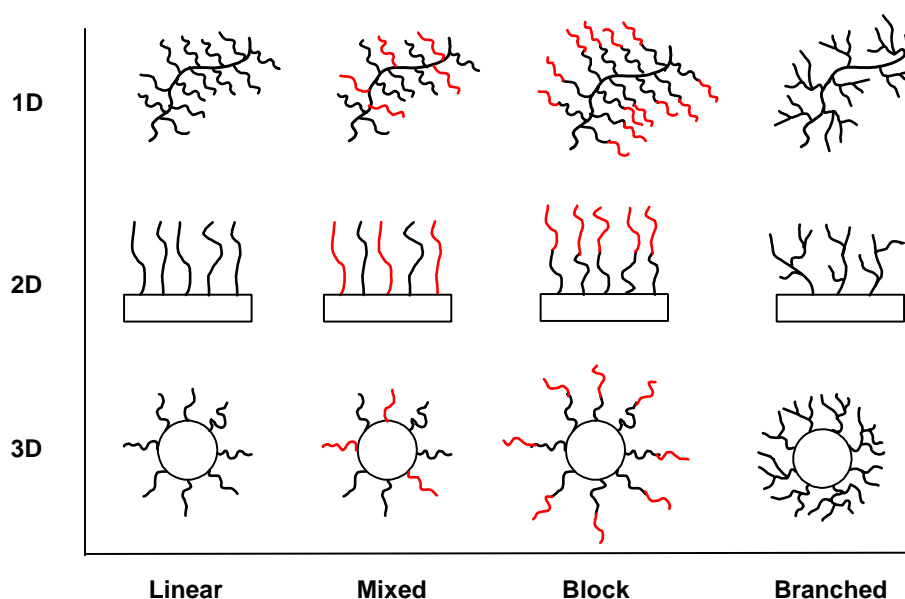
The synthesis of novel materials with improved properties and performance is a continually expanding frontier at the interface of chemistry and materials science. In this pursuit, the ability to control molecular structure on atomic and microscopic dimensions is a key parameter in designing materials with desired properties. A significant advance in this area is the synthesis of nanocomposites where the structural order within the material can be controlled on nanometer/submicron scales.

The field of organic-inorganic nanocomposite materials has been widely recognized as one of the most promising and rapidly emerging research areas in materials chemistry. The spatial organization of dissimilar and commonly incompatible components in these hybrid materials produces a wealth of novel structural features, physical properties, and complex functions, arising from the synergistic interaction of the individual constituents. Promising applications are expected or have already been realized in fields of electronics, optics, catalysts, and sensors, among others. Harnessing the potential of organic-inorganic nanocomposite materials requires fine-tuning of the sizes, topologies, and spatial assembly of individual domains and their interfaces. This, in turn, relies on perfecting chemical routes to these nanocomposite materials as well as an improved fundamental understanding of mechanisms.

Synthesis of inorganic nanoparticles within well-defined polymeric templates represents a very promising technique for the preparation of organic-inorganic nanocomposites, since the as-prepared nanocomposites combine the peculiar properties of inorganic nanoparticles (optic, magnetic, electronic, etc.) with very desirable processing characteristics of polymers. The dispersion and lateral distribution of nanoparticles can be controlled by the intrinsic morphology of the polymer. Recently, advances in living polymerization techniques have provided many opportunities for the synthesis of well-defined polymers with complex structure which can be used as templates/matrixes for controlled nanoparticle fabrication. In this thesis, well-defined core-shell cylindrical polymer brushes, which were synthesized via combination of anionic polymerization and atom transfer radical polymerization (ATRP), were used as single molecular templates for the controlled fabrication of magnetic/semiconductor nanoparticles.

## 1.1 Cylindrical polymer brushes

Polymer brushes refer to an assembly of polymer chains which are tethered by one end to a polymer chain or a surface of a solid. Scheme 1-1 summarizes the possible architectures of polymer brushes.<sup>1</sup> Depending on the substrates, they can be classified into 1-D, 2-D, and 3-D brushes, corresponding to brushes grafted on linear polymer chains, planar surfaces, and spherical particles, respectively. In terms of chemical compositions and architectures, polymer brushes can be also classified into homopolymer brushes, mixed homopolymer brushes, block copolymer brushes, and branched polymer brushes.

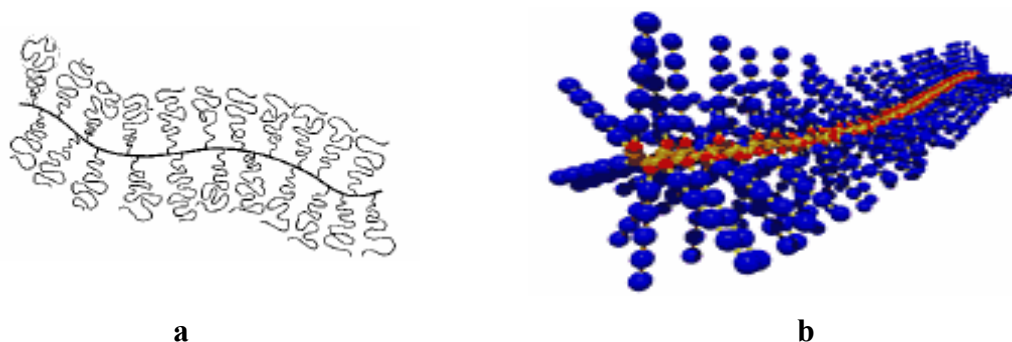


*Scheme 1-1. Possible architectures of polymer brushes.*

Cylindrical polymer brushes, which were synthesized and used as templates for inorganic nanoparticle formation in this thesis, refer to the 1D brushes possessing the same number of side chains as the degree of polymerization (DP) of the main chain. They represent an intermediate type of polymer between branched and linear polymers. Scheme 1-2 shows the schematic 2-D and 3-D structure of cylindrical polymer brushes. The multibranching structure of cylindrical polymer brushes leads to very compact molecular dimension in solution compared to the corresponding linear polymer with the same molecular weight.

One of the driving forces behind the recent interest in controlled/"living" radical polymerizations (CRP) is that these techniques permit an unprecedented opportunity to

design and control macromolecular architecture under mild reaction conditions. A good example is the success in synthesizing well-defined cylindrical polymer brushes via atom transfer radical polymerization (ATRP).

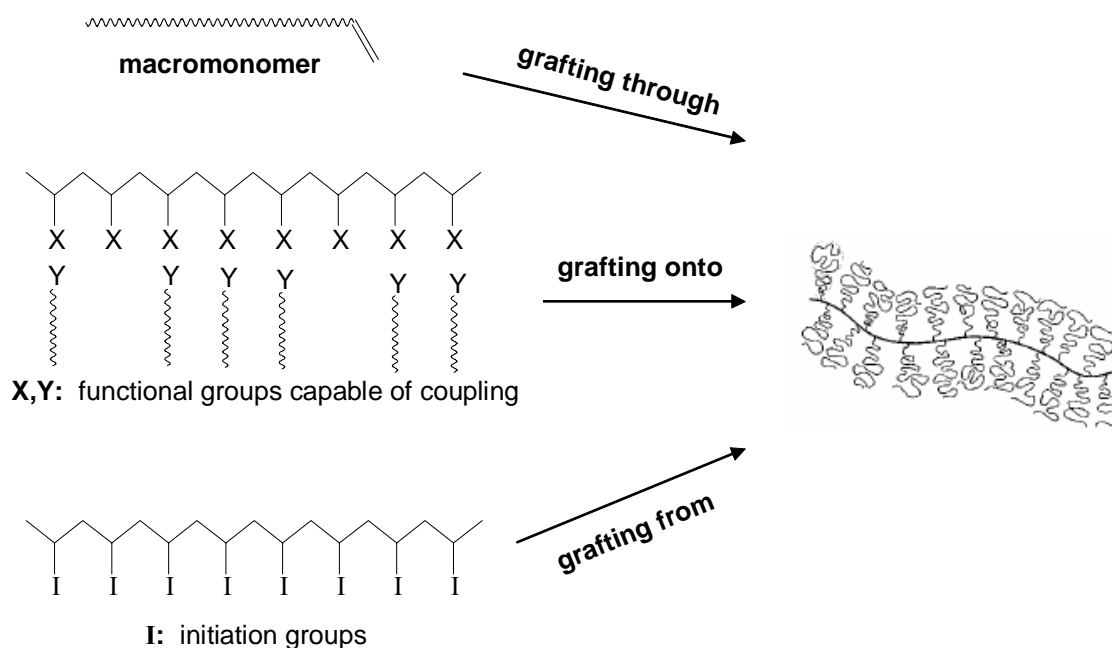


**Scheme 1-2.** Schematic 2-D (a) and 3-D (b) structure of cylindrical polymer brush.<sup>2</sup>

### 1.1.1 Synthesis of cylindrical polymer brushes

As shown in Scheme 1-3, there are three different methods which can be used for the synthesis of cylindrical polymer brushes: “grafting through”,<sup>3-6</sup> “grafting onto”,<sup>7,8</sup> and “grafting from”.<sup>9-11</sup> In the following these three methods are described in detail.

**“Grafting through”.** The “grafting through” method, which is the polymerization of macromonomers, is the first method applied for the synthesis of cylindrical polymer brushes. In 1989, Tsukahara et al. reported a pioneering study of the radical polymerization of macromonomers.<sup>3,4</sup> In their work, oligomers prepared by anionic polymerization were end-functionalized to obtain macromonomers possessing vinyl group at one end. The subsequent radical polymerization of macromonomers produced polymer brushes with uniform side chains. The major limitations associated with the radical polymerization of macromonomers is the difficulty of obtaining complete conversion and precise size control of the polymer brushes formed. Very often, the resulted polymer brushes have broad distributions in the backbone length, due to the nature of conventional radical polymerizations. In addition, incomplete conversion of macromonomers causes difficulties in purification, i.e., the separation of polymer brushes from residual unreacted macromonomers. So fractionation is generally required. Although living anionic polymerization<sup>12</sup> and living ring-opening metathesis polymerization<sup>13-15</sup> were also used to polymerize macromonomers aiming to produce well-defined polymer brushes, so far, high molecular weight polymers have not been prepared by these living techniques.



**Scheme 1-3.** Synthesis of cylindrical polymer brushes via three different methods.

**“Grafting onto”.** As shown in Scheme 1-3, in the “grafting onto” technique, both backbone and side chain are prepared separately. The grafting of side chains onto a backbone is carried out via coupling reaction between the pendant functional groups (X) of backbone and the end-functional groups (Y) of grafts. For example, coupling polystyryllithium with poly(2-chloroethyl vinyl ether) (PCEVE) resulted in a polymer brush with a PCEVE backbone and polystyrene (PS) side chains. The advantage of this technique is that both backbone and side chain can be well-defined because they are prepared separately. However, insufficient grafting efficiency was often obtained using the “grafting onto” method due to steric hindrance, specially for long grafts. So it is difficult to control the degree of branching and compositional heterogeneity may exist along the backbone of polymer brushes. Additionally, incomplete coupling reaction will cause the problem of purification similar to that for “grafting through” method.

**“Grafting from”** The last method, i.e. “grafting from”, appeared lately.<sup>9-11</sup> In this method a well-defined backbone is first prepared via living polymerization techniques, followed by functionalization to attach ATRP initiating groups to the backbone (one initiating group per backbone monomer unit). Side chains of polymer brush are then formed via ATRP initiated by the pendant initiating groups on the backbone. By this method well-defined cylindrical polymer brushes with high grafting density and narrow distributions of

both backbone and side chain can be obtained, and the purification of the resulting polymer brushes is much easier compared to the other two methods. Via the “grafting from” method, cylindrical polymer brushes with various homopolymer and block copolymer side chains have been successfully synthesized.

### 1.1.2 Properties of cylindrical polymer brushes in solution and in bulk

So far, there have been intensive studies on the properties of cylindrical polymer brushes, induced by their peculiar structure, in solution and also in bulk. Most investigations were performed in dilute solutions with emphasis on their molecular shape and dimensions.<sup>16-21</sup> It is known that these polymer brushes have much higher main chain stiffness than linear flexible polymers in solution, due to the intramolecular repulsion between adjacent side chains. The persistence length ( $l_p$ ) or Kuhn statistical segment length ( $l_k$ ) of polymer brushes increases monotonously with increasing side chain length, and the contour length per main chain monomer unit was found to approach the limiting value, 0.25 nm, for large side chain lengths. Based on their stiff main chains, cylindrical polymer brushes have been also named as “rodlike combs”<sup>5</sup> or “bottlebrushes”.<sup>6,22</sup>

By combining gel permeation chromatography (GPC) with multi-angle light scattering and viscosity detectors, Schmidt et al. reported a structural characterization of cylindrical polymer brushes with fixed side chain length in terms of absolute molar mass,  $M$ , the radius of gyration,  $R_g$ , and intrinsic viscosity,  $[\eta]$ .<sup>5</sup> It was found that, for polymer brushes with fixed side chain (PS) length but variable main chain (polymethacrylate, PMA) length, the relation of  $R_g$  vs.  $M$  was excellently described by the Kratky-Porod wormlike chain model,<sup>23</sup> whereas the same model did not fit well to the Mark-Houwink (i.e.,  $[\eta]$  vs.  $M$ ) relation. It was supposed that the wormlike chain theory for intrinsic viscosity failed for polymer brushes with large chain cross-section exhibiting no sharp boundaries but rather a gradually decaying segment density towards the not well-defined cylinder surface. Subsequently, they did a more comprehensive study on the same type of polymer brushes in dilute benzene solution.<sup>6</sup> They concluded that these polymer brushes exhibit a bottlebrush structure in that the PMA main chain adopts an extremely stiff conformation surrounded by the expanded but still flexible PS side chains. Qualitatively similar conclusions were drawn from dynamic light scattering and sedimentation velocity measurements.<sup>21</sup> In a concentrated solution, these polymer brushes were reported to form a lyotropic phase.<sup>24</sup>

To avoid the influence from the chemical heterogeneity between backbone and side chain, Nakamura et al. synthesized a series of polymer brushes containing PS backbone and PS side chain (with fixed side chain length), and studied their solution properties by static light scattering and viscosity measurements.<sup>18-20</sup> Analysis of the measured  $z$ -average mean-square radii of gyration based on the Kratky-Porod wormlike chain model<sup>23</sup> showed the Kuhn segment length to be one order of magnitude larger than that of the linear chain at the  $\Theta$  point, indicating that the high segment density around the main chain remarkably stiffens the backbone of the polymer brush. In addition, repulsions between the main chain and side chain and between neighbouring side chains play an important role in the high stiffness of polymer brushes. Furthermore, they found that the Mark-Houwink relation can be described almost quantitatively by the wormlike chain model when the end effect arising from side chains near the main chain end is considered.

The intrinsic shape and size of polymer brushes in solution were also studied by small-angle X-ray scattering, aiming at investigating the cross-sectional characteristics of polymer brushes.<sup>25</sup> A conformational change of the backbone was speculated to take place when the degree of polymerization (DP) of main chain exceeded a certain limiting value. An elliptical cylinder was found to outline the polymer brush in solution at large DP of main chain.

Besides the investigations on the solution properties, there are also studies on the bulk state of polymer brushes, about the glass transition and film-forming properties, as well as the presence of liquid-crystalline mesophases resulting from the molecular anisotropy of polymer brushes.<sup>26-29</sup> Tsukahara et al. found that the polymer brushes with PMA main chain and long PS side chains and without any mesogenic groups, formed a mesomorphic phase.<sup>28</sup> The formation of the liquid-crystalline phase indicates that these polymer brushes, possessing large branch number and sufficient branch length, behave as rod-like molecules. Rheological measurements of the polymer brushes showed that the master curve of the storage dynamic shear modulus  $G'$  did not show the so-called plateau region and  $G'$  decreased gradually from the edge of the glass transition region to the terminal flow zone with decrease in frequency. These results indicate that the intermolecular chain entanglement might be strongly restricted in polymer brush systems due to the multibranch structure with high branch density.<sup>29</sup>

## 1.2 Polymer-controlled synthesis of inorganic nanoparticles

The term “nanoparticle” describes materials having at least one dimension between 1 and 100 nm. Inorganic nanoparticles have distinct electronic, optical, magnetic, chemical and thermal properties deriving from quantum confinement effects and from their large surface areas, with the best established examples including size-dependent excitation or emission,<sup>30,31</sup> quantized conductance,<sup>32</sup> superparamagnetism,<sup>33</sup> single-electron tunneling,<sup>34</sup> and metal-insulator transition.<sup>35</sup> The ability of fabricating such nanoscale structures is essential to many fields of modern science and technology. So far, the most successful example is provided by microelectronics,<sup>36</sup> where “smaller” normally means greater performance: more component per chip, lower cost, faster operation, and lower power consumption. Miniaturization also represents a trend in a range of other technologies. For example, there are many active efforts to develop magnetic and optical storage components with nanometer dimensions in the field of information storage.<sup>37</sup>

Inorganic-organic nanocomposites are promising systems for a variety of applications due to their extraordinary properties based on the combination of different building blocks. There are several routes to these materials, but probably the most prominent one is the incorporation of inorganic building blocks into organic polymers.

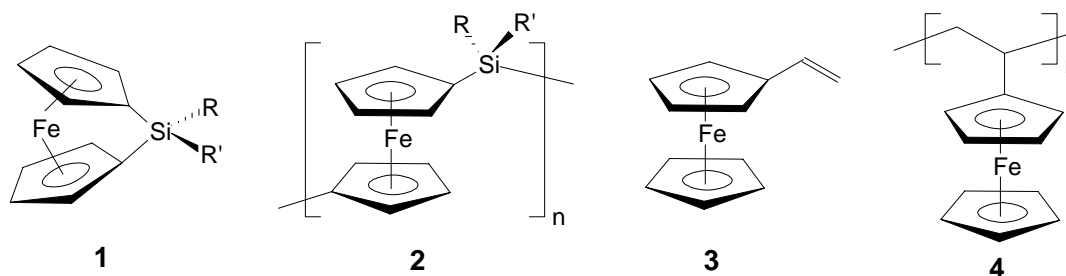
At first sight, the incorporation of inorganic materials into polymeric domains is not a trivial matter. Since most polymers are materials with low surface energy, the adhesion between metals and polymers is usually poor. Only through specific interactions like dipolar interactions, hydrogen bonding, complex formation, or covalent bonding can inorganic materials be incorporated into polymers. This is of special relevance to the controlled synthesis of inorganic nanoparticles or the controlled assembly of hybrid materials.

In the following various techniques for the polymer-directed synthesis of inorganic nanoparticles are summarized.

### 1.2.1 Metal-containing polymers

A straightforward way to incorporate metals into polymers is the use of metal-coordinated monomers for polymerization. Polymerization and copolymerization of such monomers have attracted much interest, as revealed in a number of reviews.<sup>38-41</sup> In principle, two different polymer systems can be distinguished: those in which the metal is part of the polymer main chain and others in which the metal is coordinated to pendant

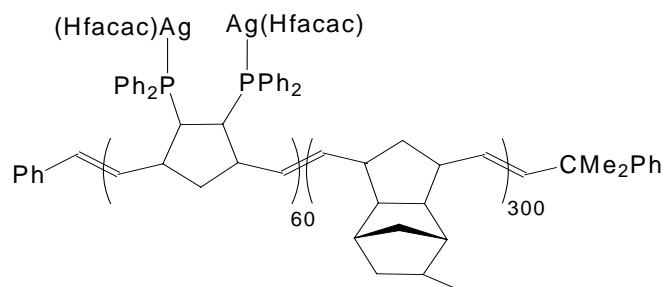
groups. As examples, Scheme 1-4 shows polymers containing the ferrocenylene moiety in the main chain (2) and in the side group (4) and the corresponding monomers (1 and 3).



**Scheme 1-4.** Structure of metal-containing monomers and polymers

Ring-opening polymerization methods have enabled the synthesis of metallocene-based polymer systems such as polyferrocenyldimethylsiloxane (PFS).<sup>42</sup> These organometallic materials are easily processed. Pyrolysis yields nanocomposites containing magnetic Fe nanoparticles. The size of Fe nanoparticles can be controlled through the pyrolysis temperature, allowing the magnetic properties to be tuned from superparamagnetic to ferromagnetic.<sup>43</sup> Block copolymers containing PFS can be synthesized via anionic ring-opening polymerization.<sup>44</sup> The diblock copolymer polyisoprene-*b*-polyferrocenyldimethylsiloxane (PI-*b*-PFS) forms cylindrical micelle in hexane with a PFS core and a PI corona. Pt catalyzed hydrosilylation of the coronal PI chain resulted in shell cross-linked permanent cylindrical nanostructures, from which PFS-derived arrays of magnetic Fe nanoparticles formed upon pyrolysis.<sup>45</sup>

An alternative method to incorporate metal into polymer is to attach it onto the pendant groups of a polymer via chemical modification. For example, Cohen et al. modified a diblock copolymer, poly(2-*exo*-3-*endo*-bis(diphenylphosphino)-bicyclo[2.2.1]heptane)-*b*-poly(methyl-tetracyclododecene) (polyNORPHOS-*b*-polyMTD) with Ag(Hfaca)(COD) (Hfaca = hexafluoroacetylacetonate; COD = 1,5-cyclo-octadiene) to obtain a block copolymer containing silver (shown in Scheme 1-5).<sup>46</sup> A bulk film of the modified block copolymer revealed a lamellar morphology. Thermal treatment lead to the formation of silver nanoparticles within the lamella containing organometallic precursor.



**Scheme 1-5.** Structure of  $[Ag_2(Hfacac)_2(NORPHOS)]_{60}[MTD]_{300}$

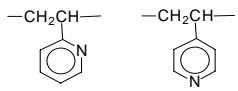
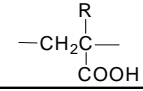
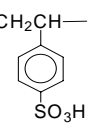
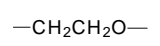
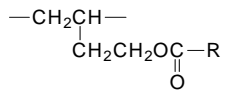
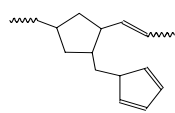
### 1.2.2 Nanoparticle formation within polymeric micelles

Amphiphilic block copolymers, in a solvent which preferentially dissolves one block, form micelles with a core consisting of the less soluble block and a highly swollen corona of the more soluble block.<sup>47</sup> Depending on the relative composition of the copolymer and the solvents, spherical and cylindrical micelles, as well as more complex polymer vesicles and compound micelles, may form. Micellar cores offer unique microenvironments (“nanoreactors”) in which inorganic precursors can be loaded and then processed by wet chemical methods to produce comparatively uniform nanoparticles. Various block copolymer micelles have been successfully used as templates and nanoreactors for nanoparticle fabrication.<sup>47</sup> Block copolymer-nanoparticle hybrids present peculiar magnetic, electro-optical, and catalytic properties arising primarily from single inorganic colloids.

As mentioned before, polymers and inorganic materials are mutually incompatible. In order to prepare stable polymer/inorganic nanoparticle hybrid material, the polymer/nanoparticle interface has to be sufficiently stabilized, especially when inorganic nanoparticles with very large interfacial areas have to be prepared. Binding functional groups in block copolymers to inorganic material can improve the adhesion between polymer and inorganic microphase and thus stabilize the hybrid material. Examples of such functional blocks are summarized in Table 1-1.

Basically, the controlled fabrication of nanoparticles within block copolymer micelles involves the following steps: micellization of block copolymer, loading of inorganic precursor into the micellar core, chemical reaction followed by nucleation and growth process to form nanoparticles. In principle, the loading-chemical reaction cycle can be carried out for several times so that core-shell or onion-type colloidal structures can be prepared.

**Table 1-1.** Common functional blocks for incorporating inorganic materials into polymers

Functional blocks	Structure	Remarks
poly(vinylpyridine)s		ligand, acid-base reactions
poly((meth)acrylic acid)		ion binding, ion exchange
poly(styrenesulfonic acid)		ion binding, ion exchange
poly(ethylene oxide)		ion binding
specific ligand-containing blocks		R = 2-mercaptopyridine, 2-mercaptobenzothiazole: binding of transition metals; R = benzoic acid: binding to ceramic surfaces and alkaline earth salts
poly(cyclopentadienylmethyl norborene)		binding of transition metal via metallocene complexes

The loading of inorganic salts into preformed block copolymer micelles has become the most common method for the incorporation of inorganic precursors into block copolymer microcompartments. It is quite versatile and can be used for a large number of precursor/block copolymer/solvent systems.<sup>48</sup> Usually, the loading of precursor into the micellar core is achieved simply by stirring the precursor salt in the micellar solution. Metal ions are bound either directly to the polymeric ligand in the micellar core or indirectly as counterions. For example, a large number of different metal ions can be loaded into the poly(4-vinylpyridine) (P4VP) core of the micelles of polystyrene-*b*-poly(4-vinylpyridine) (PS-*b*-P4VP), since P4VP is a strong metal-chelating agent.<sup>49</sup> On the other hand, when HAuCl<sub>4</sub> is mixed with PS-*b*-P4VP micellar solution, the P4VP micellar core is protonated, thereby AuCl<sub>4</sub><sup>-</sup> is bound as counterion.<sup>50</sup> Similarly, micelles of polystyrene-*b*-poly(2-vinylpyridine) (PS-*b*-P2VP),<sup>51,52</sup> polystyrene-*b*-poly(ethylene oxide) (PS-*b*-PEO),<sup>53</sup> and modified polystyrene-*b*-polybutadiene<sup>48</sup> have also been used as micellar nanoreactors for the preparation of metal and metal oxide nanoparticles.

Alternatively, it is also possible to bind inorganic precursors to the functional groups of block copolymers before the micelle formation. In most cases, the binding of the precursor will make the functional block insoluble and induce micellization. For example, neutralization of polystyrene-*b*-poly(acrylic acid) (PS-*b*-PAA) by metal hydroxides (CsOH, Ba(OH)<sub>2</sub>) or metal salts (Cd(Ac)<sub>2</sub>, Pb(Ac)<sub>2</sub>, Ni(Ac)<sub>2</sub>, Co(Ac)<sub>2</sub>) results in block ionomers, which form micelles with ionic block in the core in organic media.<sup>54</sup> Compared with their nonionic counterparts, block ionomers in solution exhibit extremely low critical micelle concentrations (cmc) and high aggregate stability.

After the loading of metal ions into the micellar core, chemical reactions can transform the metal ions into metal (via reduction), metal oxide (for example, ZnO nanoparticles can be prepared by addition of tetrabutylammonium hydroxide to Zn<sup>2+</sup>-loaded micelles), and semiconductor (for example, introduction of H<sub>2</sub>S into to Cd<sup>2+</sup>-loaded micelles) nanoparticles.<sup>47</sup>

The stability of micelles in thermodynamic equilibrium (except crew-cut micelles which exist under non-equilibrium conditions) depends strongly on external conditions, because they are formed via weak undirected forces (van der Waals forces, hydrophobic effects). Even a relatively slight change in the physical conditions that result in the original self-assembly can completely disrupt them. So it is of special interest and importance to fix the micellar structure to obtain stable micelles.

Stable micelles have been obtained via crosslinking and used as templates. Liu et al. reported the preparation of hollow triblock nanospheres which were then used as templates for the preparation of iron oxide<sup>55</sup> and palladium<sup>56</sup> nanoparticles. A triblock copolymer polyisoprene-*b*-poly(2-cinnamoyloxyethyl methacrylate)-*b*-poly(*t*-butyl acrylate), PI-*b*-PCEMA-*b*-PtBA, was used to form “onion-like” spherical micelles (with a PI corona, PCEMA shell, and PtBA core) in THF/hexane with 65 vol.% of hexane. Their structure was locked in by photo-crosslinking the PCEMA shell, followed by the hydroxylating the PI double bonds to obtain water-dispersible nanospheres. Finally the hydrolysis of the PtBA block resulted in hollow nanospheres which are capable of binding metal ions in the core for inorganic nanoparticle formation. A similar approach has also been used for the preparation of polymer nanotubes which were further used to prepare magnetic nanoparticles via templating technique.<sup>57</sup>

### 1.2.3 Nanoparticle formation within bulk block copolymer microphases

In bulk, block copolymers are microphase-separated into a number of different morphologies (sphere, cylinder, lamella, etc), depending on block length and segment-segment interaction parameter.<sup>47</sup> Typical dimensions of microdomains are 10-100 nm. Inorganic precursors can also be loaded into block copolymer microdomains. Cohen et al. synthesized a number of metal (Ag, Au, Cu, Ni, Pb, Pd and Pt) nanoparticles within a microphase-separated diblock copolymer, poly(methyltetracyclododecene)-*b*-poly(2-norbornene-5,6-dicarboxylic acid) ([MTD]<sub>400</sub>[NORCOOH]<sub>50</sub>), thin film.<sup>58,59</sup> In their method, metal ions or complexes were coordinated to carboxylic acid groups within hydrophilic polyNORCOOH domains of a copolymer thin film, which was immersed in an aqueous metal salt solution. Subsequent reduction of the metal ions by exposure to hydrogen at elevated temperatures or aqueous NaBH<sub>4</sub> resulted in the formation of metal nanoclusters.

It was reported that a non-equilibrium interconnected cylindrical morphology of the polyNORCOOH domain in [MTD]<sub>400</sub>[NORCOOH]<sub>50</sub> thin film facilitated the transport of metal ions through the polymer film. In contrast, in the film of [MTD]<sub>800</sub>[NORCOOH]<sub>30</sub>, in which isolated spherical polyNORCOOH microdomains within a hydrophobic polyMTD matrix were formed, no metal ion loading was observed.<sup>60</sup> This problem can be solved via another strategy first introduced by Möller.<sup>61</sup> He prepared metal sulfide nanoparticles within microphase-separated PS-*b*-P2VP film, via film casting from a polymer solution containing a metal salt, followed by treatment with H<sub>2</sub>S. In this case, metal salts were confined in the P2VP domains during solvent evaporation, due to the complex formation between metal ions and vinylpyridine units. Recently, Kofinas et al. reported the synthesis of CoFe<sub>2</sub>O<sub>4</sub> nanoparticles within a diblock copolymer thin film via a very similar strategy.<sup>62</sup> The advantages of this strategy include the much faster metal ion loading and the applicability to all kinds of morphologies.

Wiesner et al. used block copolymers as structure-directing molecules to prepare various silica-type nanoparticles.<sup>63-65</sup> When a polyisoprene-*b*-polyethyleneoxide (PI-*b*-PEO) block copolymer is mixed with a mixture of (3-glycidyloxypropyl)trimethoxysilane (GLYMO) and aluminium *sec*-butoxide (Al(OBu<sup>s</sup>)<sub>3</sub>) in solution followed by film casting, inorganic microdomains form within the polymer matrix, with different morphologies (sphere, cylinder, lamella) depending on metal alkoxide content.<sup>64</sup> Condensation of the metal alkoxides leads to aluminosilicate nanoobjects incorporating the PEO block of the

polymer. After dissolution, isolated hybrid objects (with PI surrounding layer) of controlled shape and size can be obtained. When iron(III) ethoxide was added in addition to GLYMO and  $\text{Al}(\text{O}i\text{Bu})_3$ , magnetic silica-type nanoparticles were obtained.<sup>65</sup>

#### 1.2.4 Nanoparticle formation within microporous polymers

Many microporous polymers, such as resin,<sup>66</sup> membrane,<sup>67</sup> have been used as templates and/or nanoreactors for nanoparticles. Ziolo et al. synthesized superparamagnetic  $\gamma\text{-Fe}_2\text{O}_3$  nanoparticles within an ion-exchange resin, which is sulfonated polystyrene cross-linked with divinylbenzene.<sup>66</sup> The microporous polymeric matrix not only provides spatially localized sites for the nucleation but also minimizes the degree of aggregation of the iron oxide nanoparticles. Specially, the as-prepared  $\gamma\text{-Fe}_2\text{O}_3$ /polymer nanocomposite is an optically transparent magnetic material. Via a similar strategy, ferrihydrite ( $5\text{Fe}_2\text{O}_3 \cdot 9\text{H}_2\text{O}$ ) nanoparticles were produced in the pores of polypropylene membranes possessing poly(acrylic acid) grafts in the pores.<sup>67</sup> In the above two cases, the microporous polymers possess functional groups (such as sulfonate or carboxylic acid) capable of binding precursor metal ions, so these polymers are not only physical templates but also nanoreactors. For those microporous polymers without functional groups, inorganic nanoparticles can also be produced within the pores simply via physical confinement. Bronstein et al. succeeded in fabricating cobalt nanoparticles within the pores of hyper-crosslinked polystyrene (HPS).<sup>68</sup> Impregnation of HPS by either  $\text{Co}_2(\text{CO})_8$  in 2-propanol or the  $[\text{Co}(\text{DMF})_6]^{2+}[\text{Co}(\text{CO})_4]^{-2}$  complex in DMF, followed by thermolysis at  $200^\circ\text{C}$ , resulted in the formation of discrete Co nanoparticles.

Ordered nanoscopic polymeric pores (channels) can be obtained via chemical modifications of microphase-separated block copolymer films. For example, degradation of one microphase would result in ordered pores (channels), which can be used as templates for the fabrication of ordered nanoparticle arrays. Synthesis of nanoparticles via chemical-deposition or electro-deposition into track-etched polymeric membranes has become a versatile and robust route to the fabrication of densely packed nanoparticle arrays. Recently, Russell et al. reported the electro-deposition of ferromagnetic cobalt nanowires<sup>69</sup> and the chemical-deposition of  $\text{SiO}_2$  nanoposts<sup>70</sup> into nanoporous films, which was generated by selective removal of hexagonally packed cylindrical poly(methyl methacrylate) (PMMA) domains from PS-*b*-PMMA thin films. The PMMA cylindrical domains were oriented normal to the surface either by application of an electric field<sup>71,72</sup> or deposition onto a

neutral substrate.<sup>73</sup> Similarly, high-density arrays of chromium (Cr) and layered gold/chromium (Au/Cr) nanodots and nanoholes in metal films were fabricated by evaporation onto these nanoporous templates.<sup>74</sup> In addition, such nanoporous membranes have been proposed for the preparation of nanoelectrode arrays.<sup>75</sup>

Another elegant method to prepare polymeric membranes with ordered channels based on a supramolecular assembly was proposed by Ikkala<sup>76,77</sup> and recently used by Minko<sup>78</sup> for the metallic nanoparticle fabrication. Well-ordered nanostructured thin polymer films can be fabricated from the supramolecular assembly of PS-*b*-P4VP and 2-(4'-hydroxybenzeneazo)benzoic acid (HABA), consisting of cylindrical microdomains formed by P4VP-HABA associates (via hydrogen bonding) within the PS matrix. Alignment of the cylindrical domains was shown to be switched upon exposure to vapours of different solvents from parallel to perpendicular to the substrate and vice versa.<sup>79</sup> Extraction of HABA with selective solvent resulted in membranes with a hexagonal lattice of hollow channels, which was then used to fabricate the ordered array of metallic nanoparticles via electrodeposition.<sup>78</sup>

### 1.2.5 Nanoparticle formation using single polymer molecules as templates

Recently, using single polymer molecules as templates have attracted much attention, since isolated nanocomposites can be obtained, which have very desirable processing characteristics. Among single molecule polymeric templates, dendrimers attract most research interests up to now.<sup>80</sup> Crooks et al. have prepared a number of metal and semiconductor nanoparticles within poly(amidoamine) (PAMAM) dendrimers.<sup>80</sup> PAMAM dendrimers have a generation-dependent number of interior tertiary amines, which are able to complex a range of metal ions. The metal ions adsorbed within the dendrimer interior can be reduced or sulfidized to yield dendrimer-encapsulated metal or semiconductor nanoparticles. Because each dendrimer contains a specific number of metal ions, the resulting metal/semiconductor nanoparticles are of nearly monodisperse size in many cases. Nanoparticles within dendrimers are stabilized by the dendrimer framework, i.e., the dendrimer acts as a stabilizer to prevent nanoparticle agglomeration. These unique composites are useful for a range of catalytic applications.

Polyelectrolytes have been also used as single molecule templates. Recently Minko et al. reported the mineralization of single flexible polyelectrolyte molecules.<sup>81</sup> They prepared single molecule templates from P2VP deposited on silicon wafer or mica. Pd<sup>2+</sup> ions were

coordinated by P2VP upon exposing the samples to palladium acetate acidic aqueous solution, followed by chemical reduction. This route resulted in wire-shaped metallic nanoparticle assemblies. Very recently, this group also used unimolecular micelles, constituted from a heteroarm PS/P2VP star-shaped block copolymer, to prepare Pd nanoparticles.<sup>82</sup>

In addition, natural scaffolds such as DNA<sup>83,84</sup> have been successfully used for the construction of synthetic nanostructures. Braun et al. have shown that DNA molecules can be uniformly coated with metal nanoparticles to form metallic conductive nanowires that can be attached to macroscopic electrodes by virtue of the DNA molecular recognition properties.<sup>83</sup>

### 1.3 Magnetic nanoparticles

The fundamental motivation for the fabrication and study of nanoscale magnetic materials is the dramatic change in magnetic properties that occurs when the size of nanoparticle is comparable to the critical length governing certain phenomena (magnetic, structural, etc.). Effects due to surfaces and/or interfaces are stronger in nanoparticle systems than in bulk.

#### 1.3.1 Basics

##### 1.3.1.1 Basic definitions

In the field of magnetism, two different unit systems (SI and CGS units) coexist. In the following the SI units are used in the basic definitions and the conversion of these two unit systems can be easily found in many books concerning magnetism.<sup>85</sup>

A magnetic solid consists of a large number of atoms with magnetic moments. The magnetization  $\mathbf{M}$  ( $\text{Am}^{-1}$ ) is defined as the magnetic moment per unit volume. Usually this vector quantity is considered in the “continuum approximation”, i. e. on a lengthscale large enough so that one does not see the graininess due to the individual atomic magnetic moments.

In free space (vacuum) there is no magnetization. The magnetic field can be described by the vector fields  $\mathbf{B}$  and  $\mathbf{H}$  which are linearly related by

$$\mathbf{B} = \mu_0 \mathbf{H} \quad \text{Eq. 1-1}$$

where  $\mu_0 = 4\pi \times 10^{-7} \text{ Hm}^{-1}$  is the permeability of free space. The two magnetic fields  $\mathbf{B}$  and  $\mathbf{H}$  are just scaled versions of each other, the former measured in Tesla and the latter measured in  $\text{Am}^{-1}$ .

In a magnetic solid that relation between  $\mathbf{B}$  and  $\mathbf{H}$  is more complicated and the two vector fields may be very different in magnitude and direction. The general vector relationship is

$$\mathbf{B} = \mu_0(\mathbf{H} + \mathbf{M}) \quad \text{Eq. 1-2}$$

In the case that the magnetization  $\mathbf{M}$  is linearly related to the magnetic field  $\mathbf{H}$ , the solid is called a linear material, and one gets

$$\mathbf{M} = \chi \mathbf{H} \quad \text{Eq. 1-3}$$

where  $\chi$  is called the magnetic susceptibility (dimensionless). In this special case there is still a linear relationship between  $\mathbf{B}$  and  $\mathbf{H}$ , namely

$$\mathbf{B} = \mu_0(1 + \chi)\mathbf{H} = \mu_0\mu_r\mathbf{H} \quad \text{Eq. 1-4}$$

where  $\mu_r = 1 + \chi$  is the relative permeability of the material.

### 1.3.1.2 Types of magnetism

*Diamagnetism.* Diamagnetism is a basic property of all substances and involves a slight repulsion by a magnetic field. The magnetic susceptibility of a diamagnetic substance is small ( $-10^{-6}$ ), negative and independence of temperature.

*Paramagnetism.* Paramagnetic substances possess unpaired electrons which are randomly oriented on different atoms. Each atom, ion, or molecule of a paramagnetic substance can be considered as a small magnet with its own, inherent magnetic moment. When a magnetic field is applied to them they become magnetized (usually much more weakly than ferromagnetic substances). The magnetization depends linearly on the applied field and it disappears when the field is removed. Paramagnetic substances are attracted towards a magnetic field. The magnetic susceptibility of a paramagnetic substance is positive and small (0 to 0.01). It varies with temperature and its behaviour can be described by the Curie-Weiss law:

$$\chi = \frac{C}{T - \theta} \quad \text{Eq. 1-5}$$

where  $C$  is the Curie constant and  $\theta$  is the temperature where  $1/\chi$  vanishes. When  $\theta$  equals to zero, Equation 1-5 is known as the Curie law.

The temperature dependence of  $\chi$  is the result of two opposite tendencies: as the temperature rises, the increased alignment of the magnetic moments is opposed by the stronger thermal vibrations, hence  $\chi$  decreases. Below a certain temperature, depending on the substance, a transition to a magnetically ordered state can happen and the substance becomes ferromagnetic, antiferromagnetic, or ferrimagnetic. The transition temperature is termed as the Curie temperature ( $T_C$ ) for ferromagnetic and ferrimagnetic substances and Néel temperature ( $T_N$ ) for antiferromagnetic substances.

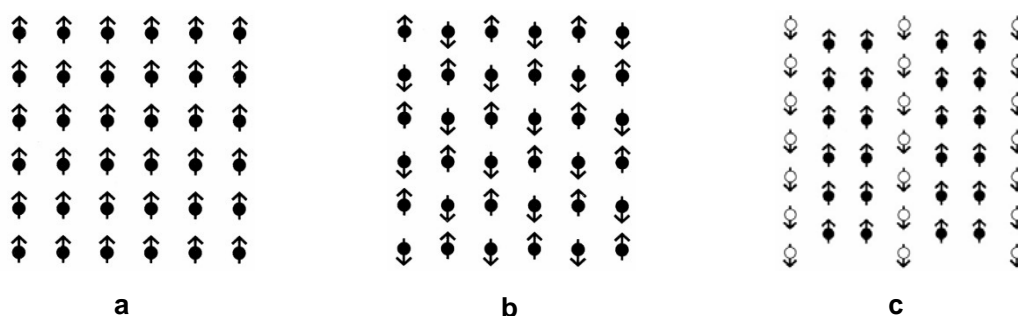
Ferro- and ferrimagnetic substances are strongly attracted by a magnetic field. They contain unpaired electrons whose moments are, as a result of interactions between

neighbouring spins, at least partially aligned even in the absence of a magnetic field. The spin coupling energy is positive.

*Ferromagnetism.* In a ferromagnetic substance, the alignment of the electron spins is parallel (Scheme 1-6a). Such substances have a net magnetic moment and a large positive susceptibility ( $0.01-10^6$ ). With rising temperature, the ordered arrangement of the spins decreases due to thermal fluctuations of the individual magnetic moments and the susceptibility falls rapidly. Above the Curie temperature, a ferromagnetic substance becomes paramagnetic and thus its susceptibility follows the Curie-Weiss law (the constant  $\theta$  is equal to  $T_C$ ).

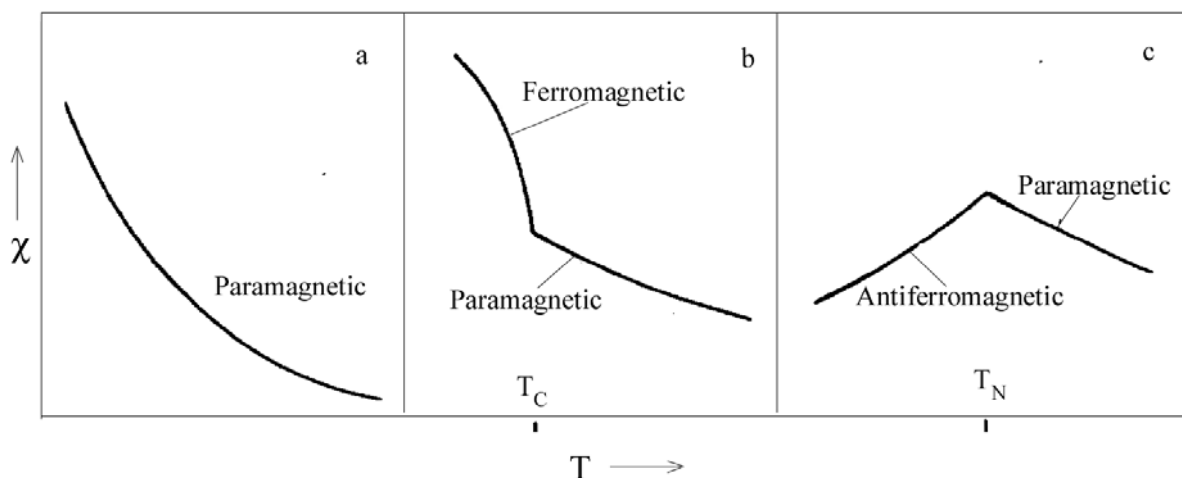
*Antiferromagnetism.* In an antiferromagnetic substance, the electron spins are of equal magnetic moment and are aligned in an antiparallel manner (Scheme 1-6b). Such substances have zero net magnetic moment, a small positive susceptibility ( $0-0.1$ ). Below the Néel temperature, increasing the temperature usually causes susceptibility to increase because the antiparallel ordering is disrupted.

*Ferrimagnetism.* Ferrimagnetic substances consist of at least two interpenetrating sublattices with antiparallel alignment of the spins. Different from antiferromagnetic substance, a ferrimagnetic has a net magnetic moment (Scheme 1-6c). Ferrimagnetic substances are superficially similar to ferromagnets. One difference is that ferromagnets are usually metallic and ferrimagnets are usually non-metals. But this is not an exclusive separation. A more reliable difference that is observed experimentally is that the susceptibility of most ferromagnets measured above  $T_C$  follows the Curie-Weiss law, but the susceptibility of most ferrimagnets does not follow this law until relatively high temperatures are reached. The graph of  $1/\chi$  against  $T$  is often hyperbolic at temperatures up to  $2T_C$ , becoming linear asymptotically.



*Scheme 1-6. Schematic illustration of the main varieties of magnetic order: (a) ferromagnetism; (b) antiferromagnetism; and (c) ferrimagnetism.*

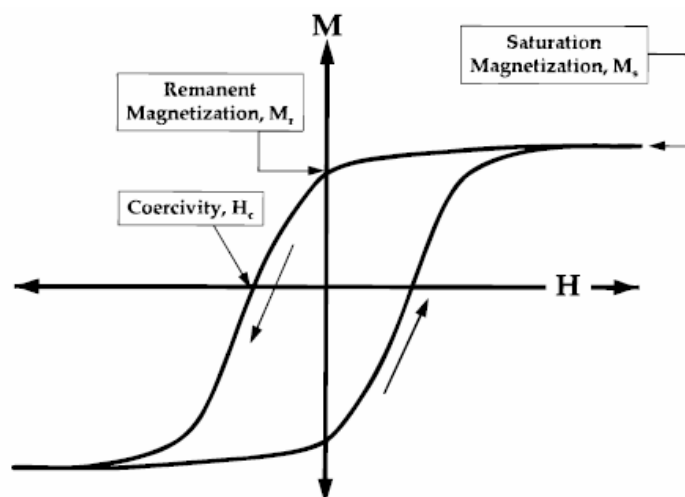
Scheme 1-7 summarizes the temperature dependence of magnetic susceptibility for different magnetic substances.



**Scheme 1-7.** Temperature dependence of magnetic susceptibility for (a) paramagnetic, (b) ferromagnetic, and (c) antiferromagnetic substances.

### 1.3.1.3 Hysteresis loop

Scheme 1-8 schematically illustrates a typical hysteresis loop with commonly measured magnetic parameters. The application of a sufficiently large magnetic field causes the spins within a material to align along the field direction. The maximum value of the magnetization achieved in this state is called the saturation magnetization,  $M_s$ . As the magnitude of the magnetic field decreases, spins cease to be aligned with the field, and the total magnetization decreases. In ferromagnets, a residual magnetic moment remains at zero field. The value of the magnetization at zero field is called the remnant magnetization,  $M_r$ . The ratio of the remnant magnetization to the saturation magnetization,  $M_r/M_s$ , is called the remanence ratio and varies from 0 to 1. The coercive field  $H_c$  is the magnitude of the field that must be applied in the opposite direction to bring the magnetization of the sample back to zero. The shape of the hysteresis loop is especially of interest for magnetic recording applications, which require a large remnant magnetization, moderate coercivity, and (ideally) a square hysteresis loop.



*Scheme 1-8. Important parameters obtained from a magnetic hysteresis loop.*

### 1.3.2 Anisotropy

Most magnetic materials contain some types of anisotropy affecting the behavior of the magnetization. The common anisotropies include (1) crystal anisotropy, (2) shape anisotropy, (3) stress anisotropy, (4) externally induced anisotropy, and (5) exchange anisotropy.<sup>86</sup> The two most common anisotropies in nanostructured materials are crystalline and shape anisotropy. The anisotropy can often be modeled as uniaxial in character and represented by

$$E = KV \sin^2 \theta \quad \text{Eq. 1-6}$$

where  $K$  is the effective uniaxial anisotropy energy per unit volume,  $\theta$  is the angle between the moment and the easy axis, and  $V$  is the particle volume.

Magnetocrystalline anisotropy arises from spin-orbit coupling and energetically favors alignment of the magnetization along a specific crystallographic direction, which is called the easy axis of the material. The magnetocrystalline anisotropy is specific to a given material and independent of particle shape. The magnitude of the magnetocrystalline anisotropy at room temperature is  $7 \times 10^6$  erg/cm<sup>3</sup> in cobalt,  $8 \times 10^5$  erg/cm<sup>3</sup> in iron, and  $5 \times 10^4$  erg/cm<sup>3</sup> in nickel. The coercivity is proportional to the anisotropy constant, so high-anisotropy materials are attractive candidates for high-coercivity applications.

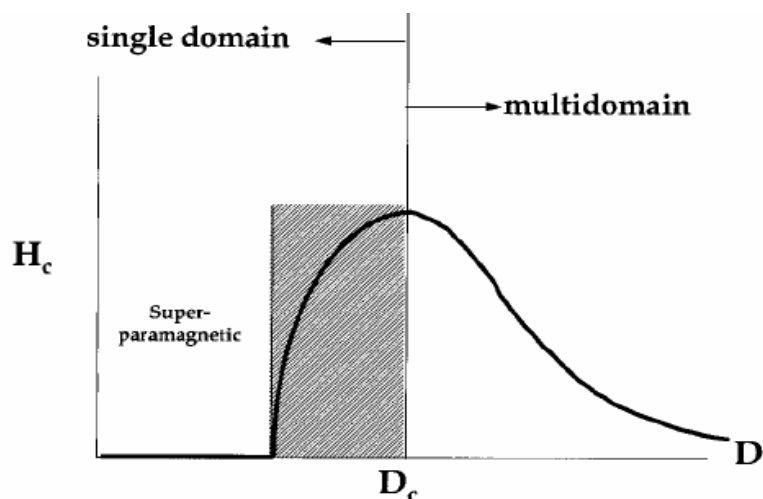
A polycrystalline sample with no preferred grain orientation has no net crystal anisotropy due to averaging over all orientations. A nonspherical polycrystalline specimen, however, can possess shape anisotropy. For example, a cylindrical sample is easier to

magnetize along the long direction than along the short directions. Shape anisotropy is predicted to produce the largest coercive forces. The departure from spherical shape does not need to be significant: an increase in the aspect ratio from 1.1 to 1.5 in single-domain iron particles with easy axis aligned along the field quadruples the coercivity. An increase in the aspect ratio to 5 produces another doubling of the coercivity. For comparison, a sample having the same coercivity as the 1.1 aspect ratio iron particle would need a crystal anisotropy of  $2.8 \times 10^6$  erg/cm<sup>3</sup>.

Stress anisotropy results from external or internal stresses due to rapid cooling, external pressure, etc. Stress anisotropy may also be induced by annealing in a magnetic field, plastic deformation, or ion beam irradiation. Exchange anisotropy occurs when a ferromagnet is in close proximity to an antiferromagnet or ferrimagnet. Magnetic coupling at the interface of the two materials can create a preferential direction in the ferromagnetic phase, which takes the form of a unidirectional anisotropy.<sup>87</sup> This type of anisotropy is most often observed in particles with antiferromagnetic or ferrimagnetic oxide forming around ferromagnetic core.

### 1.3.3 Single domain magnetic particles<sup>33</sup>

Domains – groups of spins all pointing in the same direction and acting cooperatively – are separated by domain walls, which have a characteristic width and energy associated with their formation and existence. Experimental investigations of the dependence of coercivity on particle size showed the behaviour illustrated in Scheme 1-9. In large particles, energetic considerations favour the formation of domain walls. Magnetization reversal thus occurs through the nucleation and motion of these walls. As the particle size decreases toward some critical particle diameter,  $D_c$ , the formation of domain walls becomes energetically unfavourable and the particles are called single domain. Changes in the magnetization can no longer occur through domain wall motion but via the coherent rotation of spins, resulting in larger coercivities. As the particle size continues to decrease below the single domain value, the spins are increasingly affected by thermal fluctuations which prevent a stable magnetization thus neither remanence nor coercivity exists.



**Scheme 1-9.** Qualitative illustration of the change of coercivity with the particle size.

Theoretical predications of the existence of single domain particles were made by Frenkel and Dorfman,<sup>88</sup> with estimate of the critical size made by Kittel<sup>89</sup> and others. Table 1-2 estimates the single-domain diameter for some common materials in the form of spherical particles. Note that particles with significant shape anisotropy can remain single domain to much larger dimension than their spherical counterparts.

**Table 1-2.** Estimated single-domain sizes for spherical particles

Material	Co	Fe	Ni	Fe <sub>3</sub> O <sub>4</sub>	γ-Fe <sub>2</sub> O <sub>3</sub>
$D_c$ (nm)	70	14	55	128	166

### 1.3.4 Time dependence of magnetization

The time over which the magnetization of a system will remain in a certain state is of importance for practical engineering applications as well as for probing the fundamental mechanisms of magnetization reversal. The time variation of the magnetization of any magnetic system (without application of magnetic field) can be generally described by

$$\frac{dM(t)}{dt} = -\frac{M(t) - M(t = \infty)}{\tau} \quad \text{Eq. 1-7}$$

where  $M(t = \infty)$  is the equilibrium magnetization and  $\tau$  is a characteristic relaxation time corresponding to relaxation over an energy barrier ( $\Delta E$ ):

$$\tau^{-1} = f_0 e^{-\Delta E / kT} \quad \text{Eq. 1-8}$$

where  $k$  is Boltzmann's constant, and  $T$  is the temperature in Kelvin.

For uniaxial anisotropies, the energy barrier is equal to the product of the anisotropy constant and the volume.  $f_0$  is often taken as a constant of value  $10^9 \text{ s}^{-1}$ ,<sup>90</sup> but actually depends on applied field, particle volume, and the magnitude of the anisotropy constant.<sup>91</sup> Although some experimental studies suggest that a value of  $10^{12}$ - $10^{13} \text{ s}^{-1}$  is more appropriate,<sup>92</sup> exact knowledge of the magnitude of  $f_0$  is not necessary because the behavior of  $\tau$  is dominated by the exponential argument.

The simplest solution to Equation 1-8 occurs when all components of a system have the same relaxation time; however, the expected behavior is not usually observed in real systems due to a distribution of energy barriers. The energy barrier distribution may be due to a variation of particle size, anisotropy, or compositional heterogeneity and results in a distribution of relaxation times. If the distribution of energy barriers can be approximated as nearly constant, the magnetization decays logarithmically:<sup>93</sup>

$$M(t) = M(t=0) - S \ln(t) \quad \text{Eq. 1-9}$$

where the magnetic viscosity,  $S$ , contains information about the energy barrier distribution. When the distribution function is not constant, deviations from logarithmic behavior are observed if the measurement extends to sufficiently long times.<sup>94,95</sup>

### 1.3.5 Superparamagnetism

In 1949, Néel pointed out that if a single domain particle was small enough, thermal fluctuations could cause its direction of magnetization to undergo a sort of Brownian rotation, thus  $H_c$  approaches zero for very small particles because thermal fluctuations prevent the existence of a stable magnetization.<sup>96</sup> This state is called superparamagnetic because the particle behaves similarly to paramagnetic spin but with a much higher moment.

Consider an assembly of aligned particles that are fully magnetized, the resulting remanence will vanish with time, when the field is removed, as

$$M_r = M \exp(-t/\tau) \quad \text{Eq. 1-10}$$

where  $M$  is the full magnetization,  $t$  is the time after removal of the field, and  $\tau$  is the relaxation time for the process, and is defined in Equation 1-8.

When  $\tau$  is less than or comparable to a measurement time (typically on a time scale of 100 s), such that the zero remanence corresponding to thermal equilibrium (a sufficient number of particles are reversed by thermal activation over the energy barrier) can be reached within the measuring time. In this case one will observe the superparamagnetism phenomenon. Returning to Equation 1-8, if we take an arbitrary measurement time to be  $t = 100$  s and  $f_0 = 10^9 \text{ s}^{-1}$ , then for a particle with a uniaxial anisotropy ( $\Delta E = KV$  at  $H = 0$ ) the condition for superparamagnetism becomes

$$\Delta E_{crit} = \ln(tf_0)kT = 25kT \quad \text{Eq. 1-11}$$

The strong dependence on the argument of the exponential makes exact knowledge of  $f_0$  less important. If  $f_0$  is  $10^{12} \text{ s}^{-1}$ , the criteria becomes

$$\Delta E_{crit} = 32kT \quad \text{Eq. 1-12}$$

Particles with  $\Delta E > \Delta E_{crit}$  are blocked, so they do not relax during the time of the measurement. Thus a blocking temperature,  $T_B$ , can be defined as

$$T_B = \Delta E_{crit} / 25k \quad \text{Eq. 1-13}$$

The blocking temperature in a superparamagnetic system decreases with increasing measuring fields, being proportional to  $H^{2/3}$  at large magnetic fields and proportional to  $H^2$  at lower fields.<sup>97,98</sup>

Note that the relaxation time depends critically on the particle size (as  $\exp(r^3)$ ). Assuming representative values ( $f_0 = 10^9 \text{ s}^{-1}$ ,  $K = 10^6 \text{ erg/cm}^3$ , and  $T = 300 \text{ K}$ ), a particle of diameter 11.4 nm will have a relaxation time of 0.1 s and hence will reach thermal equilibrium almost instantaneously. Increasing the particle diameter to 14.6 nm increases  $\tau$  to  $10^8$  s and hence it will be extremely stable.

The temperature-dependent magnetization exhibits a maximum under the zero-field-cooled (ZFC) conditions at the blocking temperature. Above  $T_B$ , the particles are free to align with the field during the measuring time and behave superparamagnetically. The magnetization of system of particles,  $\bar{\mu}$ , is described by the Langevin function

$$\frac{\bar{\mu}}{\mu} = L\left(\frac{\mu H}{kT}\right) = \coth\left(\frac{\mu H}{kT}\right) - \frac{kT}{\mu H} \quad \text{Eq. 1-14}$$

where  $\mu$  is the magnetic moment of a single particle. At low fields ( $\mu H \ll kT$ ), the magnetization behaves as  $\mu H/3kT$  and at high fields ( $\mu H > kT$ ), as  $1-kT/\mu H$ . If a distribution of particle sizes is present, the initial susceptibility is sensitive to the larger particles present, and the approach to saturation is more sensitive to the smaller particles present.

The experimental criteria for superparamagnetism are (1) the magnetization curve exhibits no hysteresis and (2) the magnetization curves at different temperatures must superpose in a plot of  $M$  vs  $H/T$ .<sup>33,99,100</sup> Imperfect  $H/T$  superposition can result from a broad distribution of particle sizes, changes in the spontaneous magnetization of the particle as function of temperature, or anisotropy effects.

### 1.3.6 Ferrofluids<sup>101</sup>

Ferrofluids are stable colloidal dispersions of nano-sized particles of ferro- or ferrimagnetic particles in a carrier liquid. Ferrofluids attract more and more research interest since they were first synthesized in the middle of 1960-ies.<sup>102-104</sup> A wide range of carrier liquids have been employed, depending on particular applications. For most applications a low viscosity, low vapor pressure and chemical inertness are desirable for the carrier liquid. Many ferrofluids are now commercially available.

Generally the magnetic particles are of approximately 10 nm in diameter so that the colloidal suspension remains stable. Particles of this size, whether they be ferrite or metal, possess a single magnetic domain only, i.e., the individual particles are in a permanent state of saturation magnetization. Thus a strong long-range magnetostatic attraction exists between individual particles, the result of which would lead to agglomeration of the particles and subsequent sedimentation unless a means of achieving a repulsive interaction can be incorporated. In order to achieve this repulsive mechanism, either the particles are coated by a surfactant or polymer to produce an entropic repulsion, or the surfaces of the particles are charged thereby producing an electrostatic repulsion.

A process for preparing a ferrofluid consists of two basic stages: preparation of magnetic colloidal-size particles and the dispersion of such particles in a carrier liquid. The main feature of this process is that both stages overlap in time: to prevent particle agglomeration due to the attractive forces, the adsorbed layers must be formed on the surface of magnetic particles immediately after their origination. Fine particles may be made by a size reduction (e.g., wet-grinding), chemical precipitation, microemulsion technique, decomposition of organo-metallic compounds, and so on.

Under an applied magnetic field, the magnetic moments of individual particles in a ferrofluid are aligned, causing the net magnetization of the fluid. There are two mechanisms of disorientation of the magnetic moments of colloidal particles. In an uniaxial single-domain particle a thermal fluctuations of the magnetic moment occurs along two opposite directions of the “easy” axis of magnetization. The second mechanism is due to the Brownian (thermal) rotation of particles relative to the carrier liquid.

Coupling of the magnetic and mechanical degrees of freedom of the particles is the main specific feature of ferrofluids. Explicit manifestation of this coupling is the increase of the viscosity of ferrofluids under application of a magnetic field, which is called magnetoviscous effect.<sup>105</sup> The appearance of magnetic field and shear dependent changes of viscosity in ferrofluids opens possibilities for future applications, e.g. in damping technologies. There have also been many studies about the other properties of ferrofluids, including magnetic, electric, rheological, thermal and acoustic characteristics.<sup>106,107</sup>

Based on their promising properties, ferrofluids have applications in a number of fields.<sup>106,108</sup> (i) in chemical engineering, ferrofluids are used as seals, lubricants, supports, bearings, dampers, and shock-absorbers; (ii) for technological applications, ferrofluids have been used for separation of ores, drag reduction, flow separation control, and heat transfer enhancement; (iii) ferrofluids have also been used in a variety of devices such as sensors, printers and acoustic radiators; and specially (iv) ferrofluids have very promising medical applications. For example, ferrofluids have been used as drug carriers in cancer therapy.<sup>101</sup>

## 1.4 Semiconductor nanoparticles

Semiconductor nanoparticles exhibit a change in their electronic properties relative to that of the bulk material: as the size of the solid becomes smaller, the band gap becomes larger. This gives chemists and materials scientists the unique opportunity to tune the electronic and chemical properties of a semiconductor simply by controlling its particle size. Semiconductor nanoparticles are expected to have potential applications in many fields such as nonlinear optics, luminescence, electronics, catalysis, solar energy conversion, and optoelectronics. For comparison and easier understanding, the introduction of the properties of bulk semiconductors is given first in the following.

### 1.4.1 Bulk semiconductors

Bulk (macrocrystalline) semiconductors, free of defects, consist of a three-dimensional network of ordered atoms. The translational periodicity of the crystal imposes a special form on the electronic wave functions. An electron in the periodic potential field of a crystal can be described using a Bloch-type wave function

$$\begin{aligned}\psi(r) &= \phi(kr)u(r) \\ u(r+n) &= u(r) \quad (n : \text{integer})\end{aligned}\tag{Eq. 1-15}$$

where  $u(r)$  represents a Bloch function modulating the plane wave  $\phi(kr)$  of wave vector  $k$ .

In a bulk semiconductor the large number of atoms leads to the generation of sets of molecular orbitals with very similar energies which effectively form a continuum. At 0 K the lower energy levels (or valence band) are filled with electrons, while the conduction band consisting of the higher energy levels is unoccupied. These two bands are separated by an energy gap ( $E_g$ ), the magnitude of which is a characteristic property of the bulk semiconductor (at a specific temperature). Materials considered as semiconductors exhibit band gaps typically in the range of 0.3-3.8 eV.<sup>109</sup>

At temperatures above 0 K, electrons in the valence band may receive enough thermal energy to be excited into the conduction band across the band gap. An excited electron in the conduction band together with the resulting hole in the valence band form an “electron-hole pair”. The conductivity ( $\sigma$ ) of the semiconductor is governed by the number of electron-hole pairs, the charge carrier concentration ( $n$ ), and their mobility ( $\mu$ ). Thus conductivity can be expressed as the sum of the electrical conductivities of electrons and holes, as shown in Equation 1-16 ( $q$  is the charge of the carrier):

$$\sigma = qn_e\mu_e + qn_h\mu_h \quad \text{Eq. 1-16}$$

In conventional semiconductors electrons and holes are the charge carriers. They exist in small numbers as compared to conductors. However, the carrier mobilities in semiconductors are substantially larger than in many conductors.

The charge carriers in a semiconductor can form a bound state when they approach each other in space. This bound electron-hole pair, known as a Wannier exciton, is delocalized within the crystal lattice and experiences a screened Coulombic interaction. The Bohr radius of the bulk exciton is given by Equation 1-17 ( $\epsilon$  represents the bulk optical dielectric coefficient,  $e$  the elementary charge, and  $m_e^*$  and  $m_h^*$  the effective mass of the electron and hole, respectively)

$$\alpha_B = \frac{\eta^2 \epsilon}{e^2} \left( \frac{1}{m_e^*} + \frac{1}{m_h^*} \right) \quad \text{Eq. 1-17}$$

#### 1.4.2 Nanocrystalline semiconductors

Two fundamental factors, both related to the size of the individual nanocrystal, distinguish their behavior from the corresponding macrocrystalline material. The first is the large surface/volume ratio associated with the particles, with both the physical and chemical properties of the semiconductor being particularly sensitive to the surface structure. The second factor is the actual size of the particle, which can determine the electronic and physical properties of the material. The absorption and scattering of incident light in larger colloidal particles is described by Mie's theory. However the optical spectra of nanocrystalline compound semiconductors which show blue shifts in their absorption edge as the size of the particle decreases cannot be explained by classical theory. Such size dependent optical properties are examples of the size quantization effect<sup>110</sup> which occurs when the size of the nanoparticle is smaller than the bulk-exciton Bohr radius,  $a_B$  (Equation 1-17), of the semiconductor. Equation 1-18 defines, for a spherical crystallite of radius  $R$ , the region of intermediate character between that of a "molecule" and that of the bulk material ( $l$  is the lattice spacing)

$$l \leq R \leq \alpha_B \quad \text{Eq. 1-18}$$

Charge carriers in semiconductor nanocrystallites are confined within three dimensions by the crystallite. In the case of ideal quantum confinement the wave function in Equation 1-15 has to satisfy the boundary conditions of

$$\psi(r \geq R) = 0 \quad \text{Eq. 1-19}$$

For nanoparticles the electron and hole are closer together than in the macrocrystalline material, and as such the Coulombic interaction between electron and hole cannot be neglected; they have higher kinetic energy than in the macrocrystalline material. On the basis of the effective mass approximation, Brus<sup>111</sup> showed for CdE (E = S or Se) nanocrystallites that the size dependence on the energy of the first electronic transition of the exciton (or the band gap shift with respect to the typical bulk value) can be approximately calculated using

$$\Delta E \cong \frac{\eta^2 \pi^2}{2R^2} \left( \frac{1}{m_e^*} + \frac{1}{m_h^*} \right) - \frac{1.8e^2}{\epsilon R} \quad \text{Eq. 1-20}$$

In Equation 1-20 the Coulomb term shifts the first excited electronic state to lower energy,  $R^{-1}$ , while the quantum localization terms shift the state to higher energy,  $R^{-2}$ . Consequently, the first excitonic transition (or band gap) increases in energy with decreasing particle diameter. This prediction has been confirmed experimentally for a wide range of semiconductor nanocrystallites, with a blue shift in the onset of the absorption of light being observed with decreasing particle size. Moreover, the valence and conduction bands in nanocrystalline materials consist of discrete sets of electronic levels and can be viewed as a state of matter between that of molecular and the bulk material.

Equation 1-20 does not account for a number of other important effects observed in real nanocrystallites, such as the coupling of electronic states and effects attributable to surface structure. However, from a practical point of view this model is particularly useful and the size-dependent energy shift for a number of nanocrystalline semiconductors can be estimated. Furthermore, the model also provides a useful qualitative understanding of the quantum confinement effects observed in semiconductor nanocrystallites.

## 1.5 One-dimensional nanostructures<sup>112</sup>

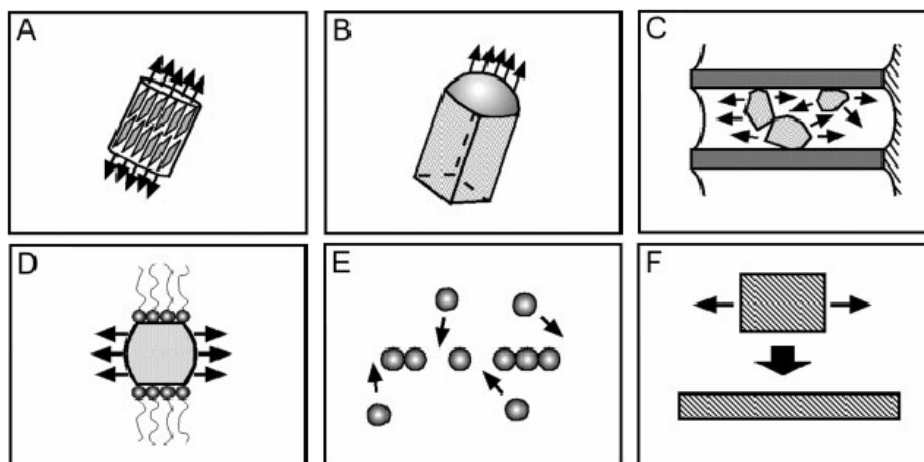
Compared to zero-dimensional (0-D, such as quantum dots)<sup>113,114</sup> and two-dimensional (2-D, such as quantum wells)<sup>115</sup> nanostructures, which have been extensively studied in past decades, the advancement of one-dimensional (1-D) nanostructures (nanowires, nanorods, nanobelts and nanotubes) has been slow until very recently, as hindered by the difficulties associated with the synthesis of these nanostructures with well-controlled dimensions, morphology, phase purity, and chemical composition. Although now 1-D nanostructures can be fabricated using various lithographic techniques, such as electron-beam or focused-ion-beam writing, proximalprobe patterning, and X-ray or UV lithography, further developments of these techniques are still needed in order to produce large quantities of 1-D nanostructures from a broad range of materials, rapidly, and at reasonably low costs. In contrast, methods based on chemical synthesis may provide an alternative and intriguing strategy for the fabrication of 1-D nanostructures in terms of material diversity, cost, throughput, and potential for large-quantity production.

It is generally accepted that 1-D nanostructures provide good systems for the investigation of the dependence of electrical, optical, mechanical and thermal properties on dimensionality and size reduction. They are also expected to play an important role as both interconnects and functional units for electronic, optoelectronic, electrochemical, and electromechanical devices with nanoscale dimensions.

As shown in Scheme 1-10, the strategies for the fabrication of 1-D nanostructures include: (i) 1-D growth; (ii) self-assembly of 0-D nanostructures; and (iii) size reduction. 1-D growth can be achieved via different methods: the control from the anisotropic crystallographic structure of a solid; confinement by a liquid droplet as in the vapor-liquid-solid process; direction by a template; and kinetic control provided by a capping reagent.

Template-directed synthesis represents a straightforward and versatile route to 1-D nanostructures. In this approach, the template acts as a scaffold within (or around) which a 1-D nanostructure is generated in situ. A number of templates have been used, including step edges on the surfaces of a solid substrate, channels within a porous material, mesoscale structures self-assembly from surfactants or block copolymers, natural macromolecules such as DNA or rod-shaped viruses, and preformed 1-D nanostructures (such as carbon nanotubes). It is generally accepted that template-directed synthesis provides a simple, high-throughput, and cost-effective procedure. However, as a major drawback, nanostructures synthesized using template-directed methods are often polycrystalline, and the quantity of

nanostructures produced in each run of the synthesis is relatively limited. Only under carefully controlled conditions, single crystals can be obtained. For example, Barbic and co-workers have demonstrated the use of electroless deposition in generating single-crystalline silver nanowires in channels of a polycarbonate membrane via a self-catalyzed process.<sup>116</sup>



**Scheme 1-10.** Schematic illustration of different strategies for the synthesis of 1-D nanostructures: (A) dictation by the anisotropic crystallographic structure of a solid; (B) confinement by a liquid droplet as in the vapor-liquid-solid process; (C) direction through the use of a template; (D) kinetic control provided by a capping reagent; (E) self-assembly of 0-D nanostructures; and (F) size reduction of a 1-D microstructure.<sup>112</sup>

Compared to bulk materials, low-dimensional nanoscale materials, with their large surfaces and possible quantum-confinement effects, exhibit distinct electronic, optical, chemical and thermal properties. In many cases, 1-D nanostructures are superior to their counterparts with larger dimensions. There have been a number of investigations about the thermal stability, mechanical properties, electron transport properties, and optical properties 1-D nanostructures.

Obviously the most promising application for 1-D nanostructures is the usage in electronics, where smaller dimensions allow the production of denser, faster circuits. There are also a number of applications for 1-D nanostructures in areas outside of electronics. Examples include, for instance, ultrasmall chemical and mechanical sensors, optical elements for optoelectronics, near-field probing, nonlinear optic conversion, information storage, and biological applications.

## 1.6 Motivation of this thesis

The motivation of this work is to use novel single molecule cylindrical templates, well-defined amphiphilic core-shell polymer brushes, for the controlled fabrication of inorganic magnetic/semiconducting nanoparticles, aiming to obtain novel 1-dimensional polymer/nanoparticle hybrid materials with peculiar properties and potential applications.

To achieve a precise size/shape control of nanoparticles, a well-defined template is needed. Combination of living anionic polymerization (for the synthesis of the polymer backbone) and atom transfer radical polymerization (for the synthesis of the side chains) ensures the well-defined structure of the obtained polymeric templates, cylindrical polymer brushes with poly(acrylic acid) core and poly(*n*-butyl acrylate) shell. Scanning force microscopy provides the direct information of the core-shell structure and size distribution of polymer brushes.

The polymer brushes can be used as nanoreactors and cylindrical templates for inorganic nanoparticle fabrication, because the carboxylate groups (after neutralization of the poly(acrylic acid)) within the polymer core are capable of coordinating with a number of different metal ions. The subsequent chemical reactions of the coordinated metal ions will result in the formation of nanoparticles within the core of polymer brushes. The shell of polymer brushes provides not only the protection of nanoparticles from aggregation but also the solubility of the hybrid nanocylinders in organic solvents.

The as-prepared hybrid materials were characterized by various techniques (such as microscopes, spectroscopies, magnetometer, etc) to obtain information about the peculiar properties of the hybrids.

## 1.7 Structure of this thesis

The following chapters in this thesis describe in detail

- Fundamentals of the polymerization techniques and characterization methods used in this work (Chapter 2)
- Synthesis and characterization of the amphiphilic cylindrical polymer brushes with poly(acrylic acid) core and poly(*n*-butyl acrylate) shell (Chapter 3)
- Synthesis and characterization of the polychelates of polymer brushes and metal ions; laser-induced formation of  $\alpha$ -Fe<sub>2</sub>O<sub>3</sub> from Fe<sup>3+</sup> ions in the polychelates (Chapter 4)
- Synthesis and characterization of superparamagnetic nanocylinders — hybrids of cylindrical polymer brushes and ultrafine magnetic nanoparticles (Chapter 5)
- Synthesis and characterization of semiconducting nanocylinders — hybrids of cylindrical polymer brushes and semiconductor nanoparticles (Chapter 6)
- Summary / Zusammenfassung (Chapter 7)
- List of publications (Chapter 8)

## References

- (1) Mori, H.; Müller, A. H. E. *Prog. Polym. Sci.* **2003**, *28*, 1403-1439.
- (2) [www.chem.cmu.edu/groups/maty/about/research/about-research-brush.html](http://www.chem.cmu.edu/groups/maty/about/research/about-research-brush.html).
- (3) Tsukahara, Y.; Mizuno, K.; Segawa, A.; Yamashita, Y. *Macromolecules* **1989**, *22*, 1546-1552.
- (4) Tsukahara, Y.; Tsutsumi, K.; Yamashita, Y.; Shimada, S. *Macromolecules* **1990**, *23*, 5201-5208.
- (5) Wintermantel, M.; Schmidt, M.; Tsukahara, Y.; Kajiwara, K.; Kohjiya, S. *Macromol. Rapid Commun.* **1994**, *15*, 279-284.
- (6) Wintermantel, M.; Gerle, M.; Fischer, K.; Schmidt, M.; Wataoka, I.; Urakawa, H.; Kajiwara, K.; Tsukahara, Y. *Macromolecules* **1996**, *29*, 978-983.
- (7) Deffieux, A.; Schappacher, M. *Macromolecules* **1999**, *32*, 1797-1802.
- (8) Ryu, S. W.; Hirao, A. *Macromolecules* **2000**, *33*, 4765-4771.
- (9) Beers, K. L.; Gaynor, S. G.; Matyjaszewski, K.; Sheiko, S. S.; Möller, M. *Macromolecules* **1998**, *31*, 9413-9415.
- (10) Cheng, G.; Böker, A.; Zhang, M.; Krausch, G.; Müller, A. H. E. *Macromolecules* **2001**, *34*, 6883-6888.
- (11) Boerner, H. G.; Beers, K.; Matyjaszewski, K.; Sheiko, S. S.; Möller, M. *Macromolecules* **2001**, *34*, 4375-4383.
- (12) Tsukahara, Y.; Inoue, J.; Ohta, Y.; Kohjiya, S.; Okamoto, Y. *Polym. J.* **1994**, *26*, 1013-1018.
- (13) Feast, W. J.; Gibson, V. C.; Johnson, A. F.; Khosravi, E.; Mohsin, M. A. *Polymer* **1994**, *35*, 3542-3548.
- (14) Heroguez, V.; Breunig, S.; Gnanou, Y.; Fontanille, M. *Macromolecules* **1996**, *29*, 4459-4464.
- (15) Heroguez, V.; Gnanou, Y.; Fontanille, M. *Macromolecules* **1997**, *30*, 4791.
- (16) Ito, K.; Tomi, Y.; Kawaguchi, S. *Macromolecules* **1992**, *25*, 1534-1538.
- (17) Tsukahara, Y.; Kohjiya, S.; Tsutsumi, K.; Okamoto, Y. *Macromolecules* **1994**, *27*, 1662-1664.
- (18) Terao, K.; Nakamura, Y.; Norisuye, T. *Macromolecules* **1999**, *32*, 711-716.
- (19) Terao, K.; Takeo, Y.; Tazaki, M.; Nakamura, Y.; Norisuye, T. *Polym. J.* **1999**, *31*, 193-198.

- (20) Terao, K.; Hokajo, T.; Nakamura, Y.; Norisuye, T. *Macromolecules* **1999**, *32*, 3690-3694.
- (21) Nemoto, N.; Nagai, M.; Koike, A.; Okada, S. *Macromolecules* **1995**, *28*, 3854-3859.
- (22) Kawaguchi, S.; Akaïke, K.; Zhang, Z.-M.; Matsumoto, H.; Ito, K. *Polym. J.* **1998**, *30*, 1004-1007.
- (23) Kratky, O.; Porod, G. *Rec. trav. chim.* **1949**, *68*, 1106-1122.
- (24) Wintermantel, M.; Fischer, K.; Gerle, M.; Ries, R.; Schmidt, M.; Kajiwara, K.; Urakawa, H.; Wataoka, I. *Angew. Chem. Int. Ed.* **1995**, *34*, 1472-1474.
- (25) Wataoka, I.; Urakawa, H.; Kajiwara, K.; Schmidt, M.; Wintermantel, M. *Polym. Int.* **1997**, *44*, 365-370.
- (26) Sheiko, S. S.; Gerle, M.; Moller, M. *Langmuir* **1997**, *13*, 5368.
- (27) Tsukahara, Y.; Tsutsumi, K.; Okamoto, Y. *Macromol. Chem., Rapid Commun* **1992**, *13*, 409-413.
- (28) Tsukahara, Y.; Ohta, Y.; Senoo, K. *Polymer* **1995**, *36*, 3413-3416.
- (29) Namba, S.; Tsukahara, Y.; Kaeriyama, K.; Okamoto, K.; Takahashi, M. *Polymer* **2000**, *41*, 5165-5171.
- (30) Murray, C. B.; Kagan, C. R.; Bawendi, M. G. *Annu. Rev. Mater. Sci.* **2000**, *30*, 545-610.
- (31) Alivisatos, A. P. *Science* **1996**, *271*, 933-937.
- (32) Krans, J. M.; van Ruitenbeek, J. M.; Fisun, V. V.; Yanson, I. K.; de Jongh, L. J. *Nature* **1995**, *375*, 767-769.
- (33) Bean, C. P.; Livingston, J. D. *J. Appl. Phys.* **1959**, *30*, 120S-129S.
- (34) Likharev, K. K. *IBM Journal of Research and Development* **1988**, *32*, 144-158.
- (35) Markovich, G.; Collier, C. P.; Henrichs, S. E.; Remacle, F.; Levine, R. D.; Heath, J. R. *Acc. Chem. Res.* **1999**, *32*, 415-423.
- (36) Eds: S. Luryi, J. X., A. Zaslavsky. *Future trends in Microelectronics: The Nano Millennium* **2002**, Wiley-Interscience, New York.
- (37) Ross, C. *Annu. Rev. Mater. Sci.* **2001**, *31*, 203.
- (38) Nguyen, P.; Gomez-Elipse, P.; Manners, I. *Chem. Rev.* **1999**, *99*, 1515-1548.
- (39) Kickelbick, G. *Prog. Polym. Sci.* **2002**, *28*, 83-114.
- (40) Biswas, M.; Mukherjee, A. *Adv. Polym. Sci.* **1994**, *115*, 89-123.
- (41) Hagihara, N.; Sonogashira, K.; Takahashi, S. *Adv. Polym. Sci.* **1981**, *41*, 149-179.
- (42) Foucher, D. A.; Tang, B. Z.; Manners, I. *J. Am. Chem. Soc.* **1992**, *114*, 6246-6248.

- (43) MacLachlan, M. J.; Ginzburg, M.; Coombs, N.; Coyle, T. W.; Raju, N. P.; Greedan, J. E.; Ozin, G. A.; Manners, I. *Science* **2000**, *287*, 1460-1463.
- (44) Ni, Y.; Rulkens, R.; Manners, I. *J. Am. Chem. Soc.* **1996**, *118*, 4102-4114.
- (45) Wang, X.-S.; Arsenault, A.; Ozin, G. A.; Winnik, M. A.; Manners, I. *J. Am. Chem. Soc.* **2003**, *125*, 12686-12687.
- (46) Sohn, B. H.; Cohen, R. E. *J. Appl. Polym. Sci.* **1997**, *65*, 723-729.
- (47) Förster, S.; Antonietti, M. *Adv. Mater.* **1998**, *10*, 195-217.
- (48) Antonietti, M.; Förster, S.; Hartmann, J.; Oestreich, S. *Macromolecules* **1996**, *29*, 3800-3806.
- (49) Klingelhofer, S.; Heitz, W.; Greiner, A.; Oestreich, S.; Förster, S.; Antonietti, M. *J. Am. Chem. Soc.* **1997**, *119*, 10116-10120.
- (50) Antonietti, M.; Wenz, E.; Bronstein, L.; Seregina, M. *Adv. Mater.* **1995**, *7*, 1000-1005.
- (51) Spatz, J. P.; Moessmer, S.; Hartmann, C.; Möller, M.; Herzog, T.; Krieger, M.; Boyen, H.-G.; Ziemann, P.; Kabius, B. *Langmuir* **2000**, *16*, 407-415.
- (52) Kaestle, G.; Boyen, H.-g.; Weigl, F.; Lengl, G.; Herzog, T.; Ziemann, P.; Riethmueller, S.; Mayer, O.; Hartmann, C.; Spatz, J. P.; Möller, M.; Ozawa, M.; Banhart, F.; Garnier, M. G.; Oelhafen, P. *Adv. Funct. Mater.* **2003**, *13*, 853-861.
- (53) Möller, M.; Spatz, J. P.; Roescher, A. *Adv. Mater.* **1996**, *8*, 337.
- (54) Moffitt, M.; Eisenberg, A. *Macromolecules* **1997**, *30*, 4363-4373.
- (55) Underhill, R. S.; Liu, G. *Chem. Mater.* **2000**, *12*, 2082-2091.
- (56) Underhill, R. S.; Liu, G. *Chem. Mater.* **2000**, *12*, 3633-3641.
- (57) Yan, X.; Liu, G.; Liu, F.; Tang, B. Z.; Peng, H.; Pakhomov, A. B.; Wong, C. Y. *Angew. Chem. Int. Ed.* **2001**, *40*, 3593-3596.
- (58) Clay, R. T.; Cohen, R. E. *Supramol. Sci.* **1996**, *2*, 183-191.
- (59) Ciebien, J. F.; Clay, R. T.; Sohn, B. H.; Cohen, R. E. *New J. Chem.* **1998**, *22*, 685-691.
- (60) Clay, R. T.; Cohen, R. E. *Supramol. Sci.* **1997**, *4*, 113-119.
- (61) Moeller, M.; Kuenstle, H.; Kunz, M. *Synth. Met.* **1991**, *41*, 1159-1162.
- (62) Ahmed, S. R.; Kofinas, P. *Macromolecules* **2002**, *35*, 3338-3341.
- (63) Templin, M.; Franck, A.; Du Chesne, A.; Leist, H.; Zhang, Y.; Ulrich, R.; Schadler, V.; Wiesner, U. *Science* **1997**, *278*, 1795-1798.

- (64) Ulrich, R.; Du Chesne, A.; Templin, M.; Wiesner, U. *Adv. Mater.* **1999**, *11*, 141-146.
- (65) Garcia, C. B. W.; Zhang, Y.; Mahajan, S.; DiSalvo, F.; Wiesner, U. *J. Am. Chem. Soc.* **2003**, *125*, 13310-13311.
- (66) Ziolo, R. F.; Giannelis, E. P.; Weinstein, B. A.; O'Horo, M. P.; Ganguly, B. N.; Mehrotra, V.; Russell, M. W.; Huffman, D. R. *Science* **1992**, *257*, 219-223.
- (67) Winnik, F. M.; Morneau, A.; Mika, A. M.; Childs, R. F.; Roig, A.; Molins, E.; Ziolo, R. F. *Can. J. Chem.* **1998**, *76*, 10-17.
- (68) Sidorov, S. N.; Bronstein, L. M.; Davankov, V. A.; Tsyurupa, M. P.; Solodovnikov, S. P.; Valetsky, P. M. *Chem. Mater.* **1999**, *11*, 3210-3215.
- (69) Thurn-Albrecht, T.; Schotter, J.; Kastle, G. A.; Emley, N.; Shibauchi, T.; Krusin-Elbaum, L.; Guarini, K.; Black, C. T.; Tuominen, M. T.; Russell, T. P. *Science* **2000**, *290*, 2126.
- (70) Kim, H.-C.; Jia, X.; Stafford, C. M.; Kim, D. H.; McCarthy, T. J.; Tuominen, M.; Hawker, C. J.; Russell, T. P. *Adv. Mater.* **2001**, *13*, 795-797.
- (71) Thurn-Albrecht, T.; DeRouchey, J.; Russell, T. P.; Jaeger, H. M. *Macromolecules* **2000**, *33*, 3250-3253.
- (72) Böker, A.; Knoll, A.; Elbs, H.; Abetz, V.; Müller, A. H. E.; Krausch, G. *Macromolecules* **2002**, *35*, 1319.
- (73) Huang, E.; Russell, T. P.; Mays, J. *Macromolecules* **1998**, *31*, 7641.
- (74) Shin, K.; Leach, K. A.; Goldbach, J. T.; Kim, D. H.; Jho, J. Y.; Tuominen, M.; Hawker, C. J.; Russell, T. P. *Nano Lett.* **2002**, *2*, 933-936.
- (75) Jeoung, E.; Galow, T. H.; Schotter, J.; Bal, M.; Ursache, A.; Tuominen, M. T.; Stafford, C. M.; Russell, T. P.; Rotello, V. M. *Langmuir* **2001**, *17*, 6396-6398.
- (76) Ruokolainen, J.; Mäkinen, R.; Torkkeli, M.; Mäkelä, T.; Serimaa, R.; Ten Brinke, G.; Ikkala, O. *Science* **1998**, *280*, 557-560.
- (77) Mäki-Ontto, R.; de Moel, K.; de Odorico, W.; Ruokolainen, J.; Stamm, M.; ten Brinke, G.; Ikkala, O. *Adv. Mater.* **2001**, *13*, 117-121.
- (78) Sidorenko, A.; Tokarev, I.; Minko, S.; Stamm, M. *J. Am. Chem. Soc.* **2003**, *125*, 12211-12216.
- (79) Fukunaga, K.; Elbs, H.; Magerle, R.; Krausch, G. *Macromolecules* **2000**, *33*, 947.
- (80) Crooks, R. M.; Lemon, B. I., III; Sun, L.; Yeung, L. K.; Zhao, M. *Top. Curr. Chem.* **2001**, *212*, 81-135.

- (81) Minko, S.; Kiriy, A.; Gorodyska, G.; Stamm, M. *J. Am. Chem. Soc.* **2002**, *124*, 10192-10197.
- (82) Gorodyska, G.; Kiriy, A.; Minko, S.; Tsitsilianis, C.; Stamm, M. *Nano Lett.* **2003**, *3*, 365-368.
- (83) Braun, E.; Eichen, Y.; Sivan, U.; Ben-Yoseph, G. *Nature* **1998**, *391*, 775-778.
- (84) Richter, J.; Seidel, R.; Kirsch, R.; Mertig, M.; Pompe, W.; Plaschke, J.; Schackert, H. K. *Adv. Mater.* **2000**, *12*, 507-510.
- (85) Crangle, J. *The magnetic properties of solids* **1977**, Edward Arnold Limited, London.
- (86) Cullity, B. D. *Introduction to Magnetic Materials* **1972**, Addison-Wesley Publishing Company: Reading, MA.
- (87) Meiklejohn, W. H. *J. Appl. Phys.* **1962**, *33*, 1328-1335.
- (88) Frenkel, J.; Dorfman, J. *Nature* **1930**, *126*, 274.
- (89) Kittel, C. *Phys. Rev.* **1946**, *70*, 965-971.
- (90) Brown, W. F. *J. Appl. Phys.* **1959**, *30*, 130S.
- (91) Brown, W. F. *Phys. Rev.* **1963**, *130*, 1677.
- (92) Dickson, D. P. E.; Reid, N. M. K.; Hunt, C.; Williams, H. D.; El-Hilo, M.; O'Grady, K. *J. Magn. Magn. Mater.* **1993**, *125*, 345-350.
- (93) Chantrell, R. W. *J. Magn. Magn. Mater.* **1991**, *95*, 365-378.
- (94) Aharoni, A. *J. Appl. Phys.* **1985**, *57*, 4702-4705.
- (95) El-Hilo, M.; O'Grady, K.; Chantrell, R. W. *J. Magn. Magn. Mater.* **1992**, *109*, L164-L168.
- (96) Néel, L. *Compt. Rend.* **1949**, *228*, 664.
- (97) Chantrell, R. W.; El-Hilo, M.; O'Grady, K. *IEEE Trans. Magn.* **1991**, *27*, 3570.
- (98) Wohlfarth, E. P. *J. Phys. F: Metal Phys.* **1980**, *10*, L241-L246.
- (99) Heukelom, W.; Broeder, J. J.; van Reijen, L. L. *Journal de Chimie Physique et de Physico-Chimie Biologique* **1954**, *51*, 474-480.
- (100) Bean, C. P.; Jacobs, I. S. *J. Appl. Phys.* **1956**, *27*, 1448-1452.
- (101) Odenbach, S.; Editor. *Ferrofluids* **2002**, Springer.
- (102) Neuringer, J. L.; Rosensweig, R. E. *Phys. Fluids* **1964**, *7*, 1927.
- (103) Rosensweig, R. E.; Nestor, J. W.; Timmins, R. S. *Proc. A.I.C.H.E. (Amer. Inst. Chem. Eng.)-I. Chem. E. (Inst. Chem. Eng.) Joint Meet., London, 1965* **1965**, 104-118.

- (104) Cowley, M. D.; Rosensweig, R. E. *Journal of Fluid Mechanics* **1967**, *30*, 671-688.
- (105) McTague, J. P. *J. Chem. Phys.* **1969**, *51*, 133-136.
- (106) Fertman, V. E. *Magnetic fluids guidebook: properties and applications* **1990**, Hemisphere Publishing Co.
- (107) Blums, E.; Cebers, A.; Maiorov, M. M. *Magnetic fluids* **1997**, Walter de Gruyter, Berlin.
- (108) Berkovsky, B. M.; Medvedev, V. F.; Krakov, M. S. *Magnetic fluids engineering applications* **1993**, Oxford Science Publications.
- (109) Trindade, T.; O'Brien, P.; Pickett, N. L. *Chem. Mater.* **2001**, *13*, 3843-3858.
- (110) Haug, H.; Koch, S. W. *Quantum theory of the optical and electronic properties of semiconductors* **1990**, World Scientific Publishing Co. Pte. Ltd.; London.
- (111) Steigerwald, M. L.; Brus, L. E. *Acc. Chem. Res.* **1990**, *23*, 183-188.
- (112) Xia, Y.; Yang, P.; Sun, Y.; Wu, Y.; Mayers, B.; Gates, B.; Yin, Y.; Kim, F.; Yan, H. *Adv. Mater.* **2003**, *15*, 353-389.
- (113) Weller, H. *Adv. Mater.* **1993**, *5*, 88-95.
- (114) Fendler, J. H. *Chem. Rev.* **1987**, *87*, 877-899.
- (115) Ed: Nag, B. R. *Physics of Quantum Well Devices* **2000**, Kluwer, Dordrecht, The Netherlands.
- (116) Barbic, M.; Mock, J. J.; Smith, D. R.; Schultz, S. *J. Appl. Phys.* **2002**, *91*, 9341-9345.



## Chapter 2 Methods

### 2.1 Polymerization methods

#### 2.1.1 Atom transfer radical polymerization (ATRP)

Over the past decades, the living polymerization technique has expanded to include all chain-growth polymerization methods: cationic, anionic, transition metal-catalyzed, and recently, free radical polymerization. An ideal living polymerization is a chain-growth polymerization in which irreversible chain termination and chain transfer are absent. Therefore, once a chain is initiated, it will grow until no monomer is left. Unless a terminating agent is introduced, the living chain will remain active, so block copolymers can be synthesized via sequential addition of different monomers. Provided that the initiation efficiency is 100% and exchange between species of various reactivities is fast, the average molecular weight of the final polymer will be determined simply by the initial monomer/initiator ratio and the molecular weight distribution will be narrow. However, in practice, it is impossible to completely avoid chain transfer and chain termination reactions. Very often, the rates of these side reactions are controlled to be sufficiently slow such that well-defined polymers can be prepared. In such cases, the polymerizations are termed “controlled/‘living’ polymerizations” to indicate that, although chain transfer or chain termination may occur to some extent, the polymerizations are still as synthetically useful as the true living polymerization.

The development of living ionic polymerization methods, such as anionic polymerization, allowed for the preparation of well-defined polymers with controlled chain lengths and end functionalities, and the synthesis of well-defined block and graft copolymers. However, only a limited number of monomers can be used, and the presence of functionalities in the monomers causes undesirable side reactions. Moreover, these polymerizations have to be carried out with nearly complete exclusion of moisture and often at very low temperature.

In comparison, radical polymerizations provide numerous advantages over ionic polymerizations: suitable to a large variety of monomers, tolerant to functional groups and impurities, mild reaction conditions, and so on. So radical polymerization has become the most popular industrial method to produce materials such as plastics, rubbers and fibers.<sup>1</sup>

However, the lack of control over the polymer structure is the main drawback of conventional radical polymerization, from which polymers with high molecular weights and high polydispersities are generally produced, due to the slow initiation, fast propagation and subsequent chain transfer or termination.

Conventional radical polymerization has been revolutionized by the advent of methods named controlled/“living” radical polymerizations (CRP) to control the polymerization process with respect to molecular weight and polydispersity. A major difference between conventional radical polymerization (i.e., azobis(isobutyronitrile)/peroxide-initiated processes) and CRP is the lifetime of the propagating radical during the course of the reaction. In conventional radical processes, radicals generated by decomposition of initiator undergo propagation and bimolecular termination reactions within a second. In contrast, the lifetime of a growing radical can be extended to several hours in a CRP, enabling the preparation of polymers with predefined molecular weight, low polydispersity, controlled composition, and functionality.

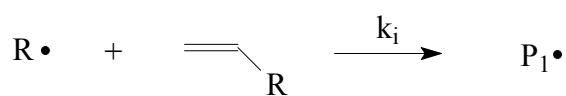
In CRP processes, the mechanism to extend the lifetime of growing radical utilizes a dynamic equilibration between dormant and active sites with rapid exchange between the two states. CRP requires the use of either persistent radical species or transfer agents to react with propagating radicals to form the dormant species. Conversely, propagating radicals can be regenerated from the dormant species by an activation reaction.

The three main CRP techniques are nitroxide-mediated polymerization (NMP),<sup>2</sup> atom transfer radical polymerization (ATRP)<sup>3</sup> and reversible addition/fragmentation chain-transfer (RAFT) polymerization.<sup>4</sup> While these three systems possess different components, general similarities in the CRP processes can be seen in the use of initiators, radical mediators (i.e., persistent radicals or transfer agents), and in some cases catalysts. Radical mediators are used to lower the radical concentration and hence significantly decrease termination events. Concomitantly, the rate of polymerization is strongly decreased. Among CRP techniques, transition-metal-mediated ATRP is regarded as the most successful method. Since Matyjaszewski<sup>3</sup> and Sawamoto<sup>5</sup> reported two different catalyst systems independently in 1995, a number of different transition-metal complexes have been used in ATRP, including systems based on Cu,<sup>3</sup> Ru,<sup>5</sup> Fe,<sup>6,7</sup> Ni,<sup>8</sup> Pd,<sup>9</sup> Rh,<sup>10</sup> Re,<sup>11</sup> and Mo.<sup>12</sup> So far, copper(I)-catalyzed ATRP is the most popular and successful one.

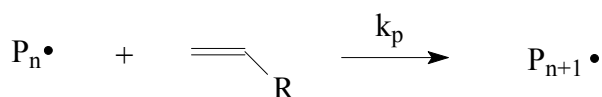
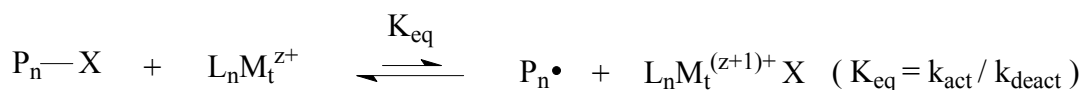
### 2.1.1.1 Mechanism and kinetics of ATRP

In ATRP, the propagating radicals are generated via reversible metal-catalyzed atom transfer, as shown in Scheme 2-1. Fast, reversible deactivation of radicals to dormant species lower the radical concentration significantly and thus minimize the irreversible termination. The dormant species can be reactivated yielding free radicals. To obtain good control on a radical polymerization, two prerequisites should be met: (i) the equilibrium between radicals and dormant species must lie strongly to the side of the dormant species to assure that the overall radical concentration remains very low and the rate of irreversible termination is negligible compared to the propagation rate; (ii) the exchange rate between radicals and dormant species must be faster than the rate of propagation so that all polymer chains have equal probability of growing.

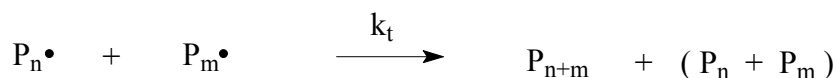
#### Initiation



#### Propagation



#### Termination



**Scheme 2-1.** General mechanism for ATRP (*RX*: alkyl halide, initiator; *L<sub>n</sub>*: ligand; *M<sub>t</sub>*: transition metal)

The kinetics of ATRP is discussed using copper-mediated ATRP as an example. In homogeneous systems, the rate of ATRP has shown to be the first order with respect to the monomer and initiator. The rate of the polymerization is also influenced by the ratio of

activator to deactivator. By neglecting the termination step and using a fast equilibrium approximation<sup>13</sup> one can obtain the rate of propagation,  $R_p$

$$R_p = k_{app} [P \cdot][M] = k_p K_{eq} [I] \frac{[Cu(I)]}{[Cu(II)]} [M] \quad \text{Eq. 2-1}$$

$$\text{where } K_{eq} = \frac{k_{act}}{k_{deact}} = \frac{[P \cdot][Cu(II)]}{[PX][Cu(I)]}$$

Consistent with the derived rate law, kinetic studies of ATRP using soluble catalyst systems have proven that the rate of polymerization is first order with respect to monomer, alkyl halide (initiator), and copper(I) complex concentrations.<sup>13</sup>

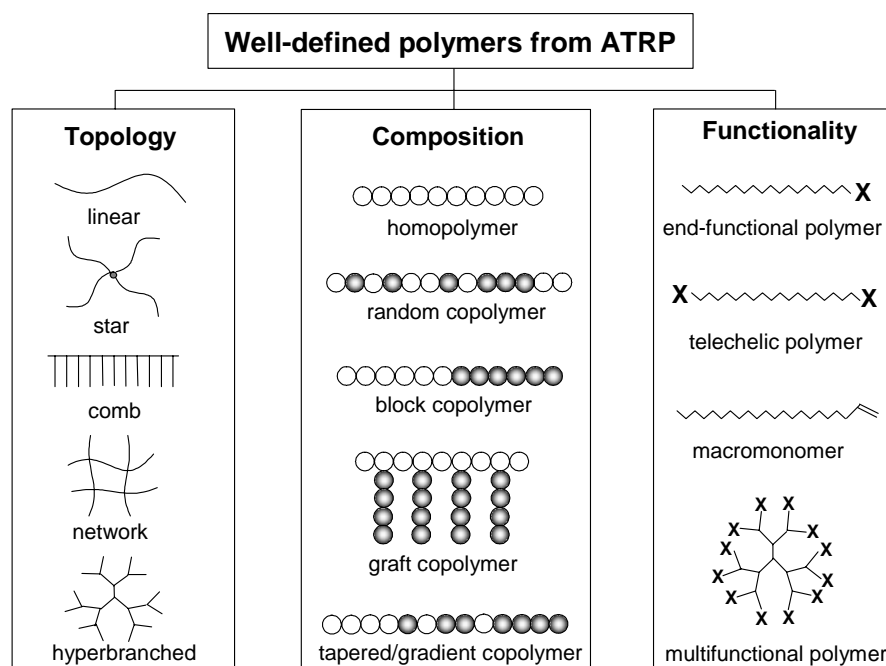
Determining the precise kinetic order with respect to the deactivator (Cu(II) complex) concentration was complicated due to the spontaneous generation of Cu(II) during the polymerization via the persistent radical effect.<sup>13</sup> As shown in Scheme 2-1, a reactive radical and a stable Cu(II) species are generated in the atom transfer step. If the initial concentration of Cu(II) is not high enough to ensure a fast deactivation ( $R_{deact} = k_{deact}[Cu(II)][R \cdot]$ ), the irreversible coupling and/or disproportionation of radicals will occur, and the concentration of Cu(II) builds up. Eventually, the concentration of Cu(II) is sufficiently high that the deactivation step is much faster than the rate at which the radicals react with each other in an irreversible termination step. This is so called the persistent radical effect. Thus, a controlled/“living” polymerization will be achieved.

As an example, in the bulk polymerization of styrene using 1-phenylethyl bromide as the initiator and CuBr/4,4'-di(5-nonyl)-2,2'-dipyridyl as the catalyst,<sup>13</sup> the equilibrium constant,  $K_{eq}$ , is approximately  $4 \times 10^{-8}$  at 110 °C.<sup>13</sup> The initial concentrations of all the species are  $[RBr]_0 = [Cu(I)]_0 = 0.1$  M and  $[R \cdot]_0 = [Cu(II)]_0 = 0$  M. The concentrations of Cu(I) and halide end groups will remain approximately constant throughout the polymerization, and thus  $[R \cdot][CuBr_2] = K_{eq}[RX][CuBr] = 4 \times 10^{-10}$  M<sup>2</sup>. During the initial stage of the polymerization, the radical and Cu(II) concentrations will increase to about  $10^{-6}$  M. At these concentrations the radicals will couple rapidly, resulting in the formation of Cu(II) irreversibly. Along with the polymerization more Cu(II) will be formed until a radical concentration of  $10^{-7}$  M and a deactivator concentration of  $10^{-3}$  M are reached. At these concentrations the rate of radical coupling ( $k_t[R \cdot]^2$ ) will be much slower than the rate of deactivation ( $k_{deact}[R \cdot][Cu(II)]$ ), and a controlled/“living” polymerization will ensue. It has been found that a small amount of the polymer chains are terminated during this

initial non-stationary stage, the majority of the chains will continue the polymerization and thus well-defined polymers can still be obtained.

As shown in Scheme 2-2, ATRP has been used for the synthesis of well-defined polymers with various topologies, compositions, and functionalities, by using functional initiators, functional monomers and copolymerization. Because of its radical nature, ATRP is tolerant to many functional groups in monomers leading to polymers with functionalities along the chains. By using functional initiators, functionalities such as vinyl, hydroxyl, epoxide, cyano and other groups have been incorporated at one chain end, while the other chain end remains alkyl halide capable of reinitiating the polymerization of other monomers.

A unique combination of initiator, metal, ligand, deactivator, solvent, temperature, and reaction time must be employed for the ATRP of each particular monomer. Therefore, understanding the role of each component of ATRP is crucial for obtaining well-defined polymers and for expanding the scope of ATRP to other monomers.



**Scheme 2-2.** Various well-defined polymers with different topologies, compositions, and functionalities which can be synthesized via ATRP.

### 2.1.1.2 Monomers

ATRP has been used for the controlled polymerizations of a wide range of vinyl monomers such as styrenes,<sup>13-15</sup> acrylates,<sup>16,17</sup> methacrylates,<sup>18,19</sup> acrylonitrile,<sup>20</sup> (meth)acrylamides,<sup>21,22</sup> dienes<sup>23</sup> and other monomers which contain substituents capable of stabilizing propagation radicals. Very recently, living radical polymerizations of vinyl acetate<sup>24</sup> and vinyl chloride,<sup>25</sup> which lack a conjugating substituent (for the stabilization of radicals), were reported by Sawamoto and Percec respectively using special designed catalyst systems. The current generation of catalyst systems is not sufficiently efficient to polymerize less reactive monomers, such as ethylene and  $\alpha$ -olefins, which produce non-stabilized, highly reactive radicals. Acrylic and methacrylic acid cannot be polymerized with currently available ATRP catalysts, because these monomers react rapidly with the metal complexes to form metal carboxylates which cannot be reduced to active ATRP catalysts. In addition, nitrogen-containing ligands can be protonated, which interferes with the metal complexation ability. However, the corresponding *tert*-butyl esters of these monomers, which are easily hydrolyzed, can be polymerized using ATRP. A better understanding of the transition metal chemistry involved in ATRP and better ligand design may allow these monomers to be polymerized directly.

### 2.1.1.3 Initiators

Alkyl halides (RX) are the most common initiators for ATRP. The halide group, X, must rapidly and selectively migrate between the growing chain and the transition metal complex. So far, bromine and chlorine are the halogens affording the best molecular weight control. Iodine works well for acrylate polymerizations; however, in styrene polymerizations the heterolytic elimination of hydrogen iodide is too fast at high temperatures.<sup>26</sup> Some pseudohalogens, specifically thiocyanates, have also been used successfully to initiate polymerizations of acrylates and styrenes.<sup>26</sup>

In general, any alkyl halide with activating substituents on the  $\alpha$ -carbon, such as aryl, carbonyl, and allyl groups, can potentially be used as ATRP initiators. Polyhalogenated compounds (CCl<sub>4</sub> and CHCl<sub>3</sub>) and compounds with a weak R-X bond, such as N-X, S-X, and O-X, can also presumably be used as ATRP initiators. There is an upper limit to the stability of the initiating radicals beyond which it also becomes an inefficient initiator. For example, trityl halides are poor initiators for ATRP. The list of potential ATRP initiators

includes not only small molecules but also macromolecular species (macroinitiator or polyinitiator) that can be used to synthesize block/graft copolymers.

Generally, for the selection of ATRP initiators one has to consider the ratio of the apparent initiation rate constant ( $k_i K_0$ , where  $k_i$  and  $K_0$  are defined in Scheme 2-1) to the apparent propagation rate constant ( $k_p K_{eq}$ , defined in Scheme 2-1 as well). If the product  $k_i K_0$  is much less than  $k_p K_{eq}$ , then initiation will be incomplete during the polymerization, consequently the molecular weights and polydispersities will be high.

To select an initiator for a monomer in ATRP, the structure of the alkyl group (R) in the initiator should be similar to that of the dormant polymer species. Thus, 1-phenylethyl halides resemble dormant polystyrene chain ends,  $\alpha$ -halopropionates approximate dormant acrylate end groups, and  $\alpha$ -halopropionitriles are homologous to dormant acrylonitrile chain ends. This guideline holds true for secondary radicals but not for tertiary radicals. For example,  $\alpha$ -haloisobutyrate are not the best initiators for MMA, most likely due to the  $\beta$ -strain effect.<sup>27</sup> For the selection of initiators that are not structurally related to the dormant polymer chain end, it is better to use organic halides that form less reactive radicals with higher efficiency than the dormant polymer chain ends. For example, alkyl 2-chloroisobutyrate and arenesulfonyl chlorides are good initiators for styrene, alkyl acrylates, and alkyl methacrylate ATRP, but chloroacetates, 2-chloropropionates, and 1-phenylethyl chloride are poor initiators for the polymerization of methyl methacrylate.

#### 2.1.1.4 Catalyst system: transition metals and ligands

In the case of copper-mediated ATRP, the role of the Cu(I) complex is the generation of radicals via atom transfer. In general, the rate of polymerization is first order with respect to the concentration of ATRP catalyst.

There are several important criteria for the successful design of ATRP catalysts: (i) the metal must possess an accessible one-electron redox couple to promote atom transfer, (ii) the oxidation potential should be low, but optimal for reversible halogen atom transfer, (iii) there should be good reversibility between the reduced and oxidized forms of the catalysts — favored by ligands which minimize changes to the metal coordination sphere between the reduced and oxidized states, and (iv) the metal center must be sterically unencumbered in its reduced form to allow a halogen atom to be accommodated.

The most important system variables in selecting or designing good ATRP catalysts are the position of the atom transfer equilibrium and the dynamics of exchange between the dormant and active species. The position of equilibrium depends upon the nature of the metal and ligands. Generally, more electron donating ligands better stabilize the higher oxidation state of the metal and accelerate the polymerization. The equilibrium constant required for the successful polymerization of methacrylates, styrenes, acrylates, and acrylonitrile is ranging from  $10^{-6}$  to  $10^{-10}$ . The dynamics of exchange between dormant and active species is also important for ATRP. The deactivation step must be very fast, ( $k_d \approx 10^{7\pm 1} \text{ M}^{-1}\text{s}^{-1}$ ), otherwise the polymerization will display poor control over molecular weights.

For ATRP catalysts that are insoluble in relatively non-polar media such as styrene and methyl methacrylate, ligands possessing long alkyl chains serve to increase the complex's solubility, hence a homogeneous polymerization system can be obtained. For example, when bipyridine is used in copper-mediated ATRP, the copper halide is sparingly soluble in the polymerization medium. Bipyridyl ligands with long alkyl chains at the 4,4'-positions (such as dNbipy, 4,4'-di(5-nonyl)-2,2'-bipyridine) can completely solubilize the copper halide.<sup>28</sup> Qualitatively, ATRP behaves in a similar manner whether or not the catalyst is soluble in the polymerization medium, because the catalyst is not bound to the growing chain. Only somewhat higher polydispersities are observed in heterogeneous copper-mediated ATRP due to the lower concentration of the Cu(II) complex (deactivator) and consequently a slower deactivation process.

### 2.1.1.5 Deactivator

The deactivator in ATRP is the higher oxidation state metal complex formed after atom transfer, and it plays an important role in ATRP in reducing the polymerization rate and the polydispersity of the final polymer. Equation 2-2 defines the relationship between polydispersity and concentration of deactivator for a system with fast initiation and deactivation.<sup>29,30</sup>

$$\frac{M_w}{M_n} = 1 + \left( \frac{2}{p} - 1 \right) \left( \frac{[\text{RX}]_0 k_p}{k_{deact} [\text{D}]} \right) \quad \text{Eq. 2-2}$$

where  $p$  is the monomer conversion,  $[RX]_0$  is the concentration of initiator, and  $[D]$  is the concentration of deactivator.

For complete conversion ( $p = 1$ ), Equation 2-2 can be simplified

$$\frac{M_w}{M_n} = 1 + \left( \frac{[RX]_0 k_p}{k_{deact} [D]} \right) \quad \text{Eq. 2-3}$$

From Equation 2-3 several conclusions can be drawn. First, the final polydispersity should be higher for shorter polymer chains, because of the higher value of  $[RX]_0$ . This result can be rationalized by the fact that relative to longer chains, the growth of smaller chains involves fewer activation-deactivation steps and therefore fewer opportunities for controlled growth. Second, the final polydispersity should be higher for higher values of the ratio,  $k_p/k_{deact}$ . Thus, for the hypothetical polymerization of two monomers with different  $k_p$  values, such as methyl acrylate and styrene, and the same  $k_{deact}$ , the polymerization with the larger  $k_p$ , methyl acrylate in this case, will yield polymer with the higher polydispersity. Third, the polydispersity of the final polymer should decrease with an increasing concentration of deactivator.

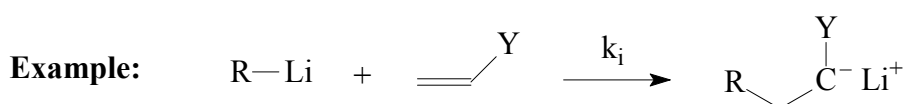
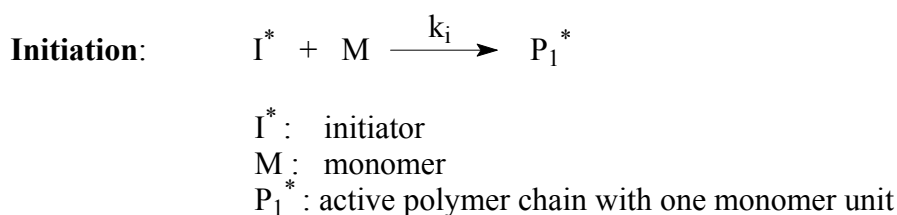
In ATRP the concentration of deactivator continuously, but slowly, increases with increasing conversion due to the persistent radical effect. While the final molecular weights do not depend upon the concentration of deactivator, the rate of polymerization will decrease with its increasing concentration. In the case of copper-mediated ATRP, it is possible to increase the observed polymerization rate by adding a small amount of metallic Cu(0), which comproportionates with Cu(II) to regenerate Cu(I). This approach also allows for a significant reduction in the amount of catalyst required for polymerization.<sup>31</sup>

### 2.1.2 Anionic polymerization

The interest in anionic polymerization has increased continuously since Szwarc first reported the living nature of the anionic polymerization of styrenes and dienes in 1956.<sup>32,33</sup> One important aspect of the term living polymerization refers to the fact that the polymerization occurs in the absence of irreversible termination and chain transfer. Thus the molecular weight is determined by the stoichiometry of the reaction and the monomer conversion. The living nature of the propagating chain allows the synthesis of block copolymers. Living anionic polymerization has been used to prepare well-defined polymers varying in topology, composition, end functionality, and tacticity.

Similar to other polymerizations, anionic polymerization proceeds in three principal steps: initiation, propagation, and finally termination of the reaction by an electrophile.

The initiation step is the formation of the carbanionic adduct by a nucleophilic attack of an initiator on the double bond of a monomer. The carbanion of this adduct ( $P_1^*$ ) possesses an electronic structure which remains nearly the same through further addition of monomer units during the polymerization.



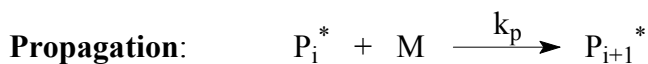
Y: electron withdrawing group

**Scheme 2-3.** Reaction scheme for the initiation step of an anionic polymerization

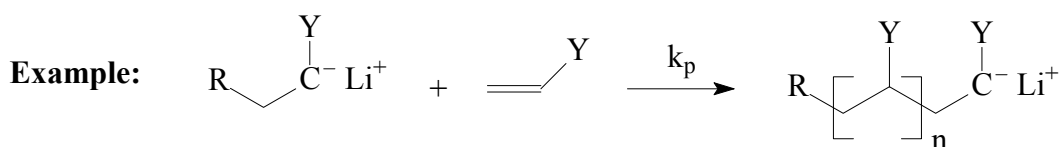
The initiator required to polymerize a monomer depends on the reactivity of the monomer towards nucleophilic attack. The monomer reactivity increases with increasing ability to stabilize the carbanion charge. Very strong nucleophiles such as amide anions<sup>34</sup> or alkyl carbanions are needed to polymerize monomers with relatively weak electron-withdrawing substituents, such as styrene and butadiene. Weaker nucleophiles, such as alkoxide or hydroxide ions, can initiate the polymerization of monomers with strong

electron-withdrawing substituents, such as acrylonitrile, methyl methacrylate and methyl vinyl ketone.

The propagation step proceeds with the rate constant constant,  $k_p$ .

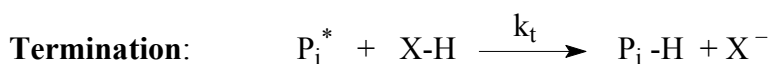


$P_i^*$  : active polymer chain with i monomer units

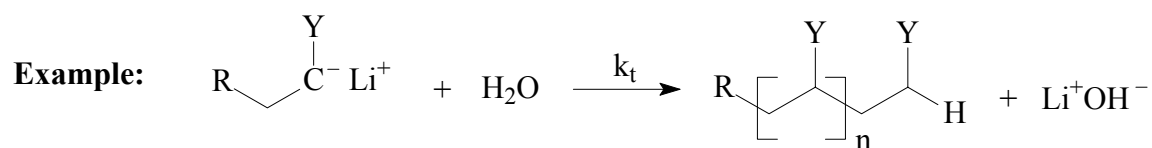


*Scheme 2-4. Reaction scheme for the propagation step of an anionic polymerization*

As a requirement to obtain a constant number of carbanionic centers and high initiating efficiency, the rate of initiation must be higher than the rate of propagation. Above a certain limit,  $k_i/k_p \geq 4/DP_{n,max}$  ( $DP_{n,max}$  is the maximum degree of polymerization), initiation occurs with sufficient rate constant and no effect of the rate of initiation is observed on the molecular weight distribution.<sup>35,36</sup>



X-H : hydrogen transfer agent



*Scheme 2-5. Reaction scheme for the termination step of an anionic polymerization*

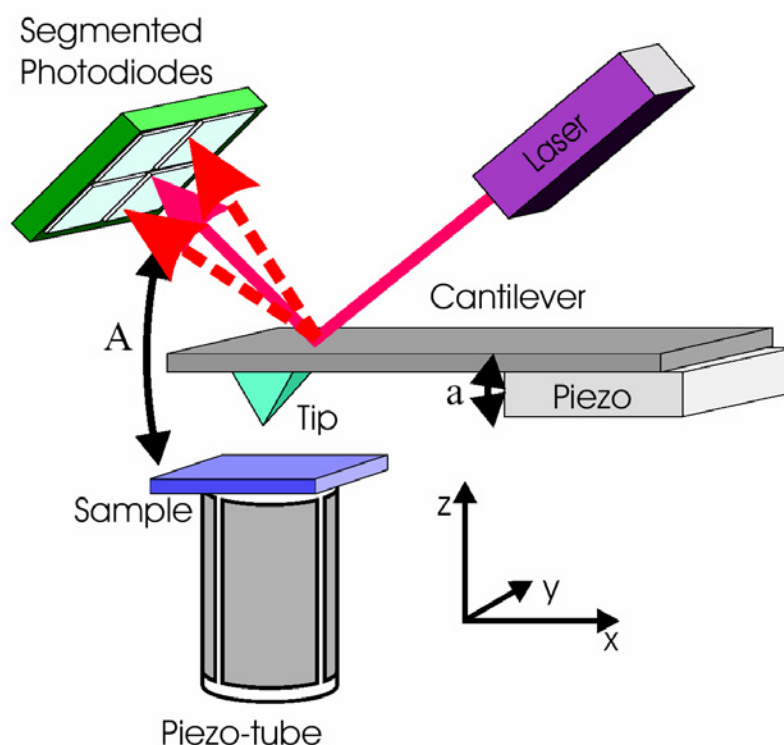
Termination occurs mainly by a hydrogen transfer agent, which can be present as impurity in the reaction system or is added after the complete consumption of monomer. In some cases  $X^-$  is able to reinitiate, then the reaction shown Scheme 2-5 is a transfer reaction. Sometimes, termination is also observed as a side reaction of propagating chain with functional group of monomer.

## 2.2 Characterization methods

In this part, characterization methods that are not of common use in the laboratory are described in more detail. For the common methods, only a brief description of the instrument's characteristics is given.

### 2.2.1 Scanning force microscopy (SFM)

SFM has become a versatile method for characterization of the microstructure of polymeric materials in the nanometer scale.<sup>37</sup> In addition to the topological resolution, SFM can distinguish surface areas differing in local mechanical properties and composition, respectively.<sup>38,39</sup> Mechanical properties, such as viscoelasticity, friction, and adhesion, as well as long-range electrostatic and steric forces can be characterized in the scale of a few nanometers.



**Scheme 2-6.** Schematic setup of a scanning force microscope. The tip is located at the end of a cantilever. A laser is reflected from the cantilever onto a photodiode. Either the tip or the sample is positioned in 3D space by a piezo element. In a dynamic mode of operation the cantilever is excited by a piezo element causing its vibration at an amplitude  $A$ .

A schematic setup of a scanning force microscope is shown in Scheme 2-6. A tip positioned at the very end of a cantilever is used as probe. A laser is focussed onto the end of the cantilever and reflected into the center of a segmented photodiode. Any forces acting on the tip result in a bending (vertical forces) or twisting (lateral forces) of the cantilever and therefore result in a different reflection angle. The difference of the output of the photodiodes is used as output signal, which is proportional to the deflection of the cantilever. Depending on the mode of operation the photodiode signal is used directly or as a feedback signal as discussed below. A feedback loop continuously checks the feedback signal, compares it to some user defined setpoint value and adjusts the height of the tip over the sample such that the difference is minimized. Stable operation is possible if the feedback signal is monotonous in the tip-surface distance. The tip is then kept at a height corresponding to a constant interaction over the sample surface. Either the cantilever or the sample is mounted to a piezoelectric element, which provides the necessary means to position the tip relative to the sample in 3D space.

The instrument used in this work is a Digital Instruments Dimension 3100 SFM with a Nanoscope III Controller. Of particular interest in determining topography and phase morphology of polymers is Tapping Mode SFM.

Tapping Mode measures topography by lightly tapping the surface with an oscillating probe tip. This technique eliminates lateral forces that can damage soft samples and reduce image resolution. Tapping Mode imaging is implemented in ambient air by oscillating the cantilever at or near its resonance frequency using a piezoelectric crystal. The piezo motion causes the cantilever to oscillate with a high amplitude (typically equal or greater than 20 nm) when the tip is not in contact with the surface. The oscillating tip is then moved toward the surface until it begins to slightly touch, or “tap” the surface. During scanning, the vertically oscillating tip alternately contacts the surface and lifts off, generally at a frequency of 250 - 350 kHz. As the oscillating cantilever begins to intermittently contact the surface, the cantilever oscillation amplitude is reduced due to energy loss caused by the tip contacting the surface. The oscillation amplitude of the tip is measured. A digital feedback loop then adjusts the tip-sample separation to maintain a constant amplitude. The reduction in oscillation amplitude is used to identify and measure surface features.

Two important types of images which are used in this work described in the following:

**Height image:** The vertical position of the probe tip is monitored by noting changes in the length of the z-axis on the xyz scanning piezo tube. The input voltage to the scanning

piezo tube is proportional to the length of the tube. The change in the z-axis is plotted as a topographical map of the sample surface. Height data is a good measure of the height of surface features but does not show distinct edges of these features.

**Phase image:** This type of imaging monitors the change in phase offset, or phase angle, of the oscillating cantilever with respect to the phase offset of the input drive signal (to the drive piezo). The phase of the drive signal is compared to the phase of the cantilever response signal on the photo diode detector. The phase offset between the two signals is defined as zero for the cantilever oscillating freely in air. As the probe tip engages the sample surface, the phase offset of the oscillating cantilever changes by a certain angle with respect to the phase offset of the input drive signal. As regions of differing elasticity are encountered on the sample surface, the phase angle between the two signals changes. These changes in phase offset are due to differing amounts of damping experienced by the probe tip as it rasters across the sample surface. This phase shift is very sensitive to variations in material properties such as adhesion and viscoelasticity. Applications include contaminant identification, mapping of components in composite materials, and differentiating regions of high and low surface adhesion or hardness.

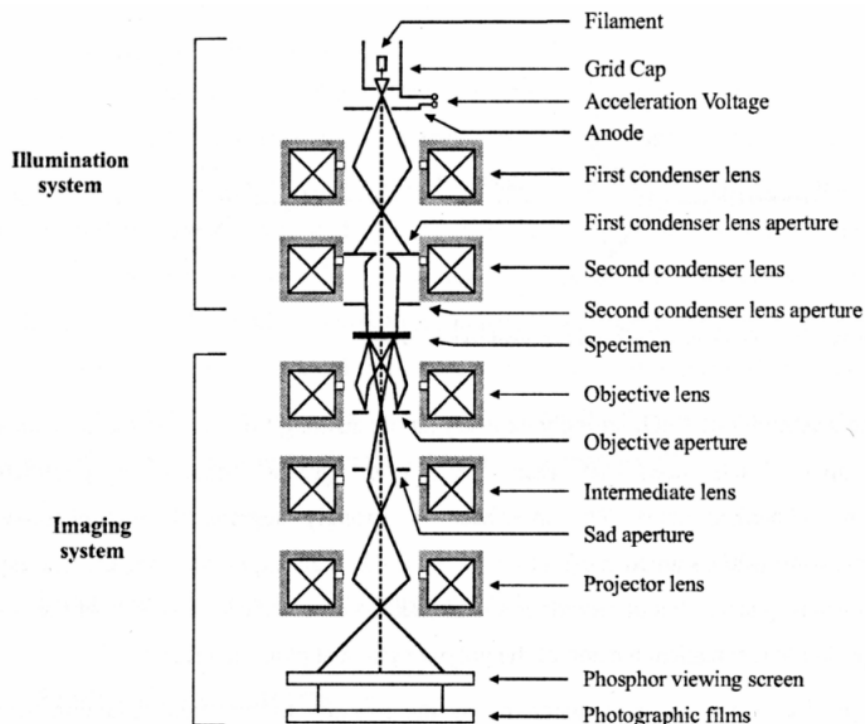
### 2.2.2 Transmission electron microscopy (TEM)<sup>40,41</sup>

TEM is one of the most popular analytical tools for the investigation of polymer microstructures. It has been widely used in the characterization of polymer morphologies. The transmission electron microscope overcomes the limitation of the optical microscope, the spatial resolution of which is limited to about half the wavelength of the visible light. In the 1930's, TEM provided the first insight into structural features on a sub-micrometer scale.

Presently, the resolution limit in transmission electron microscopy is in the order of about 0.1 nm using an acceleration voltage of about  $10^4$ - $10^5$  V. Scheme 2-7 shows a schematic cross-section of a transmission electron microscope which typically contains two parts, the illumination and the imaging system.

The former consists of the electron gun and the first and second condenser lenses. Electrons are emitted from a V-shaped heated tungsten filament whereas the emitted electron density is controlled by the voltage applied at the filament. A grid cap fading out parts of the electron emitting cathode allows the generation of a spot-shaped electron beam.

A high voltage field accelerates the emitted electrons which reach the system of condenser lenses in the illumination system after crossing the ring anode. These lenses regulate the intensity and refocus the electron beam. The specimen is then hit by an intense, parallel beam of monoenergetic electrons.



*Scheme 2-7. Schematic cross section of a conventional transmission electron microscope*

The imaging system is built up by the objective lens, the intermediate lens and their corresponding apertures, the projector lens, a phosphor viewing screen, and the photographic film. The most important parts of the imaging system are the objective lens and objective aperture which can either generate a bright-field or a dark-field image of the specimen. The apertures act as filters mainly for elastically or inelastically scattered or transmitted electrons and are necessary to create a phase contrast in the sample. Specimens of low-density hydrocarbon materials like polymers must be less than 100 nm thick while high-density metals should be less than 20 nm thick.

Bright field is the most widely used mode of transmission electron microscopy imaging, selecting the weakly scattered and transmitted electrons by an objective aperture. In consequence dark areas in the image correspond to strongly scattering areas in the

specimen corresponding to areas of higher mass thickness (density  $\times$  thickness). For dark-field imaging only elastically scattered electrons in defined angles are used.

Usually, due to relatively similar electron densities, the contrast between most organic polymers is rather limited and sometimes too low to render an image via TEM. A variety of methods are now available to enhance the contrast in TEM images. Staining is one of the most popular techniques for contrast enhancement, in which a staining agent (for example, chemicals with high electron density like heavy metals) selectively reacts with or diffuses into one phase of the polymer microstructure. In this work, the poly(acrylic acid) core of polymer brushes are selectively stained via coordination with transition metal ions.

In this work, TEM images were taken with a Zeiss CEM 902 electron microscope operated at 80 kV or a LEO 922 OMEGA electron microscope operated at 200 kV. Both machines are equipped with an in-column energy filter, which is important for analytical purposes such as electron spectroscopic imaging (ESI) and electron energyloss spectroscopy (EELS). So these machines are also called energy filtering transmission electron microscopes (EFTEM).

### 2.2.3 Light scattering

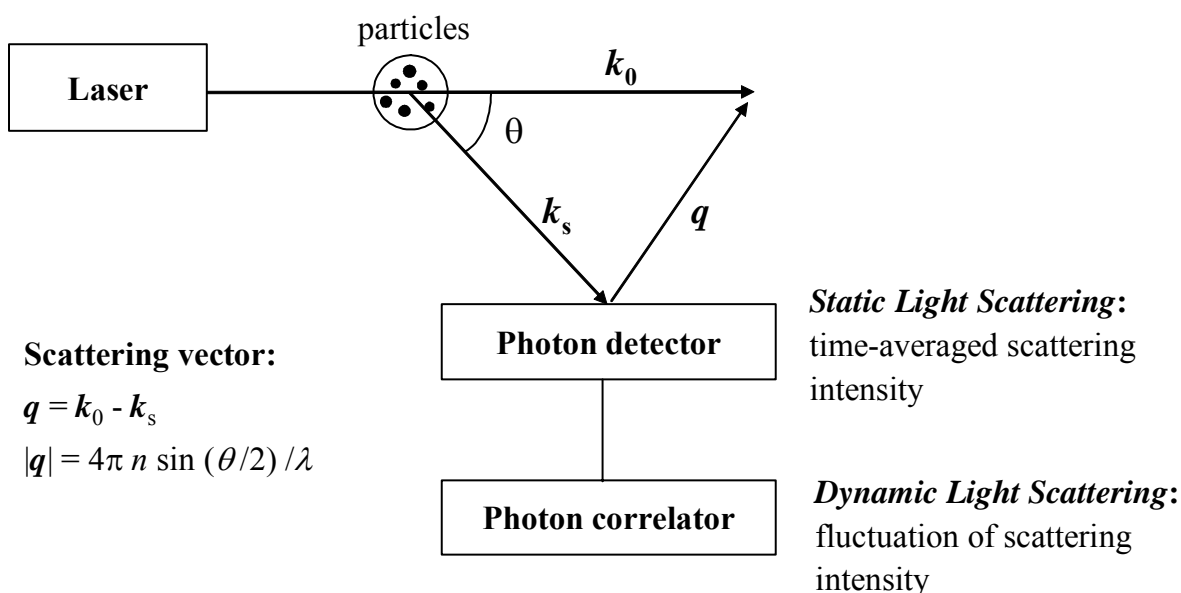
When an incident light of intensity  $I_0$  penetrates a medium, a loss of intensity may happen due to the scattering and/or absorption:

$$I_0 = I_t + I_s + (I_a) \quad \text{Eq. 2-6}$$

where  $I_t$ ,  $I_s$  and  $I_a$  denote the intensities of the transmitted, scattered and absorbed light respectively.

Light scattering is very useful in determination of the molecular weight and the size of polymer. Generally, as an characterization method for polymer solutions, light scattering includes static light scattering (SLS) and dynamic light scattering (DLS), which study the equilibrium behavior and dynamic behavior of polymer solutions respectively (Scheme 2-8). In SLS, the time-averaged “excess” scattering intensity of polymer solution above that of pure solvent is measured, which is directly proportional to the dimension of polymer as well as concentration. On the other hand, In DLS method the detector monitors the dynamic behavior of the intensity of scattered light (scattering intensity fluctuation), which is related

to the movements of scattering molecules, and therefore the diffusion coefficient and the corresponding hydrodynamic radius of the molecule can be determined.



*Scheme 2-8. Schematic illustration of light scattering*

### 2.2.3.1 Static light scattering (SLS)

The total scattering intensity of a dilute polymer solution is proportional to the polymer concentration and the molecular weight. When an isolated scattering particle (polymer molecule) is small compared to the wavelength of the incident light,  $\lambda$  (generally, diameter of molecule  $< \lambda/20$ ), the polymer molecule can be regarded as a single scattering center and in this case the scattering intensity can be calculated from Rayleigh scattering theory.

$$\frac{Kc}{R_\theta} = \frac{1}{M_w} + 2A_2c$$

$$\text{where } K = \frac{4\pi^2 n^2 (dn/dc)^2}{\lambda^4 N_A} \quad \text{and} \quad R_\theta = \frac{i_s}{I_0} \frac{r^2}{1 + \cos^2 \phi}$$

Eq. 2-7

where  $K$  is the optical constant;  $R_\theta$  is called Rayleigh ratio and is defined as the relative scattering intensity measured at an angle  $\phi$  and a distance  $r$  from the scattering center;  $c$  is the polymer concentration;  $M_w$  is the molecular weight (for a polydisperse polymer, it is the weight-average molecular weight);  $A_2$  is the second



As shown in the Zimm equation, the molecular parameters can be determined via the following extrapolations:

- (1)  $c \rightarrow 0$  and  $\theta \rightarrow 0$ :  $Kc/R_\theta = 1/M_w$
- (2)  $c \rightarrow 0$ :  $Kc/R_\theta = (1/M_w) [1 + (q^2/3)\langle r_g^2 \rangle_z]$
- (3)  $\theta \rightarrow 0$ :  $Kc/R_\theta = 1/M_w + 2A_2c$

In this work, gel permeation chromatography with multi-angle light scattering (GPC-MALS) detector was used to determine the molecular weight and radius of gyration. In this case, only one concentration (for one polymer) was used for the measurement. Because the injected dilute solution (concentration equals to a few grams per liter) is further diluted by GPC (dilute from 0.1 mL to a few mL) before the detection, so the measurement is actually done in the highly dilute region. Thus the obtained molecular weight should be very close to the absolute one. The obtained radius of gyration is the absolute value, because it is calculated from the fractional change in scattering intensity at different angles (specially low angles), and the radius calculation is independent of concentration.

### 2.2.3.2 Dynamic light scattering (DLS)

Polymer molecules in solution always undergo Brownian movements, which result in the fluctuation in scattering intensity. DLS is a technique to investigate the scattering intensity fluctuation and obtain the size information of the molecules. Molecules in solution move in all directions with the same probability and they have a continuous rate distribution. Consequently, the frequency of the scattered light is shifted to higher or lower values depending on the velocity and moving direction of the molecules relative to the detector (Doppler effect). Thus, a broadening of the spectrum is observed with respect to the frequency line of the stimulating radiation ( $\nu_0$ ). Therefore, light scattering is rather quasi-elastic than elastic.<sup>42</sup> The spectral broadening is too small to be detected by conventional spectrometers working in the frequency domain (interferometers). For this reason, measurements are performed in the time domain, and fluctuation of the scattered light with time is measured. Generally, this is done according to the Homodyn method, i.e. the scattering light is directed to the photo detector. The detector's output signal is proportional to the intensity of light  $I(t)$  and, thus, also proportional to the mean square of the electric

field  $|E(t)|^2$ . The output signal of the detector is auto-correlated with time according to the following equation:<sup>43,44</sup>

$$g_2(t) = \frac{\langle I(0) \cdot I(t) \rangle}{\langle I(0) \rangle^2} \quad \text{Eq. 2-9}$$

where  $g_2(t)$  is the normalized intensity autocorrelation function.

The field autocorrelation function  $g_1(t)$ , which describes the fluctuations of the electric field of the scattered light, can be deduced from  $g_2(t)$  using the Siegert relation:<sup>45</sup>

$$g_1(t) = \frac{\langle E(0) \cdot E(t) \rangle}{\langle E(0) \rangle^2} = \sqrt{\frac{g_2(t) - A}{B}} \quad \text{Eq. 2-10}$$

where A and B are usually equal to unity. A is determined by an experimental baseline, and B is a coherence factor accounting for deviation from ideal correlation.

For monodisperse hard spheres,  $g_1(t)$  can be described by an exponential function:

$$g_1(t) = \exp(-\Gamma \cdot t) \quad \text{Eq. 2-11}$$

where  $\Gamma$  is the fluctuation rate with  $\Gamma = Dq^2$ , and  $D$  is the translational diffusion coefficient, which can be used to calculate the hydrodynamic radius  $R_h$  via Stokes-Einstein equation.<sup>43,46</sup>

$$R_h = \frac{kT}{6\pi\eta D} \quad \text{Eq. 2-12}$$

where  $k$  is Boltzmann constant,  $T$  is the temperature Kelvin, and  $\eta$  is the solvent viscosity.

For a system of polydisperse spheres, the following equation holds:

$$g_1(q, t) = \sum_j a_j(q) \exp(-\Gamma_j t) \quad \text{Eq. 2-13}$$

with  $a_j(q)$  = relative amplitudes:

$$a_j(q) = \frac{c_j M_j P_j(q)}{\sum_j c_j M_j P_j(q)} \quad \text{Eq. 2-14}$$

where  $M_j$  and  $P_j(q)$  are the molecular weight and particle form factor, respectively, of particle  $j$ . In the case of large spheres (diameter  $> \lambda/20$  and  $P_j(q) < 1$ ),  $g_1(t)$  becomes dependent on  $q$ . Change from hard spheres to polymer molecules in solution involves rotational diffusion and internal modes in addition to translational diffusion. Rotational diffusion is of particular importance in rod-like molecules, whereas internal modes are significant in large coil-like molecules.<sup>46</sup> From a mathematical point of view, these factors

involve additional additive and multiplicative terms. The terms can be eliminated by angle-dependent measurements as the amplitudes approach zero for  $q^2 \rightarrow 0$ .<sup>43</sup>

The determination of the mean diffusion coefficient and standard deviation for polydisperse systems is best accomplished by the CONTIN method.<sup>47,48</sup> The function  $g_1(t)$  is described by a continuous distribution:

$$g_1(t) = \int_{\Gamma_{\min}}^{\Gamma_{\max}} G(\Gamma) \exp(-\Gamma \cdot t) d\Gamma \quad \text{Eq. 2-15}$$

where  $G(I)$  denotes the fluctuation rate distribution function. Equation 2-15 can be inverted by a Laplace transformation. This inversion is problematic as there is basically an unlimited number of solutions that describe the data within experimental error. In order to minimize these solutions, the CONTIN analysis uses the following regularization:

$$R_n(G(\Gamma)) = \int_{\Gamma_{\min}}^{\Gamma_{\max}} \left( \frac{\partial^n G(\Gamma)}{\partial \Gamma^n} \right) d\Gamma \quad \text{Eq. 2-16}$$

where  $n$  is the order of regularization. Regularization of 0<sup>th</sup> order represents minimization of the integration area of function  $G(I)$ ; regularization of 2<sup>nd</sup> order corresponds to smoothing of function  $G(I)$ . The original CONTIN routine calculates a rate distribution ( $\log(I)$  scale), whereas the CONTIN routine of the ALV software calculates a time distribution ( $\log(t)$  scale) that is proportional to the distribution of hydrodynamic radius.

The ALV software also enables a direct fit of  $g_2(t)-1$  via a special algorithm. This usually yields a smoother distribution function with less artifacts as compared to  $g_1(t)$ .

$$g_2(t) - 1 = \left( \int_{t_{\min}}^{t_{\max}} e^{-t} G(t) dt \right)^2 \quad \text{Eq. 2-17}$$

Care must be exerted on interpreting results so as to avoid artifacts, especially in the case of a low signal-to-noise ratio, an inappropriate baseline or inappropriate choice of  $\Gamma_{\max}$  and  $\Gamma_{\min}$ . Thus, the signal-to-noise ratio should always be high. For evaluation of the results, it should be considered that two different distributions can only be distinguished with the CONTIN program if the respective hydrodynamic radii differ from each other by a minimal factor of two.

The radii or rather diffusion coefficients obtained by the CONTIN method are  $z$ -average values. In order to eliminate the influence of form factors for large molecules, the  $D$  and  $R_h$  values, respectively, measured at different angles have to be extrapolated for  $q^2 \rightarrow 0$ .

### 2.2.4 Superconducting quantum interference device (SQUID) magnetometer

A superconducting quantum interference device (SQUID) is a technique used to measure extremely weak signals, such as subtle changes in the human body's electromagnetic energy field. Using a device called a Josephson Junction, a SQUID can detect a change of energy as much as 100 billion times weaker than the electromagnetic energy that moves a compass needle.

#### 2.2.4.1 The Josephson junction

A Josephson junction is made by sandwiching a thin layer of a nonsuperconducting material between two layers of superconducting material. The devices are named after Brian Josephson, who predicted in 1962 that pairs of superconducting electrons could "tunnel" right through the nonsuperconducting barrier from one superconductor to another. He also predicted the exact form of the current and voltage relations for the junction. Experimental work proved his predictions, and he was awarded the 1973 Nobel Prize in physics.

To understand the unique and important features of Josephson junctions, it's first necessary to understand the basic concepts and features of superconductivity. When many metals and alloys are cooled down to very low temperatures (within 20 degrees or less of absolute zero), a phase transition occurs. At this "critical temperature", the metal goes from the normal state to the superconducting state, where there is essentially no electrical resistance to the flow of direct electrical current. What occurs is that the electrons in the metal become paired. Above the critical temperature, the net interaction between two electrons is repulsive. Below the critical temperature, though, the overall interaction between two electrons becomes very slightly attractive, a result of the electrons' interaction with the ionic lattice of the metal. This very slight attraction allows them to drop into a lower energy state, opening up an energy "gap". Because of the energy gap and the lower energy state, electrons can move (and therefore current can flow) without being scattered by the ions of the lattice. When the ions scatter electrons, it causes electrical resistance in metals. There is no electrical resistance in a superconductor, and therefore no energy loss. There is, however, a maximum supercurrent that can flow, called the critical current. Above this critical current the material is normal.

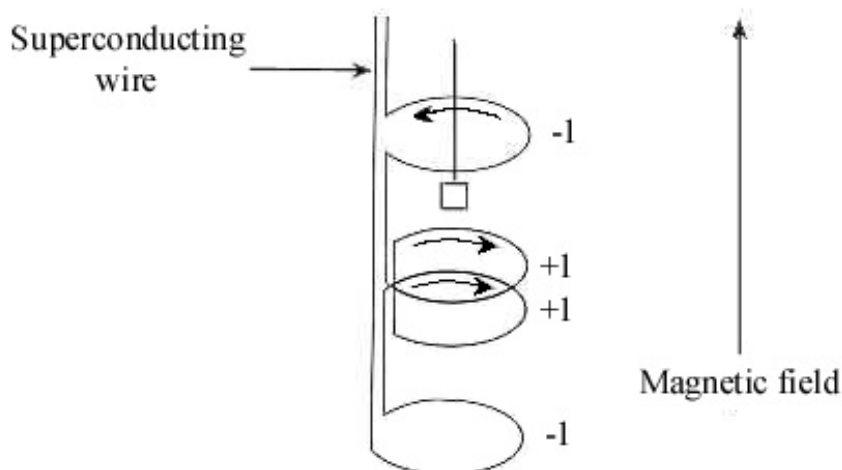
In a Josephson junction, the nonsuperconducting barrier separating the two superconductors must be very thin. If the barrier is an insulator, it has to be on the order of 30 angstroms thick or less. If the barrier is a nonsuperconducting metal, it can be as much as

several microns thick. Until a critical current is reached, a supercurrent can flow across the barrier; electron pairs can tunnel across the barrier without any resistance. But when the critical current is exceeded, another voltage will develop across the junction. That voltage will depend on time - that is, it is an AC voltage.

There are two main types of SQUID, DC and RF (or AC). RF SQUIDS have only one Josephson junction whereas DC SQUIDS have two or more junctions. This makes DC SQUIDS more difficult and expensive to produce, but DC SQUIDS are much more sensitive.

#### 2.2.4.2 SQUID magnetometer

The SQUID magnetometer used in this work consists of superconducting wires, operating as pickup coils, through which the sample is moved with constant speed (Scheme 2-10). The pickup coils and the detection coils form a superconducting flux transformer that “carries” the magnetic flux changes in the pickup coils (because of the sample movement) to the SQUID detector. The SQUID is inductively coupled to a resonant circuit, which is referred to as the “flux locked loop”, providing a linear read-out of the input signal to the SQUID. This means that the output voltage is proportional to the magnetic flux through the pickup coil system.



**Scheme 2-10.** Pickup coils of the SQUID magnetometer.

The magnetometer can be operated in various modes, among them the *Zero Field Cooling* (ZFC) and *Field Cooling* (FC) modes are very important. The zero field cooling

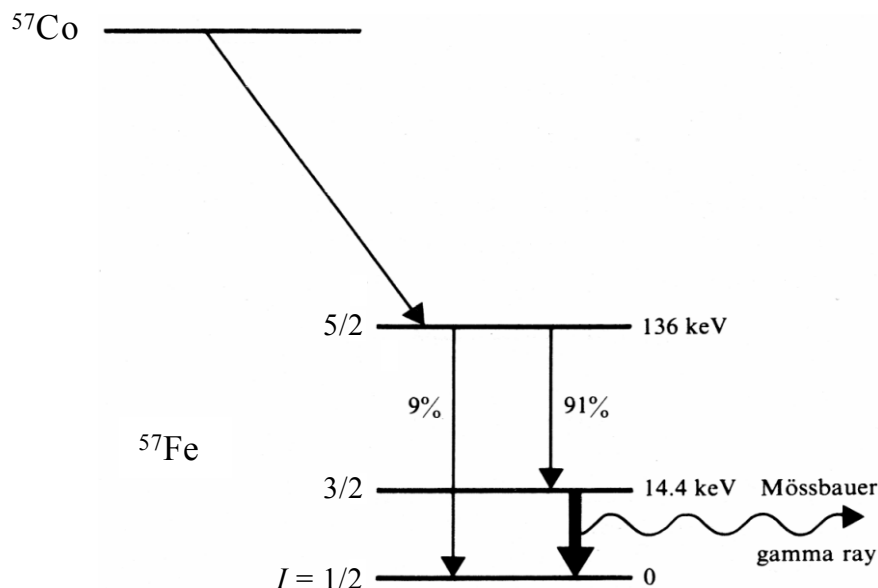
method is to cool the sample down to a desired temperature without applying any magnetic field. When the desired temperature is reached, a small magnetic field is applied and then the sample is heated again while measuring the magnetization of the material. In contrast, the magnetization of the sample under a small magnetic field as a function of decreasing temperature is termed as the field-cooled (FC) magnetization.

### 2.2.5 Mössbauer spectroscopy<sup>49,50</sup>

In 1957 Mössbauer discovered that a nucleus in a solid can sometimes emit and absorb gamma rays without recoil; because when it is in a solid matrix the nucleus is no longer isolated, but is fixed within the lattice. In this case the recoil energy may be less than the lowest quantized lattice vibrational energy and consequently the gamma ray may be emitted without energy loss. This phenomenon is called the Mössbauer effect. Many isotopes exhibiting this characteristic are called Mössbauer nuclei. As  $^{57}\text{Fe}$  (2.19 % natural occurrence) has the most advantageous combination of properties for Mössbauer spectroscopy the great majority of studies continue to involve this isotope and the technique has been widely used for the investigation of iron-containing systems.

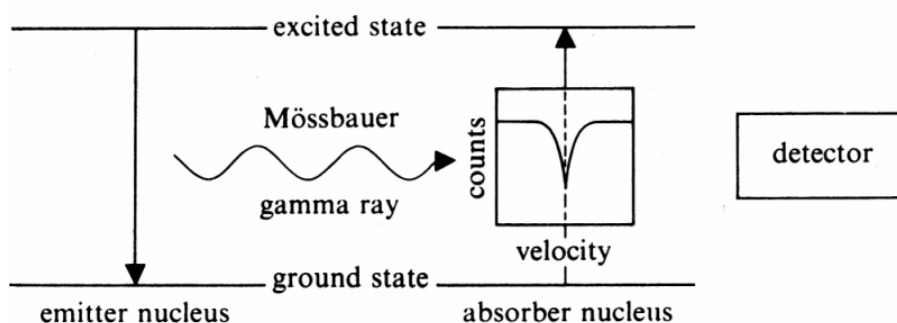
The energy levels of a nucleus situated in an atom and in a solid are influenced by the environment of the nucleus. Mössbauer spectroscopy is a technique which enables these energy levels to be investigated by measuring the energy dependence of the resonant absorption of Mössbauer gamma rays by nuclei. This is possible since the recoil-free processes arising from the Mössbauer effect lead to the resonant absorption of gamma rays with extremely precise energy. This enables the very small energy changes resulting from the hyperfine interactions between the nucleus and its surrounding electrons to be investigated and thus Mössbauer spectroscopy provides a mean of using the nucleus as a probe of its environment. Information such as oxidation state and coordination state of the Mössbauer nuclei can be obtained from Mössbauer spectrum.

The most common experimental setup for Mössbauer spectroscopy involves a radioactive source containing the Mössbauer isotope in an excited state and an absorber consisting of the material to be investigated which contains the same isotope in its ground state. For example, the source for  $^{57}\text{Fe}$  Mössbauer spectroscopy is normally radioactive  $^{57}\text{Co}$  which undergoes a spontaneous electron capture transition to give a metastable state of  $^{57}\text{Fe}$  which in turn decays to the ground state via a gamma ray cascade containing the 14.4 keV gamma ray (Scheme 2-11).



**Scheme 2-11.** Nuclear decay of  $^{57}\text{Co}$  showing the transition giving the 14.4 keV Mössbauer gamma ray.

In the normal transmission experiment the gamma rays emitted by the source pass through the absorber. In order to investigate the energy levels of the Mössbauer nucleus in the absorber it is necessary to modify the energy of the gamma rays emitted by the source so that they can have the correct energy for resonant absorption. This is usually accomplished by moving the source relative to a stationary absorber, and hence giving the gamma rays an energy shift as a result of the first-order relativistic Doppler effect. The motion of the source is normally oscillatory in order to provide an energy scan.



**Scheme 2-12.** A schematic representation of Mössbauer spectroscopy with the simplest situation of source and absorber nuclei in identical environment and showing the resulting Mössbauer spectrum with an absorption line at zero velocity.

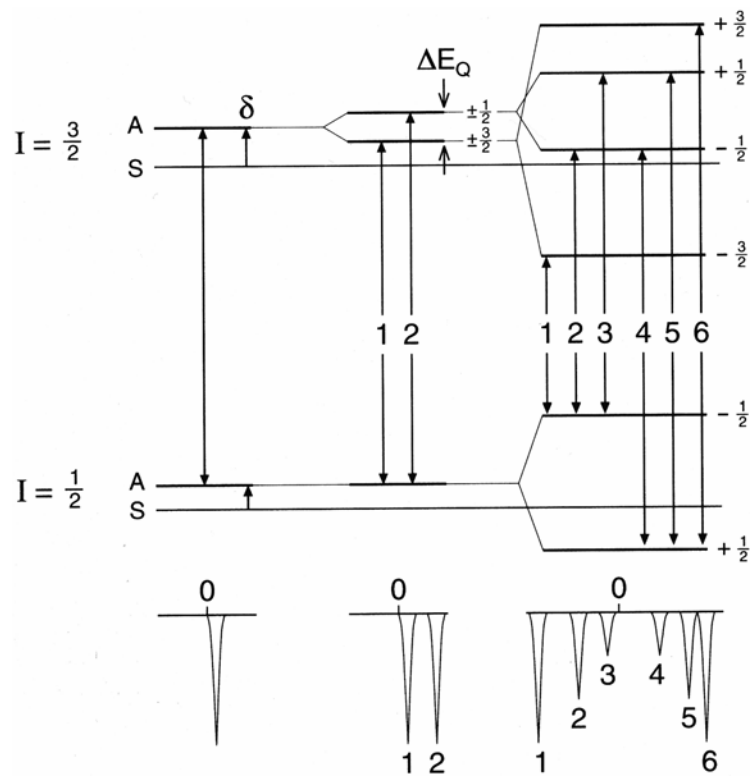
Scheme 2-12 depicts a simplest Mössbauer spectroscopy experiment. Resonant absorption occurs when the energy of the gamma ray matches the nuclear transition energy for a Mössbauer nucleus in the absorber. The resulting spectrum consists of a plot of gamma ray counts (or relative absorption) against the velocity of the source with respect to the absorber.

In the absence of a magnetic field, The Mössbauer spectrum consists of one (if the absorbing atoms are at a site of cubic symmetry) or two (symmetry distorted from cubic) absorption maxima. When a static magnetic field acts on the resonant nuclei, this splits the nuclear spin of the ground state into two and those of the excited state into four. The six allowed transition then produce a 6-line spectrum. The positions and the numbers of the absorption maxima are determined by the hyperfine interactions between the resonant nuclei and the electrons surrounding them. There are three types of hyperfine interaction (Scheme 2-13):

*Electric monopole interaction.* It is an interaction between the nuclear charge distribution over finite nuclear volume and the electric charge density over this volume. In a system where the electric monopole interaction is the only hyperfine, the nuclear ground and excited states are unsplit, but their separation is different in the source and absorber by an amount given by the isomer shift,  $\delta$ , which is defined as the velocity of the source necessary to counteract the difference between the source and the absorber. The isomer shift provides information about the coordination number, valence and spin state of iron in the sample.

*Electric quadrupole interaction.* It is generated when an electric field gradient, which is produced by an asymmetric electric charge distribution or ligand arrangement, acts on the nucleus. It gives rise to a splitting of the nuclear energy levels. From the quadrupole splitting the information about the site distortion can be derived.

*Magnetic hyperfine field.* When a nucleus is placed in a magnetic field there is a magnetic dipole interaction between the nuclear magnetic moment and the magnetic field. In the case of  $^{57}\text{Fe}$  the ground state with  $I = 1/2$  splits into two substates and the excited state with  $I = 3/2$  splits into four substates. There are six possible transitions and hence a Mössbauer spectrum consists of six absorption lines. The spectrum provides information about the valence and magnetic properties of the compound.



**Scheme 2-13.** Top: Nuclear energy levels of  $^{57}\text{Fe}$  as shifted by electric monopole (left), or split by electric quadrupole (center) or by magnetic dipole interaction (right); Bottom: Schematic Mössbauer spectra corresponding to the energy levels schematized above.

## 2.2.6 Commonly used methods

### 2.2.6.1 NMR spectroscopy

$^1\text{H}$ - and  $^{13}\text{C}$ -NMR spectra were obtained on a Bruker AC 250 at an operating frequency of 250 MHz and 62.5 MHz, respectively. Various deuterated solvents (Deutero GmbH) were used depending on the solubility of the samples. As an internal standard, either tetramethylsilane or the residual proton signal of the deuterated solvent was used.

### 2.2.6.2 UV/visible spectroscopy

UV spectra were recorded on a Perkin-Elmer Lambda15 UV/vis spectrophotometer in the wavelength range from 190 to 700 nm. Measurements were carried out in solution. The spectrum from a quartz cuvette containing pure solvent was subtracted from sample spectra.

### 2.2.6.3 IR spectroscopy

IR spectra were recorded on a Bio-Rad FT-IR spectrometer. The measurements were performed on a KBr pellet (mixture of a small amount of sample with KBr).

### 2.2.6.4 Raman spectroscopy

Raman spectra were recorded using a confocal optical setup consisting of a He-Ne laser ( $\lambda=632.8$  nm), objectives of numerical aperture 0.45 and 0.20, and a 50  $\mu\text{m}$  pinhole replacing the entrance slit of the monochromator. A CCD line detector in the exit focal plane of the monochromator was used for recording the spectra.

### 2.2.6.5 Gel permeation chromatography (GPC)

GPC measurement were performed at room temperature on a system with PSS SDVgel columns (30 x 8 mm, 5  $\mu\text{m}$  particle size) with  $10^2$ ,  $10^3$ ,  $10^4$ , and  $10^5$  Å pore sizes using RI and UV detection ( $\lambda = 254$  nm). THF was used as an eluent (flow rate 1.0 mL/min).

### 2.2.6.6 Thermogravimetric analysis (TGA)

TGA measurements were carried on a Mettler Toledo TGA/SDTA851 with the sample amount of 4-11 mg. The measurements was performed under air flow of 60 mL/min with heating from 30 °C to 1000 °C (rate: 10 °C/min) and then keeping at 1000 °C for 0.5 h.

## References

- (1) Moad, G.; Solomon, D. H. *The chemistry of free radical polymerization* **1995**, Oxford: Pergamon.
- (2) Hawker, C. J.; Bosman, A. W.; Harth, E. *Chem. Rev.* **2001**, *101*, 3661-3688.
- (3) Wang, J.-S.; Matyjaszewski, K. *J. Am. Chem. Soc.* **1995**, *117*, 5614-5615.
- (4) Chiefari, J.; Chong, Y. K.; Ercole, F.; Krstina, J.; Jeffery, J.; Le, T. P. T.; Mayadunne, R. T. A.; Meijs, G. F.; Moad, C. L.; Moad, G.; Rizzardo, E.; Thang, S. H. *Macromolecules* **1998**, *31*, 5559-5562.
- (5) Kato, M.; Kamigaito, M.; Sawamoto, M.; Higashimura, T. *Macromolecules* **1995**, *28*, 1721.
- (6) Zhu, S.; Yan, D. *J. Polym. Sci., Part A: Polym. Chem.* **2000**, *38*, 4308-4314.
- (7) O'Reilly, R. K.; Gibson, V. C.; White, A. J. P.; Williams, D. J. *J. Am. Chem. Soc.* **2003**, *125*, 8450-8451.
- (8) Granel, C.; Dubois, P.; Jerome, R.; Teyssie, P. *Macromolecules* **1996**, *29*, 8576-8582.
- (9) Lecomte, P.; Drapier, I.; Dubois, P.; Teyssie, P.; Jerome, R. *Macromolecules* **1997**, *30*, 7631-7633.
- (10) Moineau, G.; Granel, C.; Dubois, P.; Jerome, R.; Teyssie, P. *Macromolecules* **1998**, *31*, 542-544.
- (11) Kotani, Y.; Kamigaito, M.; Sawamoto, M. *Macromolecules* **1999**, *32*, 2420-2424.
- (12) Le Grogne, E.; Claverie, J.; Poli, R. *J. Am. Chem. Soc.* **2001**, *123*, 9513-9524.
- (13) Matyjaszewski, K.; Patten, T. E.; Xia, J. *J. Am. Chem. Soc.* **1997**, *119*, 674-680.
- (14) Qiu, J.; Matyjaszewski, K. *Macromolecules* **1997**, *30*, 5643-5648.
- (15) Percec, V.; Barboiu, B. *Macromolecules* **1995**, *28*, 7970-7972.
- (16) Davis, K. A.; Paik, H.-j.; Matyjaszewski, K. *Macromolecules* **1999**, *32*, 1767-1776.
- (17) Matyjaszewski, K.; Coca, S.; Jasieczek, C. B. *Macromol. Chem. Phys.* **1997**, *198*, 4011-4017.
- (18) Wang, J.-L.; Grimaud, T.; Matyjaszewski, K. *Macromolecules* **1997**, *30*, 6507-6512.
- (19) Haddleton, D. M.; Jasieczek, C. B.; Hannon, J. H.; Shooter, A. J. *Macromolecules* **1997**, *30*, 2190.
- (20) Matyjaszewski, K.; Jo, S. M.; Paik, H.-j.; Gaynor, S. G. *Macromolecules* **1997**, *30*, 6398-6400.

- (21) Teodorescu, M.; Matyjaszewski, K. *Macromol. Rapid Commun.* **2000**, *21*, 190-194.
- (22) Matyjaszewski, K.; Beers, K. L.; Muhlebach, A.; Coca, S.; Zhang, X.; Gaynor, S. G. *Polym. Mater. Sci. Eng.* **1998**, *79*, 429-430.
- (23) Matyjaszewski, K.; Wang, J. S., WO Pat. 9630421, U.S. Pat. 5763548.
- (24) Wakioka, M.; Baek, K.-Y.; Ando, T.; Kamigaito, M.; Sawamoto, M. *Macromolecules* **2002**, *35*, 330-333.
- (25) Percec, V.; Popov, A. V.; Ramirez-Castillo, E.; Monteiro, M.; Barboiu, B.; Weichold, O.; Asandei, A. D.; Mitchell, C. M. *J. Am. Chem. Soc.* **2002**, *124*, 4940-4941.
- (26) Davis, K.; O'Malley, J.; Paik, H.-J.; Matyjaszewski, K. *Polym. Prepr.* **1997**, *38*, 687-688.
- (27) Brown, H. C.; Fletcher, R. S. *J. Am. Chem. Soc.* **1949**, *71*, 1845-1854.
- (28) Patten, T. E.; Xia, J.; Abernathy, T.; Matyjaszewski, K. *Science* **1996**, *272*, 866-868.
- (29) Litvinenko, G.; Mueller, A. H. E. *Macromolecules* **1997**, *30*, 1253-1266.
- (30) Matyjaszewski, K. *J. Phys. Org. Chem.* **1995**, *8*, 197-207.
- (31) Matyjaszewski, K.; Coca, S.; Gaynor, S. G.; Wei, M.; Woodworth, B. E. *Macromolecules* **1997**, *30*, 7348-7350.
- (32) Szwarc, M. *Nature* **1956**, *178*, 1168.
- (33) Szwarc, M.; Levy, M.; Milkovich, R. *J. Am. Chem. Soc.* **1956**, *78*, 2656.
- (34) Antoun, S.; Teyssie, P.; Jerome, R. *J. Polym. Sci., Part A: Polym. Chem.* **1997**, *35*, 3637-3644.
- (35) Litt, M. *J. Polym. Sci.* **1962**, *58*, 429-454.
- (36) Müller, A. H. E. *Compr. Polym. Sci.*; **1988**; *3*, 387.
- (37) Sheiko, S. S.; Möller, M. *Chem. Rev.* **2001**, *101*, 4099-4123.
- (38) Akari, S.; Horn, D.; Kellar, H.; Schrepp, W. *Adv. Mater.* **1995**, *7*, 549-551.
- (39) Noy, A.; Sanders, C. H.; Vezenov, D. V.; Wong, S. S.; Lieber, C. M. *Langmuir* **1998**, *14*, 1508-1511.
- (40) Thomas, E. L. *Encycl. Polym. Sci. Eng.* **1986**, *5*, 644-687.
- (41) Tsuji, M. *Compr. Polym. Sci.* **1989**, *1*, 785-840.
- (42) Santos, N. C.; Castanho, M. A. R. B. *Biophys. J.* **1996**, *71*, 1641.
- (43) Berne, B. J.; Pecora, R. *Dynamic Light Scattering*; John Wiley & Sons: New York, 1976.

- 
- (44) Schmitz, K. S. *An Introduction to Dynamic Light Scattering by Macromolecules*; Academic Press, Inc.: San Diego, 1990.
- (45) Siegert, A. J. F. *MIT Rad. Lab. Report* **1943**, 465.
- (46) Burchard, W.; Richterling, W. *Progr. Colloid Polym. Sci.* **1989**, 80, 151.
- (47) Provencher, S. W. *Makromol. Chem.* **1979**, 180, 201.
- (48) Provencher, S. W. *Computer Phys. Commun.* **1982**, 27, 229.
- (49) Dickson, D. P. E.; Berry, F. J.; Editors. *Mössbauer spectroscopy* **1986**, Cambridge University Press.
- (50) Cornell, R. M.; Schwertmann, U.; Editors. *The iron oxides: structure, properties, reactions, occurrence and uses* **1996**, 349.



## Chapter 3

# Amphiphilic cylindrical brushes with poly(acrylic acid) core and poly(*n*-butyl acrylate) shell and narrow length distribution\*

### Abstract

Core-shell cylindrical polymer brushes with poly(*t*-butyl acrylate)-*b*-poly(*n*-butyl acrylate) (PtBA-*b*-PnBA) diblock copolymer side chains were synthesized via “grafting from” technique using atom transfer radical polymerization (ATRP). The formation of well-defined brushes was confirmed by GPC and <sup>1</sup>H-NMR. Multi-angle light scattering (MALS) measurements on brushes with 240 arms show that the radius of gyration scales with the degree of polymerization of the side chains with an exponent of  $0.57 \pm 0.05$ . The hydrolysis of the PtBA block of the side chains resulted in amphiphilic core-shell cylindrical polymer brushes with poly(acrylic acid)-*b*-poly(*n*-butyl acrylate) (PAA-*b*-PnBA) side chains. In order to obtain a narrow length distribution of the brushes, the backbone, poly(2-hydroxyethyl methacrylate), was synthesized by anionic polymerization in addition to ATRP. The characteristic core-shell cylindrical structure of the brush was directly visualized on mica by scanning force microscopy (SFM). Brushes with 1500 block copolymer side chains and a length distribution of  $l_w/l_n = 1.04$  at a total length  $l_n = 179$  nm were obtained. By choosing the proper solvent in the dip-coating process on mica, the core and the shell can be visualized independently by SFM.

\* Part of this chapter (3.1-3.3.5) has been published in Mingfu Zhang, Thomas Breiner, Hideharu Mori, Axel H. E. Müller *Polymer*, 2003, 44, 1449-1458.

### 3.1. Introduction

It is well known that solution and bulk properties of polymer are dramatically influenced by their chain architecture. Cylindrical polymer brushes which have the same number of side chains as degree of polymerization of the main chain, are architecturally interesting for both experimental and theoretical chemists because of the possibility to form extended chain conformations, based on the intramolecular excluded-volume interactions between side chains densely grafted to the backbone. Since Tsukahara et al.<sup>1,2</sup> first succeeded in the synthesis of polymer brushes by radical polymerization of macromonomers in 1989, this type of polymers attracted considerable attention over the past years.<sup>3-20</sup>

Generally, there are three methods to synthesize cylindrical polymer brushes. The first one, which was widely used in the past decade, is the conventional radical polymerization of macromonomers.<sup>1-8</sup> In this method, end-functionalized oligomers prepared by anionic polymerization are converted into polymerizable macromonomers, which form well-defined side chains of the brushes after subsequent radical polymerization. However, conventional radical polymerization of macromonomers normally yields a broad chain-length distribution of the resulting polymer. So the crude product may contain polymers with both star-like and brush-like shape in addition to residual macromonomers. It is worthy to note that living anionic polymerization<sup>21</sup> and living ring-opening metathesis polymerization (ROMP)<sup>22-24</sup> of macromonomers were also performed aiming to get well-defined polymacromonomer, however, high molecular weight polymers have not been prepared by these living polymerizations, so far. The second method is the “grafting onto” technique.<sup>9-11</sup> The grafting of side chains onto a backbone was carried out via a coupling reaction. For example, coupling polystyryllithium with poly(chloroethyl vinyl ether) (PCEVE) resulted in a polymer brush with PCEVE as backbone and polystyrene (PS) as side chains.<sup>9,10</sup> However insufficient grafting efficiency was often achieved using the “grafting onto” method. The last method, i.e. “grafting from”, appeared lately. In this method side chains of the brush are formed via atom transfer radical polymerization (ATRP)<sup>25-27</sup> initiated by the pendant initiating groups on the backbone.<sup>12,28,29</sup> By this method well-defined polymer brushes with high grafting density and rather narrow distributions of both backbone and side chains can be obtained, and the purification of resulting polymer brushes is much simpler comparing to the other two methods.

Cylindrical wormlike micelles have been investigated by many groups in recent years,<sup>30</sup> most of them being formed by aggregation of surfactants. As an example,

cetyltrimethylammonium bromide reversibly assembles into long, flexible wormlike micelles in 0.1 M KBr aqueous solution. These aggregates may dissociate or undergo structural changes under changed conditions. Similarly, block copolymers can form spherical or cylindrical micelles in selective solvents.<sup>31,32</sup> Although spheres are the most common morphology for block copolymer micelles, other types of supramolecular structures such as cylinders have also been found. For example, polyferrocenylsilane-*b*-poly(2-(*N,N*-dimethylamino)ethyl methacrylate) with a block ratio of 1:5 formed cylindrical micelles in aqueous solution.<sup>33</sup> In our case, the brushes with amphiphilic diblock copolymer (poly(acrylic acid)-*b*-poly(*n*-butyl acrylate), PAA-*b*-P*n*BA) side chains resemble the normal inverse block copolymer micelles in structure and therefore can be regarded as unimolecular wormlike micelles. Compared to block copolymer micelles they are very stable towards environmental changes since the side chains are covalently linked to the backbone. In addition, their length can be controlled in a much better way than for self-associating micelles. The ability of the hydrophilic PAA core of the amphiphilic core-shell brushes to coordinate with different metal cations can be used for the synthesis of novel nanosized organic/inorganic hybrids.

So far, there have only a few reports about the synthesis of polymer brushes with amphiphilic side chains, whose peculiar topology makes them very attractive for applications involving unimolecular micelles.<sup>8,24</sup> Gnanou et al.<sup>24</sup> first reported the ROMP of norbornenyl-endfunctionalized polystyrene-*b*-poly(ethylene oxide) macromonomers. Although complete conversion of macromonomer was achieved, the degree of polymerization was very low. Consequently, the polymacromonomer adopted a globular rather than a cylindrical shape. Moreover, the difficulty in this method lies more in the synthesis of the macromonomer than in the polymerization. Later, Schmidt et al.<sup>8</sup> synthesized amphipolar cylindrical brushes with poly(2-vinylpyridine)-*b*-polystyrene side chains via radical polymerization of the corresponding block macromonomer. Similar polymer brushes with poly( $\alpha$ -methylstyrene)-*b*-poly(2-vinylpyridine) side chains were also synthesized by Ishizu via radical polymerization.<sup>34</sup> Again, the problem is the very wide length distribution of the obtained polymer brushes. To find an efficient and convenient methodology for the synthesis of well-defined amphiphilic cylindrical brushes still remains a challenge. Very recently, we succeeded in the synthesis of the core-shell cylindrical brushes with amphiphilic block copolymer, poly(acrylic acid)-*b*-polystyrene (PAA-*b*-PS) or PS-*b*-PAA, as side chains by ATRP using the “grafting from” technique.<sup>28</sup> Compared to the

macromonomer route, this method is quite versatile and effective. ATRP is tolerant to many functionalities, so a multitude of monomers, including those with functional groups, can be polymerized to form the side chains. At the same time, the living character of ATRP enables the control of the distributions of backbone as well as side chains, so the resulting amphiphilic brushes have a well-defined structure.

As part of our continuous effort for the synthesis and applications of amphiphilic core-shell cylindrical brushes, we synthesized and characterized well-defined amphiphilic brushes with a PAA core and a soft *P**n*BA shell. The chemical compatibility between the core and the shell of these brushes is somewhat better, compared to the amphiphilic brushes with PAA core and PS shell we synthesized before.<sup>28</sup>

In the synthesis of cylindrical brushes with side chains containing PS block, we found that sometimes cross-linking occurred during the polymerization of styrene, probably due to intermolecular coupling reactions between spatially neighboring radical sites on the side chains. Using a high molar ratio of monomer to initiator and quenching the polymerization at quite low conversion of styrene (< 5 %) we could suppress this undesirable side reaction.<sup>28</sup> Adding Cu(II) to decrease the radical concentration in ATRP and using 2,2'-bipyridine or its derivatives as ligands were also useful to avoid the coupling reaction, however, in this case the polymerization is very slow.<sup>29</sup> The polymerization of *n*-butyl acrylate (*n*BA) to form the shell can go to relatively high conversion (about 20%) without any cross-linking and the polymerization of *n*BA is quite fast under mild conditions.

In our previous syntheses<sup>28</sup> we prepared poly(2-hydroxyethyl methacrylate), poly(HEMA), which forms the backbone, via ATRP in ethanol. We now use an improved method to obtain more narrow molecular weight distribution (MWD). However, it is very hard to synthesize poly(HEMA) with high molecular weights as well as very narrow MWD. Thus anionic polymerization was carried out, using 2-(trimethylsilyloxy)ethyl methacrylate as a protected monomer. Using the poly(HEMA) synthesized via anionic polymerization, very uniform amphiphilic polymer brushes were obtained.

## 3.2. Experimental Part

### 3.2.1 Materials

2-Hydroxyethyl methacrylate (HEMA, Acros, 96%) was purified according to literature.<sup>35</sup> *t*-Butyl acrylate (*t*BA, BASF AG) was fractionated from CaH<sub>2</sub> at 45 mbar, stirred over CaH<sub>2</sub>, degassed and distilled in high vacuum. *n*-Butyl acrylate (*n*BA, BASF AG) was vacuum distilled just before use. CuBr (95%, Aldrich) was purified by stirring overnight in acetic acid. After filtration it was washed with ethanol, diethyl ether, and then dried. 2,2'-Bipyridine (bpy) was recrystallized from ethanol to remove impurities.  $\alpha$ -Bromoisobutyryl bromide and N,N,N',N'',N''-pentamethyl-diethylenetriamine (PMDETA) were purchased from Aldrich and used as received without further purification.

2-(Trimethylsilyloxy)ethyl methacrylate (TMS-HEMA, 97%, Aldrich) was purified according to the method described in the polymerization part. Trioctylaluminum (25 wt% in hexane, Aldrich) and *sec*-butyllithium (*sec*-BuLi, 1.3M in cyclohexane, Aldrich) were used without further purification. 1,1-Diphenylethylene (DPE, 97%, Aldrich) was vacuum distilled and dried by adding a small amount of *sec*-BuLi solution until the color changed to light yellow. Lithium chloride (LiCl, >98%, Fluka) was dried at 300 °C under vacuum overnight, and then dissolved in THF. THF (p.a., Merck) was purified first by distillation under nitrogen from CaH<sub>2</sub> and then by refluxing over potassium.

### 3.2.2 Synthesis of poly(2-hydroxyethyl methacrylate), poly(HEMA)

Both anionic polymerization and atom transfer radical polymerization were used to synthesize poly(HEMA).

(a) *via anionic polymerization.*<sup>36,37</sup>

The silyl-protected monomer (2-(trimethylsilyloxy)ethyl methacrylate, TMS-HEMA) was purified on a vacuum line using home-made glassware consisting of two flasks connected by a glass bridge, as shown in Figure 3-1. Into one flask 50 mL of TMS-HEMA were added and degassed by three freeze-pump-thaw cycles. A small amount of trioctylaluminum solution (in hexane) was added until the color changed to light yellow, indicating the complete removal of water. The monomer was then frozen by liquid N<sub>2</sub> and evacuated. During thawing, hexane evaporated and was caught in the cooling trap of vacuum line. Now the second flask was cooled with liquid N<sub>2</sub> and the monomer was

condensed into this flask under gentle heating. After thawing the monomer was transferred into the reactor with a syringe equipped with a stainless steel needle (dry, flush with N<sub>2</sub>). For the anionic polymerization, 300 mL of THF were placed into the reactor and cooled down to -75 °C. Then LiCl solution (in THF, tenfold molar excess with respect to the initiator used) was added. After the system changed to a light red color (indicating absence of water) by adding a small amount of sec-BuLi solution, the calculated amount of sec-BuLi was added via a syringe. Then, a fourfold molar excess of DPE (with respect to the amount of sec-BuLi) was placed into the reactor. Ten minutes later, when the formation of the 1,1-diphenyl-3-methylpentyl-lithium initiator species was completed, the monomer was added. The polymerization proceeded for 2.5 hours at -75 °C and finally was terminated by adding 1 mL of a well degassed methanol/acetic acid (10/1) mixture. After the polymerization THF was removed by rotating evaporation. The resulting polymer was dissolved in methanol and precipitated in water mixed with several drops of HCl solution (32%). The final deprotected product, poly(HEMA), was freeze-dried from dioxane. <sup>1</sup>H-NMR (CD<sub>3</sub>OD): δ = 4.04 (-CH<sub>2</sub>-OCO), 3.77 (-CH<sub>2</sub>-OH), 2.20-1.40 (-CH<sub>2</sub>-C), 1.30-0.70 (-CH<sub>3</sub>) ppm.

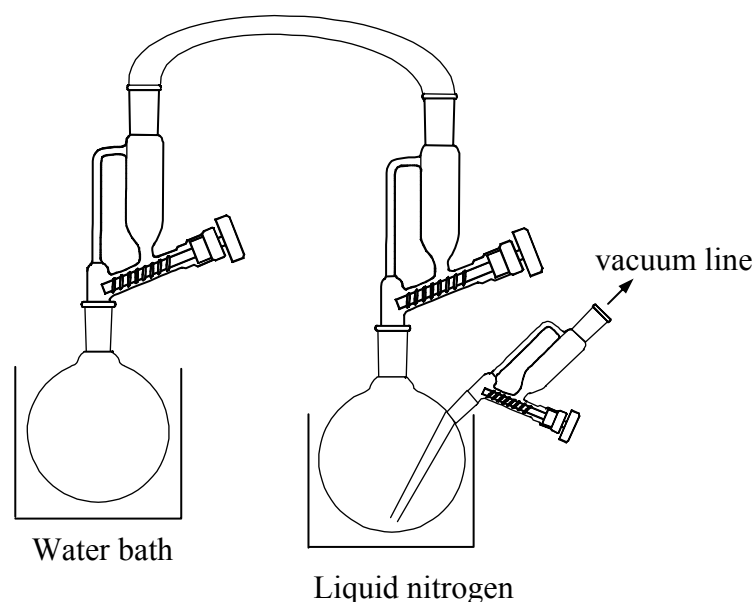


**Figure 3-1.** Glassware for the purification of TMS-HEMA.

(b) via ATRP.<sup>35</sup>

Inside a glove-box, CuCl (0.0393 g, 0.4 mmol), 2,2'-bipyridine (0.127 g, 0.81 mmol) were added into a 50 mL round flask. Afterwards methylethyl ketone (7 mL), 1-propanol (3 mL), HEMA (10.427 g, 80 mmol) as well as octane (2 mL, internal standard) were added

and the mixture was stirred for 20 minutes. An initial sample was taken for the monomer conversion measurement via gas chromatography (GC). Finally the initiator, ethyl 2-bromoisobutyrate (0.081 g, 0.42 mmol) was added. The flask was then sealed and placed in a thermostated oil bath with temperature of 50°C. The polymerization was stopped after one hour by cooling to room temperature and exposure to air. A sample was taken from the final reaction mixture for GC measurement, and the monomer conversion was determined to be 57.6 %. To remove the catalyst (Cu(II)), 120 mL DMF was added and the solution was passed through a neutral alumina column. Most of the solvent (DMF) was removed by rotating evaporator and finally the polymer was precipitated in diethyl ether. 4.45 g poly(HEMA) was obtained after freeze-drying from dioxane.

### 3.2.3 Preparation of poly(2-(2-bromoisobutyryloxy)ethyl methacrylate (PBIEM))

As shown in Scheme 2, esterification of poly(HEMA) by  $\alpha$ -bromoisobutyryl bromide produced the polyinitiator (PBIEM) for ATRP. The reaction proceeded as follows: 4.45 g poly(HEMA) (-OH groups, 0.0342 mol) was dissolved in 60 mL anhydrous pyridine. 16.24 g (0.0706 mol)  $\alpha$ -bromoisobutyryl bromide was added dropwise at 0°C in one hour. The reaction mixture was stirred for 3 h at 0 °C followed by stirring at room temperature for 22 h under inert gas. The insoluble salt was then removed by filtration and the solvent was removed by a rotating evaporator. The produced polymer was purified by passing through a basic alumina column using toluene as solvent, followed by precipitation in methanol. 6.42 g PBIEM (yield = 67.3 %) was obtained after freeze-drying from benzene.  $^1\text{H-NMR}$  ( $\text{CDCl}_3$ ):  $\delta = 4.37, 4.21$  ( $-\text{CH}_2\text{-OCO}$ ),  $2.20\text{-}1.40$  ( $-\text{CH}_2\text{-C}$ ),  $1.97$  [ $-\text{C}(\text{Br})(\text{CH}_3)_2$ ],  $1.30\text{-}0.70$  ( $-\text{CH}_3$ ) ppm.

### 3.2.4 Typical ATRP procedure for the synthesis of brushes

All operations except the polymerization were carried out inside glove box under nitrogen atmosphere. CuBr (or CuCl), initiator (PBIEM or the purified polymer brushes with homopolymer side chains), monomer, acetone (which was added in some cases) and decane (internal standard, 1/10 molar ratio relative to monomer) were added into a round flask. The mixture was stirred until all the initiator was dissolved completely. Then an initial sample was taken for GC measurement and finally the ligand, PMDETA, was added. The flask was then sealed and immersed in an oil bath at a preset temperature for a certain time. The

polymerization was stopped by cooling to room temperature and exposed the reaction mixture to air. A sample was taken from the final reaction mixture for GC measurement. After polymerization, the catalyst was removed by an adsorption filtration through an alumina column and the resulting polymer was precipitated from chloroform into mixture of methanol and water (v/v = 4/1 to 3/1). The produced polymer was dissolved in benzene and freeze-dried.

### 3.2.5 Hydrolysis of the poly(*t*-butyl acrylate) blocks<sup>38</sup>

The brush was dissolved in CH<sub>2</sub>Cl<sub>2</sub> and then a fivefold molar excess of CF<sub>3</sub>COOH (with respect to the amount of the *t*-butyl group in the brush) was added. The reaction mixture was stirred at room temperature for 24 h. During the hydrolysis, the resulting brush with PAA-*b*-P*n*BA side chains precipitated in CH<sub>2</sub>Cl<sub>2</sub> gradually. Finally, solvent and CF<sub>3</sub>COOH were removed by rotating evaporation followed by freeze-drying. Traces of CF<sub>3</sub>COOH in the polymer were removed by vacuum drying at 40 °C overnight.

### 3.2.6 Analysis

Monomer conversion was determined by gas chromatography (GC) from the concentration of residual monomer with decane as an internal standard, using a polymethylsiloxane capillary column. Proton and carbon nuclear magnetic resonance (<sup>1</sup>H-NMR and <sup>13</sup>C-NMR) spectra were recorded with a Bruker AC-250 spectrometer at room temperature in CDCl<sub>3</sub> or CD<sub>3</sub>OD (or mixture of them). The apparent molecular weights of the brushes were measured by gel permeation chromatography (GPC) using THF as eluent at a flow rate of 1.0 mL/min at room temperature. Column set: 5μ SDV gel, 10<sup>5</sup>, 10<sup>4</sup>, 10<sup>3</sup>, 10<sup>2</sup> Å, 30 cm each (PSS, Germany); detectors: Waters 410 differential refractometer and Waters photodiode array detector operated at 254 nm. PS standards (PSS) were used for the calibration of the column set. The samples for scanning force microscopy (SFM) measurements were prepared by dip-coating from dilute solutions of brushes in different solvents, with concentration of 10<sup>-6</sup>-10<sup>-4</sup> g/ml, onto freshly cleaved mica surface. The SFM images were taken with a Digital Instruments Dimension 3100 microscope operated in Tapping Mode (free amplitude of the cantilever ≈ 30 nm, set point ratio ≈ 0.98).

Membrane osmometry was performed in toluene at 35 °C in order to determine the true number-average molecular weight of the polyinitiator (forming the backbone) using a

cellulose triacetate membrane with a Gonotec Osmomat 090 (Gonotec GmbH, Germany). GPC with a multi-angle light scattering detector (GPC-MALS) was used to determine the absolute molecular weights of the brushes. THF was used as eluent at a flow rate of 1.0 mL/min. Column: 30 cm linear SDV 5 $\mu$  (PSS); detectors: DAWN DSP-F MALS and PSS ScanRef interferometer, both equipped with 632.8 nm He-Ne laser. The ScanRef interferometer was also used to measure refractive index increment ( $dn/dc$ ) in the offline mode.

Static light scattering (SLS) measurements was carried out on a Sofica goniometer with He-Ne laser (632.8 nm) at different temperatures. Prior the measurements, sample solutions were filtered through Millipore Teflon filters of pore size 0.45  $\mu$ m. A Zimm plot was used to evaluate the data. A ScanRef laser interferometer was used to measure refractive index increment,  $dn/dc$ , of the polymer solution. The temperature dependence of  $dn/dc$  of polymer brush with deuterated PS side chains was found to be negligible in the temperature range used.

Dynamic light scattering (DLS) measurements were performed on an ALV DLS/SLS-SP 5022F compact goniometer system with an ALV 5000/E correlator and a He-Ne laser. Prior to the light scattering measurements the sample solutions were filtered using Millipore Teflon filters with a pore size of 0.45  $\mu$ m. The measured field correlation function  $g_I(t)$  was analyzed by means of a cumulant expansion

$$\ln g_1(q, t) = \ln(A) - \Gamma_1(q)t + \Gamma_2(q)t^2 / 2 - \dots \quad \text{Eq. 3-1}$$

$\Gamma_1$  is the first cumulant which is related to the translational diffusion coefficient via  $D = \Gamma_1 q^{-2}$ .  $\Gamma_2$  is the second cumulant which is related to the relative standard deviation  $\sigma = \sqrt{\Gamma_2} / \Gamma_1$ . Then average hydrodynamic radius was calculated via the Stokes-Einstein relation. The viscosity data of chloroform at different temperatures are calculated according to

$$\log \eta = A + B / (C - T) \quad \text{Eq. 3-2}$$

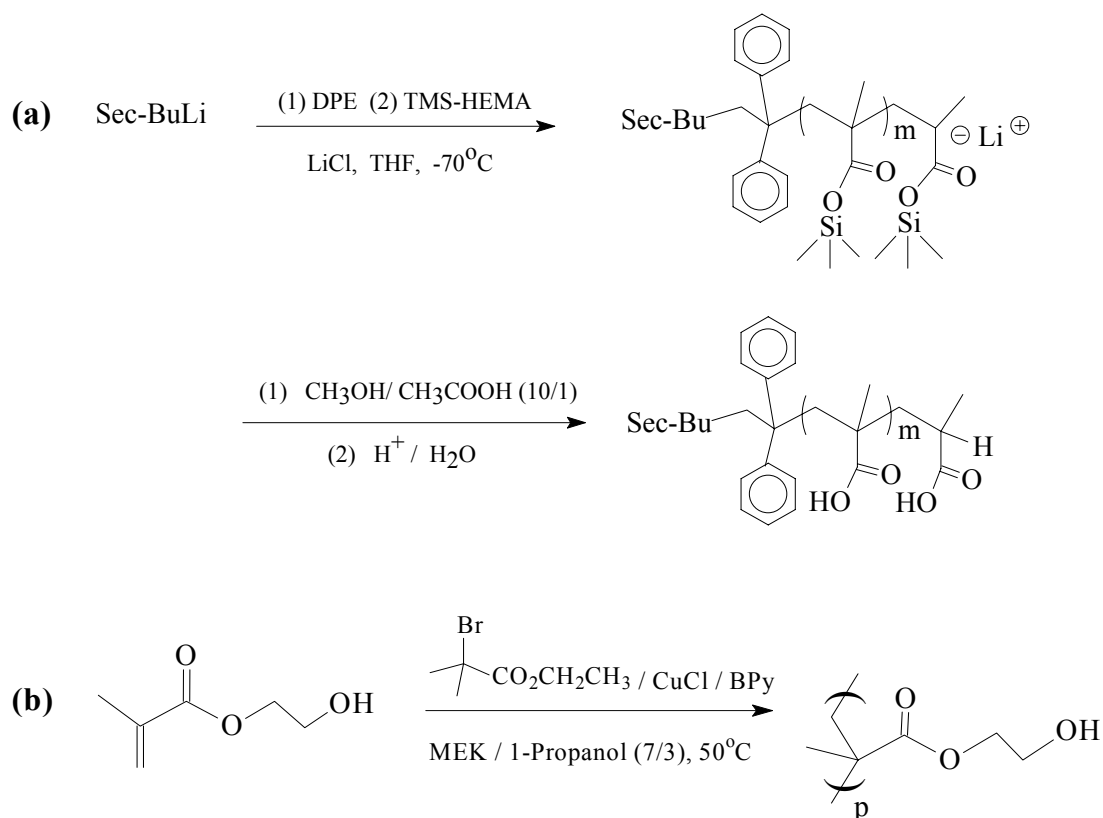
where A, B and C are constants and equal to -4.4573, -325.76 and 23.789 respectively, and  $T$  is the absolute temperature.<sup>39</sup>

Cryogenic-transmission electron microscopy (Cryo-TEM) measurements were carried out with a CEM 902 (Zeiss) transmission electron microscope with an acceleration voltage of 80 kV.

### 3.3. Results and Discussion

#### 3.3.1 Synthesis of poly(2-hydroxyethyl methacrylate), poly(HEMA)

Poly(HEMA), which has functional hydroxy group at each monomer unit, can be easily modified to obtain ATRP initiator via the esterification of the hydroxy groups with chemicals like  $\alpha$ -bromoisobutyryl bromide. Both anionic polymerization and atom transfer radical polymerization were used to synthesize poly(HEMA), as depicted in Scheme 3-1.



**Scheme 3-1.** Synthesis of poly(HEMA) via (a) anionic polymerization and (b) ATRP.

Obviously poly(HEMA) will form the backbone of the polymer brush, and the length distribution of the cylindrical polymer brushes is dependent only on the molecular weight distribution (MWD) of the backbone. Thus the synthesis of poly(HEMA) with a narrow MWD is crucial to get uniform polymer brushes. Although ATRP can give quite good control on the polymerization of many monomers, normally anionic polymerization provides better control on the polymerization and thus polymers with very narrow MWD could be obtained, despite of its strict purification procedure for monomer, solvents and all additives. In order to protect the reactive hydroxy group of HEMA, trimethylsilyl-protected

HEMA (TMS-HEMA) was used as monomer in anionic polymerization, and it is very easy to remove the trimethylsilyl groups of the produced polymer. For comparison, ATRP was also carried out to synthesize poly(HEMA).

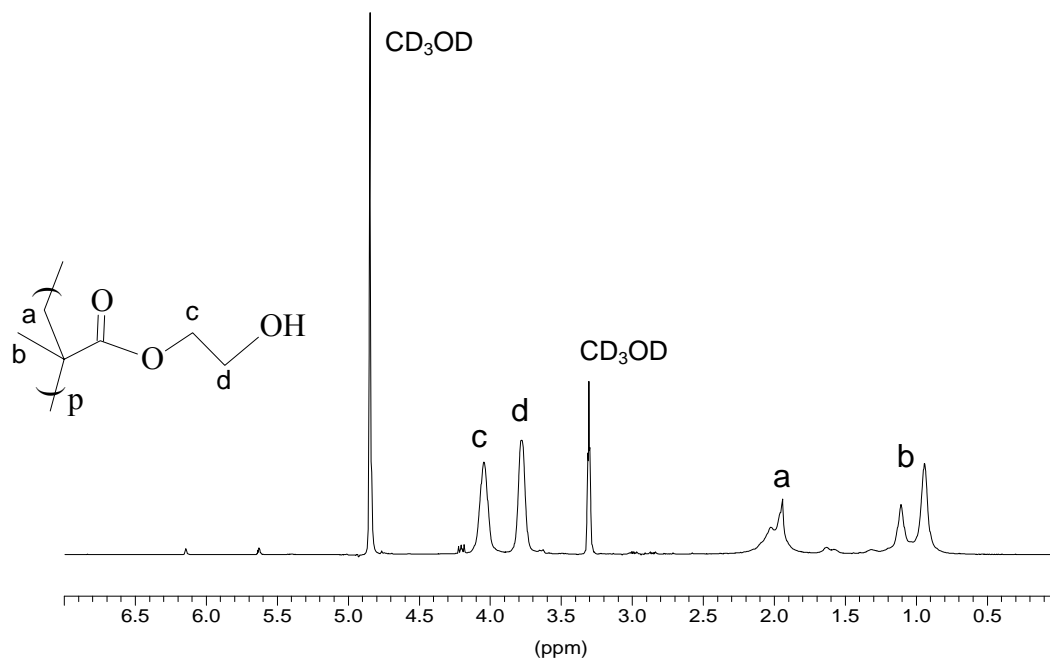


**Figure 3-2a.**  $^1\text{H-NMR}$  spectrum of poly(HEMA) in  $\text{CD}_3\text{OD}$ .

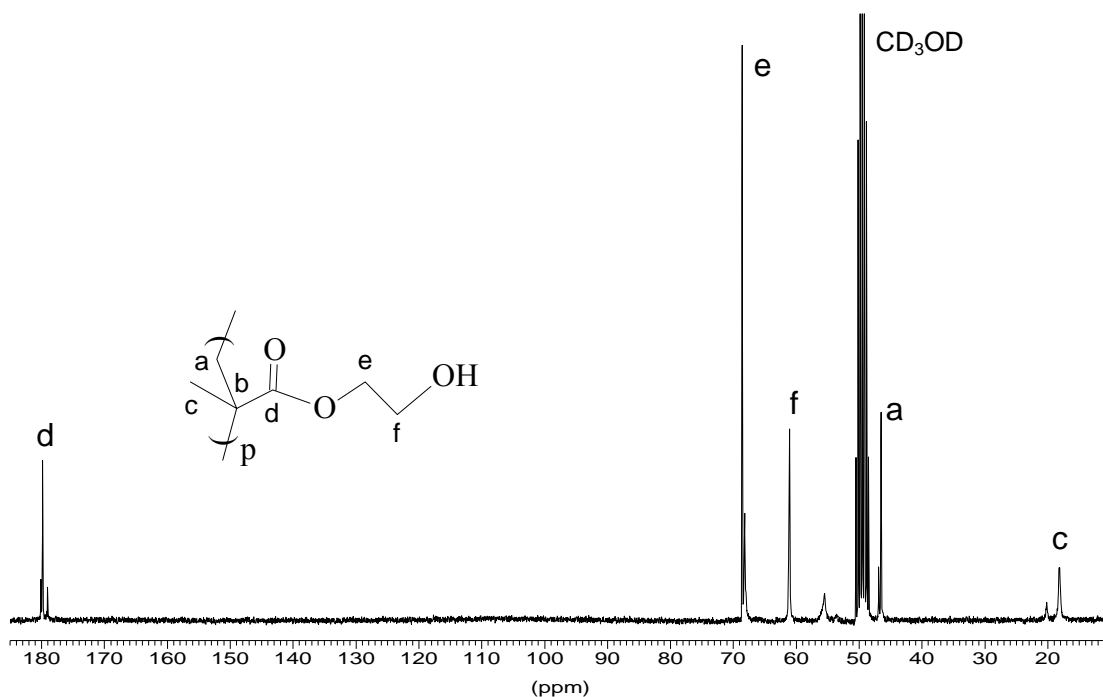
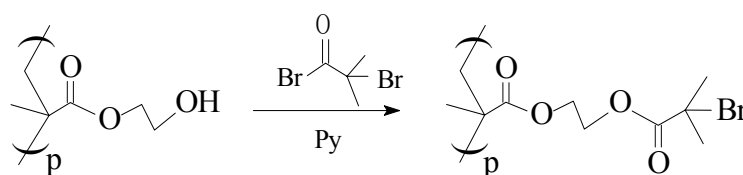


**Figure 3-2b.**  $^{13}\text{C-NMR}$  spectrum of poly(HEMA) in  $\text{CD}_3\text{OD}$ .

Figures 3-2a and 3-2b shows the  $^1\text{H}$ - and  $^{13}\text{C}$ -NMR spectra of poly(HEMA), which are in agreement with those reported in literature. The limited solubility of poly(HEMA) in THF and its adsorption to the column material prevent the direct analysis of the MWD under standard conditions of GPC. However the esterification product of poly(HEMA) with  $\alpha$ -bromoisobutyryl bromide is THF-soluble. The information of molecular weight and MWD can be obtained from that of the corresponding ester (see below).

### 3.3.2 Synthesis of polyinitiator (poly(2-(2-bromoisobutyryloxy)ethyl methacrylate, PBIEM)

As shown in Scheme 3-2, esterification of poly(HEMA) with  $\alpha$ -bromoisobutyryl bromide results in the polyinitiator for ATRP. Complete esterification of the hydroxy groups of poly(HEMA) with  $\alpha$ -bromoisobutyryl bromide was confirmed by  $^1\text{H}$ -NMR and  $^{13}\text{C}$ -NMR (Figure 3-3). In  $^1\text{H}$ -NMR spectrum, no peak is observed at 3.77 ppm, which is assigned to methylene protons adjacent to the hydroxy group in poly(HEMA). Instead, a new peak at 4.37 ppm appears, which represent the methylene protons designated as d in Figure 3-3a. Additionally, a strong peak at 1.97 ppm represents the end methyl protons in PBIEM.  $^{13}\text{C}$ -NMR spectrum also confirms the successful formation of PBIEM, indicated by the appearance of new peaks (g, h, and i in Figure 3-3b).



**Scheme 3-2.** Synthesis of PBIEM via esterification of poly(HEMA) with  $\alpha$ -bromoisobutyryl bromide.

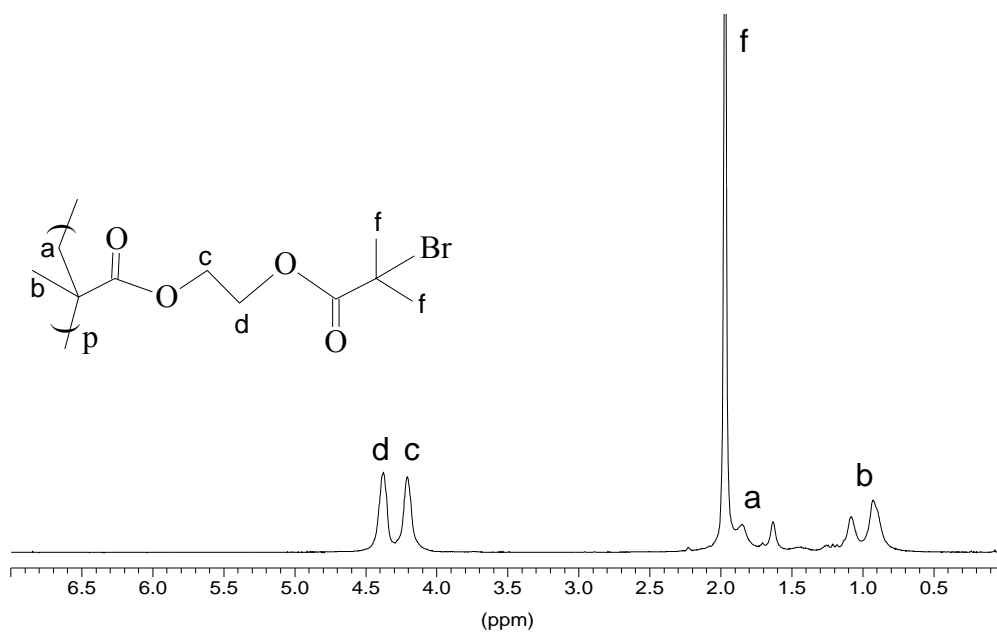


Figure 3-3a.  $^1\text{H-NMR}$  spectrum of PBIEM in  $\text{CDCl}_3$ .

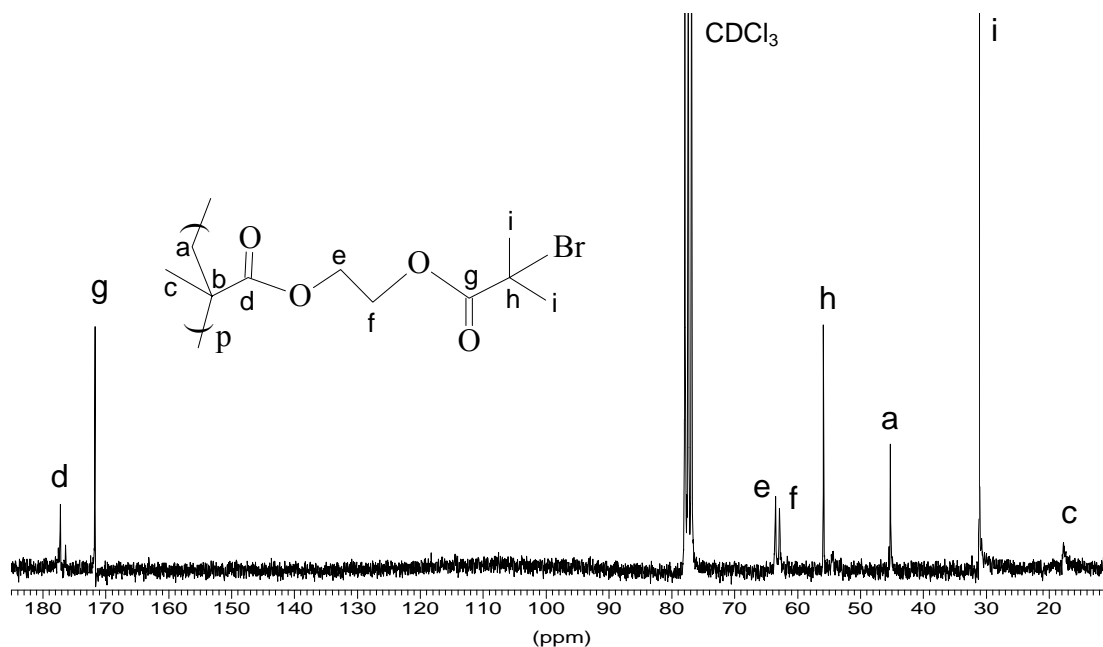
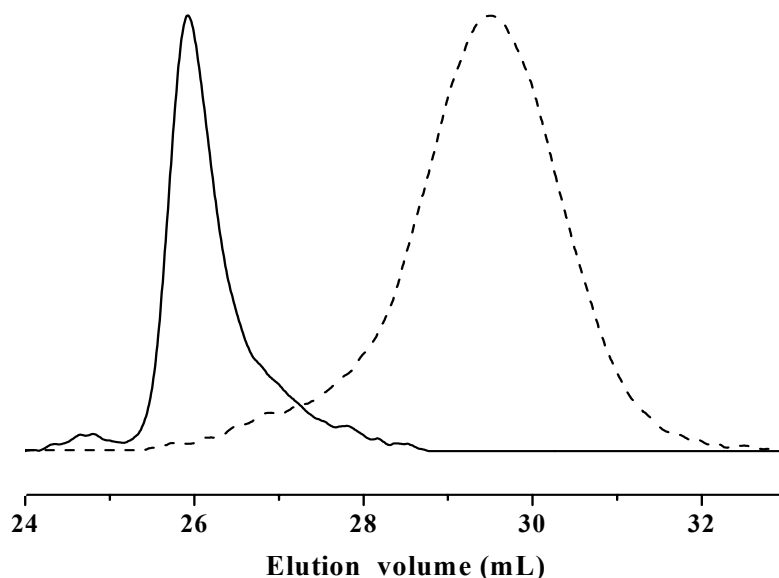


Figure 3-3b.  $^{13}\text{C-NMR}$  spectrum of PBIEM in  $\text{CDCl}_3$ .



**Figure 3-4.** GPC traces of two polyinitiators (PBIEMs) synthesized via anionic polymerization (solid line) and ATRP (dash line) respectively.

GPC measurements (Figure 3-4) clearly show that the polyinitiator synthesized via anionic polymerization has a more narrow MWD than that from ATRP. In addition, much higher molecular weight can be achieved by anionic polymerization. It is worth to mention that a small peak with double molecular weight was observed in the GPC trace of PBIEM-II synthesized via anionic polymerization, indicating that probably some side reactions occurred during the termination of the living polymer chain. This has been attributed to an attack of the anionic chain end on the TMS group.<sup>37</sup> Nevertheless the amount of the polymer with double molecular weight is very small (1.3 mol%) and the polydispersity of the PBIEM-II is very low (PDI = 1.08).

Since the polyinitiator will form the backbone of the brush, the knowledge of its true molecular weight (or degree of polymerization) is very important for the further characterization of the brushes. Thus, membrane osmometry was used here to determine the true number-average molecular weights of polyinitiators. The results are shown in Figure 3-5 and Table 3-1. The number-average molecular weights of the two polyinitiators are  $6.68 \times 10^4$  and  $4.18 \times 10^5$ , corresponding to number-average degrees of polymerization  $DP_n = 240$  and 1500, respectively. By using these two polyinitiators, amphiphilic cylindrical brushes with different backbone lengths were obtained. The reduced osmotic pressure,  $\Pi/c$ , of the polyinitiator solution in toluene at 35 °C was almost constant in the concentration

range from 1-13 g/L (Figure 3-5), which indicates the membrane osmometry measurements of polyinitiators were done near the theta condition.

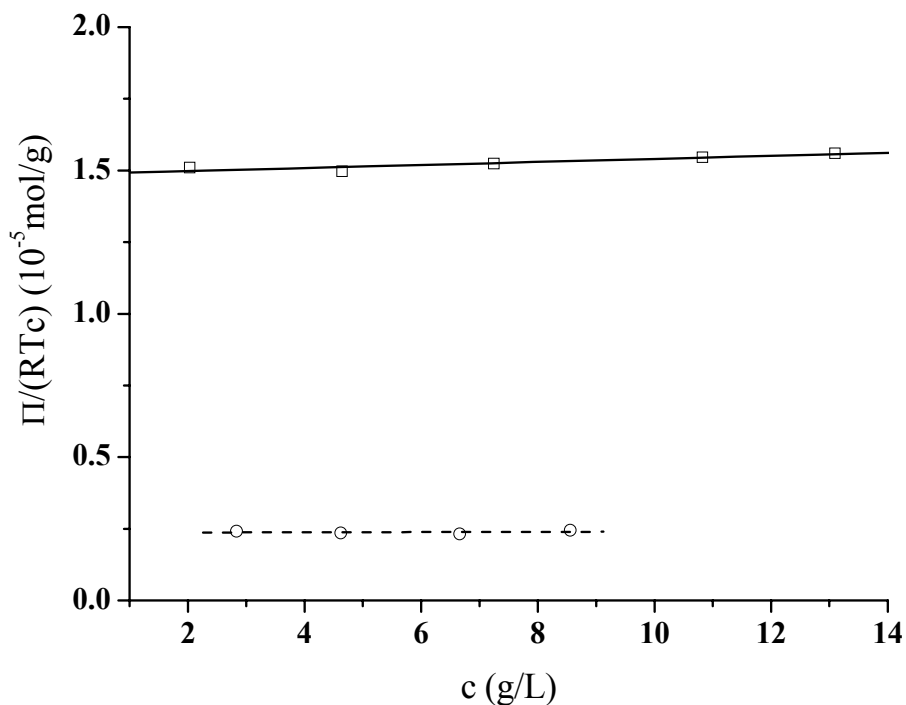


**Figure 3-5.** Membrane osmometry measurements of two polyinitiators synthesized via anionic polymerization (open circle) and ATRP (open square).

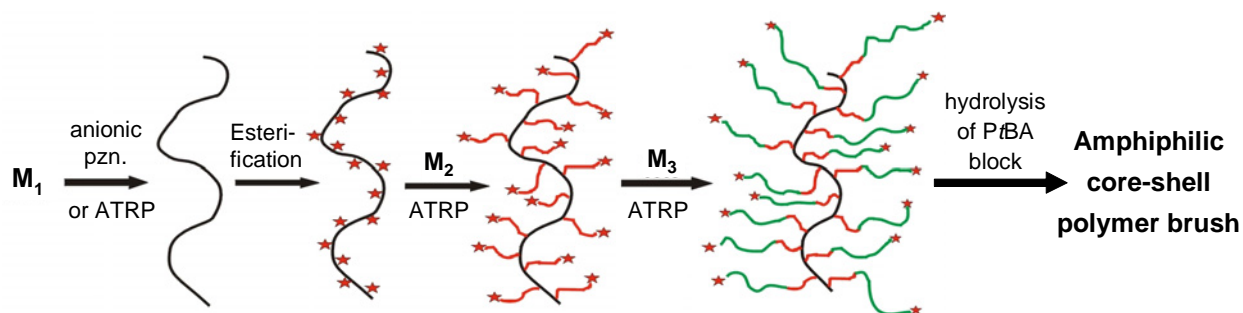
**Table 3-1.** Characterization of PBIEMs synthesized via different polymerization methods

Code	Polymerization method	$10^{-4} \times M_{n, GPC}^a$	$10^{-4} \times M_{n, osm}^b$	$PDI_{GPC}$	$DP_{n, osm}$
PBIEM-I	ATRP	2.05	6.68	1.16	240
PBIEM-II	Anionic polymerization	8.01	41.82	1.08	1500

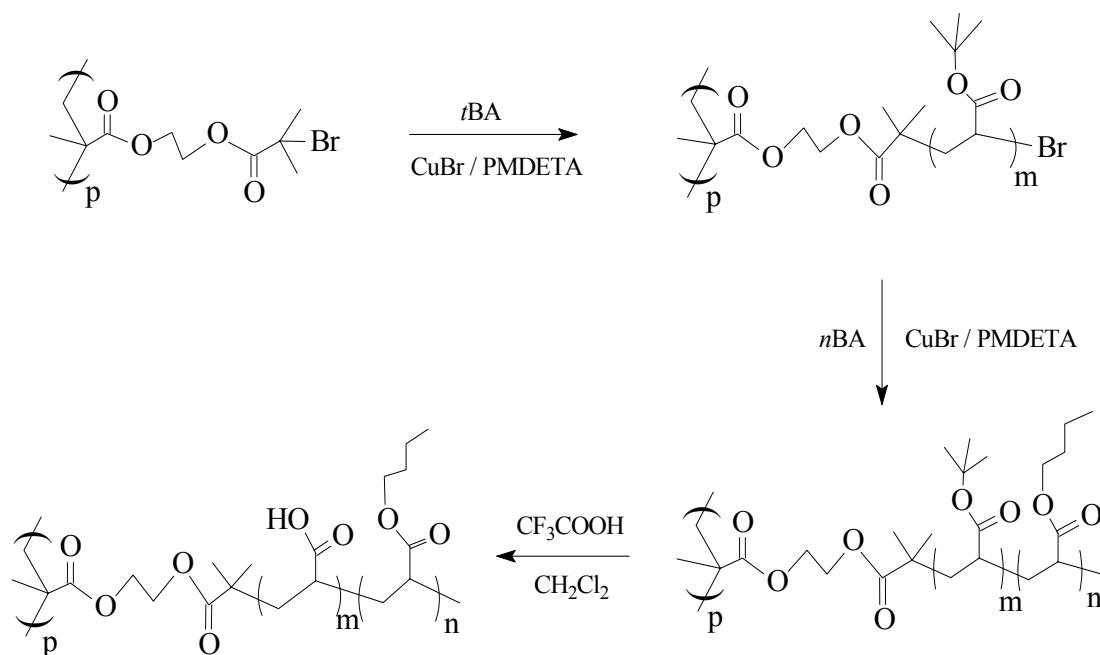
(a) calibrated against linear polystyrene standards; (b) obtained by membrane osmometry.

### 3.3.3 Synthesis of cylindrical brushes with poly(*t*-butyl acrylate) (*PtBA*) core and poly(*n*-butyl acrylate) (*PnBA*) shell

The general synthetic approach for core-shell cylindrical polymer brushes is schematically shown in Scheme 3-3. For the amphiphilic cylindrical brushes with PAA core and *PnBA* shell, the synthetic route is shown in Scheme 3-4. First, ATRP of *t*-butyl acrylate (*tBA*) initiated by the polyinitiator formed the core block of polymer brushes. After purification (removal of the unreacted *tBA*), the polymer brush with *PtBA* side chains was used as poly(macroinitiator) for the polymerization of *n*-butyl acrylate (*nBA*) to form the *PnBA* shell block of polymer brushes. Finally, selective hydrolysis of *PtBA* produced well-defined amphiphilic core-shell polymer brushes.



**Scheme 3-3.** Schematic route to amphiphilic core-shell cylindrical polymer brush ( $M_1$ : HEMA;  $M_2$ : *tBA* (or styrene/*nBA*),  $M_3$ : styrene/*nBA* (or *tBA*).



**Scheme 3-4.** Synthetic procedure for amphiphilic brush with PAA core and *PnBA* shell.

Tables 3-2 and 3-3 present the results of ATRP by using two different polyinitiators. Well-defined polymer brushes with homopolymer and diblock copolymer side chains were obtained, as confirmed by the monomodal GPC eluograms (Figures 3-6 and 3-7). The molecular weight distributions of the resulting brushes are quite low in most cases ( $PDI < 1.3$ ), indicating that intermacromolecular coupling reactions during the polymerization are negligible. The polymerizations of both *t*BA and *n*BA are fast and can go to relatively high conversion without the occurrence of cross-linking. In the case of the polymerization of *n*BA, the reaction system became very viscous at the final stage of polymerization, but coupling reaction was not observed. In contrast, when styrene was used as monomer to form the polymer shell instead of *n*BA, cross-linking happened very often at quite low monomer conversion when PBIEM-II was used as polyinitiator, although different polymerization conditions (such as ligand type, monomer/initiator ratio, and solvent addition) were tried.

**Table 3-2** Synthesis and characterization of short cylindrical brushes initiated by PBIEM-I

Brush	Initiator	M	[CuX]/ [PMDETA] /[Br] <sup>a</sup> /[M]	T (°C)	Time (min)	Conv. (%)	$10^{-5} \times$ $M_{n,GPC}$ <sup>b</sup>	PDI <sup>b</sup>	$10^{-6} \times$ $M_{n,MALS}$	$R_g$ (nm)	Formula <sup>c</sup>
1	PBIEM-I	<i>t</i> BA	1 <sup>d</sup> /2 / 1 / 200	50	20	29.3	2.98	1.17	1.44	16.3	[ <i>t</i> BA <sub>45</sub> ] <sub>240</sub>
2	PBIEM-I	<i>t</i> BA	1 <sup>e</sup> /1 / 1 / 250	50	30	10.8	2.07	1.15	0.93	11.6	[ <i>t</i> BA <sub>28</sub> ] <sub>240</sub>
3	PBIEM-I	<i>t</i> BA	1 <sup>d</sup> /2 / 1 / 250	50	20	22.8	2.95	1.16	1.25	16.0	[ <i>t</i> BA <sub>39</sub> ] <sub>240</sub>
4	Brush 3	<i>n</i> BA	3.2 <sup>d</sup> /6.1 / 1 <sup>f</sup> /890	70	65	18.1	5.55	1.25	4.90	33.5	[ <i>t</i> BA <sub>39</sub> - <i>n</i> BA <sub>118</sub> ] <sub>240</sub>
5	PBIEM-I	<i>t</i> BA	0.5 <sup>e</sup> /0.5 / 1 / 300	50	35	12.2	2.41	1.17	1.12	12.9	[ <i>t</i> BA <sub>34</sub> ] <sub>240</sub>
6	Brush 5	<i>n</i> BA	1.6 <sup>e</sup> /3.2 / 1 <sup>f</sup> /520	70	85	9.1	3.65	1.27	3.29	23.4	[ <i>t</i> BA <sub>34</sub> - <i>n</i> BA <sub>71</sub> ] <sub>240</sub>

(a) molar concentration of initiating bromine groups in PBIEM or polymer brush with *t*BA side chains; (b) calibrated against linear PS standards; (c) DP of the side chain is calculated from the number-average molecular weight from GPC-MALS measurement ( $M_{n,MALS}$ ); (d) CuCl; (e) CuBr; and (f) calculated from  $M_{n,MALS}$ .

**Table 3-3** Synthesis and characterization of long cylindrical brushes initiated by PBIEM-II

Brush	Initiator	M	[CuX]/ [PMDETA] /[Br] <sup>a</sup> /[M]	T (°C)	Time (min)	Conv. (%)	10 <sup>-5</sup> × M <sub>n,GPC</sub> <sup>b</sup>	PDI <sup>b</sup>	10 <sup>-6</sup> × M <sub>n,MALS</sub>	R <sub>g</sub> (nm)	Formula
7	PBIEM-II	<i>t</i> BA	0.5 <sup>e</sup> /0.5 / 1 / 300	50	35	10.0	6.83	1.31	7.57	51.6	[ <i>t</i> BA <sub>37</sub> ] <sub>1500</sub> <sup>c</sup>
8	Brush 7	<i>n</i> BA	1.9 <sup>e</sup> /3.9 / 1 <sup>f</sup> / 575	70	75	7.0	7.72	1.40	22.16	81.3	[ <i>t</i> BA <sub>37</sub> - <i>n</i> BA <sub>76</sub> ] <sub>1500</sub> <sup>c</sup>
9	PBIEM-II	<i>t</i> BA	0.5 <sup>e</sup> /0.5 / 1 / 300	50	40	12.5	7.37	1.18	6.69	50.2	[ <i>t</i> BA <sub>33</sub> ] <sub>1500</sub> <sup>c</sup>
10 <sup>g</sup>	Brush 9	<i>n</i> BA	2.3 <sup>e</sup> /2.4 / 1 <sup>f</sup> / 505	70	60	9.3	8.85	1.34	–	–	[ <i>t</i> BA <sub>33</sub> - <i>n</i> BA <sub>44</sub> ] <sub>1500</sub> <sup>h</sup>
11	PBIEM-II	<i>t</i> BA	0.5 <sup>e</sup> /0.5 / 1 / 300	50	15	8.5	6.45	1.16	–	–	[ <i>t</i> BA <sub>25</sub> ] <sub>1500</sub> <sup>i</sup>
12 <sup>g</sup>	Brush 11	<i>n</i> BA	2 <sup>e</sup> /2 / 1 <sup>i</sup> / 450	70	13	13.5	7.60	1.29	–	–	[ <i>t</i> BA <sub>25</sub> - <i>n</i> BA <sub>61</sub> ] <sub>1500</sub> <sup>i</sup>

(a)-(f): see Table 3-2; (g) adding 30 vol.% of acetone; (h) calculated according to <sup>1</sup>H NMR; and (i) calculated from monomer conversion.

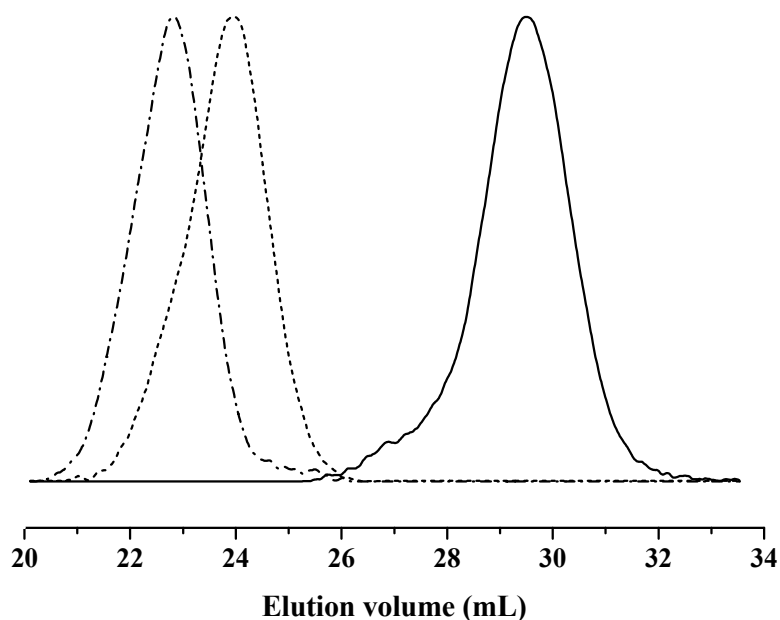


**Figure 3-6.** GPC traces of PBIEM-I and the corresponding brushes with homopolymer and diblock copolymer side chains (—: PBIEM-I; --: Brush 5, [*t*BA<sub>34</sub>]<sub>240</sub>; -·-: Brush 6, [*t*BA<sub>34</sub>-*n*BA<sub>71</sub>]<sub>240</sub>).

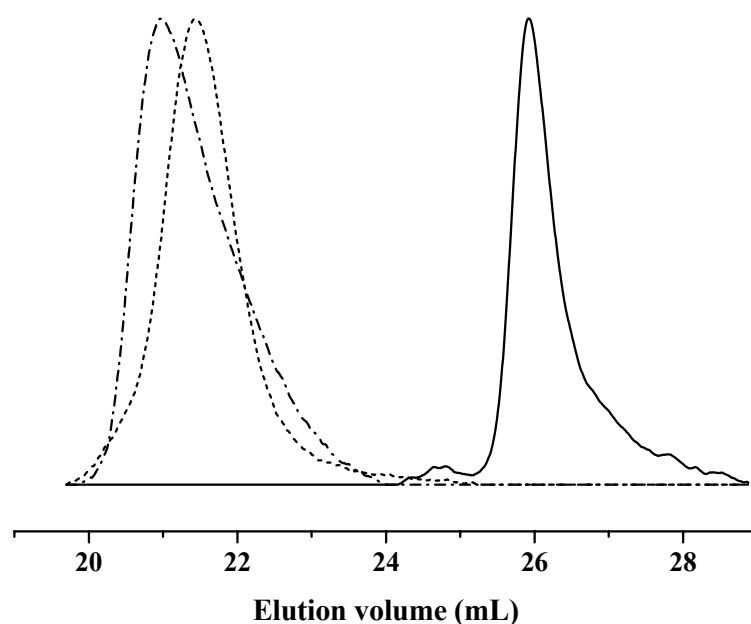


**Figure 3-7.** GPC traces of PBIEM-II and the corresponding brushes with homopolymer and diblock copolymer side chains (—: PBIEM-II; --: Brush 9, [tBA<sub>33</sub>]<sub>1500</sub>; ···: Brush 10, [tBA<sub>33</sub>-nBA<sub>44</sub>]<sub>1500</sub>).

It has been reported that in ATRP potentially active macromolecules terminated with bromine could be converted into inactive macromolecules devoid of terminal bromine due to the degradative transfer reaction.<sup>40</sup> In this procedure, ligands such as PMDETA act as a transfer agent. This side reaction normally takes place at the end of the polymerization only (e.g. high monomer conversion is achieved), and it may be to some extent reduced by decreasing the [ligand]/[CuBr]/[initiator] ratio and/or temperature. For the synthesis of core-shell polymer brushes, it is very important to avoid the loss of bromine end group when the core block of the side chain (PtBA) is formed, since the side chain devoid of terminal bromine can not initiate the further polymerization of the second monomer (*n*-butyl acrylate), and thus well-defined core-shell structure could not be obtained. In order to avoid this side reaction, the polymerizations of *t*-butyl acrylate, were stopped at relatively low conversion (< 30%), and in most cases, less PMDETA ([PMDETA]<sub>0</sub>/[CuBr]<sub>0</sub>/[initiator]<sub>0</sub> = 0.5/0.5/1.0) was used, compared to normal ATRP of acrylates.

It has to be pointed out that since the polyinitiator and poly(macroi)niator (i.e., the brushes with PtBA side chains) are solids, the polymerization mixture (catalyst, initiator, monomer, internal standard, and solvent) had to be stirred until all initiator was completely

dissolved before starting the polymerization by adding ligand and placing the flask into an oil bath. Especially the polyinitiator with high molecular weight (PBIEM-II) dissolves in monomer (*t*BA) much slower than PBIEM-I. Thus, if the time of stirring before the addition of ligand is not long enough (which means the polyinitiator is incompletely dissolved), the MWD of the final product will be somehow broader (such as Brush 7 in Table 3-3), because in this case not all the polyinitiator molecules start the polymerization at the same time. After the formation of *Pt*BA side chains, the molecular weights of the resulting brushes are very high, and correspondingly their solubility in the second monomer (*n*BA) decreases. In order to dissolve these brushes, adding suitable solvent such as acetone is helpful. As shown in Table 3-3 (Brushes 10 and 12) and Figure 3-7, a core-shell brush with more narrow MWD was obtained after adding 30 vol% of acetone.

Obviously, the molecular weights of these brushes obtained from GPC against linear PS standards are just the apparent ones. The absolute molecular weights as well as the radii of gyration,  $R_g$ , in THF of these brushes were determined by GPC-MALS. With the same backbone but longer side chain length,  $R_g$  of the brushes increase with a scaling law  $R_g \propto DP_{sc}^{0.57 \pm 0.05}$ , as shown in Figure 3-8. To our best knowledge this is the first experimental quantitative investigation about the influence of side chain length on radius of gyration of the cylindrical brushes with exactly identical backbone length. Further systematic study on this relationship is needed since only a few data points are available at the moment. Nevertheless, polymer brushes synthesized via “grafting from” method are the best candidates to study the independent influence of side chain length on overall dimensions of the brushes, because the length of backbone is fixed. On the other hand, polymacromonomer method is suitable for the investigation of the relationship between the radius of gyration and the backbone DP since here the side chain DP is fixed and a broad MWD of backbone is obtained. Using GPC-MALS coupling such measurements were performed by Schmidt et al.<sup>3,4</sup> It is expected that the main chain stiffness of the polymer brush increases with increasing side chain length, because the stronger overcrowding of longer side chains forces the otherwise flexible main chain into a more stretched conformation.

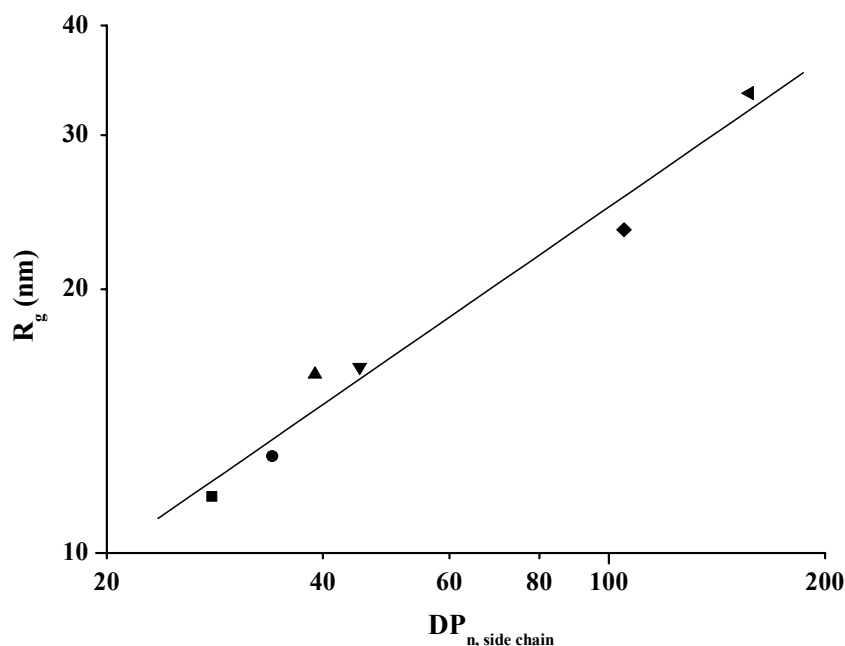


**Figure 3-8.** Radius of gyration versus DP of side chain of the brushes with PBIEM-I as backbone (■: Brush 2; ●: Brush 5; ▲: Brush 3; ▼: Brush 1; ◆: Brush 6; ◄: Brush 4).

Figure 3-9 shows the  $^1\text{H-NMR}$  spectra of different polymer brushes, and for direct comparison, the  $^1\text{H-NMR}$  spectrum of the polyinitiator is shown again in Figure 3-9A. After the formation of the brush with *Pt*BA side chains, a characteristic strong peak at 1.44 ppm (peak c) corresponding to methyl protons in *t*-butyl group ( $-\text{C}(\underline{\text{C}}\text{H}_3)_3$ ) appears, as shown in Figure 3-9B. The successful formation of the core-shell brush with *Pn*BA shell is confirmed by the appearance of several new peaks in Figure 3-9C, such as the typical triple peak at 0.94 ppm and the peak at 4.04 ppm, corresponding to the terminal methyl protons ( $-\text{O}(\text{CH}_2)_3\underline{\text{C}}\text{H}_3$ ) and the methylene protons adjacent to oxygen ( $-\text{O}\underline{\text{C}}\text{H}_2(\text{CH}_2)_2\text{CH}_3$ ) in the *n*-butyl group, respectively. The protons from the other two methylene groups in the *n*-butyl group can also be seen at 1.35 ppm (which is overlapped with protons from the *t*-butyl group) and 1.60 ppm.

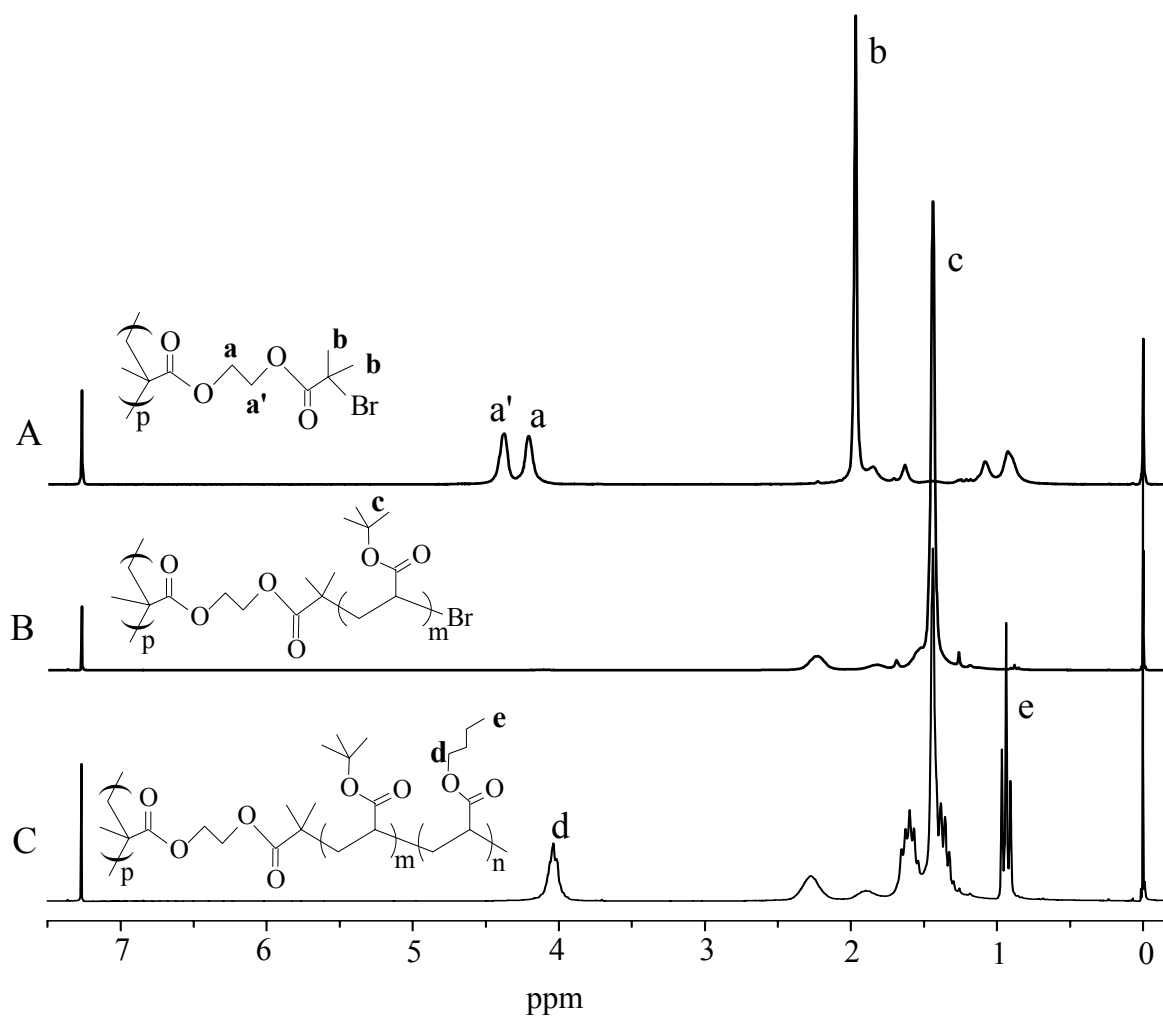


**Figure 3-9.**  $^1\text{H-NMR}$  spectra of (A) polyinitiator (PBIEM-I); (B) brushes with PtBA homopolymer side chains (Brush 5); and (C) brushes with PtBA-b-PnBA diblock copolymer side chains (Brush 6).

### 3.3.4 Formation of amphiphilic core-shell cylindrical brushes

By selective hydrolysis of the *Pt*BA block of the side chains, amphiphilic core-shell cylindrical brushes with poly(acrylic acid) (PAA) core and *Pn*BA shell were obtained. The hydrolysis procedure was very simple and effective. As shown in Figure 3-10, the disappearance of the characteristic strong peak at 1.44 ppm corresponding to the methyl protons of the *t*-butyl group demonstrates the successful hydrolysis of *Pt*BA block of the side chains. The resulting brushes resemble inverse cylindrical micelles of amphiphilic block copolymers in non-polar solvents, thus can be regarded as unimolecular cylindrical micelles. By simply changing the type and quality of solvents, one can easily adjust the sizes of the core and the shell of these amphiphilic brushes.<sup>28</sup>

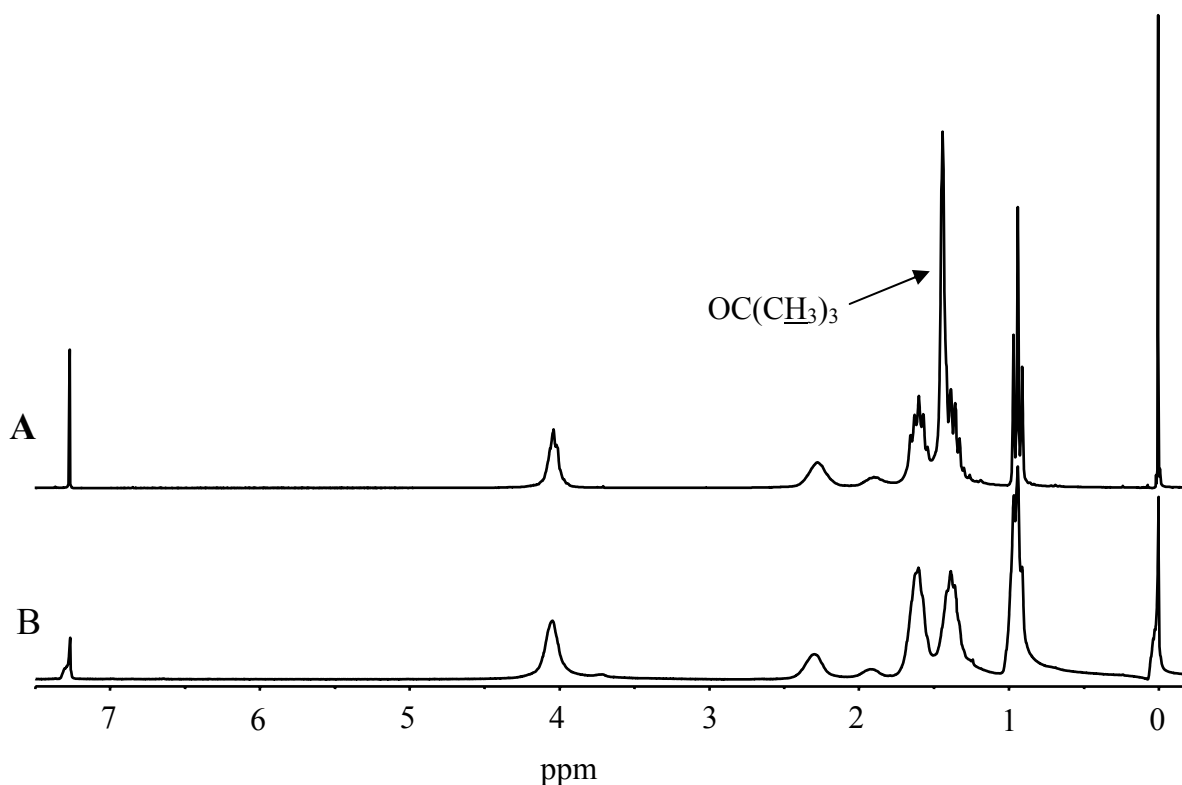


**Figure 3-10.**  $^1\text{H-NMR}$  spectra of core-shell brushes (A) Brush 6,  $[\textit{tBA}_{34}\text{-nBA}_{71}]_{240}$ ; and (B) the hydrolysis product of Brush 6,  $[\textit{AA}_{34}\text{-nBA}_{71}]_{240}$ .

Dynamic light scattering was used to characterize the amphiphilic core-shell brushes in dilute THF solution. Figure 3-11A shows the typical normalized field correlation functions of a long amphiphilic core-shell brush (hydrolysis product of Brush 8) at room temperature. The CONTIN<sup>41</sup> analysis of these autocorrelation functions shows a monomodal decay time distribution at all scattering angles. Apparent hydrodynamic radii of the amphiphilic brushes

were calculated according to Stokes-Einstein equation under the assumption that the scattering particles behave as hard spheres. Figure 3-11B shows the hydrodynamic radius distribution of this amphiphilic brush in THF at scattering angle of  $30^\circ$ . The z-average hydrodynamic radius of this brush at  $30^\circ$  is 72.4 nm.

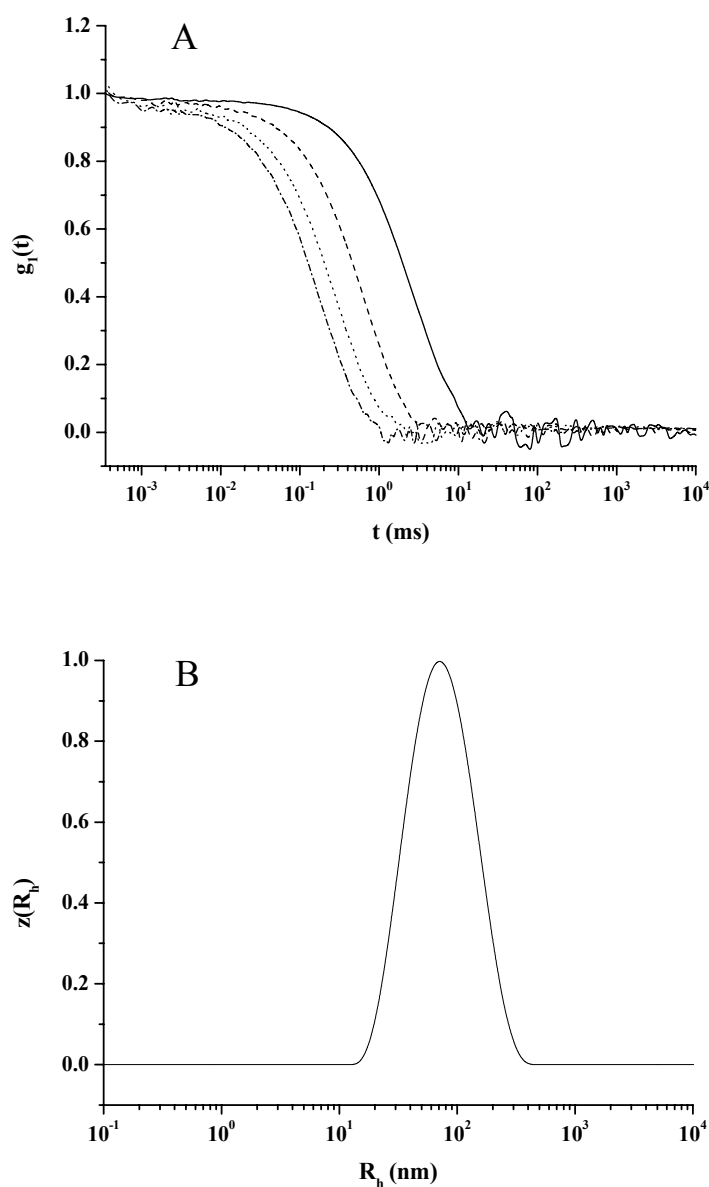
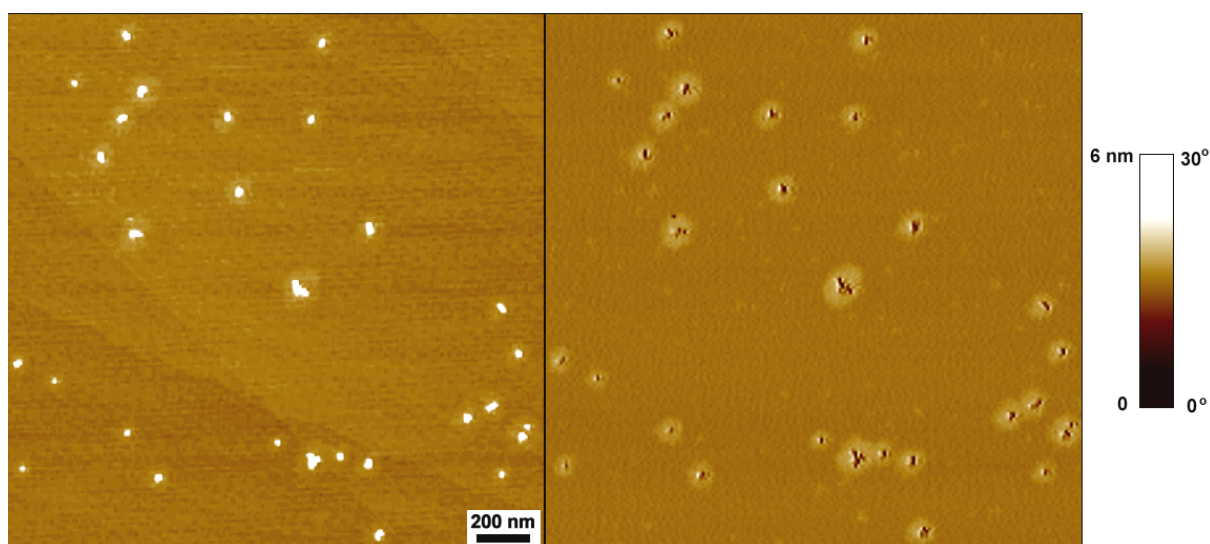


**Figure 3-11.** (A) Normalized field correlation functions of the hydrolysis product of Brush 8,  $[AA_{37-n}BA_{76}]_{1500}$ , in THF ( $c = 1.0$  g/L) at different angles (—:  $30^\circ$ ; --:  $60^\circ$ ; ....:  $90^\circ$ ; -·-·:  $120^\circ$ ); (B) The corresponding hydrodynamic radius distribution of this brush at  $30^\circ$ .

### 3.3.5 Scanning force microscopy (SFM) characterization of cylindrical brushes

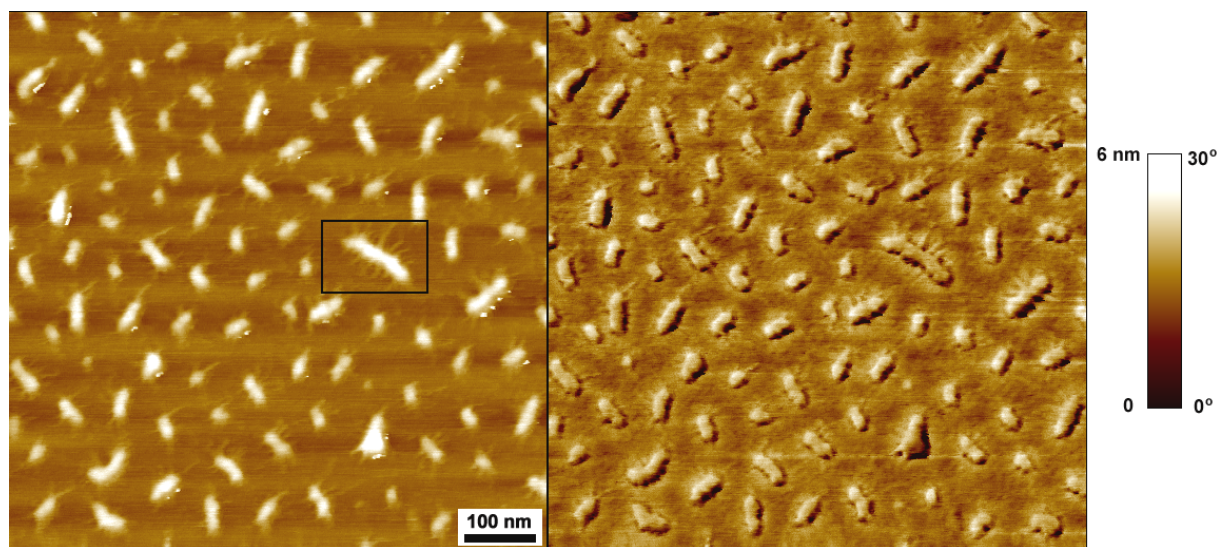
The core-shell brushes were further characterized by SFM in order to visualize the unimolecular cylinders. All samples for SFM were prepared by dip-coating from dilute solutions using freshly cleaved mica as substrate.

Figure 3-12 shows the SFM images of one amphiphilic brush  $[AA_{39}\text{-}nBA_{118}]_{240}$  (hydrolysis product of Brush 4), dip-coated from 1-butanol on mica. From SFM images this polymer appears starlike rather than brushlike, because of its very long side chains and somewhat short backbone. From the phase image one can easily observe a core with a surrounding corona. In the case of the brushes with PAA-*b*-PS side chains we did not see this apparent phase difference from SFM image.<sup>28</sup> Similar SFM images were also found for the cylindrical brush with P*n*BA core and PS shell, and the driving force was claimed to be the collapse of the PS block on mica (because the nonpolar PS block has weak interaction with the polar substrate mica).<sup>29</sup> However, for the amphiphilic brush  $[AA_{39}\text{-}nBA_{118}]_{240}$ , both PAA and P*n*BA have attractive interactions with mica, therefore the core as well as the shell of this brush should be tightly absorbed to the substrate. Thus, we conclude that the core shown in the SFM images corresponds to PAA and the backbone of the brush whereas the corona corresponds to the P*n*BA shell. This apparent phase difference stems from the large difference of stiffness between PAA and P*n*BA, taking into account that the glass transition temperature of P*n*BA is much lower than that of PAA (and also P*t*BA).



**Figure 3-12.** SFM images of the amphiphilic brush  $[AA_{39}\text{-}nBA_{118}]_{240}$  (hydrolysis product of Brush 4), dip coated from dilute 1-butanol solution on mica: (left) height image and (right) phase image.

In order to obtain polymers exhibiting cylindrical shape, one has to increase the aspect ratio, corresponding to the ratio between the backbone and the side chains lengths. Figure 3-13 presents SFM images of another core-shell brush  $[tBA_{34-n}BA_{71}]_{240}$  (Brush 6), with exactly the same backbone as the above brush but shorter side chains on a mica surface. The polymer cylinders are directly visualized. One can clearly observe some millipede-like structures, especially in the phase image. The cross section analysis of the cylinder marked with a rectangle shows that its height ( $2.5 \pm 0.2$  nm) is much smaller than its diameter ( $20 \pm 2$  nm, neglecting the length of hairs), indicating a strong deformation of the cylindrical profile on mica. This is due to the attractive interaction between the side chains and the substrate. The length distribution of the polymer cylinders in Figure 3-13 is somehow broad, although the MWD of the polyinitiator (PBIEM-I) for these cylinders is not very high (PDI = 1.16). This also indicates the necessity of synthesizing polyinitiators with very narrow distribution in order to get uniform polymer cylinders.



**Figure 3-13.** SFM image of the brush  $[tBA_{34-n}BA_{71}]_{240}$  (Brush 6), dip coated from dilute THF solution on mica: (left) height image and (right) phase image.

When using the polyinitiator synthesized via anionic polymerization (PBIEM-II), long amphiphilic core-shell cylinders with much more narrow backbone length distribution were obtained. Figure 3-14 shows the SFM images of the amphiphilic brush  $[AA_{37-n}BA_{76}]_{1500}$  (hydrolysis product of Brush 8). The high uniformity as well as the regular cylindrical shape of the polymer cylinders enables us to perform a statistical analysis. The results of length distribution is shown in Figure 3-15. The number-average and weight-average lengths of 249 individual cylinders in Figure 3-14 (neglecting those cylinders which overlap) are  $l_n =$

179 nm and  $l_w = 186$  nm respectively, with a polydispersity  $l_w/l_n = 1.04$  which agrees well with the polydispersity of the backbone ( $M_w/M_n = 1.08$ ). It has to be noted that the results of statistical analysis is somehow dependent on the selected area on a SFM image. Nevertheless, it is clear from SFM images that the polymer brushes with PBIEM-II as backbone are very uniform and have a narrow length distribution.

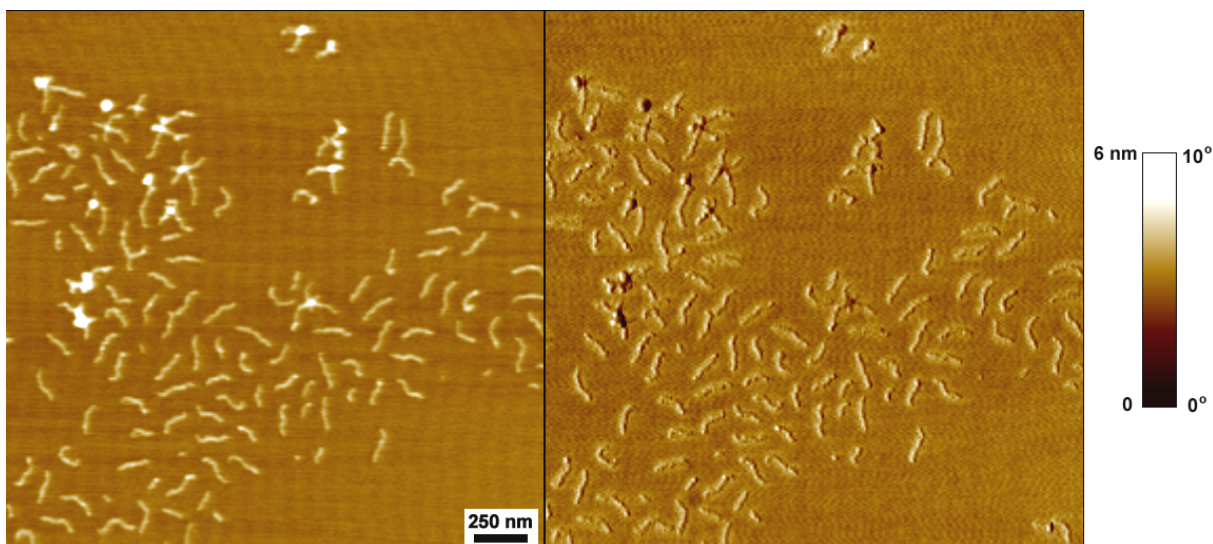


**Figure 3-14.** SFM image of the brush,  $[AA_{37-n}BA_{76}]_{1500}$  (hydrolysis product of Brush 8) dip coated from dilute  $CH_3OH/CHCl_3$  (4/1) solution on mica: (left) height image and (right) phase image.

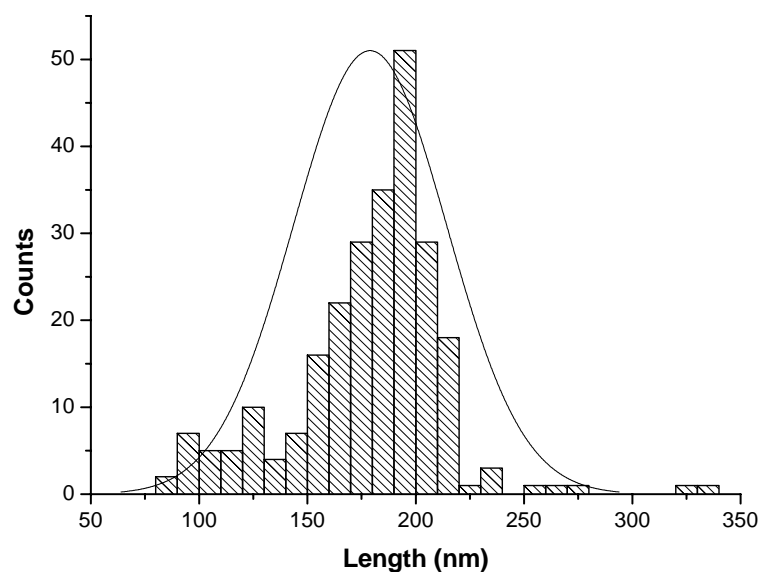


**Figure 3-15.** Length distribution of the brushes shown in Figure 3-14, obtained from statistical analysis.

Since the DP of the backbone is 1500 and the number-average length obtained from SFM image is 179 nm for the brush  $[AA_{37}-nBA_{76}]_{1500}$ , the length per monomer unit of the backbone is calculated to be  $l_{\text{unit}} = 0.12$  nm. This value is lower than  $l_{\text{unit}} = 0.25$  nm for the all-trans conformation of an aliphatic chain, but it is comparable to that of the brush with poly(methyl acrylate) main chain and poly(methyl methacrylate) side chain.<sup>15</sup>

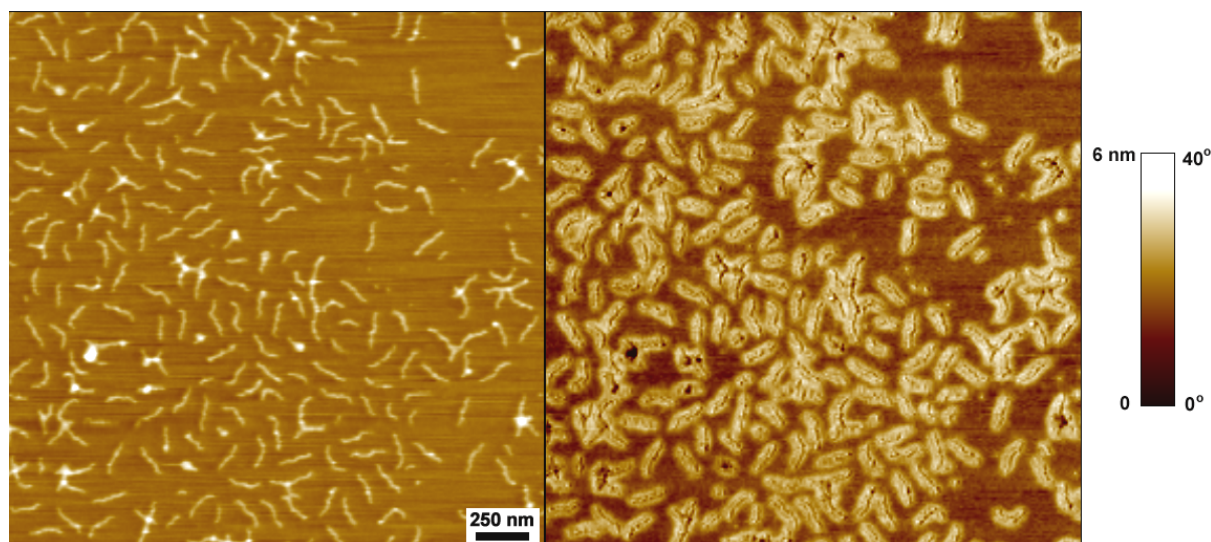
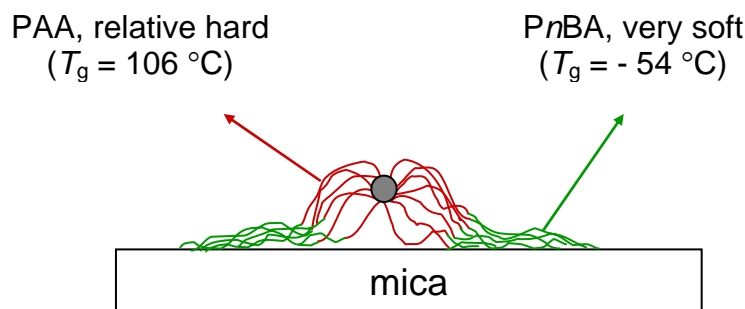


**Figure 3-16.** SFM image of the brush,  $[AA_{37}-nBA_{76}]_{1500}$  (hydrolysis product of Brush 8) dip coated from dilute  $CH_3OH/CHCl_3$  (1/1) solution on mica: (left) height image and (right) phase image.

The phase difference between the core and the shell is not very clear in Figure 3-14, probably because the shell (PnBA) is not well extended in the mixture of methanol and chloroform with volume ratio of 4/1. However, the phase difference is enhanced dramatically when the ratio of the two solvents was changed to 1/1, as shown in Figure 3-16. In the height image the corona is invisible, probably because the height of the PnBA shell is too small to be detectable. However, in the phase image the corona is very clear, making it possible to obtain size information about the core and the shell directly from the SFM height and phase images, respectively. For example, the average diameter of the core of cylinders in Figure 3-16 is measured to be about 25 nm and the diameter of whole cylinder (core and shell) is about 65 nm.

Scheme 3-5 shows the schematic structure of amphiphilic polymer brushes on mica. As mentioned before, the soft PnBA shell totally collapses on the substrate, thus it is invisible in the height image.



**Scheme 3-5.** Schematic illustration of the structure of the amphiphilic polymer brushes with PAA core and PnBA shell on mica.

### 3.3.6 Synthesis of other polymer brushes and investigation of solution properties

Via similar approach, polymer brushes with protonated polystyrene (PS) or deuterated polystyrene (PSD) homopolymer or polystyrene-*b*-poly(acrylic acid) (PS-*b*-PAA) block copolymer side chains were also synthesized. Table 3-4 summarizes the characterization results of these brushes.

**Table 3-4.** Characterization of cylindrical brushes with PS, PSD, or PS-*b*-PAA side chains

Brush	Initiator	Side chain	$10^{-6} \times M_{w,SLS}^b$	$PDI_{GPC}^c$	Formula
13	PBIEM-III <sup>a</sup>	PS	1.20	1.45	$[S_{23}]_{310}^d$
14	Brush 13	PS- <i>b</i> -PtBA	–	1.34	$[S_{23-tBA_{186}}]_{310}^e$
14H	–	PS- <i>b</i> -PAA	–	–	$[S_{23-AA_{186}}]_{310}$
15	PBIEM-II	PSD	11.3	1.47	$[(S-d8)_{43}]_{1500}^d$

(a) PBIEM-III, synthesized via ATRP,  $PDI = 1.24$ ,  $DP = 310$  from membrane osmometry;<sup>28</sup> (b) weight-average molecular weight from the SLS measurement; (c) polydispersity obtained from GPC measurement using linear PS as standards; (d) DP of side chain is calculated from  $M_{w,SLS}$  and  $PDI_{GPC}$ ; and (e) DP of PtBA is calculated from the block ratio of the side chain according to <sup>1</sup>H NMR.

The shape/size of polymer brushes observed by SFM depends not only on their original shape/size in solution but also on the interaction between the polymer and the substrate,

since interaction of the monomer units with a flat substrate changes the orientation of the side chains relative to the backbone and breaks the symmetry and the dimensionality of the system.<sup>42</sup> Therefore the shape/size of polymer brushes observed by SFM may somehow differ from that in solution.

In contrast to SFM, cryogenic transmission electron microscopy (cryo-TEM) is a tool to obtain the original shape and size of polymers in solution directly, since the sample is frozen during the measurement. For Brush 14H, because its outer hydrophilic PAA block of the side chain is much longer than the inner hydrophobic PS block, it can be dissolved in basic aqueous solution (0.083 M NaOH) and measured with cryo-TEM to visualize its morphology in solution. As depicted in Figure 3-17, rod-like shapes of these brushes were clearly observed, indicating a rather high persistence length of the cylinders in solution. There are also many dot-like objects in the cryo-TEM image. Since only the projection of the cylinders on the observation plane are seen, these are attributed to cylinders oriented unparallel to the observation plane and/or probably some very short cylinders.

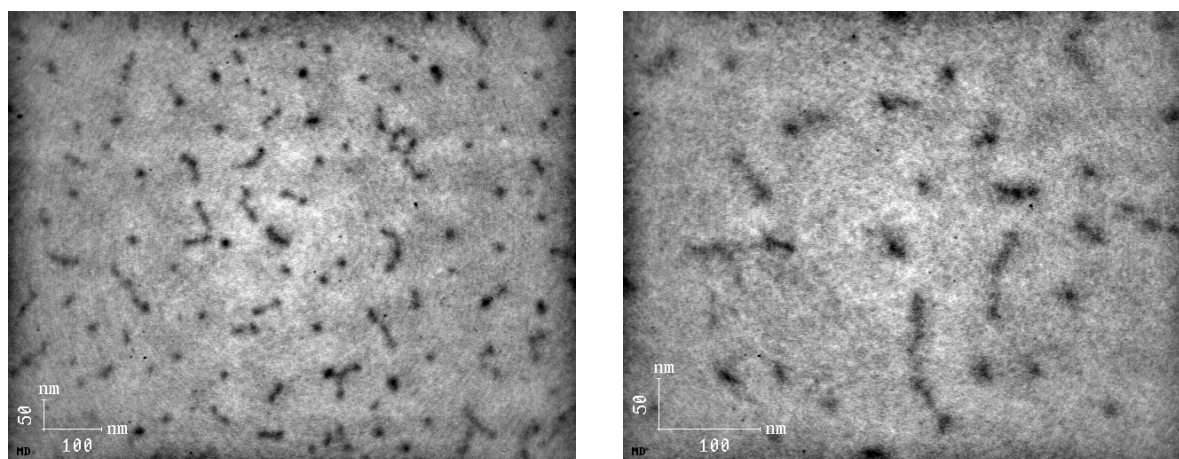


**Figure 3-17.** Cryo-TEM image of amphiphilic polymer brush  $[S_{23-AA_{186}}]_{310}$  (Brush 14H).

Light scattering techniques, such as static and dynamic light scattering (SLS and DLS), are widely used in the structural characterization of polymers in solution. Here dilute solutions of the cylindrical brush with PSD homopolymer side chains are studied by SLS and DLS in chloroform at different temperatures. Figure 3-18 shows a typical Zimm plot of Brush 15 in chloroform at 20°C.

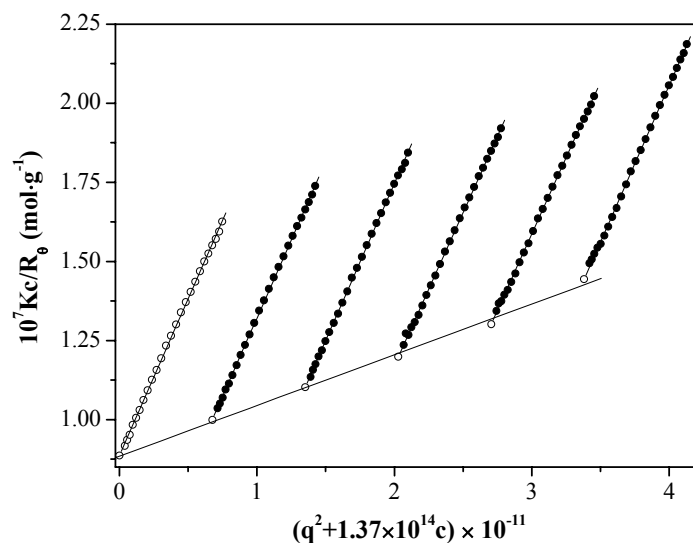


**Figure 3-18.** Zimm plot of Brush 15 ( $[(S-d8)_{43}]_{1500}$ ) in chloroform at  $20^\circ\text{C}$ , where  $K$  denotes the optical constant, and  $R_\theta$  is the Rayleigh ratio at scattering angle of  $\theta$  (cgs unit). Solid circles denote the experimental data and open circles denote the extrapolated data at zero scattering angle and zero concentration.  $M_w = 1.13 \cdot 10^7$  g/mol,  $\langle R_g^2 \rangle^{1/2} = 59.6$  nm.

The typical scattering behavior of semiflexible polymers at large values of the dimensionless quantity  $u = qR_g$  allows the determination of the molar mass per unit contour length,  $M_L = M/L$  (where  $M$  and  $L$  are the molar mass and contour length of polymer respectively) from Holtzer plot, which is a plot of  $qR_\theta/Kc$  versus  $qR_g$ . For polymer brushes with very high molecular weights a pronounced maximum was observed in Holtzer plot before the asymptote was obtained at high  $q$  values, and this asymptote is indicative of rigid-rod behavior. However for brushes with lower molecular weight a monotonously increasing curve was observed which leveled off at high  $q$ , and the Holtzer plateau,  $\pi M_L$ , was obtained.<sup>15,43</sup> The Holtzer plot of Brush 15 is shown in Figure 3-19. Very similar to the observation for the polymer brushes with PS side chains and relative low molecular weights,<sup>43</sup> a monotonously rising curve with decreasing slope was observed. It is difficult to obtain the accurate experimental value of  $M_L$  from Figure 3-19 due to the lack of data points at large  $u$  value. However, according to the experimental observation for similar polymer brushes with PS side chains,<sup>43</sup> for Brush 15 probably the maximum does not exist and the Holtzer curve approaches to a plateau at highest  $q$  value. An estimation can be made in this case and the apparent  $M_L$  is calculated to be  $53,730$  g/(mol-nm), which leads the cylinder length per main chain monomer unit,  $l_{unit} = M_0/M_L$  (where  $M_0 = M_{brush}/1500$ ), to be  $l_{unit,w} =$

0.14 nm and  $l_{unit,n} = 0.95$  nm. This  $l$  value is comparable to that for the polymer brushes with PS side chains in THF (0.145 nm).<sup>43</sup>

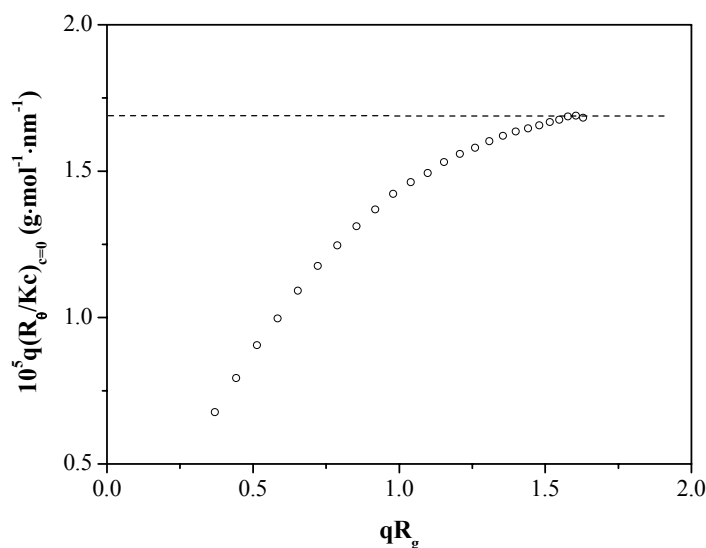


**Figure 3-19.** Holtzer plot of Brush 15 in chloroform at 20°C.

The SLS measurements of Brush 15 in chloroform were carried out at different temperatures aiming to investigate the temperature dependence of molecular dimension. As shown in Figure 3-20a,  $\langle R_g^2 \rangle_z^{1/2}$  was evaluated from the initial slope of the curve  $Kc/R_\theta$  vs.  $q^2$  (extrapolated data at  $c = 0$ ). The values of  $\langle R_g^2 \rangle_z^{1/2}$  (z-average root-mean-square radius of gyration) at different temperatures are shown in Figure 3-20b.

Interestingly, above 20°C the radius of gyration decreases almost monotonously with increasing temperature. For the cylindrical polymer brushes consisting of PS main chain and PS side chains, Nakamura *et al* found that in the theta solvent cyclohexane  $\langle R_g^2 \rangle_z$  increased with rising temperature, although the temperature dependence was much weaker than that for linear PS with same molecular weight.<sup>16,17</sup> In our case, the system is more complex because of the chemical heterogeneity between the main chain and the side chain (and therefore different polymer-solvent interactions of different parts of the brushes). Generally, linear polymer chains should expand in good solvents with rising temperature, thus  $R_g$  increases. Chloroform is a good solvent for both the main chain (polymethacrylate) and the side chain (deuterated PS) of Brush 15. Thus, when the temperature increases, the main chain stretches longitudinally while the side chains stretch along the direction perpendicular to the backbone of the brush. The stretch of the main chain and the side chain leads to an increase in the molecular dimension. However, the stretch of the side chain also leads to a

decrease of the steric overcrowding of side chains near the backbone (which is exactly the origin of the high main chain stiffness of polymer brushes), thus the main chain contracts and  $R_g$  decreases correspondingly. Therefore the increase in temperature has two contrary effects on the dimension of polymer brushes. For Brush 15 in chloroform, above 20°C, the contraction of main chain is the major effect thus  $R_g$  decrease with rising temperature. From dynamic light scattering measurements similar temperature dependence of the hydrodynamic radius were also observed (see below). Further investigations are needed to clarify this phenomenon.

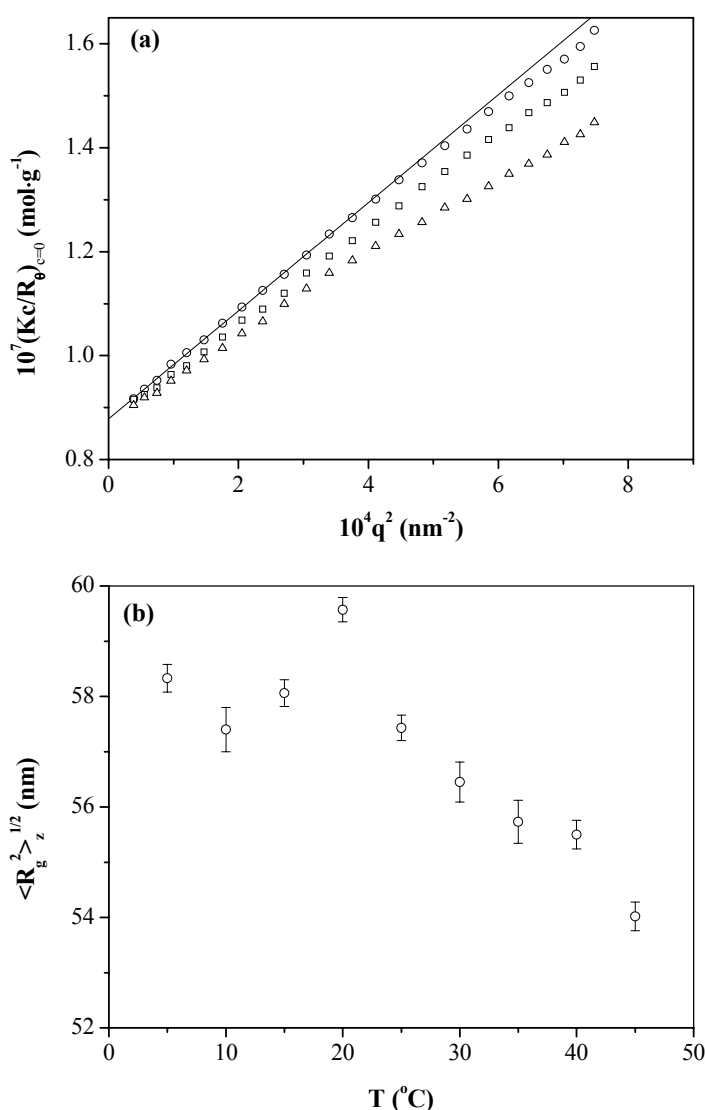


**Figure 3-20.** SLS measurements of Brush 15 in chloroform at different temperatures: (a) angular dependence of extrapolated  $Kc/R_\theta$  ( $c = 0$ ) at 20°C ( $\circ$ , and the solid line indicates the initial slope), 30°C ( $\square$ ) and 45°C ( $\triangle$ ); and (b) temperature dependence of radius of gyration.

Figure 3-21 shows the temperature dependence of the second virial coefficient  $A_2$  of Brush 15 in chloroform. It is quite similar to that of radius of gyration. Comparing to the  $A_2$  value of linear PS in chloroform ( $6.56 \times 10^{-4} \text{ mol}\cdot\text{ml}/\text{g}^2$  at  $25^\circ\text{C}$ ),<sup>44</sup> the  $A_2$  values for Brush 15 in chloroform are much smaller.

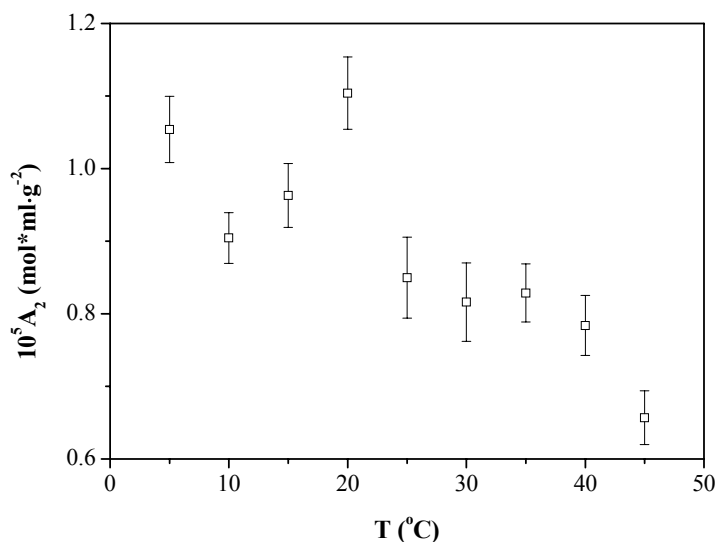


**Figure 3-21.** Temperature dependence of second virial coefficient ( $A_2$ ) of Brush 15 in chloroform.

To further confirm the temperature dependence of the size of Brush 15 observed from static light scattering, DLS was performed on a dilute chloroform solution of this polymer brush. Figure 3-22 depicts the typical normalized field correlation functions of Brush 15 at different temperatures (20 -  $45^\circ\text{C}$ ) and different scattering angles ( $30^\circ$  and  $90^\circ$ ). Cumulant analysis was then applied for data evaluation. The curves of  $\Gamma_1 q^{-2}$  vs.  $q$  at different temperatures are shown in Figure 3-23a. In principle, the translational diffusion coefficient  $D$  ( $\equiv \lim_{q \rightarrow 0} (\Gamma_1 q^{-2})$ ) can be obtained via linear extrapolation of the data of  $\Gamma_1 q^{-2}$  vs.  $q$  and therefore the hydrodynamic radius can be calculated according to the Stokes-Einstein relation. From Figure 3-23a it is obvious for  $T \leq 25^\circ\text{C}$ , the linear extrapolation looks reasonable. However at higher temperatures, the data points at the lowest  $q$  value increasingly deviate from the linear relation. We have no explanation for this phenomenon at the moment. Nevertheless, the apparent diffusion coefficients obtained at the lowest scattering angle ( $30^\circ$ ) should be closest to the real diffusion coefficients. The temperature dependence of the apparent hydrodynamic radii of Brush 15 obtained at scattering angle of  $30^\circ$  is shown in Figure 3-23b. For comparison, the extrapolated data (linear extrapolation of

$\Gamma_1 q^{-2}$  vs.  $q$  from the experimental data at scattering angles of  $60^\circ$ ,  $90^\circ$ ,  $120^\circ$  and  $150^\circ$ ) are also shown. A decrease of the apparent hydrodynamic radius ( $R_h$ ) with increasing temperature was clearly observed at scattering angle of  $30^\circ$ , which agrees well with what we observed from SLS, whereas at extrapolated  $R_h$  is almost independent of temperature.

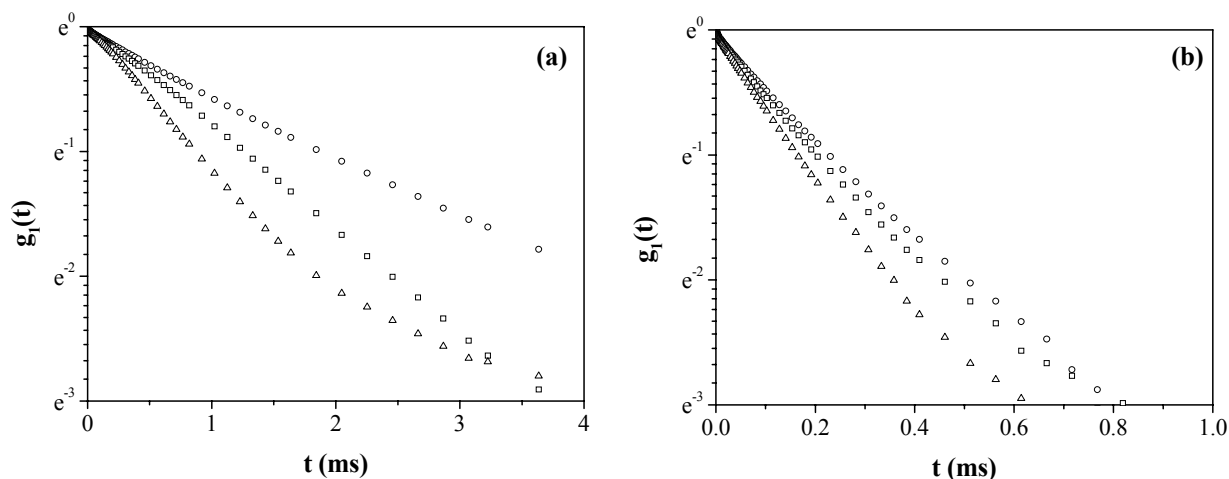


**Figure 3-22.** Normalized field correlation functions of Brush 15 in chloroform ( $c = 0.5$  g/L) at different temperatures ( $\circ$ :  $20^\circ\text{C}$ ;  $\square$ :  $30^\circ\text{C}$ ;  $\triangle$ :  $45^\circ\text{C}$ ): (a) scattering angle of  $30^\circ$ ; and (b) scattering angle of  $90^\circ$ .

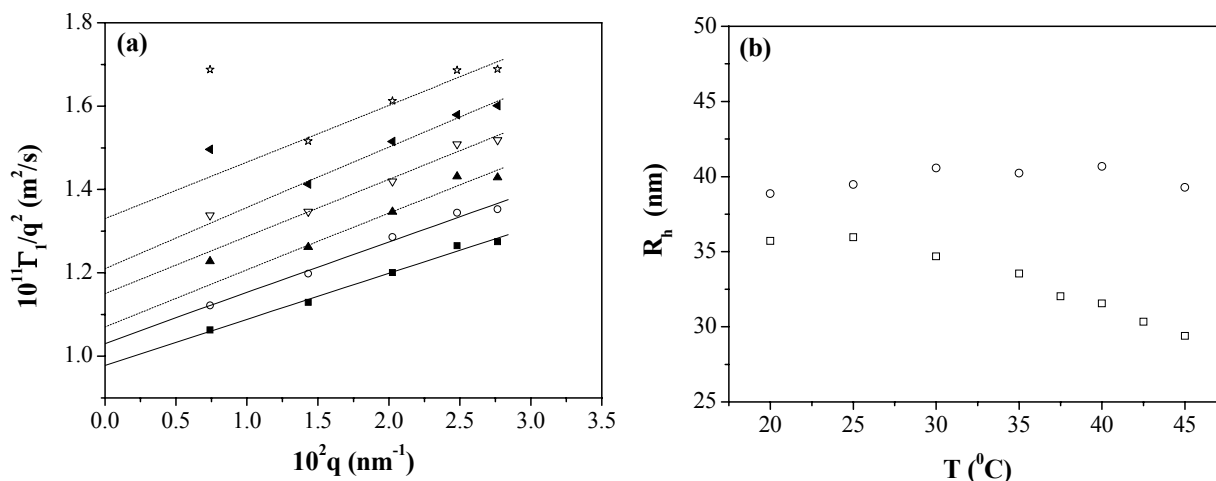


**Figure 3-23.** (a)  $q$  dependence of the first cumulant  $\Gamma_1$  in the form of  $\Gamma_1 q^{-2}$  vs  $q$  (solid line: linear fit of the data at all scattering angles; dash line: linear fit of the data without the scattering angle of  $30^\circ$ ) of Brush 15 in chloroform at different temperatures (from bottom to top:  $20^\circ\text{C}$  ( $\blacksquare$ );  $25^\circ\text{C}$  ( $\circ$ );  $30^\circ\text{C}$  ( $\blacktriangle$ );  $35^\circ\text{C}$  ( $\nabla$ );  $40^\circ\text{C}$  ( $\blacktriangleleft$ ); and  $45^\circ\text{C}$  ( $\star$ )); and (b) temperature dependence of hydrodynamic radius of Brush 15 in chloroform ( $\square$ : scattering angle of  $30^\circ$ ;  $\circ$ : extrapolated data).

### 3.4 Conclusions

Via combination ATRP and anionic polymerization, well-defined amphiphilic core-shell polymer brushes with PAA-*b*-PnBA side chains were synthesized using "grafting from" technique. Polymer brushes with different morphology (from star shape to cylindrical shape) were obtained via changing the ratio of DP between the backbone and the side chain. Due to the coordination ability of carboxylic acid with various metal ions, these amphiphilic polymer brushes can be used as unimolecular cylindrical template for inorganic nanoparticle formation.

### Acknowledgements

This work was supported by the *Deutsche Forschungsgemeinschaft*. We want to thank A. Krökel for the osmotic pressure measurements.

**References**

- (1) Tsukahara, Y.; Mizuno, K.; Segawa, A.; Yamashita, Y. *Macromolecules* **1989**, *22*, 1546-1552.
- (2) Tsukahara, Y.; Tsutsumi, K.; Yamashita, Y.; Shimada, S. *Macromolecules* **1990**, *23*, 5201-5208.
- (3) Wintermantel, M.; Schmidt, M.; Tsukahara, Y.; Kajiwara, K.; Kohjiya, S. *Macromol. Rapid Commun.* **1994**, *15*, 279-284.
- (4) Wintermantel, M.; Gerle, M.; Fischer, K.; Schmidt, M.; Wataoka, I.; Urakawa, H.; Kajiwara, K.; Tsukahara, Y. *Macromolecules* **1996**, *29*, 978-983.
- (5) Sheiko, S. S.; Gerle, M.; Möller, M. *Langmuir* **1997**, *13*, 5368.
- (6) Dziezok, P.; Sheiko, S. S.; Fischer, K.; Schmidt, M.; Möller, M. *Angew. Chem. Int. Ed.* **1998**, *36*, 2812-2815.
- (7) Kawaguchi, S.; Akaike, K.; Zhang, Z.-M.; Matsumoto, H.; Ito, K. *Polym. J.* **1998**, *30*, 1004-1007.
- (8) Djalali, R.; Hugenberg, N.; Fischer, K.; Schmidt, M. *Macromol. Rapid Commun.* **1999**, *20*, 444-449.
- (9) Schappacher, M.; Billaud, C.; Paulo, C.; Deffieux, A. *Macromol. Chem. Phys.* **1999**, *200*, 2377-2386.
- (10) Deffieux, A.; Schappacher, M. *Macromolecules* **1999**, *32*, 1797-1802.
- (11) Ryu, S. W.; Hirao, A. *Macromolecules* **2000**, *33*, 4765-4771.
- (12) Beers, K. L.; Gaynor, S. G.; Matyjaszewski, K.; Sheiko, S. S.; Möller, M. *Macromolecules* **1998**, *31*, 9413-9415.
- (13) Nemoto, N.; Nagai, M.; Koike, A.; Okada, S. *Macromolecules* **1995**, *28*, 3854-3859.
- (14) Wataoka, I.; Urakawa, H.; Kajiwara, K.; Schmidt, M.; Wintermantel, M. *Polym. Int.* **1997**, *44*, 365-370.
- (15) Gerle, M.; Fischer, K.; Roos, S.; Mueller, A. H. E.; Schmidt, M.; Sheiko, S. S.; Prokhorova, S.; Moeller, M. *Macromolecules* **1999**, *32*, 2629-2637.
- (16) Terao, K.; Takeo, Y.; Tazaki, M.; Nakamura, Y.; Norisuye, T. *Polym. J.* **1999**, *31*, 193-198.
- (17) Terao, K.; Nakamura, Y.; Norisuye, T. *Macromolecules* **1999**, *32*, 711-716.
- (18) Rouault, Y. *Macromolecular Theory and Simulations* **1998**, *7*, 359-365.

- (19) Saariaho, M.; Subbotin, A.; Ikkala, O.; Brinke, G. t. *Macromol. Rapid Commun.* **2000**, *21*, 110-115.
- (20) Subbotin, A.; Saariaho, M.; Stepanyan, R.; Ikkala, O.; ten Brinke, G. *Macromolecules* **2000**, *33*, 6168-6173.
- (21) Tsukahara, Y.; Inoue, J.; Ohta, Y.; Kohjiya, S.; Okamoto, Y. *Polym. J.* **1994**, *26*, 1013-1018.
- (22) Feast, W. J.; Gibson, V. C.; Johnson, A. F.; Khosravi, E.; Mohsin, M. A. *Polymer* **1994**, *35*, 3542-3548.
- (23) Heroguez, V.; Breunig, S.; Gnanou, Y.; Fontanille, M. *Macromolecules* **1996**, *29*, 4459-4464.
- (24) Heroguez, V.; Gnanou, Y.; Fontanille, M. *Macromolecules* **1998**, *30*, 4791.
- (25) Wang, J.-S.; Matyjaszewski, K. *J. Am. Chem. Soc.* **1995**, *117*, 5614-5615.
- (26) Kotani, Y.; Kato, M.; Kamigaito, M.; Sawamoto, M. *Macromolecules* **1996**, *29*, 6979-6982.
- (27) Matyjaszewski, K.; Xia, J. *Chem. Rev.* **2001**, *101*, 2921-2990.
- (28) Cheng, G.; Böker, A.; Zhang, M.; Krausch, G.; Müller, A. H. E. *Macromolecules* **2001**, *34*, 6883-6888.
- (29) Börner, H. G.; Beers, K.; Matyjaszewski, K.; Sheiko, S. S.; Möller, M. *Macromolecules* **2001**, *34*, 4375-4383.
- (30) Cates, M. E.; Candau, S. J. *J. Phys.: Condens. Matter* **1990**, *2*, 6869-6892.
- (31) Munk, P.; Ramireddy, C.; Tian, M.; Webber, S. E.; Prochazka, K.; Tuzar, Z. *Macromol. Chem., Macromol. Symp.* **1992**, *58*, 195-199.
- (32) Moffitt, M.; Khougaz, K.; Eisenberg, A. *Acc. Chem. Res.* **1996**, *29*, 95-102.
- (33) Wang, X.-S.; Winnik, M. A.; Manners, I. *Macromol. Rapid Commun.* **2002**, *23*, 210-213.
- (34) Tsubaki, K.; Ishizu, K. *Polymer* **2001**, *42*, 8387-8393.
- (35) Beers, K. L.; Boo, S.; Gaynor, S. G.; Matyjaszewski, K. *Macromolecules* **1999**, *32*, 5772-5776.
- (36) Mori, H.; Wakisaka, O.; Hirao, A.; Nakahama, S. *Macromol. Chem. Phys.* **1994**, *195*, 3213-3224.
- (37) Breiner, T.; Schmidt, H.-W.; Muller, A. H. E. *e-Polymers* **2002**, Paper No. 22.
- (38) Burguiere, C.; Pascual, S.; Bui, C.; Vairon, J.-P.; Charleux, B.; Davis, K. A.; Matyjaszewski, K.; Betremieux, I. *Macromolecules* **2001**, *34*, 4439-4450.

- 
- (39) Viswanath, D. S.; Natarajan, G. *Databook on the Viscosity of Liquids*, 1988.
- (40) Bednarek, M.; Biedron, T.; Kubisa, P. *Macromol. Chem. Phys.* **2000**, *201*, 58-66.
- (41) Provencher, S. W. *Computer Phys. Commun.* **1982**, *27*, 229.
- (42) Sheiko, S. S.; Prokhorova, S. A.; Beers, K. L.; Matyjaszewski, K.; Potemkin, I. I.; Khokhlov, A. R.; Möller, M. *Macromolecules* **2001**, *34*, 8354-8360.
- (43) Fischer, K.; Schmidt, M. *Macromol. Rapid. Commun.* **2001**, *22*, 787-791.
- (44) Wolinski, L.; Witkowski, K.; Turzynski, Z. *Makromol. Chem.* **1979**, *180*, 2399-2418.



## Chapter 4

### **Polychelates of amphiphilic core-shell cylindrical polymer brushes with iron cations\***

#### **Abstract**

Well-defined amphiphilic cylindrical polymer brushes with poly(acrylic acid) core and poly(*n*-butyl acrylate) shell were synthesized via atom transfer radical polymerization. Unimolecular polymer cylinders were directly visualized on mica by scanning force microscopy (SFM). The hydrophilic core of polymer brushes, poly(acrylic acid), was neutralized by NaOH and afterwards iron cations ( $\text{Fe}^{3+}$  and  $\text{Fe}^{2+}$ ) were loaded into the polymer core via ion exchange. The formation of polychelates of polymer brushes and iron cations were confirmed and characterized by various techniques such as fourier transform infrared spectroscopy (FTIR), UV/vis spectroscopy, transmission electron microscopy (TEM) and SFM. Formation of crystalline  $\alpha\text{-Fe}_2\text{O}_3$  (hematite) was observed during the He-Ne laser irradiation in the confocal Raman microscopy measurement of the polychelate containing  $\text{Fe}^{3+}$  ions.

\* This chapter combines two papers which have been published or accepted for publication:

1. "Polychelates of amphiphilic cylindrical core-shell polymer brushes with iron cations"  
Mingfu Zhang, Pierre Teissier, Marina Krekhova, Valérie Cabuil, Axel H. E. Müller  
*Progress in Colloid and Polymer Science*, **2004**, in press.
2. "*In situ* laser-induced formation of  $\alpha\text{-Fe}_2\text{O}_3$  from  $\text{Fe}^{3+}$  ions in a cylindrical core-shell polymer brush"  
Carmen Pérez León, Lothar Kador, Mingfu Zhang, Axel H. E. Müller  
*Journal of Raman Spectroscopy*, **2004**, 35, 165.

## 4.1 Introduction

Cylindrical polymer brushes, which have long side chain at each main chain monomer unit, have attracted extensive interest, due to the possibility to form extended chain conformations and their peculiar properties.<sup>1-6</sup>

Polymerization of macromonomer<sup>1-3</sup> as well as the “grafting from” technique<sup>4-6</sup> have been used to synthesize of cylindrical polymer brushes. In the latter method, the backbone of the brush is first synthesized and then modified to carry an initiating group at each monomer unit. The subsequent polymerization initiated by the pendant initiating groups on backbone forms side chains. Using this method well-defined polymer brushes with high grafting density and narrow distributions of both backbone and side chain can be obtained.

With amphiphilic block copolymers as side chains, polymer brushes have a core-shell structure and can be regarded as unimolecular micelles. Very recently, we succeeded in the synthesis of core-shell cylindrical brushes with amphiphilic block copolymer side chains, such as poly(acrylic acid)-*b*-polystyrene (PAA-*b*-PS)<sup>5</sup> or poly(acrylic acid)-*b*-poly(*n*-butyl acrylate) (PAA-*b*-P*n*BA).<sup>6</sup> Specially, the amphiphilic polymer brushes with PAA-*b*-P*n*BA side chains were synthesized via combination of anionic polymerization (for the backbone) and atom transfer radical polymerization (ATRP, for the side chain). The living nature of these two polymerization techniques enables the control of the distributions of both backbone and side chain, so the resulting amphiphilic brushes have well-defined sizes.

Due to the well known coordination between carboxylate groups and metal cations, we are able to synthesize composite materials of polymer brushes (with PAA core) and metal cations. Such composite materials are named as polychelates, due to their polymeric structure.<sup>7</sup> It is easy to expect that the polychelates containing metal cations are precursors to polymer-nanoparticle composites, which are of special interest. It seems also reasonable to expect that polychelates might provide some additional heterofore unknown functions, in light of the high number of metal ions that can be coordinated to a single polymer molecule and their well-defined position in the polymer brush. For example, the close proximity of metal ions in such materials might result in cooperative catalytic properties, which is often observed in natural enzymatic materials. Additionally, metallic salts of polymeric acids have elastic moduli several times greater than those of the common thermoplastic materials, a high softing temperature, good thermal stability and a very low coefficient of thermal expansion.<sup>8</sup>

As part of our continuous effort for the synthesis and applications of amphiphilic core-shell cylindrical brushes, we report here the synthesis and characterization of the polychelates of amphiphilic brushes and iron cations, utilizing the coordination between carboxylate groups and iron cations.

Further chemical reaction of the iron cations within the polychelates, such as alkalization or reduction, are expected to produce magnetic nanoparticles inside the cores of polymer brushes, forming a new class of hybrid nanoparticles.

Although only iron cations were used here for the formation of polychelates, it is obvious that many other metal ions can be used as well. It will be shown in Chapter 6 that cadmium cations ( $\text{Cd}^{2+}$ ) have been also successfully loaded into polymer brushes and semiconductor (CdS) nanoparticles can be formed via sulfidization.

Confocal Raman microscopy is a powerful tool for the nondestructive analysis of materials on the micrometer scale. It has found applications in many different fields such as biology,<sup>9,10</sup> medicine,<sup>11,12</sup> food analysis,<sup>13</sup> archeology,<sup>14</sup> and materials science, e.g., regarding polymers.<sup>15-20</sup> Scanning the sample with respect to the laser focus yields the possibility to obtain two- or three-dimensional images of the chemical composition<sup>18,21</sup> or molecular orientations.<sup>20</sup> Usually the wavelength and the focal intensity of the laser are chosen such that no degradation of the sample occurs. It is also possible, however, to observe and characterize light-induced chemical alterations or degradation reactions *in situ*. It is shown here that crystalline  $\alpha\text{-Fe}_2\text{O}_3$  (hematite) formed during the He-Ne laser irradiation in the confocal Raman microscopy measurement of the polychelate containing  $\text{Fe}^{3+}$  ions.

## 4.2 Experimental section

### 4.2.1 Materials

FeCl<sub>3</sub> (Merck, anhydrous, for synthesis), FeCl<sub>2</sub>·4H<sub>2</sub>O (Fluka, analytical grade) and NaOH (Merck, analytical grade) were used as received. All organic solvents were of analytical grade and used without further purification. Water was ultra pure obtained from Milli-Q plus system (Millipore). The synthesis of amphiphilic core-shell cylindrical polymer brushes was reported in our previous papers.<sup>5,6</sup>

### 4.2.2 Polymer characterization

Monomer conversion in polymerization was determined by gas chromatography (GC) using a polymethylsiloxane capillary column. Apparent molecular weights of polymer brushes were measured by gel permeation chromatography (GPC) using THF as eluent at a flow rate of 1.0 ml/min at room temperature. Column set: 5 μ SDV gel, 10<sup>5</sup>, 10<sup>4</sup>, 10<sup>3</sup>, 10<sup>2</sup> Å, 30 cm each (PSS); detectors: Waters 410 differential refractometer and photodiode array detector operated at 254 nm. Polystyrene standards (PSS) were used for the calibration of the column set. Membrane osmometry was performed at 35°C in toluene to determine the true molecular weight of the backbone of polymer brush using a cellulose triacetate membrane with a Gonotec 090 Osmometer. The samples for scanning force microscopy (SFM) measurements were prepared by dip-coating from dilute solutions of polymer brushes or polychelates onto freshly cleaved mica surface. The SFM images were taken with a Digital Instruments Dimension 3100 microscope operated in Tapping Mode.

### 4.2.3 Preparation and characterization of polychelates

A typical procedure for the synthesis of the polychelates of polymer brushes and Fe<sup>3+</sup> ions is described in the following: amphiphilic polymer brushes were dissolved in a mixture of methanol and chloroform (v/v = 3/5 to 1/1). Then a calculated amount of 1.0 M NaOH (= 80% of the molar amount of COOH group in polymer) was added to the polymer solution, followed by stirring overnight. Afterwards a 3-fold excess of FeCl<sub>3</sub> (1.0 M aqueous solution) was added and the mixture was stirred for one day. The unassociated ferric cations were removed by dialysis against the solvent mixture which was used to dissolve polymer. Dialysis was carried out in one week (and the solvent was changed once a day) using a regenerated cellulose membrane tube with molecular weight cutoff 6-8,000.

The synthesized polychelates were characterized by fourier transform infrared spectroscopy (FTIR, Bio-Rad), UV/vis spectrophotometer (Lambda 15, Perkin-Elmer), SFM and transmission electron microscopy (TEM). A small drop of polychelate dilute solution was placed on a copper grid coated with formvar-carbon film. After drying, the grid was used for TEM measurements using a Zeiss CEM 902 electron microscope operated at 80 kV.

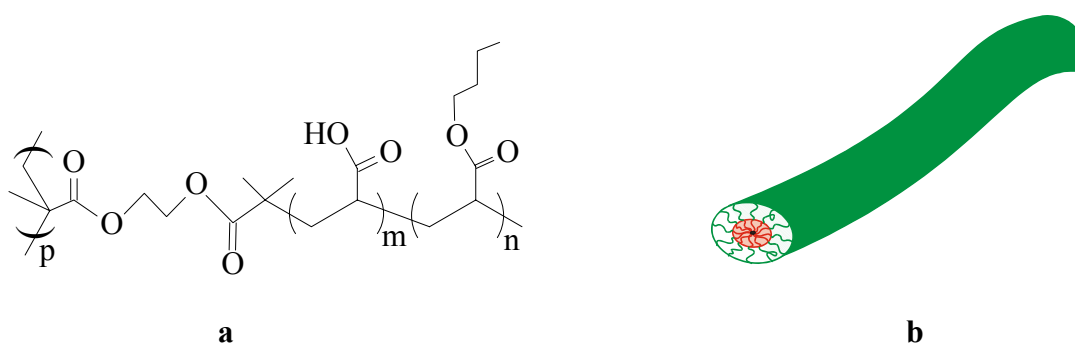
#### 4.2.4 *In situ* laser-induced formation of $\alpha$ -Fe<sub>2</sub>O<sub>3</sub> from Fe<sup>3+</sup> ions in the polychelates

The experimental set-up was similar as described previously.<sup>18</sup> It is centered around an inverted microscope Swift M 100 with an objective Leica PL Fluotar 100×/0.75 for focusing the laser and collecting the scattered light. For some of the measurements a PlanApo objective 20×/0.75 was used. The set-up was equipped with a linearly polarized He-Ne laser ( $\lambda = 632.8$  nm) with approximately 3 mW power on the sample. It was focused to a spot size of 0.5  $\mu\text{m}$ , corresponding to a focal intensity of about 1.5 MW/cm<sup>2</sup>. Spectral dispersion was performed in a single monochromator (Acton Research SpectraPro-500i) with a grating of 300 grooves per mm. The entrance slit of the monochromator was replaced with a 50  $\mu\text{m}$  pinhole for confocal depth selection. The Rayleigh line was suppressed by a factor of 10<sup>6</sup> with a holographic notch filter (Kaiser Optical Systems). Raman spectra were recorded with a liquid-nitrogen-cooled CCD detector with 1340×100 pixels (Princeton Instruments); typical acquisition times ranged between 15 s and 5 min.

### 4.3 Results and discussion

#### 4.3.1 Synthesis and characterization of amphiphilic polymer brushes

The synthesis of polymer brushes was carried out as described in detail previously.<sup>5,6</sup> The structure of amphiphilic core-shell polymer brushes with PAA-*b*-P*n*BA side chains is illustrated in Scheme 4-1. Due to the core-shell cylindrical structure and the amphiphilicity of the side chain these polymer brushes can be regarded as unimolecular micelles.



**Scheme 4-1.** Chemical (a) and 3-D (b) structure of amphiphilic core-shell cylindrical polymer brush with poly(acrylic acid)-*b*-poly(*n*-butyl acrylate) side chains.

The backbone of polymer brush was synthesized via anionic polymerization. GPC measurement showed that the backbone had a very narrow distribution ( $M_w/M_n = 1.08$ ), and its degree of polymerization was determined as  $DP_n = 1500$  from its absolute molecular weight obtained by membrane osmometry measurement.<sup>6</sup>

**Table 4-1.** Characterization results of polymer brushes with PAA core and P*n*BA shell

Polymer brush <sup>a</sup>	$10^{-5} \times M_{n,GPC}$ <sup>b</sup>	$M_w/M_{n,GPC}$ <sup>b</sup>	$DP_{core}$ <sup>c</sup>	$DP_{shell}$ <sup>c</sup>
Brush 1	9.3	1.40	37	48
Brush 2	7.7	1.40	29	32

(a)  $DP_{backbone} = 1500$ ; (b) number-average molecular weight and polydispersity of unhydrolyzed brushes (with P*t*BA core and P*n*BA shell) obtained from GPC measurements; (c)  $DP$  = degree of polymerization, calculated according to initial monomer/initiator ratio and monomer conversion.

Core-shell cylindrical brushes with poly(*t*-butyl acrylate)-*b*-poly(*n*-butyl acrylate) (PtBA-*b*-PnBA) side chains were formed via sequential atom transfer radical polymerizations (ATRP). Selective hydrolysis of the core block of side chain, PtBA, into PAA resulted in amphiphilic brushes. Table 4-1 shows the characterization results of polymer brushes used for the synthesis of polychelates.

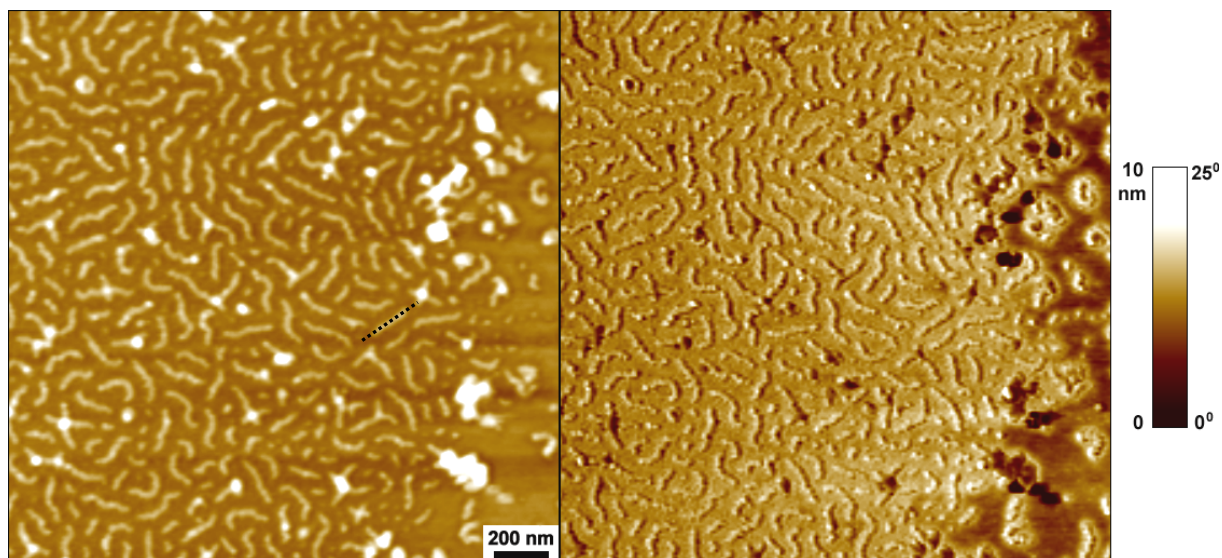


**Figure 4-1a.** SFM image of Brush 1: (left) height image; and (right) phase image.

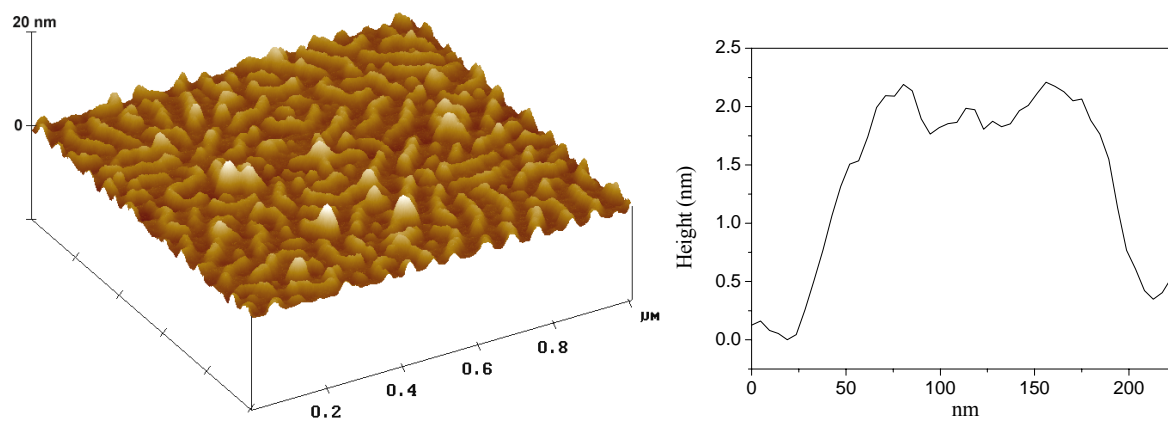


**Figure 4-1b.** (left) 3-D image; and (right) cross-section analysis of one cylinder which is marked by the dash line in the height image of Figure 4-1a.

The morphology of the amphiphilic brush was characterized by SFM. Figure 4-1 shows a typical SFM image of Brush 1, dip-coated from dilute  $\text{CHCl}_3/\text{CH}_3\text{OH}$  ( $v/v=1/1$ ) solution onto mica. Wormlike polymer cylinders can be clearly visualized. Statistical analysis shows that the average length of cylinders are about 180 nm.

### 4.3.2 Formation and characterization of polychelates of amphiphilic polymer brushes and iron cations

To understand the mechanism of the complex formation between polymer brushes (the PAA core, actually) and iron ions, examination of stability constants,  $K_n$ , between various cations ( $\text{H}^+$  and metal cations) and carboxylate anions, is very important. Because of the structural similarity of acetate anion ( $\text{CH}_3\text{COO}^-$ ) to the carboxylate anion within polymer brushes and availability of literature data, acetate anion is chosen for discussion. The stability constant between various cations and the acetate anion is defined as



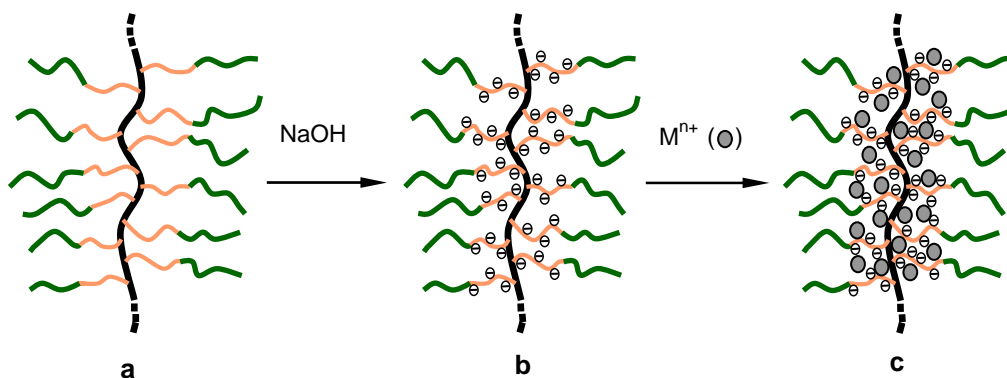
$$K_n = \frac{[\text{ML}_n]}{[\text{ML}_{n-1}][\text{L}]} \quad \text{Eq. 4-2}$$

where M represents the cation ( $\text{H}^+$  or metal cation), and L represents the acetate anion.

It is known that  $\text{H}^+$  ions bind strongly to acetate anions,  $K_1 \sim 10^5$  ( $\text{mol/L}^{-1}$ ) (Ref.<sup>22</sup>), transition metal and rare earth ions bind to acetate anions with intermediate strength,  $K_1 \sim 3$ -2500 ( $\text{mol/L}^{-1}$ ) (Ref.<sup>22,23</sup>), and  $\text{Na}^+$  ions bind weakly to acetate anions,  $K_1 \sim 0.7$  ( $\text{mol/L}^{-1}$ ) (Ref.<sup>22,23</sup>). Addition of NaOH into the solutions of polymer brushes will exchange  $\text{H}^+$  ions from carboxylic acid groups for  $\text{Na}^+$  ions due to the formation of  $\text{H}_2\text{O}$ . Transition metal or rare earth ions are then substituted for the more weakly binding  $\text{Na}^+$  ions. Thus polychelates (complexes of polymer brushes and metal ions) form.

In the case that no neutralization of polymer brushes is performed, exchange between transition metal/rare earth ions and  $\text{H}^+$  ions from carboxylic acid groups is more difficult due to the high stability constants of  $\text{H}^+$  and carboxylate ions. Specially, when metal chlorides are used, the cation exchange causes the formation of HCl, whose  $K_1$  is essentially zero thus free  $\text{H}^+$  ions prevent significant metal ion binding to the polymer core. However, when metal acetates are used, the cation exchange is remarkably enhanced due to that  $\text{H}^+$  ions liberated from carboxylic acid groups become bound to acetate ions to form stable acetic acid.<sup>24</sup>

It is well-known that carboxylic acid or carboxylate can coordinate with various metal cations to form the corresponding chelates. Due to the peculiar structure of amphiphilic polymer brushes, the coordination will induce uptake of metal ions solely into the core of the brushes, since the shell doesn't interact with metal ions strongly. As discussed above, conversion of carboxylic acid groups to sodium carboxylate results in large increase in extent of transition metal ion uptake, thus the carboxylic acid groups in amphiphilic polymer brushes were first neutralized by NaOH aiming to load more iron cations into the polymer core. The synthetic routine for the polychelates of polymer brushes and iron ions ( $\text{Fe}^{2+}$ ,  $\text{Fe}^{3+}$ ) is schematically shown in Scheme 4-2.



**Scheme 4-2.** Schematic illustration for the synthesis of polychelates of amphiphilic core-shell polymer brushes and metal ions: (a) the polymer brush with PAA core and PnBA shell; (b) the neutralized polymer brush with poly(sodium acrylate) core ( $\text{Na}^+$  is not shown); and (c) the polychelate of the brush and  $\text{M}^{n+}$  ( $\text{Fe}^{2+}$ ;  $\text{Fe}^{3+}$ ) ions.

FTIR measurements verified the uptake of iron ions into the core of polymer brushes. A unneutralized polymer brush (Brush 2) was used here, because neutralization with NaOH will induce a very similar change in the FTIR spectrum as that from the coordination of COOH with  $\text{Fe}^{2+}$ . Figure 4-2 shows the FTIR spectra of Brush 2 and its complex with  $\text{FeCl}_2$ . Besides the peak at  $1735\text{ cm}^{-1}$ , which corresponds to carbonyl groups of  $-\text{COOH}$  and  $-\text{COO}(\text{CH}_2)_3\text{CH}_3$  in polymer brush, a new peak at  $1595\text{ cm}^{-1}$  appeared when Brush 2 was mixed with  $\text{FeCl}_2$ . This new peak is associated with asymmetric stretching of carboxylate salts, indicating the coordination of between  $\text{Fe}^{2+}$  ions and COOH groups. The intensity of the peak at  $1595\text{ cm}^{-1}$  increases with increasing the amount of  $\text{FeCl}_2$ . It has been reported that  $\text{FeCl}_3$  has a similar behavior when it reacts with carboxylic acid group of polymer.<sup>25</sup>

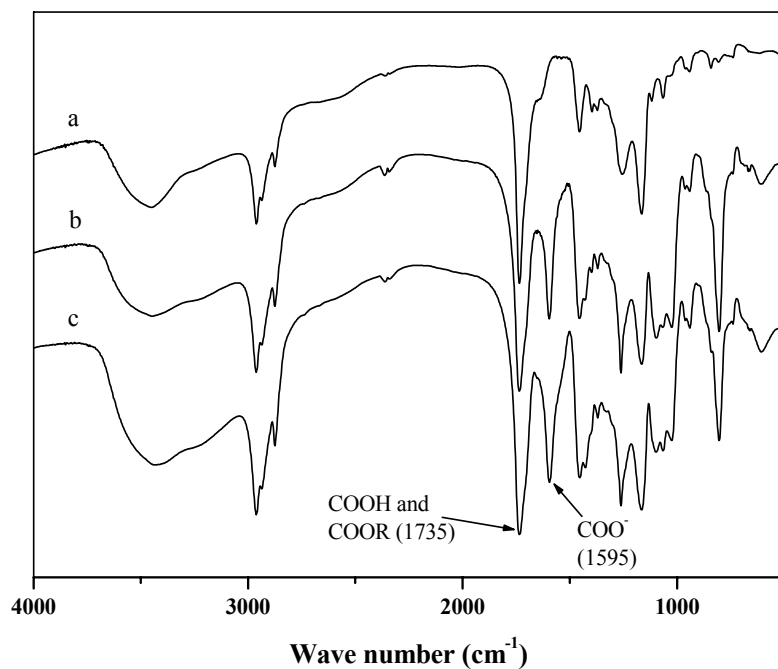


**Figure 4-2.** FTIR spectra of (a) Brush 2, and complexes of Brush 2 with  $FeCl_2$ : (b)  $Fe^{2+}/COOH = 0.25$ , (c)  $Fe^{2+}/COOH = 0.5$ . Measurements were performed on KBr pellets.

As mentioned before, conversion of carboxylic acid groups to carboxylate increase the extent of transition metal ion uptake dramatically. Thus for the formation of polychelates, neutralization was carried out before the loading of iron ions in most cases. SFM measurements showed there were no apparent changes in morphology and size before and after neutralization, as shown in Figure 4-3.

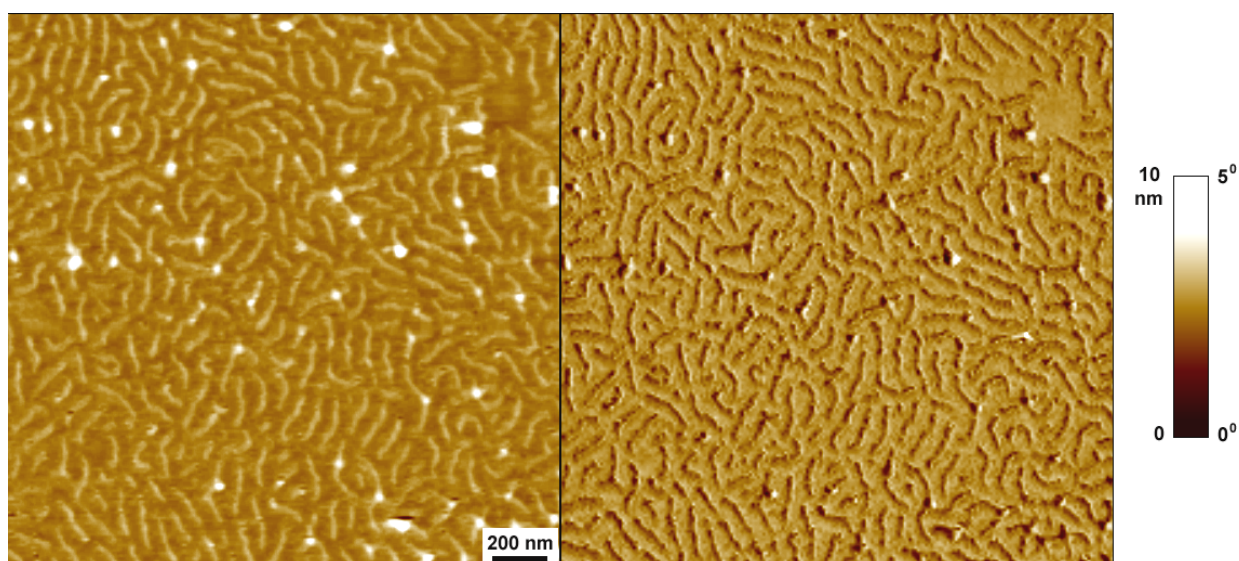


**Figure 4-3.** SFM image of Brush 1 after 80 % neutralization : (left) height image; and (right) phase image.

When iron salts ( $\text{FeCl}_2$  or  $\text{FeCl}_3$ ) were added to the solution of neutralized polymer brush, polychelates formed via ion exchange, indicated by the results of various analytical techniques. To obtain purified polychelates free of uncoordinated iron ions, various methods were tried to remove unreacted iron salts, such as dialysis, precipitation and ultracentrifugation. All these methods have their advantages and disadvantages, as shown below.

- *Dialysis.* Dialysis was carried out in membrane tube against pure solvent which is used to dissolve polymer brushes (such as mixture of methanol and chloroform). The purification procedure can be easily monitored by the diffusion of free iron salts into the dialysis solvent, due to the characteristic color of salts. During the dialysis, polychelates are kept in the same solvent, so finally stable solution of polychelates can be obtained. However, dialysis is a slow process thus it is not suitable for the purification of a big amount of polychelates.
- *Precipitation.* In contrast to dialysis, precipitation can purify a big amount of polychelates quickly. Polychelates were precipitated out when a small amount of water was added into the solution. In this case the unreacted iron salts stayed in the supernatant. Obviously precipitation is a fast method, compared to dialysis. However, sometimes the purified polychelates can not be redissolved in the solvents completely. This might be due to the limited solubility of polychelate (because of the huge size).
- *Ultracentrifugation.* Due to the huge size of the polychelate, ultracentrifugation was also carried out to purify the polychelates. However, only part of polychelate, probably with bigger size and corresponding bigger gravity, can precipitate out. Interestingly, the precipitate from ultracentrifugation can be redissolved again. The rest of polychelates in the supernatant has to be purified by either precipitation or dialysis.

In practice, one of the above methods or the combinations of ultracentrifugation and precipitation were used. The complete removal of unreacted ferric cations was confirmed by SFM, since unreacted iron salts generally formed spherical particles on mica. Figure 4-4a depicts a typical SFM image of the polychelate of Brush 1 and  $\text{FeCl}_3$  after purification by dialysis. Obviously the morphology and size of polychelate differ significantly from that of pure polymer brush. Peculiar “pearl necklace” structure was clearly observed for the polychelate. In contrast to the smooth contour of Brush 1 (as shown in Figure 4-1),

polychelates have periodic undulations in height and diameter along the backbone. Moreover, the height of the polychelate is much higher than that of polymer brush, indicating that the loading of  $\text{Fe}^{3+}$  cations into the polymer core stiffens the polymer cylinder dramatically. Interestingly, the morphology change solely happened in the core region of polymer brush, confirming again  $\text{Fe}^{3+}$  ions coordinated selectively with carboxylate (or residual carboxylic acid) groups.

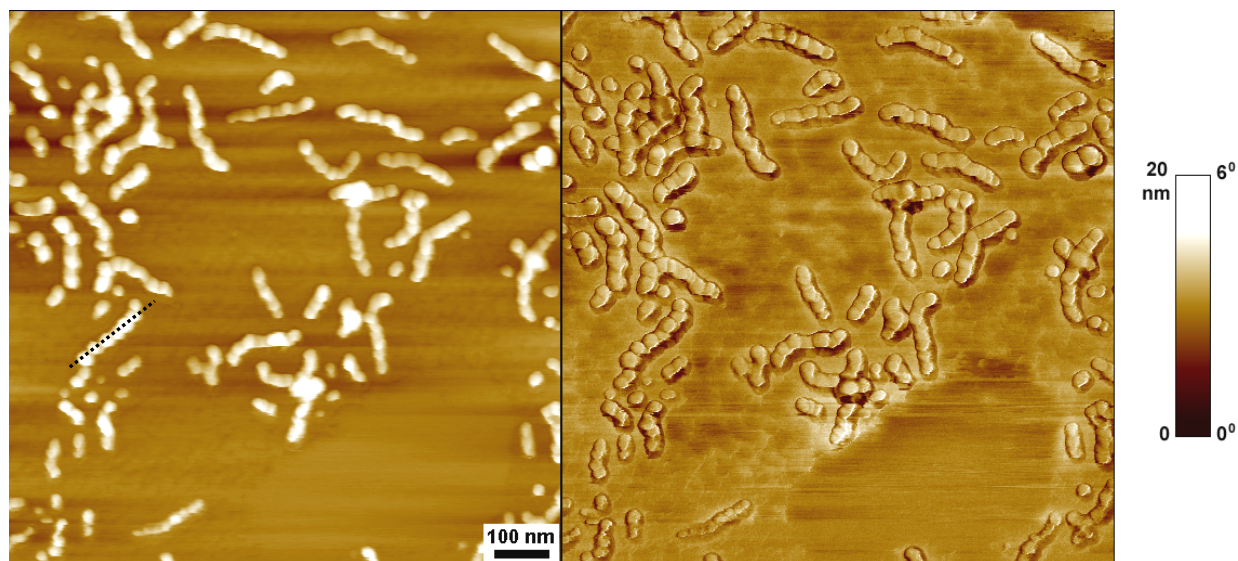


**Figure 4-4a.** SFM image of the polychelate of Brush 1 and  $\text{FeCl}_3$  after dialysis: (left) height image and (right) phase image.

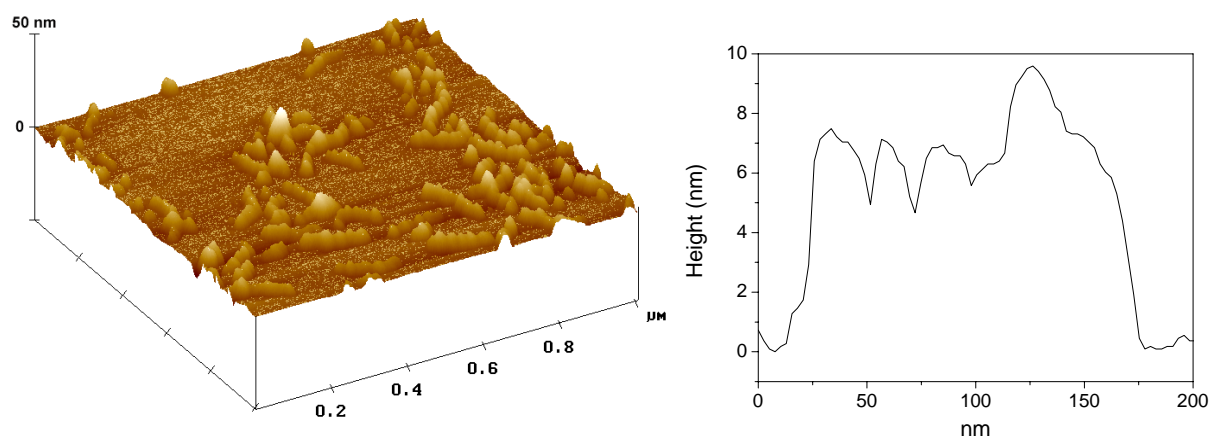
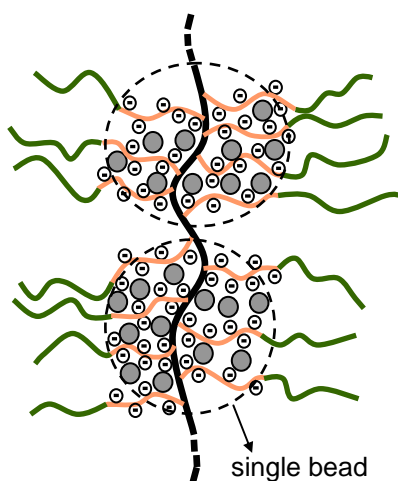


**Figure 4-4b.** (left) 3-D image; and (right) cross-section analysis of one polychelate which is marked by the dash line in the height image of Figure 4-4a.

We speculate that the “pearl necklace” structure of polychelate may be due to the cross-linking of side chains via coordination of multivalent  $\text{Fe}^{3+}$  cations with monovalent carboxylate groups from different side chains. The schematic structure of polychelate is shown in Scheme 4-3. Similar phenomenon was also observed in  $\text{Fe}^{2+}$  loaded microporous membranes containing PAA grafts in the pores. Winnik *et al* found that, the “cross-linking” between carboxylic acid groups on the grafted chains and the bridging  $\text{Fe}^{2+}$  ions caused the high brittleness of the membrane loaded with  $\text{Fe}^{2+}$  ions ( compared to the parent membrane). However, after the formation of iron oxide particles, the membrane recovered their original mechanical properties and were no longer brittle, since the “cross-linking” vanished.<sup>26</sup>



**Scheme 4-3.** Schematic illustration of the “pearl necklace” structure of the polychelate.

UV/vis measurements also confirmed the formation of polychelates. Figure 4-5 shows the UV/vis spectra of the neutralized Brush 1,  $\text{FeCl}_3$  and the corresponding polychelate. With the same polymer concentration, polychelate has a much stronger absorption than that of polymer. Comparison between the spectra of polychelate and  $\text{FeCl}_3$  indicates that the absorption of polychelate mainly originates from the coordinated  $\text{Fe}^{3+}$  cations.

Although the polymer brush itself is not visible by TEM, the core of polychelate should be visible due to the high electron density of  $\text{Fe}^{3+}$  ions. A TEM image of polychelate of Brush 1 and  $\text{FeCl}_3$  is depicted in Figure 4-6. As expected, thin wormlike cylinders are clearly seen.  $\text{Fe}^{3+}$  worked as a staining agent in this case. The fine structure of the polychelate (“pearl necklace” structure) was not observed, due to the insufficient resolution of the electron microscope we used (Zeiss CEM 902 operated at 80 kV). It will be shown in

the following two chapters that by using another microscope with higher resolution the “pearl necklace” structure of polychelates can be observed by TEM as well.

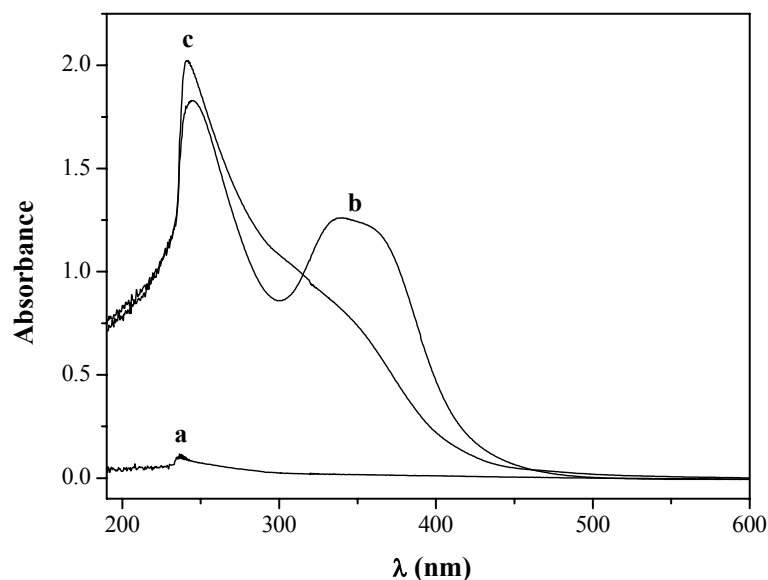


**Figure 4-5.** UV/vis spectra of (a) Brush 1 neutralized with NaOH (= 80% COOH, polymer concentration  $C_p = 0.25$  g/L); (b)  $\text{FeCl}_3$  ( $c = 0.042$ g/L); and (c) polychelate of Brush 1 and  $\text{FeCl}_3$  (after dialysis) with  $C_p = 0.25$  g/L. Solvent:  $\text{CHCl}_3/\text{CH}_3\text{OH}$  ( $v/v = 5/3$ ).

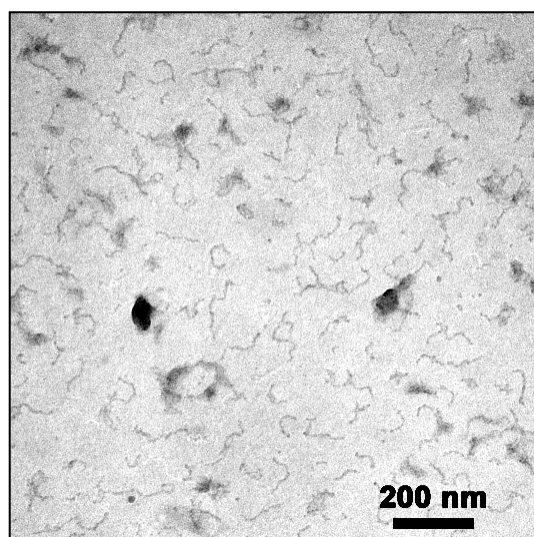


**Figure 4-6.** TEM image of the polychelate of Brush 1 and  $\text{FeCl}_3$  (after dialysis).

### 4.3.3 In situ laser-induced formation of $\alpha$ - $\text{Fe}_2\text{O}_3$ from $\text{Fe}^{3+}$ ions in polychelates

The Raman spectrum of the polychelate is very similar to that of the pure polymer brush, as shown in Figure 4-7. The latter is somewhat better defined at low Raman shift values and exhibits a shoulder at  $1670\text{ cm}^{-1}$ , whereas the spectrum of the  $\text{Fe}^{3+}$  complex shows a peak at  $1580\text{ cm}^{-1}$  which is not homogeneously present in all measured places. Its origin will be discussed (see below).

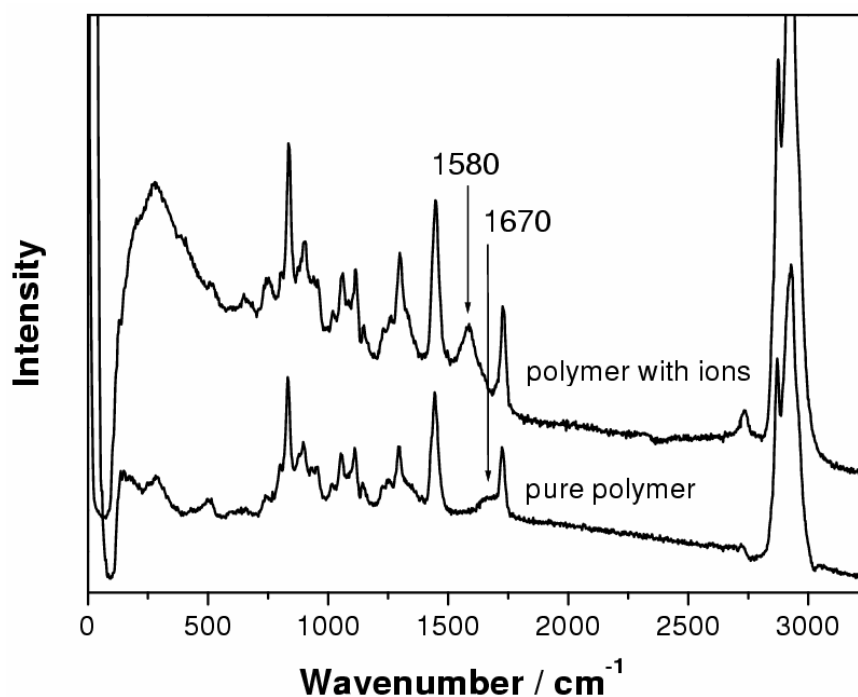


**Figure 4-7.** Raman spectra of Brush 1 (lower curve) and the polychelate of Brush 1 and  $\text{FeCl}_3$  (upper curve), recorded with 5 minutes integration time. The spectra have been shifted vertically for clarity.

During the Raman investigations the spectrum changed and the polymer underwent structural transformations, which we ascribe to laser heating. In particular the peak at  $1580\text{ cm}^{-1}$  increased and, simultaneously, a broad fluorescence background appeared, whereas the other Raman lines decreased in intensity. At a later stage the fluorescence background decreased as well, and eventually only two broad peaks around  $1330\text{ cm}^{-1}$  and  $1580\text{ cm}^{-1}$  remained, as shown Figure 4-8. These peaks correspond to the well-known D and G bands of amorphous carbon, which is a mixture of  $\text{sp}^2$  and  $\text{sp}^3$  hybridized carbon atoms.<sup>27</sup> Hence, we conclude that the high intensity in the laser focus thermally decomposes the polymer, producing amorphous carbon. After the experiment the sample indeed showed a hole at the

position of the focus. We often saw tiny liquid droplets around the irradiated spot, probably due to the water produced by the heating of the organic material. The amount of the liquid was too small to record a Raman spectrum, however.

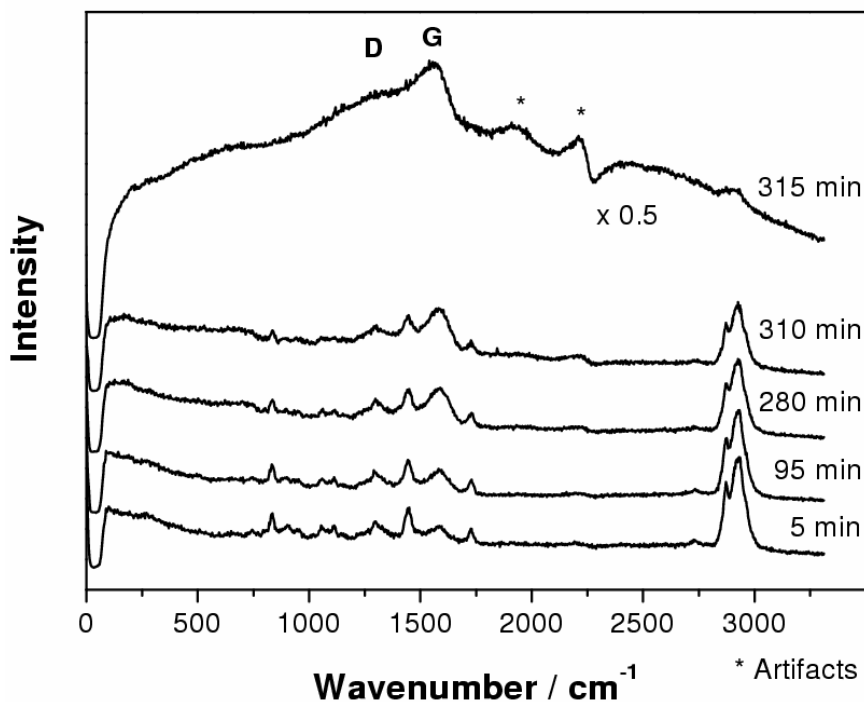


**Figure 4-8.** Temporal series of Raman spectra of the polychelate of Brush 1 and  $\text{FeCl}_3$  (from bottom to top) indicating the decomposition of the polymer. The spectra were recorded with 1 minute integration time each, and they have been shifted vertically for clarity. The times at the spectra indicate the intervals between the start of the respective scan and the beginning of the experiment. In the uppermost spectrum, D and G indicate two peaks from amorphous carbon. The features marked with asterisks are artifacts of the spectrometer.

Along with the fluorescence background and the D and G bands, several new lines began to appear at lower Raman shift values. When the fluorescence background decreased, these lines became well visible and, upon continued irradiation, they further increased in intensity, narrowed, and slightly shifted to higher wavenumbers (see Figure 4-9). These new peaks are attributed to  $\alpha\text{-Fe}_2\text{O}_3$  (hematite),<sup>28,29</sup> which is formed from the  $\text{Fe}^{3+}$  ions in the laser focus. The formation of an iron oxide from iron ions by high light intensities has, to our best knowledge, not been reported in the literature so far. Only the laser-induced transformation of other iron oxides ( $\text{Fe}_3\text{O}_4$ ,  $\gamma\text{-Fe}_2\text{O}_3$ ,  $\text{FeO}$ ) and oxyhydroxides ( $\alpha\text{-FeOOH}$ ,  $\gamma\text{-}$

FeOOH,  $\delta$ -FeOOH, Fe(III) oxyhydroxide, Fe(III) oxyhydroxysulfate) to hematite was observed.<sup>29-32</sup> So this is the first time that direct laser-induced formation of  $\alpha$ -Fe<sub>2</sub>O<sub>3</sub> from Fe<sup>3+</sup> ions has been observed.

High laser intensities can give rise to photochemical reactions and/or thermal effects. From the comparison of the hematite Stokes and anti-Stokes signals we can estimate that the temperature of the focal spot was in the range of 250 – 300°C. Therefore heating effects have to be taken into account. We cannot decide, however, whether the formation of  $\alpha$ -Fe<sub>2</sub>O<sub>3</sub> is of photochemical or thermal origin.

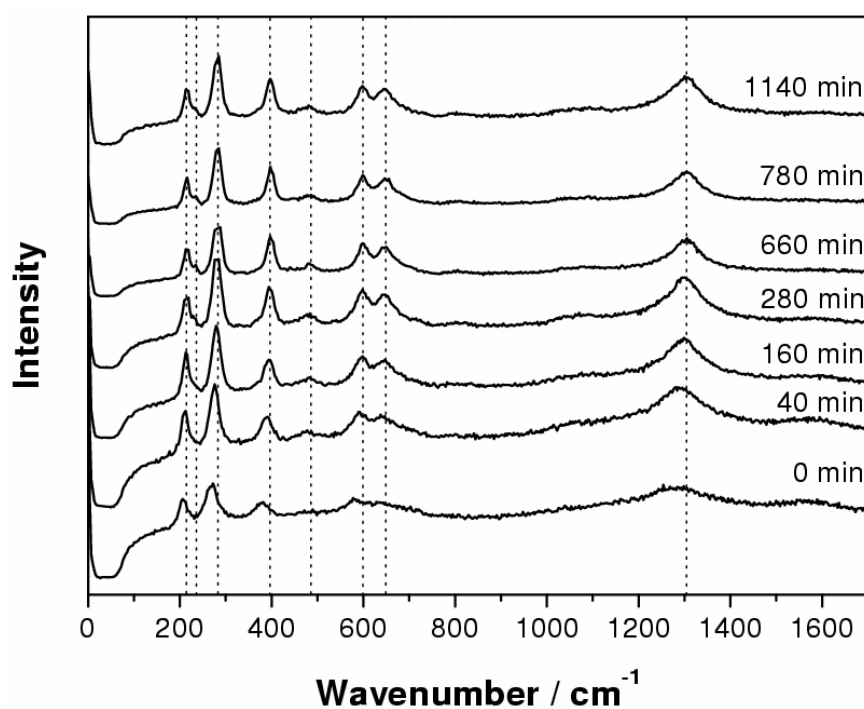


**Figure 4-9.** Series of Raman spectra of the polychelate of Brush 1 and FeCl<sub>3</sub> after prolonged laser irradiation indicating the formation of  $\alpha$ -Fe<sub>2</sub>O<sub>3</sub>. The spectra were recorded with 1 minute integration time each, and they have been shifted vertically for clarity. The times at the spectra indicate the intervals between the start of the respective scan and the start of the first scan. The vertical lines indicate the slight shift of the peaks toward higher frequencies.

Table 4-2 list the Raman shifts of peaks from the hematite produced by laser irradiation and shows the comparison with the reference data from other groups. The Raman spectra we obtained contain all the peaks reported in the literature, including some features observed and discussed by Bersani *et al.*<sup>31</sup> In our spectrum the lines at 232 cm<sup>-1</sup> and 285 cm<sup>-1</sup> appear

as shoulders of the peaks at  $216\text{ cm}^{-1}$  and  $279\text{ cm}^{-1}$ , respectively, and are often not well resolved. The larger widths of our peaks may be related to heating effects and/or smaller size of the hematite crystallites (see below).

Raman investigations on  $\alpha\text{-Fe}_2\text{O}_3$  have been performed and, due to its magnetic properties, magnon scattering in addition to phonon scattering was considered.<sup>33</sup> Hematite is antiferromagnetic below the Morin temperature (260 K) and slightly ferromagnetic between 260 K and the Néel temperature (960 K). Its corundum-type structure allows for seven Raman-active optical phonons with even symmetry at the center of the Brillouin zone ( $2 A_{1g} + 5 E_g$ ),<sup>31</sup> and all of them have frequencies below  $620\text{ cm}^{-1}$ . There is a strong band at  $1304\text{ cm}^{-1}$  which was first attributed to two-magnon scattering,<sup>28</sup> but was later interpreted as an overtone of a phonon<sup>33</sup> at approximately  $660\text{ cm}^{-1}$  which is however Raman-inactive and unobserved in perfect crystals of  $\alpha\text{-Fe}_2\text{O}_3$ . In our measurements, this peak appears at  $646\text{ cm}^{-1}$ , with intensities ranging between about 50 and 100 percent of that of the  $600\text{ cm}^{-1}$  peak. According to the literature,<sup>33</sup> this mode becomes Raman-active during the crystallization process due to symmetry breaking. Also in our case the nanocrystals generated by laser irradiation obviously lack long range order and, hence, the peak appears in the spectrum.

**Table 4-2.** Raman shift ( $\text{cm}^{-1}$ ) and assignment of the hematite Raman modes.

The laser power of the experiments is indicated.

Our results (3 mW)	Ref. <sup>29</sup> (7 mW)	Ref. <sup>29</sup> (0.7 mW)	Ref. <sup>31</sup> ( $\leq 10\ \mu\text{W}$ )	Assignment
216	219.6	226.7	226.5	$A_{1g}$
232	236.5	245.7	245.5	$E_g$
279	282.7	292.5	293.5	$E_g$
285	295.9	299.3	300	$E_g$
399	395.9	410.9	413	$E_g$
486	492.3	497.1	498.5	$A_{1g}$
601	596.0	611.9	612.5	$E_g$
646	-	-	659	disorder <sup>31,33</sup>
1304	-	1320	1318	overtone

It was observed that during laser irradiation the peaks of hematite became narrower and shift to higher frequencies, as shown in Figure 9. The changes in the spectra seem to indicate an increase of the average crystallite size. The width of our Raman peaks is slightly larger than reported in reference.<sup>29</sup> This can be a consequence of the small crystallite size or a size distribution, although we cannot completely rule out that the widths are affected by heating effects at the relatively high laser power of 3 mW.

#### 4.4 Conclusions

Amphiphilic cylindrical polymer brushes with poly(acrylic acid) core and poly(*n*-butyl acrylate) shell were synthesized via ATRP. The core of polymer brush was first partially neutralized by NaOH, then reacted with iron cations via ion exchange. The formation of the polychelates of polymer brushes and Fe<sup>3+</sup>/Fe<sup>2+</sup> ions was confirmed by various characterization techniques. The conversion of the polychelates to magnetic nanocylinders via either reduction or alkalization of iron cations inside polymer core will be shown in next chapter.

We have monitored the laser-induced decomposition of cylindrical core-shell polymer brushes containing Fe<sup>3+</sup> ions with confocal Raman micro-spectroscopy. Simultaneously with the decomposition, the Raman lines of  $\alpha$ -Fe<sub>2</sub>O<sub>3</sub> appeared in the spectrum, indicating the laser-induced formation of this oxide from the Fe<sup>3+</sup> ions. The spectral changes during laser irradiation were ascribed to growth of the crystallites.

**References**

- (1) Tsukahara, Y.; Mizuno, K.; Segawa, A.; Yamashita, Y. *Macromolecules* **1989**, *22*, 1546-1552.
- (2) Wintermantel, M.; Gerle, M.; Fischer, K.; Schmidt, M.; Wataoka, I.; Urakawa, H.; Kajiwara, K.; Tsukahara, Y. *Macromolecules* **1996**, *29*, 978-983.
- (3) Gerle, M.; Fischer, K.; Roos, S.; Mueller, A. H. E.; Schmidt, M.; Sheiko, S. S.; Prokhorova, S.; Moeller, M. *Macromolecules* **1999**, *32*, 2629-2637.
- (4) Beers, K. L.; Gaynor, S. G.; Matyjaszewski, K.; Sheiko, S. S.; Möller, M. *Macromolecules* **1998**, *31*, 9413-9415.
- (5) Cheng, G.; Böker, A.; Zhang, M.; Krausch, G.; Müller, A. H. E. *Macromolecules* **2001**, *34*, 6883-6888.
- (6) Zhang, M.; Breiner, T.; Mori, H.; Müller, A. H. E. *Polymer* **2003**, *44*, 1449-1458.
- (7) Rivas, B. L.; Seguel, G. V. *Polym. Bull.* **1998**, *40*, 431-437.
- (8) Fitzgerald, W. E.; Nielsen, L. E. *Proc. Roy. Soc. Ser. A* **1964**, *282*, 137-146.
- (9) Sijtsma, N. M.; Wouters, S. D.; De Grauw, C. J.; Otto, C.; Greve, J. *Appl. Spectrosc.* **1998**, *52*, 348-355.
- (10) Xie, C.; Li, Y.-q. *J. Appl. Phys.* **2003**, *93*, 2982-2986.
- (11) Gellermann, W.; Ermakov, I. V.; McClane, R. W.; Bernstein, P. S. *Opt. Lett.* **2002**, *27*, 833-835.
- (12) Enejder, A. M. K.; Koo, T.-W.; Oh, J.; Hunter, M.; Sasic, S.; Feld, M. S.; Horowitz, G. L. *Opt. Lett.* **2002**, *27*, 2004-2006.
- (13) De Oliveira, L. F. C.; Colombara, R.; Edwards, H. G. M. *Appl. Spectrosc.* **2002**, *56*, 306-311.
- (14) Wopenka, B.; Popelka, R.; Pasteris, J. D.; Rotroff, S. *Appl. Spectrosc.* **2002**, *56*, 1320-1328.
- (15) Voyiatzis, G. A.; Andrikopoulos, K. S. *Appl. Spectrosc.* **2002**, *56*, 528-535.
- (16) Baia, L.; Gigant, K.; Posset, U.; Schottner, G.; Kiefer, W.; Popp, J. *Appl. Spectrosc.* **2002**, *56*, 536-540.
- (17) Sato, H.; Sasao, S.; Matsukawa, K.; Kita, Y.; Ikeda, T.; Tashiro, H.; Ozaki, Y. *Appl. Spectrosc.* **2002**, *56*, 1038-1043.
- (18) Kador, L.; Schittkowski, T.; Bauer, M.; Fan, Y. *Appl. Opt.* **2001**, *40*, 4965-4970.
- (19) Liem, H.; Etchegoin, P.; Whitehead, K. S.; Bradley, D. D. C. *J. Appl. Phys.* **2002**, *92*, 1154-1161.

- (20) Labarthe, F. L.; Bruneel, J.-L.; Buffeteau, T.; Sourisseau, C.; Huber, M. R.; Zilker, S. J.; Bieringer, T. *Phys. Chem. Chem. Phys.* **2000**, *2*, 5154-5167.
- (21) Kagan, C. R.; Harris, T. D.; Harris, A. L.; Schilling, M. L. *J. Chem. Phys.* **1998**, *108*, 6892-6896.
- (22) Perrin, D. D. *"Stability Constants of Metal-Ion Complexes Part B: Organic Ligands"* **1979**, Pergamon Press, New York, p.38.
- (23) Sillen, L. G.; Martell, A. E. *"Stability Constants of Metal-Ion Complexes"* **1971**, The Chemistry Society, London, p.253.
- (24) Clay, R. T.; Cohen, R. E. *Supramol. Sci.* **1998**, *5*, 41-48.
- (25) Sohn, B. H.; Cohen, R. E. *Chem. Mater.* **1997**, *9*, 264-269.
- (26) Winnik, F. M.; Morneau, A.; Mika, A. M.; Childs, R. F.; Roig, A.; Molins, E.; Ziolo, R. F. *Can. J. Chem.* **1998**, *76*, 10-17.
- (27) Setton, R.; Bernier, P.; Lefrant, S. *Carbon Molecules and Materials* (Taylor & Francis, London) **2002**.
- (28) Martin, T. P.; Merlin, R.; Huffman, D. R.; Cardona, M. *Solid State Commun.* **1977**, *22*, 565-567.
- (29) De Faria, D. L. A.; Silva, S. V.; De Oliveira, M. T. *J. Raman Spectrosc.* **1997**, *28*, 873-878.
- (30) Witke, K.; Klaffke, D.; Skopp, A.; Schreckenbach, J. P. *J. Raman Spectrosc.* **1998**, *29*, 411-415.
- (31) Bersani, D.; Lottici, P. P.; Montenero, A. *J. Raman Spectrosc.* **1999**, *30*, 355-360.
- (32) Mazzetti, L.; Thistlethwaite, P. J. *J. Raman Spectrosc.* **2002**, *33*, 104-111.
- (33) McCarty, K. F. *Solid State Commun.* **1988**, *68*, 799-802.



## Chapter 5

### Superparamagnetic hybrid nanocylinders<sup>\*</sup>

#### Abstract

Well-defined cylindrical polymer brushes with poly(acrylic acid) (PAA) core and poly(*n*-butyl acrylate) (PnBA) shell were synthesized via combination of anionic polymerization and atom transfer radical polymerization. These amphiphilic brushes are unimolecular cylindrical micelles and can be used as single molecular templates for synthesis of inorganic nanoparticles, because the carboxylic acid groups (or carboxylate groups, after neutralization) in the polymer core can coordinate with various metal ions. Ultrafine iron oxide magnetic nanoparticles were successfully synthesized within the core of these core-shell polymer brushes, as confirmed by various characterization techniques. The as-prepared hybrid nanocylinders show typical superparamagnetic behavior indicated by the magnetization measurements.

\* This chapter contains a paper which has been accepted for publication:

“Superparamagnetic hybrid nanocylinders”

Mingfu Zhang, Claude Estournès, Werner Bietsch, Axel H. E. Müller

*Advanced Functional Materials*, **2004**, accepted.

## 5.1 Introduction

The design, synthesis and investigation of particles with nanometer dimensions, so-called nanoparticles, have become a subject of intense current interest, due to their novel electronic, optical, magnetic, and other properties arising from quantum size effect and the large surface area-to-volume ratio.<sup>1-5</sup> Magnetic nanoparticles, for example, exhibit size effects. Below a critical size, magnetic particles become single domain, in contrast to multidomain in the bulk material. With decreasing particle size the coercivity of single domain magnetic particles decreases until it vanishes, and unique phenomena such as superparamagnetism<sup>6</sup> and quantum tunneling of magnetization<sup>7</sup> appear. Due to their unique properties, magnetic nanoparticles not only are of fundamental interest but also have many potential applications in diverse areas such as information storage,<sup>8</sup> color imaging,<sup>9</sup> bioprocessing,<sup>10</sup> immunoassay,<sup>11,12</sup> magnetic refrigeration,<sup>13</sup> and ferrofluids.<sup>14,15</sup>

It is well known that nanoparticles tend to aggregate in order to reduce the energy associated with the high surface area-to-volume ratio. Thus the stabilization of nanoparticles is crucial for investigations and applications, in addition to the size control during particle formation. Polymer templates have proven to be versatile hosts and stabilizing matrices in the controlled synthesis of nanoparticles. As hosts, polymers provide functionalities and structured frameworks for the synthesis and confinement of nanoparticles. In addition to the impartation of mechanical stability to the nanoparticles, polymers contribute to the chemical and physical properties of the nanocomposite as a whole. Polymer-nanoparticle hybrid materials combine the promising properties of both components. So far, nanoparticles have been synthesized in various polymers, such as resins,<sup>16</sup> membranes,<sup>17</sup> block copolymer films,<sup>18</sup> micelles,<sup>19,20</sup> gel particles,<sup>21,22</sup> polymeric nanospheres,<sup>23</sup> nanotubes,<sup>24</sup> and dendrimers.<sup>25</sup> In particular, single molecular templates are of interest since isolated nanocomposites can be synthesized and used directly.<sup>26</sup> Very recently, gold nanoclusters were successfully fabricated within the poly(2-vinylpyridine) core of a single polymer brush molecule.<sup>27</sup>

Metals (Fe, Co, Ni, etc) and metal oxides ( $\gamma$ -Fe<sub>2</sub>O<sub>3</sub>, Fe<sub>3</sub>O<sub>4</sub>, etc) are the most common materials for magnetic nanoparticles. Generally, the production of magnetic metallic nanoparticles is difficult, as the large surfaces are easily oxidized or otherwise subject to corrosion. In contrast, magnetic metal oxide nanoparticles are not oxidation sensitive and are in high demand for magnetic recording applications.<sup>28</sup> Many oxide particles have

significant shape anisotropy, which allows the particle size to be much larger without becoming multidomain.

Recently we reported a method of synthesizing a wire-like assembly of semiconductor (CdS) nanoparticles within a novel single molecule template, an amphiphilic cylindrical polymer brush with poly(acrylic acid) (PAA) core and poly(*n*-butyl acrylate) (P*n*BA) shell (see Chapter 6).<sup>29</sup> Our technique takes advantages of each of the unique aspects of polymer structure: the core of polymer brush, which possesses carboxylate groups (after neutralization of PAA) capable of coordinating with metal ions such as Cd<sup>2+</sup>, worked as a nanoreactor for CdS nanoparticle formation and directed the particle distribution; and the shell of the polymer brush protected the fabricated nanoparticles from aggregation and provided the solubility of the hybrid material.

In this paper we report the synthesis and characterization of superparamagnetic iron oxide nanoparticles within the cylindrical polymer brushes with PAA core and P*n*BA shell. Iron oxide nanoparticles were produced within the core of the polymer brushes via alkaline oxidation of ferrous ions, proceeding in the following steps: (*i*) an coordination step to load ferrous/ferric ions into the polymer core; (*ii*) formation of ferrous hydroxides in alkaline medium (in the case that ferric ions were used, preceded by their reduction to ferrous ions); and (*iii*) oxidation of the ferrous hydroxides in alkaline medium by either oxygen or hydrogen peroxide to produce magnetic iron oxide nanoparticles. This method results in the formation of a wire-like assembly of ultrafine magnetic nanoparticles within single polymer brush molecules. The alkaline oxidation of ferrous ions has been demonstrated to yield superparamagnetic forms of maghemite ( $\gamma\text{-Fe}_2\text{O}_3$ )<sup>16,22,23</sup> or sometimes iron hydroxyoxides (such as  $\alpha\text{-FeO(OH)}$ )<sup>21</sup> in a variety of polymeric templates. It is often stated that functionalized polymeric templates can control the chemical composition of products of the alkaline oxidation of ferrous ions. Identical reactions carried out in the absence of the polymer matrix resulted in nonmagnetic large particles.<sup>16,21</sup> In addition to the general advantages offered by polymeric templates, the polymer brushes used here provide the solubility of the hybrid materials in organic solvents due to the hydrophobic polymer shell and thus stable magnetic fluids can be obtained.

The obtained hybrid magnetic nanocylinders are expected to orient under application of a magnetic field, due to the longitudinal distribution of magnetic nanoparticles along the backbone of polymer brush. Similar phenomena have been observed in nature. Some aquatic bacteria which contain a chain-like assembly of magnetic nanoparticles can orient and swim along the earth's magnetic field lines.<sup>30,31</sup> The orientation of these magnetic

nanocylinders by an applied magnetic field will result in some peculiar properties such as magnetoviscous effect<sup>32</sup> and birefringence.

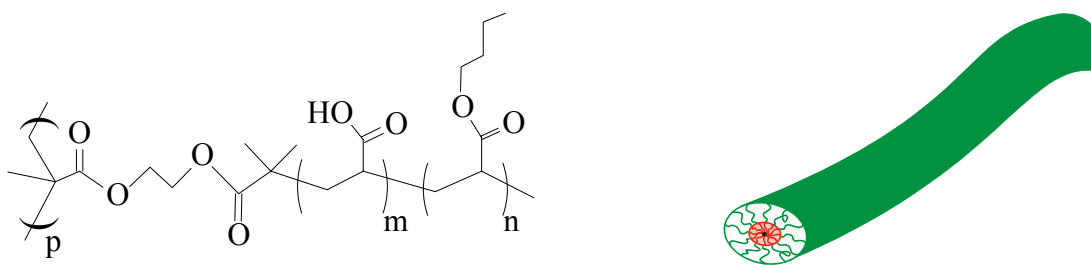
Coupling of the magnetic and mechanical degrees of freedom of the particles is the main specific feature of magnetic fluids. Explicit manifestation of this coupling is the increase of the viscosity of ferrofluids under application of magnetic field, which is so-called magnetoviscous effect. In the classical theory the magnetoviscous effect is accounted for by the hindrance to particle rotation caused by the magnetic torque.<sup>33</sup> Recently, however, dependence of the fluid effective viscosity on the magnetic field was experimentally observed to be much more than that predicted by classical theory. Odenbach *et al* demonstrated that the magnetic field-induced formation of chain-like aggregates of magnetic nanoparticles caused the strong magnetoviscous effect.<sup>32</sup> However, these chain-like aggregates can be destroyed by high shear flow and thus magnetoviscous effect decreases significantly.

In our case, chain-like assemblies of superparamagnetic nanoparticles are encapsulated within a polymeric template, so they are much more stable than the chain-like aggregates (induced by magnetic field) existing in conventional ferrofluids of spherical magnetic particles. Thus it is reasonable to expect that strong magnetoviscous effect will be observed for the solutions of superparamagnetic nanocylinders, and specially this effect will not be destroyed by the high shear flow. This will be a big advantage compared to conventional ferrofluids.

## 5.2 Experimental Section

### 5.2.1 Polymer synthesis

Amphiphilic cylindrical polymer brushes with poly(acrylic acid) (PAA) core and poly(*n*-butyl acrylate) (P*n*BA) shell, which were used as templates in this paper, were synthesized via the combination of anionic polymerization and atom transfer radical polymerization (ATRP) as described previously.<sup>34</sup> The synthetic procedure is briefly described as follows. The backbone of the polymer brushes, poly(2-hydroxyethyl methacrylate) (PHEMA), was synthesized via anionic polymerization of 2-(trimethylsilyloxy)ethyl methacrylate followed by the cleavage of the protecting trimethylsilyloxy groups. Complete esterification of the pendant hydroxyl groups of PHEMA with  $\alpha$ -bromoisobutyryl bromide resulted in the attachment of an  $\alpha$ -bromoester group to each monomer unit of PHEMA. Sequential ATRP of *t*-butyl acrylate (*t*BA) and *n*-butyl acrylate (*n*BA) initiated by the pendant  $\alpha$ -bromoester groups on the backbone formed the P*t*BA-*b*-P*n*BA block copolymer side chains. Finally, the selective hydrolysis of the P*t*BA block resulted in the amphiphilic core-shell cylindrical polymer brushes with PAA core. Due to the living nature of both anionic polymerization and ATRP, the length of the polymer brush as well as the diameters of the core and shell are well-defined. The chemical and schematic 3-dimensional structure of such a polymer brush used as templates in this paper are shown in Scheme 5-1.



**Scheme 5-1.** (left) Chemical structural formula of the polymer brushes used in the present paper, defined as  $[AA_m-nBA_n]_p$  (where  $p$ ,  $m$  and  $n$  denote the degrees of polymerization of the backbone, core block and shell block respectively); and (right) their schematic 3-D structure.

Detailed synthetic procedure and characterizations of the polymer brushes have been reported in our previous paper.<sup>34</sup> Gel permeation chromatography (GPC) was used to determine the molecular weight distribution,  $M_w/M_n$ . The degree of polymerization (DP) of the backbone was determined to be 1500 by membrane osmometry and the DP of the side chains was calculated from monomer conversion of polymerization. The characterization results are summarized in Table 5-1.

**Table 5-1** Characterization results of the polymer brushes with PAA core and PnBA shell

Polymer <sup>a</sup>	$10^{-5} \times M_{n, \text{GPC}}$ <sup>b</sup>	$M_w/M_{n, \text{GPC}}$ <sup>b</sup>	DP <sub>core</sub> <sup>c</sup>	DP <sub>shell</sub> <sup>c</sup>	Formula
Brush 1	7.60	1.29	25	61	[AA <sub>25</sub> -nBA <sub>61</sub> ] <sub>1500</sub>
Brush 2	9.34	1.40	37	48	[AA <sub>37</sub> -nBA <sub>48</sub> ] <sub>1500</sub>

(a) The backbone of the polymer brushes has degree of polymerization (DP) of 1500 determined by membrane osmometry, with a polydispersity index of 1.08; (b) polydispersity index of unhydrolyzed brushes (with PtBA core and PnBA shell) obtained from GPC measurements; (c) calculated according to initial monomer/initiator ratio and monomer conversion determined by gas chromatography.

### 5.2.2 Magnetic nanoparticle formation within the polymer brushes

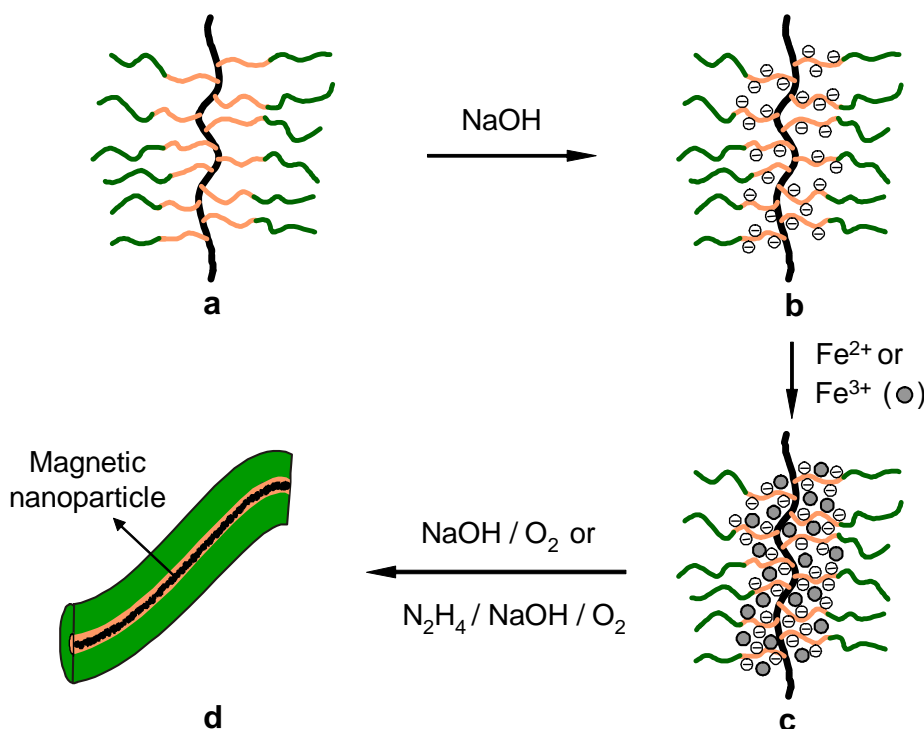
All chemicals were of analytical grade and used as received without further purification. All solvents used in the glove-box were degassed before the usage.

To synthesize magnetic iron oxide nanoparticles within polymer brushes, alkaline oxidation of ferrous ions was carried out. The schematic synthetic procedure is shown in Scheme 5-2.

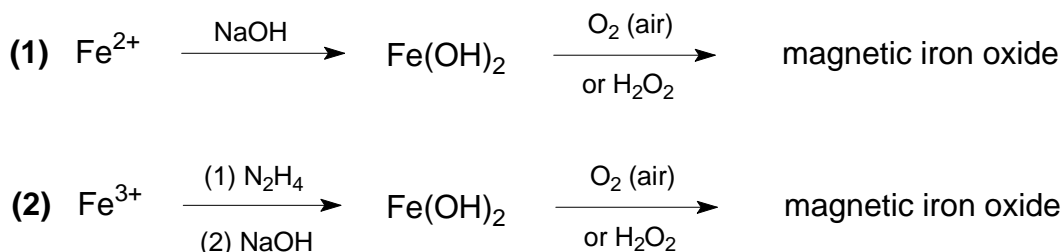
Different strategies were tried, using either ferrous ( $\text{Fe}^{2+}$ ) or ferric ( $\text{Fe}^{3+}$ ) ions as precursors (Scheme 5-3). It has been reported that maghemite ( $\gamma\text{-Fe}_2\text{O}_3$ ) nanoparticles were successfully produced within a porous polymeric resin from both two strategies shown in Scheme 5-3.<sup>16</sup> There are both advantages and disadvantages in each case.

As shown in Scheme 5-3, when  $\text{Fe}^{2+}$  ions were used, the synthesis is more straightforward. In addition, the theoretical maximum loading capacity of the PAA polymer core for  $\text{Fe}^{2+}$  (0.5 mol per mole of acrylic acid) is higher than that of  $\text{Fe}^{3+}$  (0.33 mole per mole of acrylic acid), assuming ion exchange as the only binding mechanism.<sup>35</sup> However, due to the easy oxidation of  $\text{Fe}^{2+}$  ions by oxygen in air, the uptake of  $\text{Fe}^{2+}$  ions and the

further purification had to be performed under the inert atmosphere ( $N_2$ ). This caused some difficulties in the synthesis procedure, specially in the step of removal of uncoordinated metal ions (for example, via ultracentrifugation).



**Scheme 5-2.** Schematic illustration for the synthesis of a wire-like assembly of maghemite ( $\gamma$ - $Fe_2O_3$ ) nanoparticles inside the cylindrical polymer brush: (a) polymer brush with PAA core and PnBA shell; (b) neutralized polymer brush with poly(sodium acrylate) core ( $Na^+$  ions are not shown); (c) polychelate of the brush with  $Fe^{2+}$  or  $Fe^{3+}$  ions; and (d) hybrid nanocylinder of the brush and wire-like assembly of iron oxide nanoparticles.



**Scheme 5-3.** Formation of magnetic iron oxide nanoparticles from  $Fe^{2+}$  (method 1) or  $Fe^{3+}$  ions (method 2).

**Table 5-2.** Synthetic conditions for the preparation of magnetic nanocylinders

Code of hybrid magnetic nanocylinder	Polymer brush	Solvent	Neutralization of PAA <sup>b</sup>	Iron salt	Fe <sup>n+</sup> /AA <sup>c</sup>	Oxidation agent
MC1	Brush 1	THF	—	FeCl <sub>2</sub>	0.56	O <sub>2</sub> (air)
MC2	Brush 1	CH <sub>3</sub> OH/ CHCl <sub>3</sub> <sup>a</sup>	90 %	FeCl <sub>3</sub>	0.33	O <sub>2</sub> (air)
MC3	Brush 2	CH <sub>3</sub> OH/ CHCl <sub>3</sub> <sup>a</sup>	90 %	FeCl <sub>3</sub>	0.33	O <sub>2</sub> (air)
MC4	Brush 2	CH <sub>3</sub> OH/ CHCl <sub>3</sub> <sup>a</sup>	90 %	FeCl <sub>3</sub>	0.33	H <sub>2</sub> O <sub>2</sub>

(a) volume ratio = 1/1; (b) neutralization of the poly(acrylic acid) core of polymer brushes by NaOH; (c) molar ratio.

In contrast, the loading of Fe<sup>3+</sup> ions into polymer brushes and the following purification (removal of uncoordinated Fe<sup>3+</sup> ions) can be done under air. However, the coordinated Fe<sup>3+</sup> ions within the polymer brushes have to be reduced to Fe<sup>2+</sup> ions by hydrazine, followed by alkaline oxidation to produce magnetic nanoparticles. Table 5-2 summarizes the preparation conditions for the synthesis of various magnetic nanocylinders.

(i) Ferrous ions (Fe<sup>2+</sup>) as precursors (for the magnetic nanocylinder MC1)

Inside a glove-box filled with N<sub>2</sub>, 104.2 mg of Brush 1, [AA<sub>25</sub>-*n*BA<sub>61</sub>]<sub>1500</sub> (containing 0.29 mmol of acrylic acid), were dissolved in THF (15 mL). Then, FeCl<sub>2</sub> (0.15 mmol FeCl<sub>2</sub>·4H<sub>2</sub>O, in 5 mL THF) was added. The mixture was stirred overnight, and a transparent yellowish-green solution was obtained. Addition of a mixture of methanol (40 mL) and water (8 mL) induced precipitation of the Fe<sup>2+</sup>-loaded brushes. After removal of the supernatant containing the uncoordinated ferrous chloride, the precipitate was washed first with methanol containing 5 vol.% of water and then with methanol. The composite of the polymer brush and the coordinated iron ions is designated as polychelate.

The polychelate, however, was not well soluble in THF. It was dispersed in THF (80 mL) and the turbid dispersion was stable over hours without appreciable precipitation. Into 60 mL of the dispersion a saturated methanolic solution of NaOH was added until the pH value reached about 11. Upon addition of the NaOH solution, the dispersion turned olive-green, which is the typical color of Fe(OH)<sub>2</sub>.

After stirring for one hour, the reaction mixture was removed from the glove-box and bubbled with air for 3 hours. The color of the mixture turned brown instantly upon air bubbling. Addition of water (15 mL) into the mixture induced precipitation, and the brown precipitate was washed with a mixture of methanol and water (v/v = 5/1) until neutral pH.

(ii) Ferric ions ( $\text{Fe}^{3+}$ ) as precursors (for the magnetic nanocylinders MC2-4)

409.4 mg of Brush 2,  $[\text{AA}_{37-n}\text{BA}_{48}]_{1500}$  (containing 1.73 mmol of acrylic acid), were dissolved in a mixture of methanol and chloroform (250 mL, v/v = 1/1). Then NaOH (1.55 mmol, in 12 mL methanol containing 2 vol.% water) was added to partially neutralize the PAA core of the polymer brush. The mixture was stirred overnight. Afterwards,  $\text{FeCl}_3$  (0.58 mmol, in 2.9 mL methanol) was added and a brown solution was obtained. To remove the uncoordinated ferric ions, two methods were tried. First ultracentrifugation (20,000 rpm with relative centrifugal force of 47,800 g, Sorvall RC-5B centrifuge, Du Pont Instruments) was carried out to separate the  $\text{Fe}^{3+}$ -loaded polymer brushes from solution. However, the supernatant still contained considerable amounts of the  $\text{Fe}^{3+}$ -loaded polymer brushes. Thus, the supernatant was concentrated via rotating evaporation until precipitation occurred. The precipitates (from both ultracentrifugation and precipitation) were washed with methanol for 3 times. The precipitates obtained from both methods were soluble in a mixture of methanol and chloroform (300 mL, v/v = 1/1) and a clear brown solution was obtained.

In a vacuum line, 240 mL of the solution of the polychelate was first degassed and put under  $\text{N}_2$ . Afterwards, degassed  $\text{N}_2\text{H}_4\cdot\text{H}_2\text{O}$  (9.23 mmol,  $\text{N}_2\text{H}_4/\text{FeCl}_3 = 20$ ) was added and the mixture was stirred for 1.5 hours. The color of the solution changed from brown to yellowish-green, indicating the reduction of  $\text{Fe}^{3+}$  to  $\text{Fe}^{2+}$ .

Addition of NaOH (4.66 mmol, in 36 mL methanol containing 2 vol.% water,  $\text{NaOH}/\text{FeCl}_3 = 10$ ) into the above solution resulted in a color change from yellowish-green to olive-green, indicating the formation of  $\text{Fe}(\text{OH})_2$ . The mixture was stirred under  $\text{N}_2$  for 1.5 hours. Without stirring, we observed an olive-green floccular precipitate.

The obtained dispersion was divided into two equal parts. Two oxidization agents, e.g.  $\text{O}_2$  (air) and  $\text{H}_2\text{O}_2$ , were used separately to oxidize  $\text{Fe}(\text{OH})_2$ . One part of the dispersion was bubbled with air for 2.5 hours. The color instantly changed to reddish brown. Into the other part of the dispersion  $\text{H}_2\text{O}_2$  (2.31 mmol, 30 wt.% in  $\text{H}_2\text{O}$ ,  $\text{H}_2\text{O}_2/\text{FeCl}_3 = 10$ ) was added and the color of the mixture also changed to reddish brown immediately. The mixture was stirred for 2.5 hours. In both cases a reddish brown precipitate, the hybrid nanocylinder of

the polymer brush and iron oxide nanoparticles, was obtained and washed with methanol until neutral pH.

Although the as-prepared magnetic nanocylinders mentioned above are not soluble, soluble magnetic nanocylinders can be produced by fine-tuning the synthetic conditions. For example, when Brush 1 was used, the hybrid nanocylinder (MC2) synthesized using  $\text{Fe}^{3+}$  as precursor and  $\text{O}_2$  as oxidation agent was soluble in a mixture of methanol and chloroform ( $v/v = 1/1$ ). Thus a stable magnetic fluid (solution of the magnetic nanocylinders) can be obtained.

### 5.2.3 Characterization

Scanning force microscopy (SFM) images were recorded on a Digital Instruments Dimension 3100 microscope operated in Tapping Mode<sup>TM</sup> (free amplitude of the cantilever  $\approx 20$  nm, amplitude set point  $\approx 0.98$ ). The standard silicon nitride probes were driven at 3% offset below their resonance frequencies in the range of 250-350 KHz. The samples were prepared by dip-coating from dilute solutions (about  $10^{-5}$  g/mL) of the polymer brush, polychelate, or hybrid nanocylinder in methanol/chloroform ( $v/v=1/1$ ) mixture onto freshly cleaved mica. An image analysis software, ImageJ, was used for the statistical analysis of SFM images to obtain the average lengths of polymer brushes.

Transmission electron microscopy (TEM) images were taken on a LEO 922 OMEGA electron microscope operated at 200 kV. A 5  $\mu\text{L}$  droplet of a dilute solution (in dioxane), was dropped onto a copper grid (300 mesh) coated with Formvar/carbon film, followed by drying at room temperature.

UV/visible absorbance spectra of samples in methanol/chloroform ( $v/v = 1/1$ ) were recorded on a Perkin-Elmer Lambda 15 UV/visible spectrophotometer. The spectrum from a quartz cuvette containing pure solvent was subtracted from all sample spectra.

Dynamic light scattering (DLS) measurements of Brush 1 (0.2 g/L) and the hybrid nanocylinder MC2 (about 0.1 g/L) in a mixture of methanol and chloroform (volume ratio = 1/1) were performed on an ALV DLS/SLS-SP 5022F compact goniometer system with an ALV 5000/E correlator and a He-Ne laser. Prior to the light scattering measurements the sample solutions were filtered using Millipore Teflon filters with a pore size of 1  $\mu\text{m}$ . CONTIN<sup>36</sup> analysis of the autocorrelation functions was carried out.

Thermal gravimetric analysis (TGA) measurements were carried on a Mettler Toledo TGA/SDTA851 with the sample amount of 4-11 mg. The measurements was performed

under air flow of 60 mL/min with heating from 30 °C to 1000 °C (rate: 10 °C/min) and then keeping at 1000 °C for half an hour. Before TGA measurements samples were dried in vacuum oven at 50 °C for at least one day.

Magnetic properties of the samples were studied with a quantum design MPMS-XL superconducting quantum interference device (SQUID) magnetometer between 295 and 2 K, with a maximum applied field of 50 kOe (= 5 T). The magnetization was also measured as a function of temperature at a given applied field in the field cooled and zero field cooled modes. For the zero field cooled (ZFC) measurements, the sample was first cooled down to 2 K in zero magnetic field. Subsequently, a magnetic field of 20 Oe was applied and the magnetization was measured while the temperature was increased until 400 K. Afterwards, the magnetization of the sample under a magnetic field of 20 Oe as a function of decreasing temperature (till 2 K) was measured as the field-cooled (FC) magnetization.

Mössbauer analyses were carried out using a triangular waveform spectrometer (Wiessel) and a source of  $^{57}\text{Co}$  (50 mCi) diffused into a rhodium matrix. Mössbauer experiments without a magnetic field were performed at 300 K. The values of the isomer shift are quoted relative to that of  $\alpha\text{-Fe}$  foil at room temperature. The hyperfine parameters were refined using a least-square fitting procedure in the MOSFIT program.<sup>37</sup>

In the absence of an external magnetic field, the Mössbauer spectrum shows the information of the magnetic spin fluctuations among the easy axes of magnetization. The average time necessary to move the magnetization from one axis to another is denoted the superparamagnetic relaxation time ( $\tau$ ). Both crystallite size and temperature determine the relaxation time. Thus, for a given measuring temperature, if the relaxation of the particle is faster than the Mössbauer time scale ( $\approx 10^{-8}$  s), a doublet will be observed on the spectrum consistent with a superparamagnetic behavior. If the relaxation of the particle is slower than the Mössbauer time scale, the magnetization of the particle will appear blocked and a sextet will be observed consistent with a magnetic blocked state. In the case of size-distributed particles, a broadening of the hyperfine structure will be observed due to the distributed relaxation time.

## 5.3 Results and Discussion

### 5.3.1 Synthesis and characterization of magnetic nanocylinders

The polymer templates used in this paper, amphiphilic cylindrical polymer brushes with poly(acrylic acid) (PAA) core and poly(*n*-butyl acrylate) (P*n*BA) shell, are well-defined in structure, due to the living/controlled nature of both anionic polymerization and atom transfer radical polymerization (ATRP) which were used for the polymer synthesis.<sup>34</sup> Figure 5-1 shows a typical SFM image of Brush 1 ([AA<sub>25</sub>-*n*BA<sub>61</sub>]<sub>1500</sub>) on the substrate mica. The worm-like morphology of the polymer brushes can be easily visualized. A statistical analysis of the SFM image shows that the number- and weight-average lengths of Brush 1 are  $L_n = 166$  nm and  $L_w = 180$  nm respectively, with a polydispersity index  $L_w/L_n = 1.08$ , which is identical to the molecular weight distribution of the backbone. The core-shell structure of the polymer brushes could be directly observed in the SFM phase image (Figure 1b), because of the apparent contrast produced by the large difference in hardness between the relatively hard PAA (glass transition temperature  $T_g = 106$  °C<sup>38</sup>) and the very soft P*n*BA ( $T_g = -54$  °C<sup>39</sup>). However, in the corresponding height image (Figure 5-1a) the shell is invisible because it is totally collapsed on the mica surface, thus its height is too small to be detected by the SFM tip we used. A three-dimensional height image, as shown in Figure 1c, clearly reveals the cylindrical shape of the polymer brushes. The SFM image shows that these polymer brushes are structurally well-defined.

It is well known that carboxylic acid and carboxylate groups can coordinate with various metal ions such as Fe<sup>2+</sup> and Fe<sup>3+</sup>.<sup>35</sup> Therefore the polymer brushes with PAA core can be used as nanoreactors and cylindrical templates for magnetic iron oxide nanoparticle formation. Consequently, the size control during the particle formation and the directed distribution of nanoparticles along the backbone of the polymer brushes can be achieved. Scheme 5-2 shows the procedure for the synthesis of magnetic iron oxide nanoparticles within the polymer brushes. It includes: (1) neutralization of the PAA core of the polymer brush (a→b; This step is optional.); (2) uptake of Fe<sup>2+</sup> or Fe<sup>3+</sup> ions into the polymer core (b→c, the complexes of the polymer brushes and iron ions are named polychelates); and (3) in situ formation of magnetic nanoparticles (c→d), via the reactions shown in Scheme 3.

Although metal ions can be coordinated directly to carboxylic acid groups, experiments have shown that conversion of carboxylic acid to sodium carboxylate significantly increases both the rate and the extent of metal ion uptake.<sup>35</sup> In this paper, polymer brushes with either

PAA core or poly(sodium acrylate) core were used as templates for magnetic nanoparticle fabrication. The uptake of iron ions into the polymer core was confirmed by various characterization techniques including FT-IR,<sup>40</sup> UV/visible spectroscopy, SFM and TEM,<sup>40</sup> besides the apparent color change before and after the iron ion uptake.

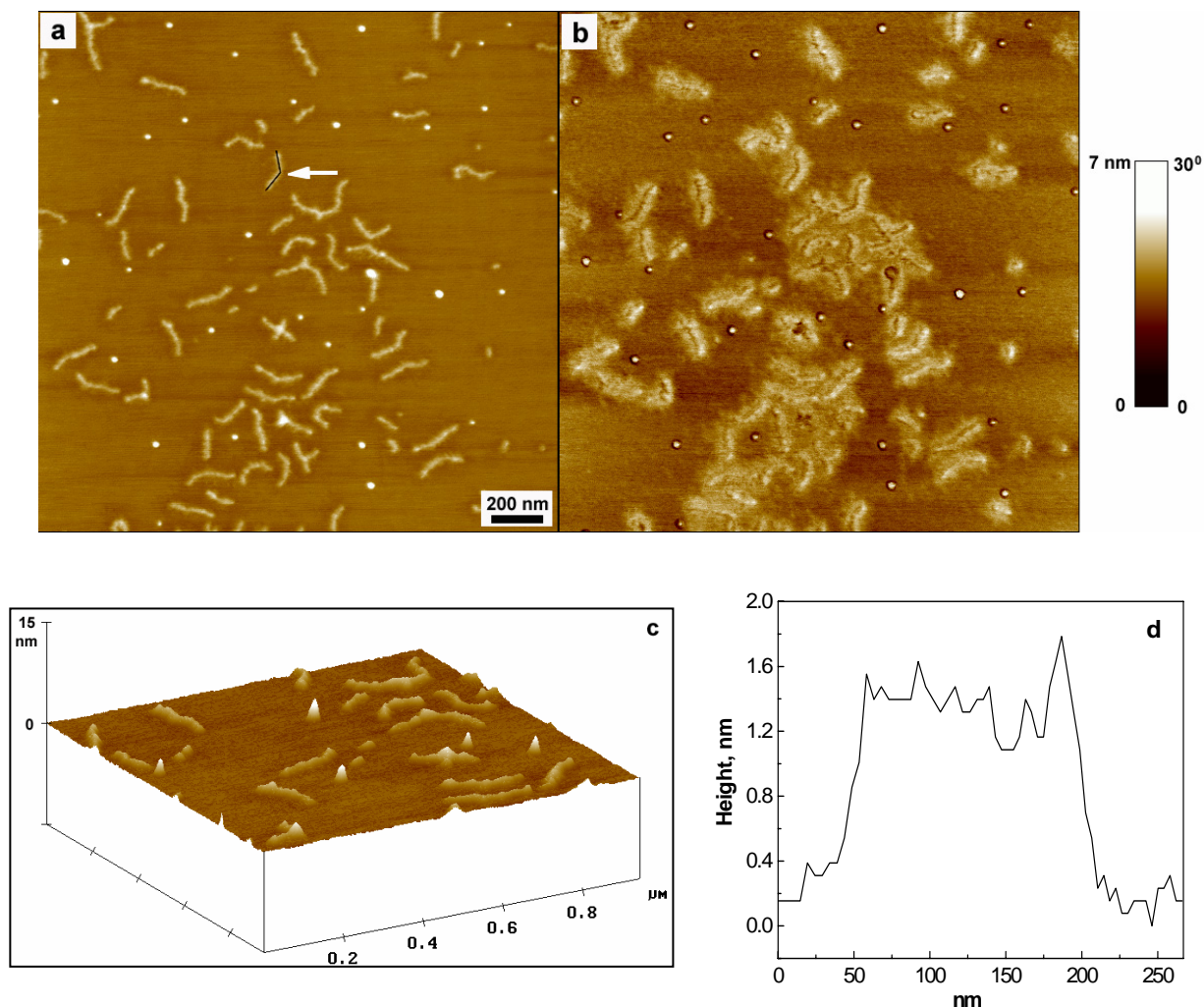


**Figure 5-1.** Tapping-Mode SFM images of Brush 1: (a) height image; (b) phase image; (c) three-dimensional height image; and (d) cross-section of one cylindrical polymer brush molecule indicated by an arrow in the height image (along the black solid line). We present the cross-section from original SFM images without deconvolution.

Removal of uncoordinated iron ions from the iron ion-loaded polymer brushes (polychelates) is very important, since otherwise big iron oxide particles (with dimensions in the micrometer range<sup>16</sup>) will form in solution. Various methods were tried to remove uncoordinated iron ions, such as precipitation and ultracentrifugation. Precipitation was carried out via concentration or addition of water, and the iron ion-loaded polymer brushes

precipitated while unreacted iron salts stayed in the supernatant. However, sometimes the precipitates could not be completely redissolved, especially when the precipitation was induced by addition of water. This might be due to the limited solubility of polychelates resulting from the huge molecular weights (more than  $10^7$ ) of the polymer brushes used. Alternatively, ultracentrifugation can separate polychelates from the solution without changing the solubility. However, experiments showed that only part of polychelates, which have larger size and correspondingly larger sedimentation coefficient, can be separated from solution via ultracentrifugation. So the rest of polychelates in the supernatant have to be purified by other methods like precipitation. We observed that combination of ultracentrifugation and precipitation can remove uncoordinated iron ions while keeping the solubility of polychelates.

The uptake of iron ions induced a dramatic change in the morphology of polymer brushes, as revealed in SFM images. In contrast to the smooth cylindrical shape of pure polymer brushes, a “pearl necklace” structure was observed for polychelates, as shown in Figure 5-2. The three-dimensional height image and cross-section analysis clearly demonstrate the height (and also the diameter) undulation along the backbone. Moreover, the height of the polychelate of Brush 1 and  $\text{Fe}^{3+}$  ion ( $h = 3.4 \pm 1.5$  nm) is much larger than that of Brush 1 ( $h = 1.4 \pm 0.3$  nm). From the comparison between the SFM images of the pure polymer brush and the polychelate, one can easily observe that the morphology change solely happened in the core region of the polymer brushes, supporting that  $\text{Fe}^{3+}$  ions coordinated selectively with carboxylate groups.

We speculate that the “pearl necklace” structure of polychelates is produced by the cross-linking of side chains via coordination between the multivalent  $\text{Fe}^{3+}$  ions and the monovalent carboxylate groups from different side chains. Thus,  $\text{Fe}^{3+}$  ions work as a bridging agents. We also found that loading of bivalent  $\text{Cd}^{2+}$  ions into polymer brushes induced the formation of a “pearl necklace” structure.<sup>29</sup> In contrast, neutralization of the PAA core of polymer brushes by NaOH did not change the apparent morphology of polymer brushes, as indicated by SFM measurements, since  $\text{Na}^+$  is monovalent and can not induce the cross-linking of side chains.

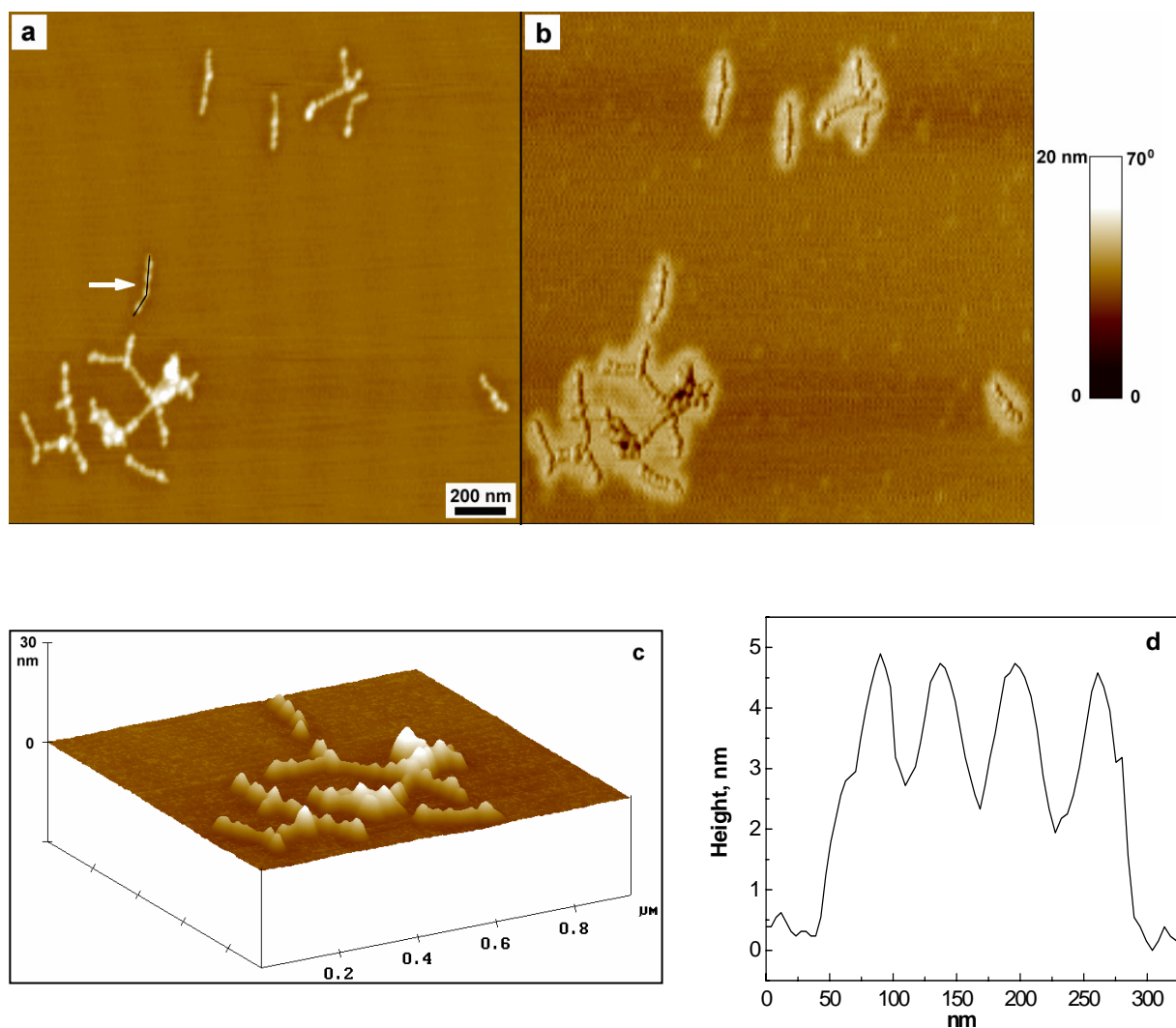


**Figure 5-2.** Tapping-Mode SFM images of the polychelate of Brush 1 with  $\text{Fe}^{3+}$  ions: (a) height image; (b) phase image; (c) three-dimensional height image; and (d) cross-section of one cylindrical polymer brush molecule indicated by an arrow in the height image (along the black solid line).

Besides SFM measurements, transmission electron microscopy (TEM) measurements can also provide the information of successful iron ion uptake. Although pure polymer brushes are invisible due to lack of contrast, after the formation of polychelates the iron ions with high electron density stained the core of polymer brushes thus the polymer core should be visible. This is actually the case, as shown in Figure 5-3. In Figure 5-3a, wire-like dark objects are clearly observed after iron ion ( $\text{Fe}^{3+}$ ) uptake. A TEM image with higher magnification (Figure 5-3b) shows the presence of the “pearl necklace” structure, similar to that observed in SFM images.

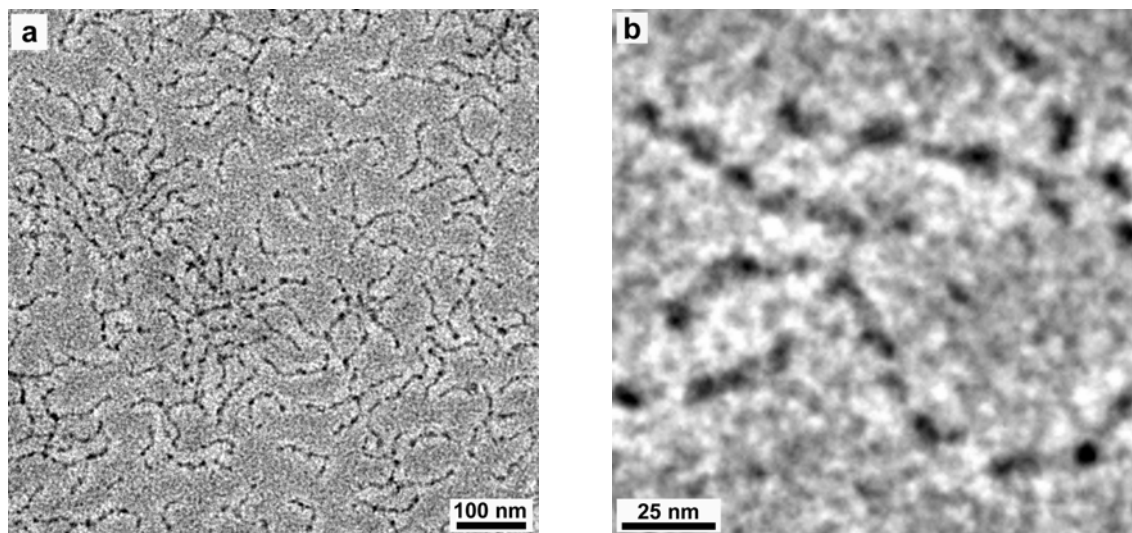


**Figure 5-3.** Non-stained TEM image of the polychelate of Brush 1 and  $Fe^{3+}$  ions.

For the polychelates containing  $Fe^{2+}$  ions, addition of NaOH will produce  $Fe(OH)_2$ , which can be easily oxidized to form magnetic iron oxide nanoparticles. In the case of the polychelates containing  $Fe^{3+}$  ions, reduction of  $Fe^{3+}$  to  $Fe^{2+}$  by hydrazine<sup>16,41</sup> was carried out before the formation of  $Fe(OH)_2$ . After the formation of iron oxide nanoparticles, cross-linking of side chains via iron ions should vanish and thus the “pearl necklace” structure should disappear. As expected, we observed an apparent morphology change of polymer brushes upon the particle formation: the “pearl necklace” structure disappeared and the morphology of the magnetic nanocylinders (hybrids of polymer brushes and iron oxide nanoparticles) was very similar to that of pure polymer brushes (Figure 5-4). In particular, the cross-section analysis shows that the height of the magnetic nanocylinders ( $h = 1.4 \pm 0.3$  nm for the magnetic nanocylinder MC2) is very close to that of the corresponding pure polymer brushes, indicative of the very small size of the fabricated iron oxide nanoparticles which did not change the size of the polymer template remarkably. From the cross-section analysis, one can conclude that the single iron oxide nanoparticle must be smaller than 1.7 nm (in diameter), which is the maximum height of the hybrid nanocylinder.

Consistent with the SFM observations, TEM images of as-prepared hybrid magnetic nanocylinders show wire-like objects with smooth contour, in contrast to the “pearl necklace” structure of the polychelates. As shown in Figure 5-5, the dark wire-like objects with diameter of about 6 nm correspond to the assemblies of tiny magnetic nanoparticles whose diameter is smaller than 1.7 nm (as observed in SFM images). It has to be noted that the wire-like objects observed in TEM images are not perfect cylinders with circular cross-

section, but rather collapsed cylinders due to a strong deformation of the soft polymer brushes on the substrate.<sup>34</sup> As reported previously, polycrystalline particles rather than single crystalline particles were produced within the polymer brushes.<sup>29</sup>

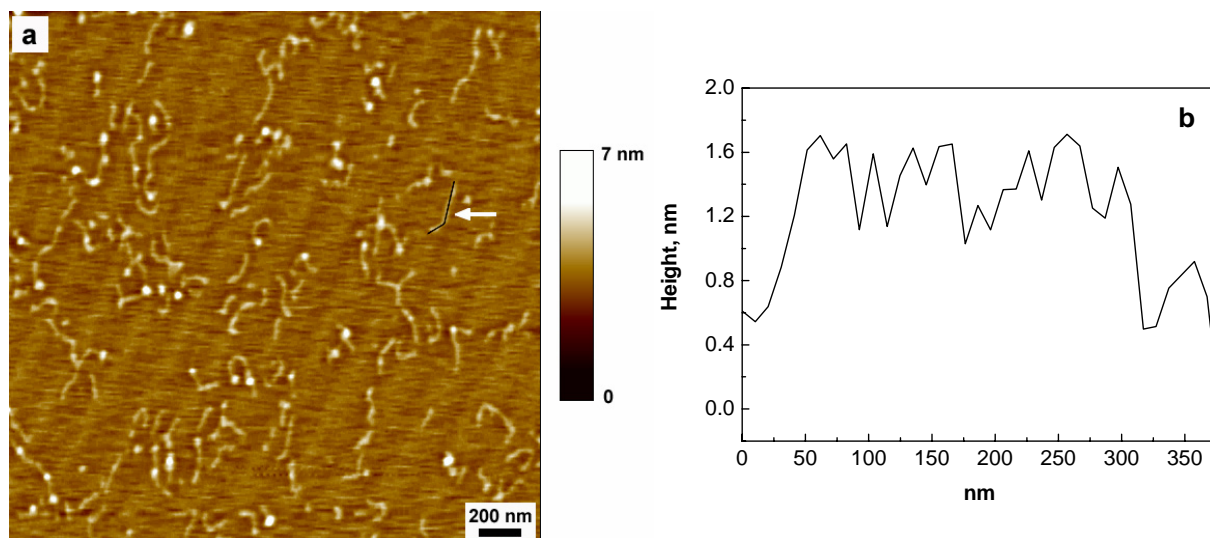


**Figure 5-4.** Tapping-Mode SFM image of the magnetic nanocylinder MC2 (hybrid of Brush 1 and magnetic iron oxide particles): (a) height image; (b) cross-section of one cylindrical polymer brush molecule indicated by an arrow in the height image (along the black line).

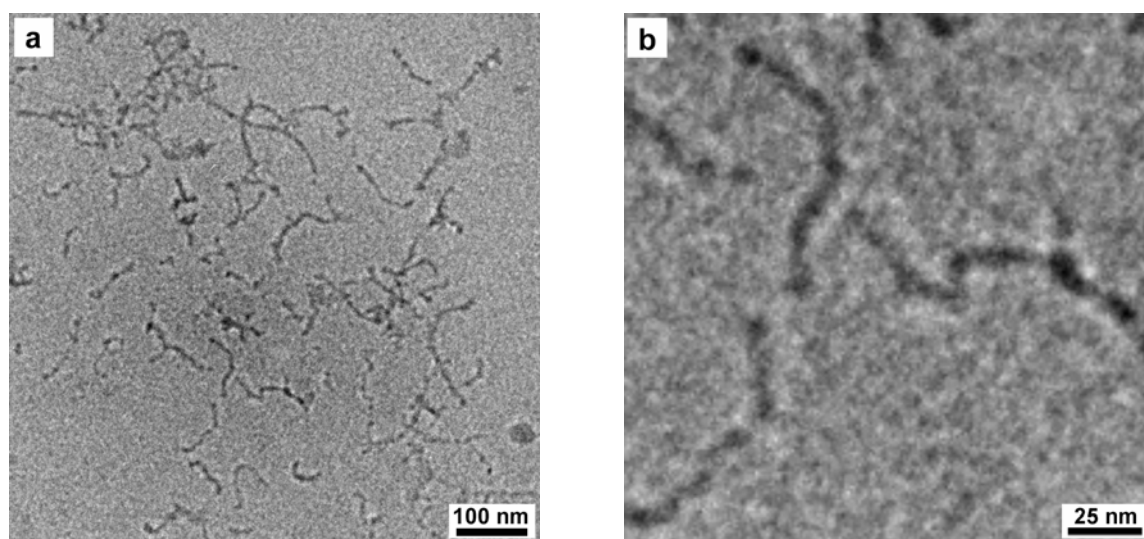


**Figure 5-5.** Non-stained TEM image of the hybrid magnetic nanocylinder MC2.

Dynamic light scattering (DLS) measurements were carried out to investigate the size change of polymer brushes in solution upon iron oxide particle formation. Figure 5-6 shows a comparison of the hydrodynamic radii between the magnetic nanocylinder MC2 and the corresponding polymer brush (Brush 1). One can observe a slight increase (ca. 9%) of the hydrodynamic radius of the polymer brush after the formation of iron oxide particles. This might be due to one or a combination of the following reasons: (1) the influence of the encapsulated iron oxide nanoparticles within the polymer core; (2) the repulsion between the side chains with negatively charged core block (poly (sodium acrylate)); or (3) the fractionation during the removal of uncoordinated iron ions by ultracentrifugation and precipitation, since during purification short brushes with higher solubility may stay in the supernatant rather than precipitate. Nevertheless, the formation of iron oxide particles did not change the size of the polymer brush significantly, in agreement with the observations from SFM measurements.

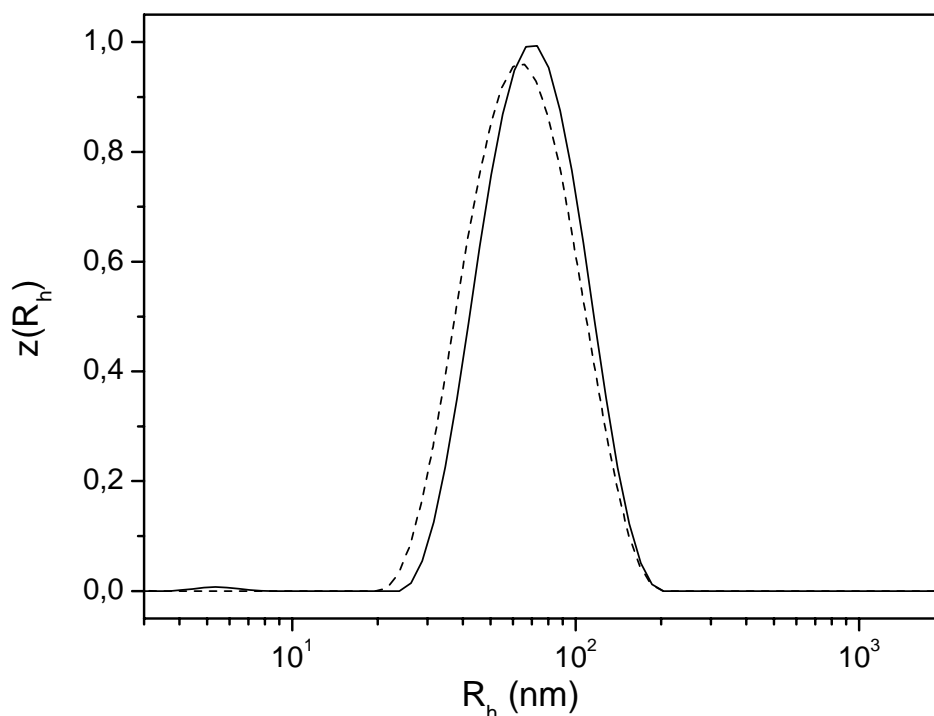


**Figure 5-6.** Hydrodynamic radius distribution of Brush 1 (dash line) and magnetic nanocylinder MC2 (solid line), in a mixture of methanol and chloroform (volume ratio = 1/1) at a scattering angle of  $90^\circ$ . The apparent  $z$ -average hydrodynamic radii of Brush 1 and MC2 at this scattering angle are 64.0 nm and 69.9 nm respectively.

The procedure of the polymer brush-directed formation of iron oxide nanoparticles was also monitored by UV/visible spectroscopy, as shown in Figure 5-7. The polychelate of Brush 1 and  $\text{Fe}^{3+}$  ion has an absorption edge of about 425 nm, with a distinct shoulder at around 350 nm which corresponds to the broad absorption peak of  $\text{FeCl}_3$  at this position. Since the pure polymer brush has almost no absorption in the observation wavelength range,<sup>40</sup> the absorbance of the polychelate can be attributed exclusively to the coordinated  $\text{Fe}^{3+}$  ions. After the formation of iron oxide particles, the absorption shoulder at 350 nm disappears. Compared to the polychelate, the absorption edge of the magnetic nanocylinder MC2 is slightly shifted toward longer wavelengths. This observation agrees well with that reported by Cohen et al. in the investigation of block copolymer films containing superparamagnetic iron oxide nanoclusters.<sup>42</sup>

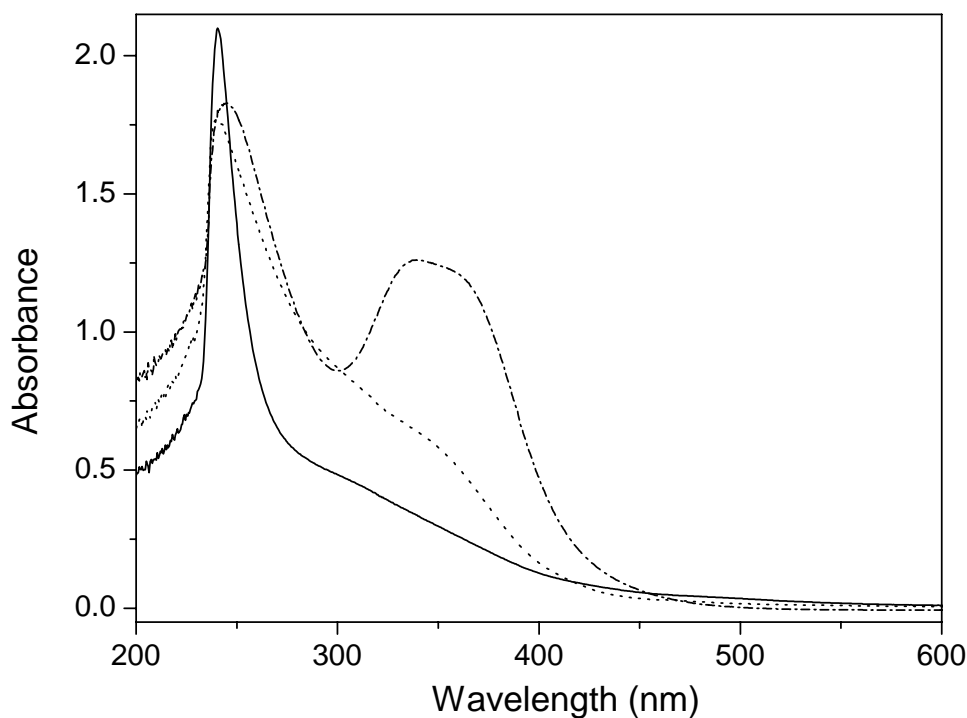


**Figure 5-7.** UV/visible spectra of  $\text{FeCl}_3$  (dash dot line, about 0.04 g/L), polychelate of Brush 1 with  $\text{Fe}^{3+}$  ion (dot line, about 0.2 g/L) and magnetic nanocylinder MC2 (solid line, about 0.1 g/L) in a mixture of methanol and chloroform. Pure solvent was measured and subtracted from the spectra of the samples.

To determine the content of iron oxide particles in the hybrid magnetic nanocylinders, thermal gravimetric analysis (TGA) measurements were performed, as shown in Figure 5-8.

When the samples were heated up to 1000 °C under air flow and kept at this temperature for half an hour, the organic templates should be completely burned away. TGA measurements of pure Brushes 1 and 2 showed that the residual masses after burning were less than 1 wt.% of the original masses (0.87 wt.% for Brush 1 and 0.74 wt.% for Brush 2). Since a large excess of NaOH was used to form  $\text{Fe}(\text{OH})_2$ , polymer brushes should be fully neutralized after the particle formation. TGA measurements of neutralized polymer brushes showed large increase in residual mass, because some inorganic materials, probably sodium oxide,<sup>43,44</sup> formed from the poly(sodium acrylate) core of polymer brushes. After the subtraction of the contribution from neutralized polymer brushes, the contents of iron oxide particle in hybrid magnetic nanocylinders can be obtained from the residual masses in TGA. Table 5-3 summarizes the TGA results.

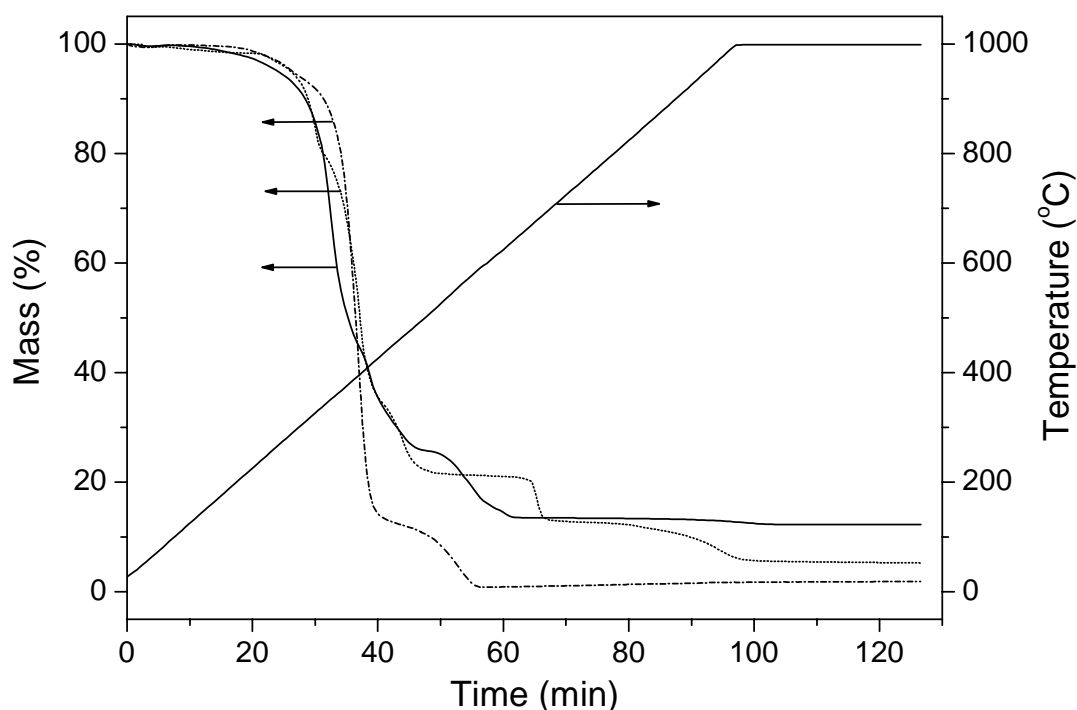


**Figure 5-8.** TGA analysis of Brush 1 (dash dot line), neutralized Brush 1 (dot line) and magnetic nanocylinder MC2 (solid line). The measurements were carried out under air flow of 55-60 mL/min.

Comparison of the iron oxide contents between the magnetic nanocylinders MC1 and MC2 shows that the conversion of carboxylic acid to sodium carboxylate increased the loading capacity of the polymer core significantly (although  $\text{FeCl}_3$  rather than  $\text{FeCl}_2$  was used for MC2, experiments have shown that sodium carboxylate has similar loading

capacity for  $\text{FeCl}_2$  and  $\text{FeCl}_3^{35}$ ). In principle, the hybrid nanocylinders MC3 and MC4 should have the same iron oxide content provided that they contain the same form of iron oxide, since all the preparation conditions except oxidization agent were the same for these two magnetic nanocylinders. However, a small difference (about 0.86 wt.%) in the iron oxide content was observed between MC3 and MC4. This might be caused by the experimental error of TGA measurements, considering that about 6 mg of samples was used for these two measurements and 0.86 wt.% means only about 0.05 mg. No matter what form of iron oxide or iron hydroxyoxide formed within polymer brushes, the final product after TGA measurements should be haematite ( $\alpha\text{-Fe}_2\text{O}_3$ ), which is the most stable component at high temperature.<sup>45</sup>

**Table 5-3.** TGA analysis of magnetic nanocylinders

Code of magnetic nano-cylinder	Polymer <sup>a</sup>	Iron ion used	Theoretical max. amount of iron oxide, $m_{\text{th,io}}$ (wt%) <sup>b</sup>	Residual mass of neutralized brush, $m_{\text{r,nb}}$ (wt%)	Residual mass of magnetic nanocylinder, $m_{\text{r,mc}}$ (wt%)	Iron oxide content $m_{\text{exp,io}}$ (wt%) <sup>c</sup>
MC1	Brush 1	$\text{Fe}^{2+}$	9.07	5.28	8.77	3.68
MC2	Brush 1	$\text{Fe}^{3+}$	6.21	5.28	12.27	7.38
MC3	Brush 2	$\text{Fe}^{3+}$	9.35	8.05	16.67	9.37
MC4	Brush 2	$\text{Fe}^{3+}$	9.35	8.05	17.46	10.23

(a) Residual masses of pure Brushes 1 and 2 in TGA measurements are 0.87 wt.% and 0.74 wt.% respectively; (b) assuming formation of  $\text{Fe}_2\text{O}_3$  and complete neutralization of PAA core after the particle formation; and (c) iron oxide content  $m_{\text{exp,io}} = (m_{\text{r,mc}} - m_{\text{r,nb}}) / (1 - m_{\text{r,nb}})$ .

To identify the composition of the as-prepared magnetic iron oxide nanoparticles, Mössbauer analyses were carried out. The hyperfine interactions observed at  $^{57}\text{Fe}$  nuclei provide relevant information on structural and local magnetic properties, especially in the case of nanometer sized crystalline systems where the lack of long-distance range order prevents to get accurate characteristics from X-ray diffraction (XRD).

Zero-field  $^{57}\text{Fe}$  Mössbauer spectra were recorded at 300 K on the samples (MC1-4). The Mössbauer lines of the 300 K spectrum are well defined, but fairly asymmetrical. All the spectra show a unique quadrupolar doublet. The asymmetry of the spectra suggests that (i) the Fe sites have different atomic environments and/or (ii) the magnetic domains are

size-distributed. Figure 5-9 shows the room-temperature Mössbauer spectrum of the magnetic nanocylinder MC3.

For all the four hybrid nanocylinders, only doublets are observed, giving a first indication that all the samples are superparamagnetic at room temperature. This is due to the rapid spin relaxation for superparamagnetic particles - otherwise for ferrimagnetic particles sextets should be observed. The values of the isomer shift of the quadrupole doublets are characteristic of  $\text{Fe}^{3+}$  and there is no evidence for the presence of any significant  $\text{Fe}^{2+}$  phase (see Table 5-4). For the magnetic nanocylinders MC2-4 the Mössbauer parameters are the almost same (IS is about 0.45 mm/s and QS is about 0.70 mm/s) and correspond to  $\text{Fe}^{3+}$  in octahedral environment. While for the magnetic nanocylinder MC1 the parameters seem to indicate that the  $\text{Fe}^{3+}$  is in tetrahedral environment (IS is about 0.33 mm/s and QS is about 0.52 mm/s, lower than those of MC2-4). It has to be noted that the Mössbauer spectrum of MC1 is noisy due to the limited amount of sample available for the measurement. From the Mössbauer results the existence of magnetite ( $\text{Fe}_3\text{O}_4$ ) in hybrid magnetic nanocylinders can be ruled out, and the possible form of the magnetic nanoparticles might be maghemite ( $\gamma\text{-Fe}_2\text{O}_3$ ) or goethite ( $\alpha\text{-FeO(OH)}$ ). It is reported that the alkaline oxidation of ferrous ions often produces maghemite.<sup>16,22,23</sup>

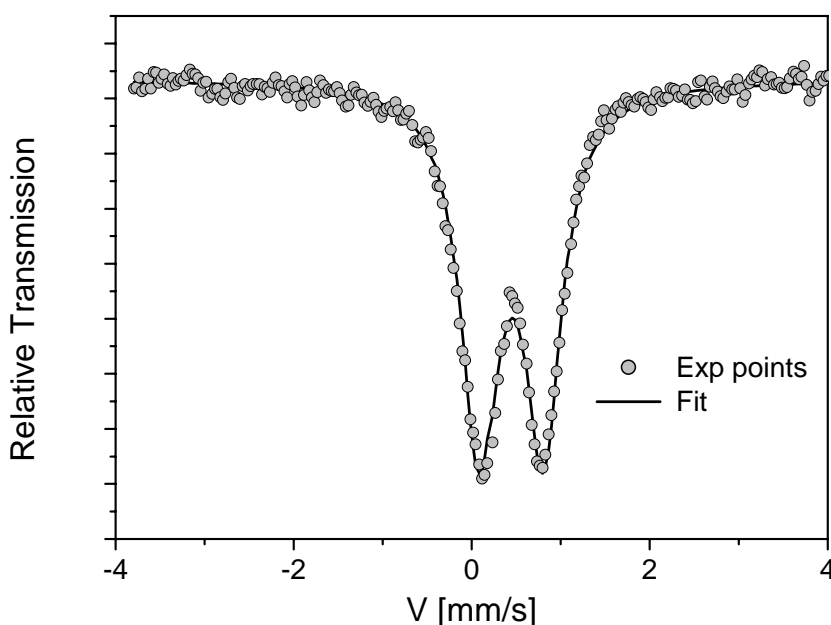


**Figure 5-9.** Mössbauer spectrum of the magnetic nanocylinder MC3 at 300 K.

### 5.3.2 Magnetic properties of the hybrid nanocylinders

Magnetic properties of hybrid nanocylinders were studied using a superconducting quantum interference device (SQUID) magnetometer at temperatures ranging from 2 K to 295 K. Figure 5-10 shows the magnetization curves of the hybrid nanocylinder MC1, which was synthesized using  $\text{FeCl}_2$  as precursor. Due to the very small particle size, we expect that the particles should behave superparamagnetically at room temperature, which means that they are easily magnetized but do not retain their magnetization once the field is removed. As shown in Figure 5-10 the fabricated nanoparticles in MC1 are superparamagnetic at 295 K as expected, since no hysteresis was observed (both remanence and coercivity are zero). Only at very low temperature such as 2 K, SQUID measurement showed a symmetric hysteresis loop with a coercivity of 640 Oe and a remanence of 0.12 emu/g, and in this case the particles are in the blocked state (ferrimagnetic). Additionally, the magnetization at room temperature was low (0.30 emu per gram of the hybrid or 8.15 emu per gram of iron oxide at 50 kOe) and was not saturated at 50 kOe. With decreasing temperature the magnetization increased and reached about 1.07 emu per gram of the hybrid (29.08 emu per gram of iron oxide) at 50 kOe. The low magnetization and lack of magnetic saturation result from the quantum-size effects in ultrasmall nanoparticles.<sup>46</sup>

Starting from  $\text{FeCl}_3$ , superparamagnetic nanoparticles were also produced within the polymer brushes, as indicated by the SQUID measurements. The as-prepared magnetic nanocylinders, MC2-4, showed very similar magnetic behavior to that of MC1. As an example, the magnetization curves of MC3 at various temperatures are shown in Figure 5-11. It is superparamagnetic at temperatures above 25 K, and ferrimagnetic at very low temperature (2 K). Consequently the blocking temperature ( $T_b$ ), defined as the temperature above which the particles are free to align with the magnetic field during the measurement time and thus behave superparamagnetically, of the particles must be between 2 K and 25 K. Below the blocking temperature the magnetic moment of the particles is fixed, i.e., their approach to thermodynamic equilibrium is blocked, thus a hysteresis appears.

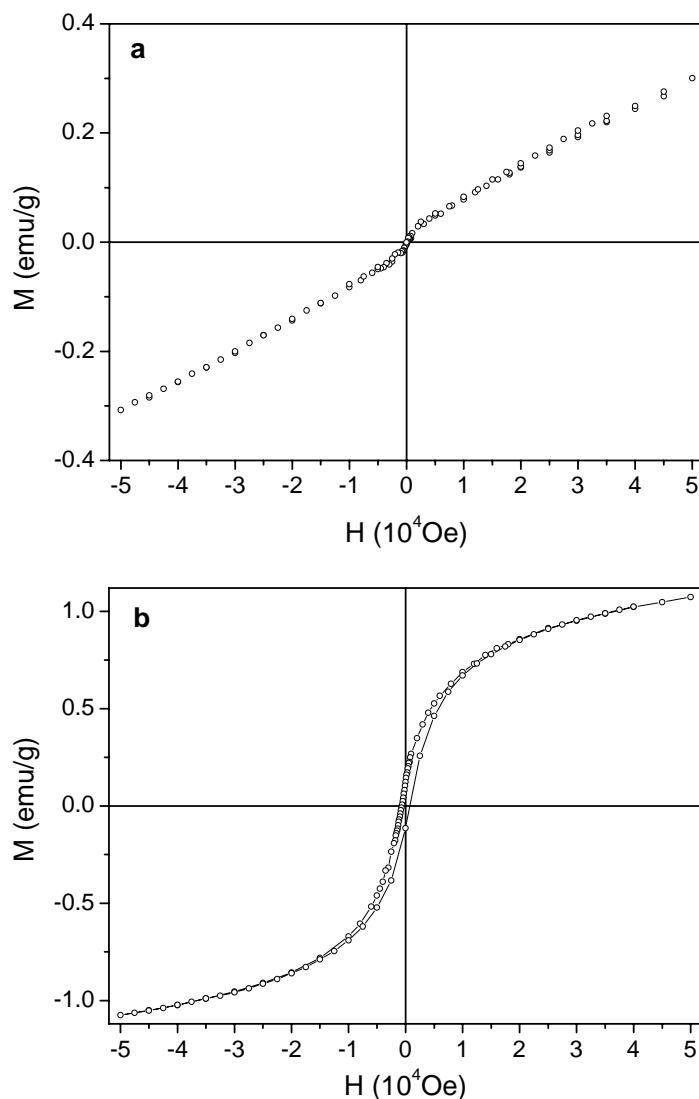


**Figure 5-10.** Magnetization curves for the hybrid nanocylinder MC1 at (a) 295 K and (b) 2 K.

The experimental criteria for superparamagnetism include not only that (i) the magnetization curve exhibits no hysteresis but also that (ii) the magnetization curves at different temperatures should superpose in a plot of  $M$  versus  $H/T$ .<sup>6,47</sup> As shown in Figure 5-11c, data of  $M$  versus  $H/T$  for MC3 at 295 K and 100 K superpose perfectly, and only at 25 K a small deviation is observed. This imperfect  $H/T$  superposition may be due to the changes in spontaneous magnetization of particles as a function of temperature, anisotropy effects, inter-particle dipolar interactions, or a broad size distribution. It will be shown below that the size effect can be ruled out.<sup>47</sup>

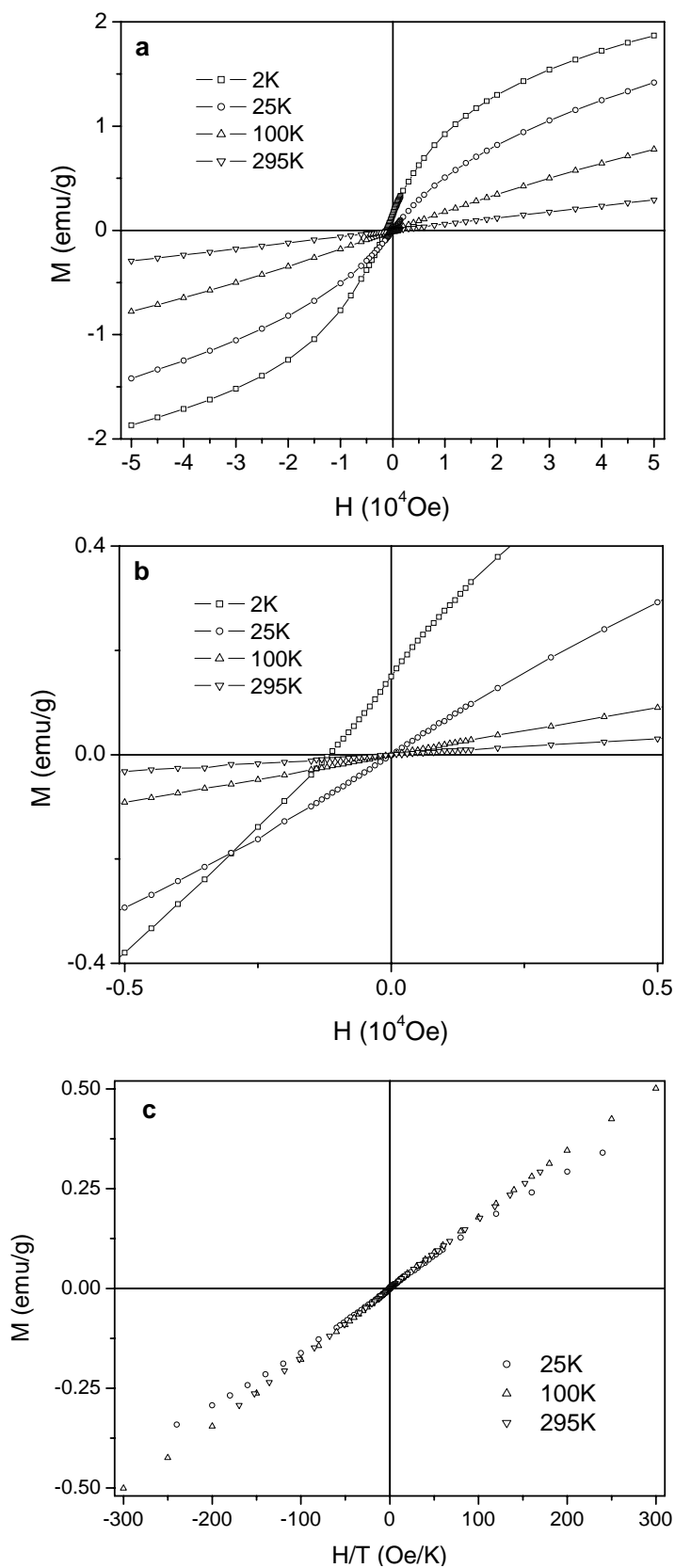


**Figure 5-11.** (a) Magnetization curves for the hybrid nanocylinder MC3 at different temperatures; (b) magnification of the central part of plot shown in (a); and (c) curves of  $M$  vs.  $H/T$ .

It has been reported that the conversion of  $\text{Fe}(\text{OH})_2$  to  $\gamma\text{-Fe}_2\text{O}_3$  is accelerated by heating or addition of  $\text{H}_2\text{O}_2$  and may take place through intermediates such as  $\text{FeO}(\text{OH})$  and  $\text{Fe}_3\text{O}_4$ .<sup>16,48</sup> Heating was not applied here because this may induce the hydrolysis of polymers in strong basic medium. In our case, except for the magnetic nanocylinder MC4, a mild oxidation agent,  $\text{O}_2$  (in air), was used because of the easy oxidation of the fabricated tiny particles with large surface. We observed that both  $\text{O}_2$  and  $\text{H}_2\text{O}_2$  induced instant color change from olive-green (the color of  $\text{Fe}(\text{OH})_2$ ) to reddish brown. SQUID measurements show similar curves for MC3 and MC4, which were produced using  $\text{O}_2$  and  $\text{H}_2\text{O}_2$  as oxidation agents respectively. Only the magnetization of the produced nanoparticles was slightly enhanced for oxidation with  $\text{H}_2\text{O}_2$ , as shown in Table 5-4. This agrees well with that reported by other groups.<sup>49</sup>

**Table 5-4.** Results from Mössbauer and SQUID measurements

Code of magnetic nanocylinder	Isomer shift (mm/s)	Quadrupole splitting (mm/s)	$M_{295\text{K}}$ at 50 kOe (emu/g) <sup>a</sup>	$M_{2\text{K}}$ at 50 kOe (emu/g) <sup>b</sup>	$M_r$ at 2K (emu/g) <sup>c</sup>	$H_c$ at 2K (Oe) <sup>d</sup>
MC1	0.33	0.52	0.30 <sup>e</sup> (8.15) <sup>f</sup>	1.07 <sup>e</sup> (29.08) <sup>f</sup>	0.12 <sup>e</sup> (3.26) <sup>f</sup>	640
MC2	0.45	0.72	0.20 (2.71)	2.29 (31.03)	0.07 (0.95)	370
MC3	0.44	0.70	0.29 (3.09)	1.87 (19.96)	0.15 (1.60)	1160
MC4	0.44	0.70	0.33 (3.22)	2.37 (23.17)	0.18 (1.76)	1000

(a) Magnetization at 295 K under an applied field of 50 kOe; (b) Magnetization at 2 K under an applied field of 50 kOe; (c) remnant magnetization at 2 K; (d) coercivity at 2K; (e) magnetization per gram of hybrid nanocylinder; and (f) magnetization per gram of iron oxide.

Figure 5-12 shows temperature-dependent magnetization plots of MC3 at 20 Oe for the zero-field-cooled (ZFC) and the field-cooled (FC) cases. The results are representative of the behavior of all the samples. At high temperature the two curves coincide and follows the Curie-Weiss law (linear relationship between  $M^1$  and  $T$ ), as shown in the inset of Figure 5-12a, while at low temperature they start to deviate from each other. Typically for superparamagnetic nanoparticles, the ZFC curve shows a maximum at low temperature

which is associated with the average blocking temperature of the particles. The maximum in the ZFC curve shifts toward lower temperatures as the particle size decreases. As shown in Figure 5-11b, a maximum at about 5 K was observed in the ZFC curve of MC3, indicative of an average blocking temperature of 5 K. Such a small blocking temperature indicates again the small particle size.

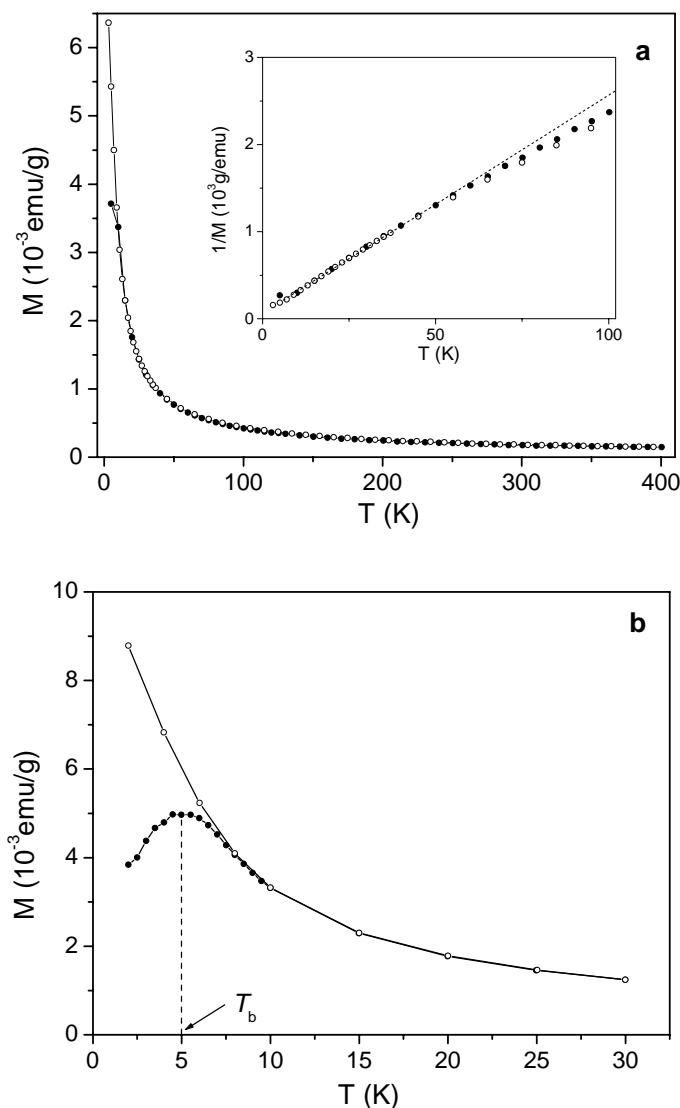


**Figure 5-12.** (a) ZFC (full circles) and FC (open circles) magnetization measured as a function of temperature (5–400 K for ZFC and 400–3 K for FC) for the hybrid nanocylinder MC3. The inset displays inverse magnetization as a function of temperature; and (b) refined ZFC and FC curves with the temperature ranging from 2 K to 30 K (aiming to determine the blocking temperature).

According to superparamagnetic theory,<sup>28,50</sup> the mean volume of spherical,  $V$ , can be determined from the blocking temperature based on the following relationship:

$$\tau_m = \tau_0 \exp\left(\frac{KV}{k_B T_b}\right) \quad \text{Eq. 5-1}$$

where  $\tau_m$  is the experimental measurement time (100 s for the SQUID measurement),  $\tau_0$  is the time constant characteristic for the material,  $K$  is the anisotropy constant, and  $k_B$  is the Boltzmann constant. Provided that  $\gamma\text{-Fe}_2\text{O}_3$  nanoparticles were produced in our case, taking the  $K$  and  $\tau_0$  values of  $10^5 \text{ Jm}^{-3}$  and  $10^{-10} \text{ s}$  which are estimated and used by several groups,<sup>51,52</sup> the calculated average  $\gamma\text{-Fe}_2\text{O}_3$  particle size is about 1.7 nm in radius for  $T_b = 5 \text{ K}$ . Equation 1 is derived for isolated and non-interacting magnetic particles, and in our case inter-particle interaction may exist (as indicated by a deviation from linearity in the plot of  $M^1$  vs  $T$ , see Figure 5-12 a), nevertheless the above calculation still provide a clue of the small size of the magnetic nanoparticles encapsulated in polymer brushes.

Additionally, the collapse temperatures (i.e., the temperature where FC and ZFC curves deviate from each other) of all the four magnetic nanocylinders (MC1-MC4) are around 10 K. Such a low collapse temperature is a strong indication of a narrow size distribution of the particles within the matrix.<sup>46,52</sup>

## 5.4 Conclusions

In conclusion, magnetic iron oxide nanoparticles were successfully produced within the well-defined polymer brushes with PAA core and PnBA shell via single molecule templating technique, as confirmed by various techniques such as SFM, TEM, and UV/visible spectroscopy. The SQUID measurements show that the hybrid nanocylinders are superparamagnetic at room temperature. The polymer shell provides not only the stability of the nanoparticles but also the solubility of the hybrid nanocylinders.

The amount and size of the fabricated magnetic particles are controlled by the limited number of coordinated iron ions inside the polymer core. After the formation of the magnetic nanoparticles, the carboxylate coordination sites within polymer brushes are freed and ready for further coordination with more iron ions, thus it is possible to increase the amount and/or size particle of the particles by multi-cycles of iron ion loading and particle formation.

A polycrystalline sample with no preferred grain orientation has no net crystal anisotropy due to averaging over all orientations. However, a nonspherical polycrystalline specimen can possess shape anisotropy. A cylindrical sample, for example, is easier to magnetize along the long direction than along the short directions.<sup>28</sup> The investigations of the orientation of these hybrid superparamagnetic nanocylinder under a magnetic field and the related magneto-rheological behavior and birefringence are undergoing and the results will be published elsewhere.

The as-prepared hybrid nanocylinders combine of the promising properties of polymers and superparamagnetic nanoparticles and may find potential applications such as in ferrofluids.

**Acknowledgment.** This work was supported by Deutsche Forschungsgemeinschaft. The authors thank Dr. Markus Drechsler for the TEM measurements and James Lai (Polytechnic University, New York) for the assistance in SQUID measurements.

## References

- (1) Huczko, A. *Appl. Phys. A: Mater. Sci. Proc.* **2000**, *70*, 365-376.
- (2) Xia, Y.; Yang, P.; Sun, Y.; Wu, Y.; Mayers, B.; Gates, B.; Yin, Y.; Kim, F.; Yan, H. *Adv. Mater.* **2003**, *15*, 353-389.
- (3) Siegel, R. W. *Mater. Sci. Eng., B: Solid-State Mater. Adv. Technol.* **1993**, *B19*, 37-43.
- (4) Gleiter, H. *Prog. Mater. Sci.* **1989**, *33*, 223-315.
- (5) Suryanarayana, C. *Int. Mater. Rev.* **1995**, *40*, 41-64.
- (6) Bean, C. P.; Livingston, J. D. *J. Appl. Phys.* **1959**, *30*, 120S-129S.
- (7) Tejada, J.; Ziolo, R. F.; Zhang, X. X. *Chem. Mater.* **1996**, *8*, 1784-1792.
- (8) Audran, R. G.; Huguenard, A. P.: GB 1590501, **1981**.
- (9) Ziolo, R. F.: US 4474866, **1984**.
- (10) Nixon, L.; Koval, C. A.; Noble, R. D.; Slaff, G. S. *Chem. Mater.* **1992**, *4*, 117-121.
- (11) Sutor, J. J. In *PCT Int. Appl.*: WO 9637313, **1996**.
- (12) Müller-Schulte, D.; Brunner, H. *J. Chromatogr., A* **1995**, *711*, 53-60.
- (13) McMichael, R. D.; Shull, R. D.; Swartzendruber, L. J.; Bennett, L. H.; Watson, R. E. *J. Magn. Magn. Mater.* **1992**, *111*, 29-33.
- (14) Anton, I.; De Sabata, I.; Vekas, L. *J. Magn. Magn. Mater.* **1990**, *85*, 219-226.
- (15) Odenbach, S. *Adv. Colloid Interface Sci.* **1993**, *46*, 263-282.
- (16) Ziolo, R. F.; Giannelis, E. P.; Weinstein, B. A.; O'Horo, M. P.; Ganguly, B. N.; Mehrotra, V.; Russell, M. W.; Huffman, D. R. *Science* **1992**, *257*, 219-223.
- (17) Winnik, F. M.; Morneau, A.; Mika, A. M.; Childs, R. F.; Roig, A.; Molins, E.; Ziolo, R. F. *Can. J. Chem.* **1998**, *76*, 10-17.
- (18) Ciebien, J. F.; Clay, R. T.; Sohn, B. H.; Cohen, R. E. *New J. Chem.* **1998**, *22*, 685-691.
- (19) Möller, M.; Spatz, J. P.; Roescher, A. *Adv. Mater.* **1996**, *8*, 337.
- (20) Förster, S.; Antonietti, M. *Adv. Mater.* **1998**, *10*, 195-217.
- (21) Winnik, F. M.; Morneau, A.; Ziolo, R. F.; Stoeber, H. D. H.; Li, W.-H. *Langmuir* **1995**, *11*, 3660-3666.
- (22) Kroll, E.; Winnik, F. M.; Ziolo, R. F. *Chem. Mater.* **1996**, *8*, 1594-1596.
- (23) Underhill, R. S.; Liu, G. *Chem. Mater.* **2000**, *12*, 2082-2091.
- (24) Yan, X.; Liu, G.; Liu, F.; Tang, B. Z.; Peng, H.; Pakhomov, A. B.; Wong, C. Y. *Angew. Chem. Int. Ed.* **2001**, *40*, 3593-3596.

- (25) Crooks, R. M.; Lemon, B. I., III; Sun, L.; Yeung, L. K.; Zhao, M. *Top. Curr. Chem.* **2001**, *212*, 81-135.
- (26) Braun, E.; Eichen, Y.; Sivan, U.; Ben-Yoseph, G. *Nature* **1998**, *391*, 775-778.
- (27) Djalali, R.; Li, S. Y.; Schmidt, M. *Macromolecules* **2002**, *35*, 4282-4288.
- (28) Leslie-Pelecky, D. L.; Rieke, R. D. *Chem. Mater.* **1996**, *8*, 1770-1783.
- (29) Zhang, M.; Drechsler, M.; Müller, A. H. E. *Chem. Mater.* **2004**, *16*, 537-543.
- (30) Blakemore, R. *Science* **1975**, *190*, 377-379.
- (31) Frankel, R. B. *Annu. Rev. Biophys. Bioeng.* **1984**, *13*, 85-103.
- (32) Zubarev, A. Y.; Odenbach, S.; Fleischer, J. *J. Magn. Magn. Mater.* **2002**, *252*, 241-243.
- (33) McTague, J. P. *J. Chem. Phys.* **1969**, *51*, 133-136.
- (34) Zhang, M.; Breiner, T.; Mori, H.; Müller, A. H. E. *Polymer* **2003**, *44*, 1449-1458.
- (35) Clay, R. T.; Cohen, R. E. *Supramol. Sci.* **1998**, *5*, 41-48.
- (36) Provencher, S. W. *Computer Phys. Commun.* **1982**, *27*, 229.
- (37) Teillet, J.; Varret, F., MOSFIT Program, unpublished.
- (38) Mercier, J. P. *Industrie Chimique Belge* **1965**, *30*, 813-819.
- (39) Wiley, R. H.; Brauer, G. M. *J. Polym. Sci.* **1948**, *3*, 647-651.
- (40) Zhang, M.; Teissier, P.; Krekhova, M.; Cabuil, V.; Müller, A. H. E. *Prog. Colloid Polym. Sci.* **2004**, *in press*.
- (41) Anagnostopoulos, A.; Nicholls, D.; Reed, J. *Inorganica Chimica Acta* **1979**, *32*, L17-L18.
- (42) Sohn, B. H.; Cohen, R. E. *Chem. Mater.* **1997**, *9*, 264-269.
- (43) McNeill, I. C.; Sadeghi, S. M. T. *Polymer Degradation and Stability* **1990**, *30*, 213-230.
- (44) Budavari, S.; Editor. *The Merck Index* **1989**, *11th Edition*, 1359.
- (45) Cornell, R. M.; Schwertmann, U.; Editors. *The iron oxides: structure, properties, reactions, occurrence and uses* **1996**, 349.
- (46) Sohn, B. H.; Cohen, R. E.; Papaefthymiou, G. C. *J. Magn. Magn. Mater.* **1998**, *182*, 216-224.
- (47) Diandra L. Leslie-Pelecky, R. D. R. *Chem. Mater.* **1996**, *8*, 1770-1783.
- (48) Craik, D. J.; Ed. *Magnetic Oxides* **1975**, 697, Wiley, New York.
- (49) Raymond, L.; Revol, J. F.; Ryan, D. H.; Marchessault, R. H. *J. Appl. Polym. Sci.* **1996**, *59*, 1073-1086.

- (50) Aharoni, A. *Relaxation processes in small particles* **1992**, North Holland, Amsterdam.
- (51) Ennas, G.; Musinu, A.; Piccaluga, G.; Zedda, D.; Gatteschi, D.; Sangregorio, C.; Stanger, J. L.; Concas, G.; Spano, G. *Chem. Mater.* **1998**, *10*, 495-502.
- (52) Garcia, C.; Zhang, Y.; DiSalvo, F.; Wiesner, U. *Angew. Chem. Int. Ed.* **2003**, *42*, 1526-1530.

## Chapter 6

### Template-controlled synthesis of wire-like cadmium sulfide nanoparticle assembly within core-shell cylindrical polymer brushes \*

#### Abstract

A control fabrication of wire-like assemblies of cadmium sulfide (CdS) nanoparticles has been developed based on a template technique. Well-defined amphiphilic core-shell cylindrical polymer brushes were used as single molecule templates, utilizing the coordination of cadmium ions with carboxylate groups in the core of the brush. Formation of CdS nanoparticles inside the polymer brush was carried out via the reaction of the coordinated  $\text{Cd}^{2+}$  ions with  $\text{H}_2\text{S}$ . This route resulted in wire-like CdS nanoparticle assemblies of about 4-5 nm in diameter and about 170 nm long. After the formation of the CdS nanoparticles, the polymer brush resumes its original chemical structure and morphology and therefore can be used as template again. The obtained polymer-semiconductor nanocomposite is soluble and stable in organic solvents, and potential applications may be found due to the quasi-1D structure of the assembly of the CdS nanoparticles. In principle, the present synthetic approach is of general applicability to various metals and oxides.

\* The results of this chapter has been published in Mingfu Zhang, Markus Drechsler, Axel H. E. Müller *Chemistry of Materials*, **2004**, 16, 537-543.

## 6.1 Introduction

The synthesis and study of inorganic nanoparticles has become a major interdisciplinary research area in recent years,<sup>1-5</sup> resulting from their numerous applications in various areas. Particularly, research on semiconductor nanoparticles with size-dependent optical and electronic properties is motivated by potential uses in the fields of nonlinear optics,<sup>6,7</sup> light-emitting devices,<sup>8</sup> solar cells,<sup>9</sup> biological labels,<sup>10,11</sup> electronics,<sup>12,13</sup> and catalysis,<sup>14</sup> among others.<sup>4</sup> When the particles approach a size of a few nanometers, its diameter is comparable to or less than that of the bulk semiconductor exciton (the exciton diameter of cadmium sulfide is 5-6 nm<sup>15</sup>), such that quantum confinement of electron-hole pairs increases the band gap relative to that in the bulk materials. Therefore the control of particle size allows tuning the band gap to give the desired electronic and optical properties. Research has led to the fabrication of a number of devices.

Many synthetic methods for the preparation of inorganic nanoparticles have been reported, including controlled precipitation in solution and confined synthesis in structured templates.<sup>3,4</sup> Template-directed synthesis represents a straightforward route to nanoparticles. In this approach nanoparticles are generated in situ with the morphology complementary to that of the template. A number of templates have been used, including hard solid templates such as zeolites,<sup>16</sup> glasses,<sup>17</sup> layered solids,<sup>18</sup> molecular sieves,<sup>19,20</sup> alumina membranes<sup>5</sup> and self-organized media such as micelles (of surfactants and block copolymers)<sup>21-28</sup> and vesicles<sup>29-31</sup>. In the case of hard solid templates, the fabricated nanoparticles are embedded inside the matrix and thus it is hard to remove the templates after the synthesis. It is also difficult for the further processing of the nanoparticles. In contrast, templates such as micelles and vesicles can produce and stabilize dispersed nanoparticles which simplifies postprocessing. Ordered (such as hexagonal) arrays of nanoparticles have been obtained via a polymeric micellar route, and the templates can be removed completely by oxygen plasma.<sup>27,32</sup> However, the instability of these templates limits their potential applications. Once the templates decompose under harsh conditions (such as elevated temperatures or change of solvent), the nanoparticles will lose their stabilization layer and may undergo aggregation.

Recently, fabrication of inorganic nanoparticles in solid polymer matrixes has attracted more and more attention,<sup>33-40</sup> because the combination of inorganic nanoparticle and polymer provides a simple route to stable and processable materials integrating the promising properties of both components. However normally these composites cannot be

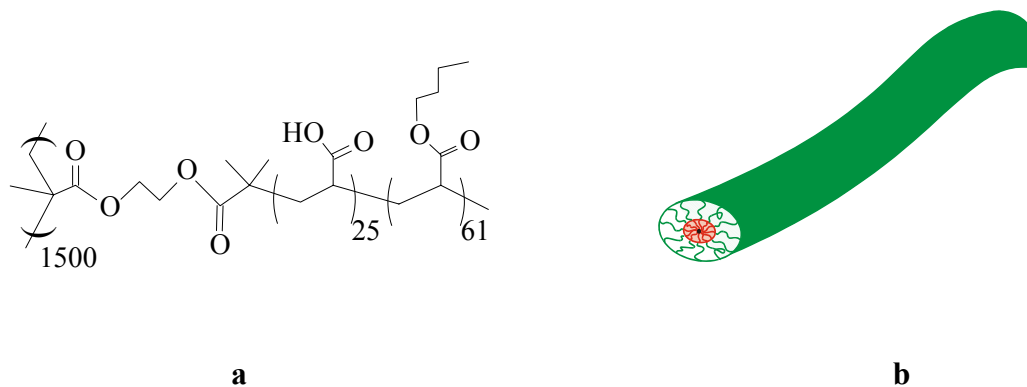
redissolved while preserving the colloidal state of nanoparticles. Among polymeric templates, the single polymer molecule represents an important type, because isolated nanocomposites based on single molecules can be obtained, which have very desirable processing characteristics. Dendrimers,<sup>41</sup> DNA<sup>42,43</sup>, and polyelectrolytes<sup>44</sup> have been used as single molecule templates for inorganic nanoparticle synthesis. Basically, all the applications based on single polymer molecule can be applied to the single molecule-nanoparticle composite as well. For example, a single DNA molecule was used as a template for the growth of a conductive silver nanowire, which was used as a nanocircuit to connect macroscopic electrodes.<sup>42</sup>

Very recently, Schmidt et al. succeeded in synthesis of gold nanoclusters and nanowires using polymer brushes with poly(2-vinylpyridine) core and polystyrene shell as templates.<sup>47</sup> However, the length distribution of those brushes was broad because they were synthesized via conventional radical polymerization of block macromonomers. Thus, control of the length of fabricated nanowires could not be achieved.

In this paper we describe the use of a amphiphilic core-shell cylindrical polymer brush with poly(acrylic acid) (PAA) core and poly(*n*-butyl acrylate) (P*n*BA) shell as template for the synthesis of wire-like assemblies of cadmium sulfide (CdS) nanoparticles. The structure of the polymer brush is shown in Scheme 6-1. It is well-defined both in length and diameter. Obviously this amphiphilic core-shell polymer brush can be regarded as a unimolecular cylindrical micelle, thus it has the advantages of both micellar templates and single molecular templates. Compared to block copolymer micelles, it has a much better stability against the change of exterior environment, because one end of the side chain is linked to the backbone of the polymer brush via strong covalent bond. Moreover, the shell of the polymer brush protects the fabricated nanoparticles from aggregation, which cannot be achieved by other single molecule wire-like templates such as polyelectrolyte and DNA.

In our method, the amphiphilic polymer brush acts as both a nanoreactor for the formation of CdS nanoparticles and a template to direct the distribution of nanoparticles inside the polymer. The core of the polymer brush carries carboxylate groups (after neutralization of PAA) capable of coordinating with Cd<sup>2+</sup> ions. The coordinated Cd<sup>2+</sup> ions were subsequently sulfidized to form a string of nanoparticles along the backbone of the polymer brush. Both chains of separated nanoclusters and continuous nanowires could be obtained, which are of equal interest.<sup>43</sup> The hydrophobic shell of the polymer brush offers

the solubility of the final composite in organic solvents, in addition to the stabilization of nanoparticles.



**Scheme 6-1.** (a) Chemical structural formula of the polymer brush used in the present paper,  $[AA_{25-n}BA_{61}]_{1500}$ ; and (b) its schematic 3-D structure.

The combination of precise size control, solubility, stability and easy processing makes the cylindrical polymer brush a unique template for the preparation of wire-like assemblies of semiconductor nanoparticles.

## 6.2 Experimental Section

All chemicals were of analytical grade and used as received without further purifications. The synthesis of polymer brushes was reported earlier.<sup>45,46</sup> The degree of polymerization (DP) of the backbone was determined by membrane osmometry and the DP of side chains was calculated from monomer conversion of polymerization.

The synthesis of CdS nanoparticles inside the core-shell polymer brushes proceeded as follows. First 29.7 mg of the polymer brush, [AA<sub>25-n</sub>BA<sub>61</sub>]<sub>1500</sub> (containing 0.077 mmol of acrylic acid), was dissolved in 20 mL of a mixture of methanol and chloroform (v/v = 1/1). Then 75  $\mu$ L of 1.0 M NaOH aqueous solution was added to neutralize the polymer core. After stirring for 6 h, 0.042 mmol of CdAc<sub>2</sub>·2H<sub>2</sub>O (0.133 M solution in methanol) was added and the reaction mixture was stirred overnight. A transparent solution was obtained.

To remove the uncoordinated Cd<sup>2+</sup> ions, dialysis was tried first. This was done in a mixture of methanol and chloroform (v/v = 1/1) using regenerated cellulose membrane tube (molecular weight cutoff = 6–8000). The solvent was changed every three days. After 20 days of dialysis, free Cd<sup>2+</sup> salt was still observed via scanning force microscopy (SFM), indicating that dialysis is a very slow process. To remove the residual free Cd<sup>2+</sup>, precipitation was carried out by addition of water. The precipitate was washed with methanol twice, and finally redissolved in 30 mL of methanol/chloroform (v/v = 1/1). The turbid dispersion of the polychelate of the polymer brush and Cd<sup>2+</sup> ions was stable in this solvent for several hours without appreciable precipitation, however, most polychelates settled to the bottom one day later. The supernatant was used to check the purity of the polychelate, and no free Cd<sup>2+</sup> salt was observed by SFM.

The turbid dispersion of the polychelate was bubbled with N<sub>2</sub> for 1 h to remove the oxygen, and then H<sub>2</sub>S was introduced under N<sub>2</sub> atmosphere. The color of the dispersion turned yellow instantly, indicating the formation of CdS. An optically clear solution was finally obtained, which was bubbled with N<sub>2</sub> for 3 h. The yellow solution was stable over several months.

Scanning force microscopy (SFM) images were recorded on a Digital Instruments Dimension 3100 microscope operated in Tapping Mode. The samples were prepared by dip-coating from dilute solutions of the polymer brush, polychelate (supernatant) and hybrid of the polymer brush and CdS nanoparticles in CHCl<sub>3</sub>/CH<sub>3</sub>OH (v/v = 1/1) onto freshly cleaved mica.

Transmission electron microscopy (TEM) images were taken on a LEO 922 OMEGA electron microscope operated at 200 kV (Figures 6-2a and b, and 3b-d), or a Zeiss CEM 902 electron microscope operated at 80 kV (Figure 6-3a). A 5- $\mu$ L droplet of a dilute solution, with the concentration similar to that for SFM samples, was dropped onto a copper grid (300 mesh) coated with a carbon or Formvar/carbon film, followed by drying at room temperature. The same sample was also used for electron diffraction (ED) measurements, which were carried out on a Philips CM 20 TEM operated at 200 kV. Energy-dispersive X-ray (EDX) analysis was performed on a LEO 1530 field emission scanning electron microscope using an X-ray detector. The samples were obtained by applying a drop of a dilute solution onto a silicon wafer followed by drying at room temperature.

UV/visible absorbance spectra of samples in methanol/chloroform (v/v = 1/1) were recorded on a Perkin-Elmer Lambda 15 UV/visible spectrophotometer. The spectrum from a quartz cuvette containing solvent was subtracted from all sample spectra.

## 6.2 Results and Discussion

Advances in living polymerizations enable us to synthesize polymers with well-defined structures and sizes. An amphiphilic cylindrical polymer brush with hydrophilic poly(acrylic acid) (PAA) core and hydrophobic poly(*n*-butyl acrylate) (*PnBA*) shell, used as the template in this paper, was synthesized via combination of anionic polymerization and atom transfer radical polymerization (ATRP), as reported in our previous paper.<sup>48</sup> A brief description of the polymer synthesis is given as follows. The backbone of the polymer brush, poly(2-hydroxyethyl methacrylate) (PHEMA), was synthesized via anionic polymerization of the silyl-protected monomer (2-(trimethylsilyloxy)ethyl methacrylate) followed by the cleavage of the protecting trimethylsilyloxy groups. Through esterification of the all pendant hydroxy groups of PHEMA with  $\alpha$ -bromoisobutyryl bromide, ATRP initiating groups were attached to the backbone. Sequential ATRP of *t*-butyl acrylate (*tBA*) and *n*-butyl acrylate (*nBA*) initiated by the pendant  $\alpha$ -bromoester groups on the backbone formed the block copolymer (*PtBA-b-PnBA*) side chains. Finally, the selective hydrolysis of the tert-butyl groups of the *PtBA* block resulted in the amphiphilic core-shell cylindrical polymer brush. Because of the living/controlled nature of both anionic polymerization and ATRP, the length of brush as well as the diameters of core and shell are well-defined. As shown in Scheme 1a, the polymer brush used here has 1500 block copolymer arms consisting of 25 acrylic acid units in the core block and 61 *n*-butyl acrylate units in the shell block (defined as [AA<sub>25</sub>-*nBA*<sub>61</sub>]<sub>1500</sub>). The polydispersity indices ( $M_w/M_n$ ) of the backbone and the polymer brush are 1.08 and 1.29, respectively.

A typical scanning force microscopy (SFM) image of the polymer brush is shown in Figure 6-1a. Wormlike cylinders are clearly visible. A statistical analysis of the SFM image shows that the number- and weight-average lengths of the polymer brushes are  $L_n = 166$  nm and  $L_w = 180$  nm respectively, with a polydispersity index  $L_w/L_n = 1.08$ , which is identical to the polydispersity index of the backbone. As shown in Figure 6-1a, one can easily see the core-shell structure in the phase image but not in the corresponding height image. The difference in hardness between the relatively hard PAA (glass transition temperature,  $T_g = 106$  °C<sup>50</sup>) core and the very soft *PnBA* ( $T_g = -54$  °C<sup>51</sup>) shell provides the apparent contrast in the phase image, thus the core-shell structure shown in the right side of Figure 6-1a should correspond to that of the polymer brush. Because of the very low glass transition temperature of *PnBA*, the shell of the polymer brush is totally collapsed on mica at room temperature and thus its height is undetectable.<sup>48</sup> The SFM image clearly shows that these polymer brushes are

structurally well-defined single molecule templates for the nanoparticle fabrication, and the controls of both the dimension of nanoparticle and the length of wire-like nanoparticle assembly can be achieved.

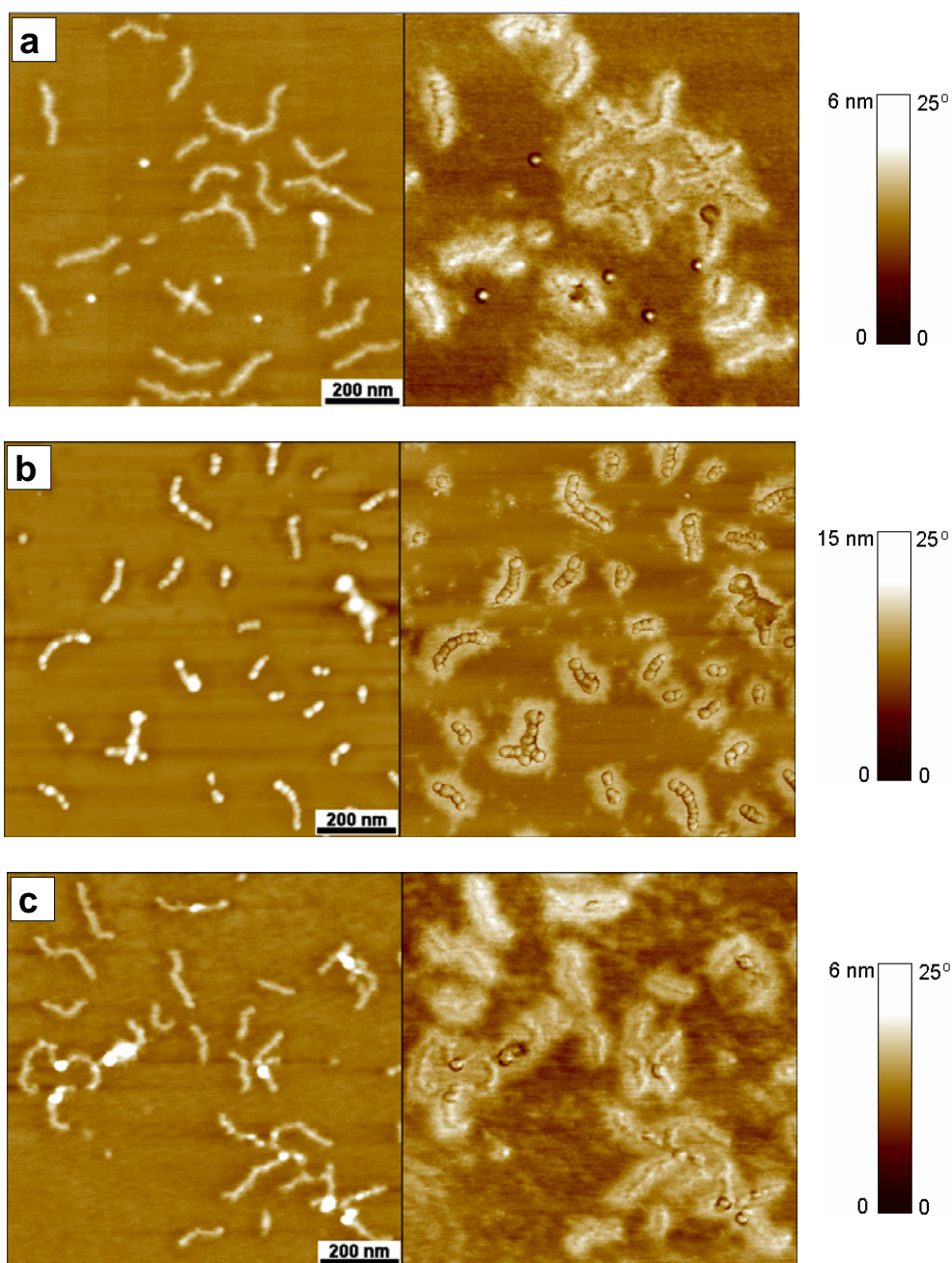


**Figure 6-1.** Tapping Mode SFM images (left: height; right: phase) of (a) the polymer brush,  $[AA_{25-n}BA_{61}]_{1500}$ ; (b) the polychelate of the polymer brush and  $Cd^{2+}$  ions; and (c) the hybrid of the polymer brush and CdS nanoparticles. All the samples were measured on mica.

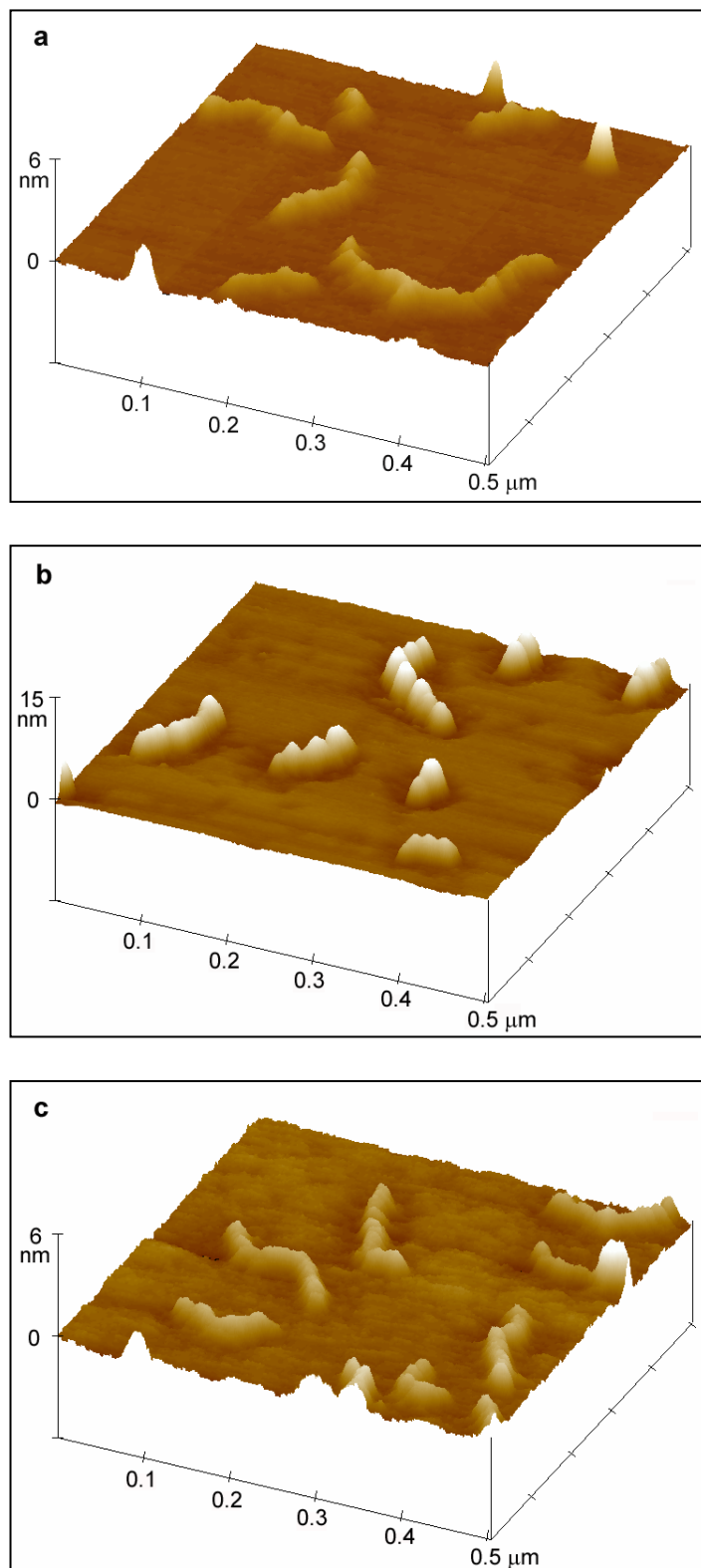
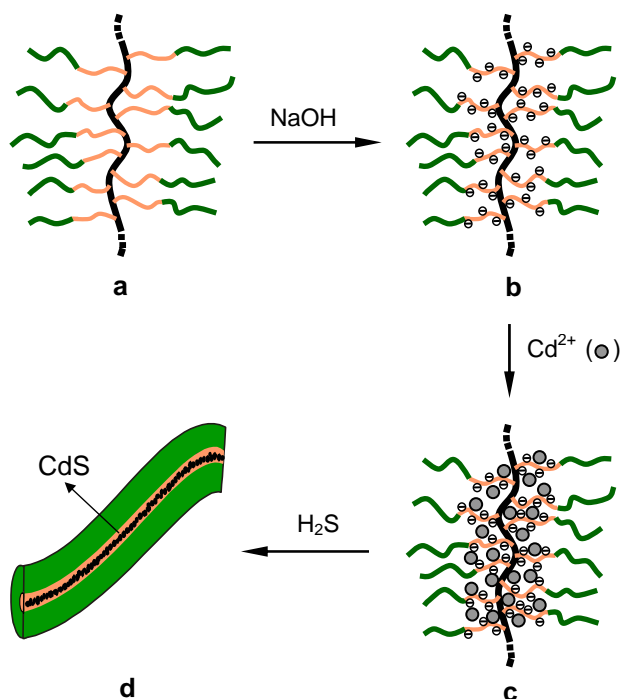


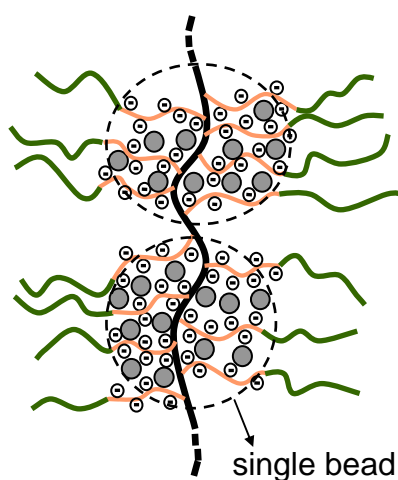
**Figure 6-2.** 3-D SFM images of (a) the polymer brush,  $[AA_{25-n}BA_{61}]_{1500}$ ; (b) the polychelate of the polymer brush and  $Cd^{2+}$  ions; and (c) the hybrid of the polymer brush and CdS nanoparticles.

Our approach in using the cylindrical polymer brush as template for the synthesis of CdS nanoparticles includes three steps, as illustrated in Scheme 6-2. In the first step (a→b), the PAA core of the polymer brush was neutralized using NaOH. It has been reported that the conversion of carboxylic acid to sodium carboxylate results in large increase in both the extent and rate of transition metal ion uptake.<sup>52</sup> Afterward, Cd<sup>2+</sup> ions were introduced into the core of the polymer brush via ion exchange between Cd<sup>2+</sup> and Na<sup>+</sup> (step 2: b→c). The uncoordinated Cd<sup>2+</sup> ions were removed by either precipitation or membrane dialysis, then the composite of the polymer brush and Cd<sup>2+</sup> ions, named as polychelate,<sup>53</sup> was obtained. In the final step (c→d), H<sub>2</sub>S gas was introduced into the dispersion of the polychelate, and CdS nanoparticles were produced, indicated by the instant color change from colorless to yellow. The size of the resulting particles was limited by the amount of Cd<sup>2+</sup> ions within the polychelate, which in principle can be controlled by varying the core size of the polymer brush, the neutralization extent of the core and the amount of cadmium salt used.



**Scheme 6-2.** Schematic illustration for the synthesis of wire-like assembly of CdS nanoparticles inside the cylindrical polymer brush: (a) the polymer brush with PAA core and PnBA shell; (b) the neutralized polymer brush with poly(sodium acrylate) core (Na<sup>+</sup> is not shown); (c) the polychelate of the brush and Cd<sup>2+</sup> ions; and (d) the hybrid of the brush and wire-like assembly of CdS nanoparticles.

SFM measurements showed that there was no apparent change in the morphology of the polymer brush before and after neutralization. However, after loading of  $\text{Cd}^{2+}$  ions, the morphology of the polymer brush changed dramatically. A peculiar “pearl necklace” structure of the polychelate was clearly observed in the SFM image (Figure 6-1b) and the corresponding 3-D image (Figure 6-2b). This structure may stem from the “cross-linking” of side chains induced by the coordination between divalent  $\text{Cd}^{2+}$  ions and monovalent carboxylate groups from different side chains. Similar phenomena were also observed in the polychelate of another polymer brush and  $\text{Fe}^{3+}$  ions,<sup>54</sup> and in  $\text{Fe}^{2+}$  loaded microporous membranes containing PAA grafts in the pores.<sup>55</sup> In contrast, monovalent ions such as  $\text{Na}^+$  did not induce the formation of the “pearl necklace” structure, simply because the “cross-linking” of different side chains cannot happen. Particularly, the morphology change was observed solely in the core region, supporting that the  $\text{Cd}^{2+}$  ions coordinate selectively with the core block of the polymer brush. Moreover, the height of the polychelate is more than two times of that of the pure polymer brush, indicating that the loading of  $\text{Cd}^{2+}$  ions stiffens the polymer brush significantly. Scheme 6-3 depicts the structure of the polychelate.



**Scheme 6-3.** Schematic illustration of the “pearl necklace” structure of the polychelate.

The pearl necklace-like morphology was also observed in the SFM image of pure polymer brushes with *Pn*BA core and polystyrene (PS) shell on mica.<sup>56</sup> However in that case the driving force for the morphology formation is different from that for polychelates. On substrate mica, the PS tails in the block copolymer brushes tend to aggregate due to dewetting of PS on mica. While aggregation of PS occurs, the *Pn*BA chain fragments remain tightly adsorbed on the substrate, leading to the necklace-like morphology. In

contrast, smooth contours were observed for the polymer brushes with PAA core and PnBA shell on mica (as shown in Figure 6-1a), because both PAA and PnBA are tightly adsorbed on the substrate due to their attractive interactions with mica. Thus the formation of the “pearl necklace” structure of polychelates can be attributed to the “cross-linking” of side chains by  $\text{Cd}^{2+}$  ions.

Removal of uncoordinated free  $\text{Cd}^{2+}$  ions via precipitation (or dialysis) ensures that the CdS nanoparticles form solely inside the polymer template. Because of the linking of side chains by  $\text{Cd}^{2+}$  ions, the solubility of the polymer brush decreased. After precipitation, the purified polychelate could not be completely redissolved in the same solvent for the pure polymer brush, and only a turbid dispersion was obtained. Without stirring, most polychelates precipitated out in one day. The supernatant of the polychelate dispersion was used for SFM characterization. One can see more short brushes in the SFM image of the polychelate (Figure 6-1b), as compared to that of the polymer brush (Figure 6-1a). This is due to that long polymer brushes in the polychelate dispersion are easier to precipitate so that there are more short brushes in the supernatant.

After the formation of CdS nanoparticles the “pearl necklace” structure disappeared (Figures 6-1c and 6-2c), and the morphology of the obtained hybrids of the polymer brush and CdS nanoparticles was almost the same as that of the pure polymer brush, indicating that the “cross-linking” of side chains induced by inter-side chain coordination via bridging  $\text{Cd}^{2+}$  ions vanished. Additionally, the height of the hybrid is similar to that of the polymer brush, indicating that the CdS nanoparticles formed inside the polymer brush must be very small such that they did not change the overall dimension of the polymer template significantly. As expected, the polymer brushes recovered their original solubility after the formation of CdS nanoparticles, and a clear yellow solution was obtained. This yellow solution was stable for several months (stored in a dark place with stirring), remaining free of precipitate or turbidity.

Without staining, the contrast for the polymer brush is too weak to render an image via transmission electron microscopy (TEM). However, a good contrast was observed when  $\text{Cd}^{2+}$  ions were loaded, as shown in Figure 6-3a. Wormlike dark domains in the bright-field TEM image of the polychelate present a direct proof for the successful coordination of  $\text{Cd}^{2+}$  ions with carboxylate groups in the core of the polymer brush. The diameter of the wormlike objects is about 5-6 nm, which should correspond to that of the core of the polymer brush. A closer examination of the TEM image of the polychelate (Figure 6-3b)

clearly shows string of spherical dark grains, which again confirms the “pearl necklace” structure of the polychelate as shown in the SFM image (Figures 6-1b and 6-2b).

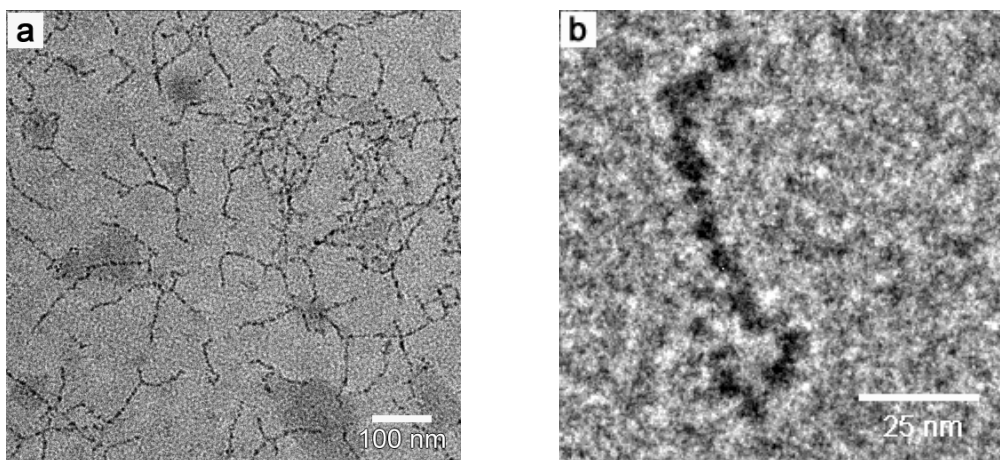


**Figure 6-3.** Non-stained TEM images of the polychelate of the polymer brush and  $\text{Cd}^{2+}$  ions on Formvar/carbon coated copper grids.

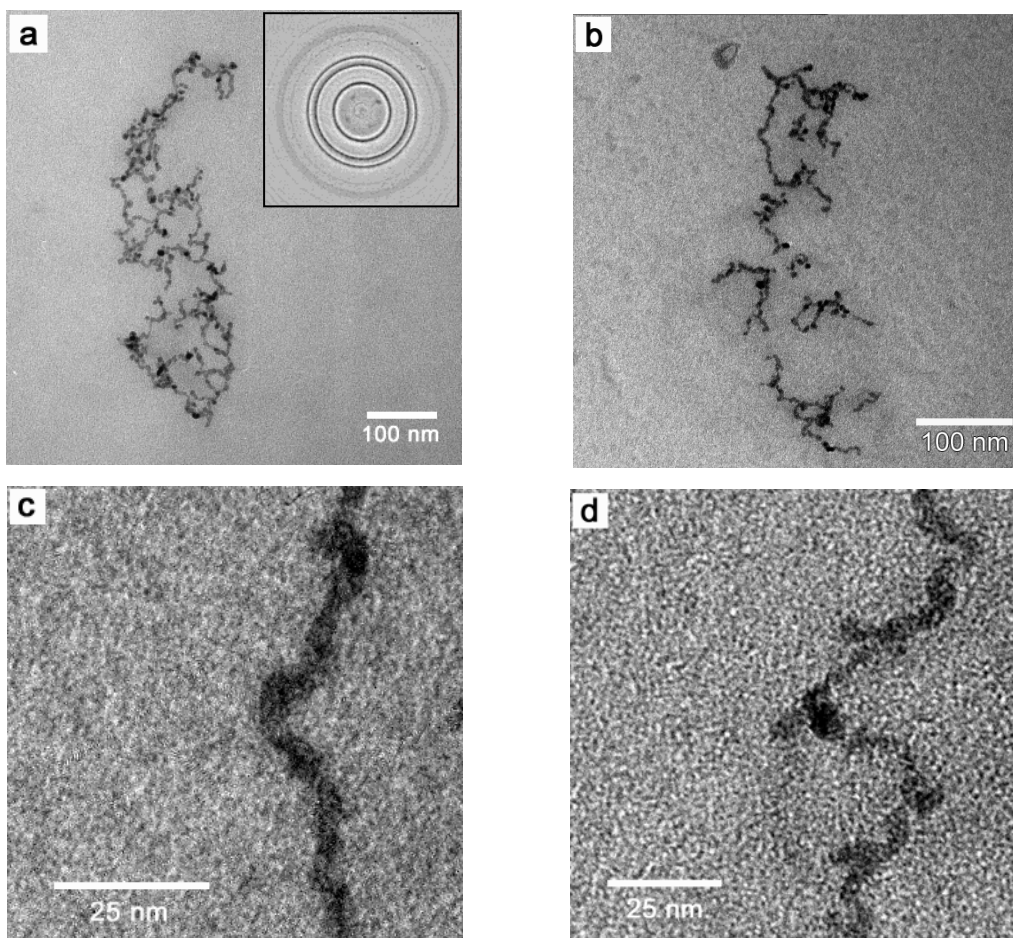


**Figure 6-4.** Non-stained TEM images of wire-like assembly of CdS nanoparticles: (a) on Formvar/carbon coated copper grid; and (b-d) on carbon coated copper grid. Inset in Figure 6-4a: electron diffraction pattern.

Figure 6-4 shows some typical TEM images of the hybrid of the polymer brush and CdS nanoparticles on different substrates. Compared to that of the polychelate, a higher contrast was observed due to the formation of CdS nanoparticles. Wire-like assemblies (with a diameter of 4-5 nm) of CdS nanoparticles were clearly visible. The diameter of these wire-like assemblies is slightly less than that of the core of the polychelate, indicating the more compact structure of CdS nanoparticles. Both continuous nanowires with regular shape (Figure 6-4c) and wire-like assemblies of discrete nanoparticles (Figure 6-4d) are observed. Although the precursors of CdS nanoparticles,  $\text{Cd}^{2+}$  ions, are confined in separated “beads”, CdS can diffuse and grow to form a continuous phase due to its weaker bonding to the carboxylic acid groups compared to that of  $\text{Cd}^{2+}$ . The nucleation, growth and interconnection of CdS nanoparticles inside the polymer brush is a complex process, and further investigation is needed to control the distribution of the nanoparticles along the polymer brush. Nevertheless, the carboxylic acid coordination sites are regenerated after the formation of CdS nanoparticles, therefore it is possible to perform multi-loading of  $\text{Cd}^{2+}$  ions followed by the treatment with  $\text{H}_2\text{S}$ . Thus, the discrete CdS nanoparticles might be further connected to generate continuous nanowires.

The electron diffraction pattern of the CdS nanoparticles, as shown in the inset of Figure 6-4a, supports the presence of a polycrystalline structure, which is often obtained in template-directed methods.<sup>5</sup> The  $d$  spacings calculated from the rings in the electron diffraction pattern are 3.29, 2.02, and 1.73 Å, which correspond to the reported  $d$  spacings for lattice planes (111), (220), and (311) of the cubic (zinc blende) phase of CdS.<sup>57,58</sup>

Elemental analysis of the hybrid was carried out using the energy dispersive X-ray (EDX) analysis of a scanning electron micrograph. Figure 6-5 shows the EDX spectrum of the hybrid of the polymer brush and CdS nanoparticles, which confirms the presence of cadmium and sulfur. The average atom ratio of Cd/S over the selected area is 1.1, quite close to the theoretical value.

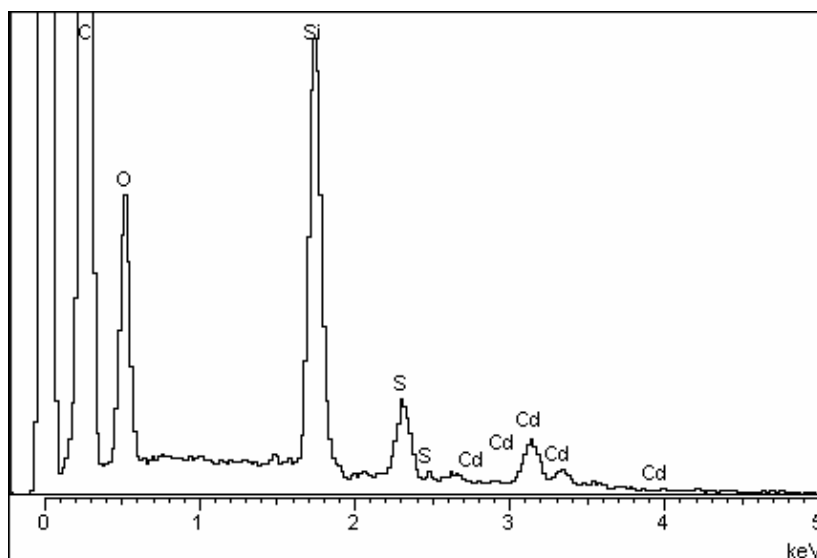


**Figure 6-5.** EDX spectrum of the hybrids of the polymer brush and CdS nanoparticles.

It is known that CdS particles larger than about 6 nm, the size of an exciton in the bulk, start to absorb at the wavelength of about 515 nm. With decreasing particle size, the absorption threshold shifts to shorter wavelengths as a result of quantum confinement effects. Figure 6-6 shows the UV/visible absorption spectrum of the hybrid of the polymer brush and CdS nanoparticles. Considering the pure polymer brush has nearly no absorption in the observed wavelength range,<sup>54</sup> the absorption shown in Figure 6-6 can be attributed exclusively to the CdS nanoparticles. The absorption spectrum illustrates characteristics similar to those of CdS colloids formed via other techniques: an absorption onset at 500 nm, a shoulder at around 450 nm and a steep rise below 300 nm.<sup>24</sup> As expected, the absorbance edge ( $\lambda_e = 478$  nm) of CdS nanoparticles in the polymer brush is blue-shifted relative to that of bulk CdS, indicating of the small particle size.

As mentioned before, the core of the polymer brush is reprotonated after the formation of CdS nanoparticles, therefore it is possible to perform further reactions. For example, loading of other metal ions may be used for surface modification of the CdS nanoparticles and core-shell and onion-type nanoparticles might be obtained.<sup>43</sup> Additionally, reneutralizing the acrylic acid units with NaOH will increase the stability of the hybrids in organic solution, since the solubility of poly(sodium acrylate) in organic solvents is much lower than that of poly(acrylic acid).

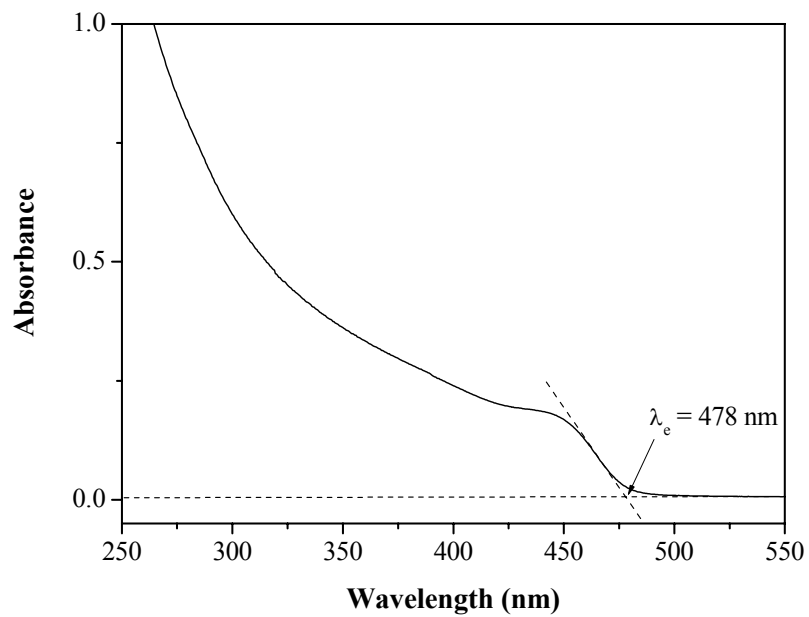


**Figure 6-6.** UV/visible spectrum of the hybrid of the polymer brush and CdS nanoparticles.

## 6.4 Conclusions

Using the amphiphilic core-shell cylindrical polymer brush with PAA core and PnBA shell as template, wire-like assemblies of CdS nanoparticles were successfully synthesized under mild solution conditions, as confirmed by SFM, TEM, EDX, and UV/visible spectroscopy. The well-defined polymer template provides good control of the formation of CdS nanoparticles and the solubility of the hybrids in organic solvents, which might be very important in some applications. Because of the promising combination of polymeric properties (stability, elasticity, and processability) with those of semiconductor nanoparticles, we might expect some interesting applications based on this hybrid material.

The reaction scheme presented here is not restricted to semiconductor nanoparticles, but can also be used for the preparation of metal or metal oxide particles. The fabrication of magnetic nanoparticles inside the polymer brush is under investigation and the results will be published soon.

**Acknowledgment.** This work was supported by Deutsche Forschungsgemeinschaft within SFB 481. We thank Ms. Astrid Göpfert and Dr. Falko Langenhorst for TEM measurements and Mrs. Clarissa Abetz for EDX measurements. We thank Dr. Hideharu Mori for the critical reading of the manuscript.

## References

- (1) Henglein, A. *Chem. Rev.* **1989**, *89*, 1861.
- (2) Weller, H. *Adv. Mater.* **1993**, *5*, 88.
- (3) Huczko, A. *Appl. Phys. A: Mater. Sci. Proc.* **2000**, *70*, 365.
- (4) Trindade, T.; O'Brien, P.; Pickett, N. L. *Chem. Mater.* **2001**, *13*, 3843.
- (5) Xia, Y.; Yang, P.; Sun, Y.; Wu, Y.; Mayers, B.; Gates, B.; Yin, Y.; Kim, F.; Yan, H. *Adv. Mater.* **2003**, *15*, 353.
- (6) Klimov, V. I.; Mikhailovsky, A. A.; Xu, S.; Malko, A.; Hollingsworth, J. A.; Leatherdale, C. A.; Eisler, H.; Bawendi, M. G. *Science* **2000**, *290*, 314.
- (7) Sundar, V. C.; Eisler, H. J.; Bawendi, M. G. *Adv. Mater.* **2002**, *14*, 739.
- (8) Colvin, V. L.; Schlamp, M. C.; Alivisatos, A. P. *Nature* **1994**, *370*, 354.
- (9) Huynh, W. U.; Dittmer, J. J.; Alivisatos, A. P. *Science* **2002**, *295*, 2425.
- (10) Bruchez, M. Jr.; Moronne, M.; Gin, P.; Weiss, S.; Alivisatos, A. P. *Science* **1998**, *281*, 2013.
- (11) Jaiswal, J. K.; Mattoussi, H.; Mauro, J. M.; Simon, S. M. *Nature Biotechnol.* **2003**, *21*, 47.
- (12) Weller, H. *Angew. Chem. Int. Ed.* **1998**, *37*, 1658.
- (13) Klein, D. L.; Roth, R.; Lim, A. K. L.; Alivisatos, A. P.; McEuen, P. L. *Nature* **1997**, *389*, 699.
- (14) Henglein, A.; Fojtik, A.; Weller, H. *Ber. Bunsen-Ges.* **1987**, *91*, 441.
- (15) Wang, Y.; Herron, N. *J. Phys. Chem.* **1991**, *95*, 525.
- (16) Spanhel, L.; Haase, M.; Weller, H.; Henglein, A. *J. Am. Chem. Soc.* **1987**, *109*, 5649.
- (17) Yu, H.; Gibbons, P. C.; Kelton, K. F.; Buhro, W. E. *J. Am. Chem. Soc.* **2001**, *123*, 9198.
- (18) Wang, Y.; Herron, N. *J. Phys. Chem.* **1987**, *91*, 257.
- (19) Shinojima, H.; Yumoto, J.; Uesugi, N.; Omi, S.; Asahara, Y. *Appl. Phys. Lett.* **1989**, *55*, 1519.
- (20) Cassagneau, T.; Hix, G. B.; Jones, D. J.; Maireles-Torres, P.; Rhomari, M.; Roziere, J. *J. Mater. Chem.* **1994**, *4*, 189.
- (21) Brenchley, M. E.; Weller, M. T. *Angew. Chem.* **1993**, *105*, 1726.

- (22) Blasse, G.; Dirksen, G. J.; Brenchley, M. E.; Weller, M. T. *Chem. Phys. Lett.* **1995**, *234*, 177.
- (23) Meyer, M.; Wallberg, C.; Kurihara, K.; Fendler, J. H. *Chem. Commun.* **1984**, 90.
- (24) Lianos, P.; Thomas, J. K. *Chem. Phys. Lett.* **1986**, *125*, 299.
- (25) Pileni, M. P.; Motte, L.; Petit, C. *Chem. Mater.* **1992**, *4*, 338.
- (26) Petit, C.; Lixon, P.; Pileni, M. P. *J. Phys. Chem.* **1990**, *94*, 1598.
- (27) Petit, C.; Jain, T. K.; Billoudet, F.; Pileni, M. P. *Langmuir* **1994**, *10*, 4446.
- (28) Antonietti, M.; Wenz, E.; Bronstein, L.; Seregina, M. *Adv. Mater.* **1995**, *7*, 1000.
- (29) Spatz, J. P.; Moessmer, S.; Hartmann, C.; Möller, M.; Herzog, T.; Krieger, M.; Boyen, H. G.; Ziemann, P.; Kabius, B. *Langmuir* **2000**, *16*, 407.
- (30) Förster, S.; Antonietti, M. *Adv. Mater.* **1998**, *10*, 195.
- (31) Tricot, Y. M.; Fendler, J. H. *J. Phys. Chem.* **1986**, *90*, 3369.
- (32) Watzke, H. J.; Fendler, J. H. *J. Phys. Chem.* **1987**, *91*, 854.
- (33) Korgel, B. A.; Monbouquette, H. G. *J. Phys. Chem.* **1996**, *100*, 346.
- (34) Boyen, H.-G.; Kastle, G.; Zurn, K.; Herzog, T.; Weigl, F.; Ziemann, P.; Mayer, O.; Jerome, C.; Möller, M.; Spatz, J. P.; Garnier, M. G.; Oelhafen, P. *Adv. Func. Mater.* **2003**, *13*, 359.
- (35) Möller, M.; Kuentle, H.; Kunz, M. *Synth. Met.* **1991**, *41*, 1159.
- (36) Moffitt, M.; McMahon, L.; Pessel, V.; Eisenberg, A. *Chem. Mater.* **1995**, *7*, 1185.
- (37) Moffitt, M.; Eisenberg, A. *Chem. Mater.* **1995**, *7*, 1178.
- (38) Moffitt, M.; Vali, H.; Eisenberg, A. *Chem. Mater.* **1998**, *10*, 1021.
- (39) Ciebien, J. F.; Clay, R. T.; Sohn, B. H.; Cohen, R. E. *New J. Chem.* **1998**, *22*, 685.
- (40) Sidorov, S. N.; Bronstein, L. M.; Davankov, V. A.; Tsyurupa, M. P.; Solodovnikov, S. P.; Valetsky, P. M. *Chem. Mater.* **1999**, *11*, 3210.
- (41) Bronstein, L. M.; Mirzoeva, E. S.; Seregina, M. V.; Valetsky, P. M.; Solodovnikov, S. P.; Register, R. A. *ACS Symp. Ser.* **1996**, *622*, 102.
- (42) Bronstein, L. M.; Chernyshov, D. M.; Valetsky, P. M.; Wilder, E. A.; Spontak, R. J. *Langmuir* **2000**, *16*, 8221.
- (43) Crooks, R. M.; Lemon, B. I., III; Sun, L.; Yeung, L. K.; Zhao, M. *Top. Curr. Chem.* **2001**, *212*, 81.
- (44) Braun, E.; Eichen, Y.; Sivan, U.; Ben-Yoseph, G. *Nature* **1998**, *391*, 775.
- (45) Richter, J.; Seidel, R.; Kirsch, R.; Mertig, M.; Pompe, W.; Plaschke, J.; Schackert, H. K. *Adv. Mater.* **2000**, *12*, 507.

- (46) Minko, S.; Kiriy, A.; Gorodyska, G.; Stamm, M. *J. Am. Chem. Soc.* **2002**, *124*, 10192.
- (47) Djalali, R.; Li, S. Y.; Schmidt, M. *Macromolecules* **2002**, *35*, 4282.
- (48) Zhang, M.; Breiner, T.; Mori, H.; Müller, A. H. E. *Polymer* **2003**, *44*, 1449.
- (49) Cheng, G.; Böker, A.; Zhang, M.; Krausch, G.; Müller, A. H. E. *Macromolecules* **2001**, *34*, 6883.
- (50) Mercier, J. P. *Ind. Chim. Belge* **1965**, *30*, 813.
- (51) Wiley, R. H.; Brauer, G. M. *J. Polym. Sci.* **1948**, *3*, 647.
- (52) Clay, R. T.; Cohen, R. E. *Supramol. Sci.* **1998**, *5*, 41.
- (53) Rivas, B. L.; Seguel, G. V. *Polym. Bull.* **1998**, *40*, 431.
- (54) Zhang, M.; Teissier, P.; Krekhov, M.; Cabuil, V.; Müller, A. H. E. *Prog. Colloid Polym. Sci.*, in press.
- (55) Winnik, F. M.; Morneau, A.; Mika, A. M.; Childs, R. F.; Roig, A.; Molins, E.; Ziolo, R. F. *Can. J. Chem.* **1998**, *76*, 10.
- (56) Börner, H. G.; Beers, K.; Matyjaszewski, K.; Sheiko, S. S.; Möller, M. *Macromolecules* **2001**, *34*, 4375.
- (57) Halaoui, L. I. *Langmuir* **2001**, *17*, 7130.
- (58) Torimoto, T.; Tsumura, N.; Miyake, M.; Nishizawa, M.; Sakata, T.; Mori, H.; Yoneyama, H. *Langmuir* **1999**, *15*, 1853.

## Chapter 7 Summary

Core-shell cylindrical polymer brushes with poly(*t*-butyl acrylate)-*b*-poly(*n*-butyl acrylate) (PtBA-*b*-PnBA) diblock copolymer side chains were synthesized via the “grafting from” technique using a combination of anionic polymerization (for the synthesis of the backbone) and atom transfer radical polymerization (ATRP, for the synthesis of the side chains). The formation of well-defined brushes was confirmed by <sup>1</sup>H-NMR and GPC. The selective hydrolysis of the PtBA block of the side chains resulted in novel amphiphilic core-shell cylindrical polymer brushes with poly(acrylic acid)-*b*-poly(*n*-butyl acrylate) (PAA-*b*-PnBA) side chains. The characteristic core-shell cylindrical structure of the brushes was directly visualized on mica by scanning force microscopy (SFM). Amphiphilic brushes with 1500 block copolymer side chains and a length distribution of  $l_w/l_n = 1.04$  at a total length  $l_n = 179$  nm were obtained. These amphiphilic polymer brushes can be regarded as unimolecular cylindrical micelles, because of the core-shell structure and the amphiphilicity of side chains.

The amphiphilic brushes can be used as single molecular templates for the synthesis of inorganic nanoparticles, because the carboxylic acid groups (or carboxylate groups, after neutralization) in the polymer core can coordinate with various metal ions.

The hydrophilic core of polymer brushes, poly(acrylic acid), was neutralized by NaOH and afterward iron cations ( $\text{Fe}^{3+}$  and  $\text{Fe}^{2+}$ ) were loaded into the polymer core via ion exchange. The formation of the polychelates of polymer brushes and iron cations was confirmed and characterized by various techniques such as Fourier transform infrared spectroscopy (FTIR), UV/vis spectroscopy, transmission electron microscopy (TEM) and SFM. A peculiar “pearl necklace” morphology was observed for the polychelates, which is caused by the physical cross-linking of the side chains via multivalent iron cations. Formation of crystalline  $\alpha\text{-Fe}_2\text{O}_3$  (hematite) was observed during the He-Ne laser irradiation in the confocal Raman microscopy measurement of the polychelate containing  $\text{Fe}^{3+}$  ions.

Magnetic nanoparticles were successfully produced from the coordinated iron cations within polymer brushes via single molecule templating technique, as confirmed by various techniques such as SFM, TEM, and UV/visible spectroscopy. Superconducting quantum interference device (SQUID) magnetization measurements show that the hybrid nanocylinders are superparamagnetic at room temperature. The polymer shell provides not

only the stability of the nanoparticles but also the solubility of the hybrid nanocylinders. After the formation of the magnetic nanoparticles, the carboxylate coordination sites within the polymer brushes are liberated and ready for further coordination with more iron ions, thus it is possible to increase the amount and/or particle size of the nanoparticles by multi-cycles of iron ion loading and particle formation. The as-prepared hybrid nanocylinders combine the promising properties of polymers and superparamagnetic nanoparticles, and may find potential applications such as in ferrofluids.

Similarly, using the amphiphilic core-shell cylindrical polymer brush with PAA core and PnBA shell as template, wire-like assemblies of CdS nanoparticles were successfully synthesized under mild solution conditions, as confirmed by various characterization techniques. Quantum confinement of the CdS nanoparticles was observed, indicated by the blue shift of the absorbance edge in UV/visible spectrum.

The technique using a single cylindrical molecule as template for inorganic nanoparticle fabrication presented in this thesis is not restricted to magnetic/semiconductor nanoparticles, but can also be used for the preparation of a number of metal, metal oxide, and metal chalcogenide nanoparticles.

## Zusammenfassung

Mit der „grafting from“-Technik wurden zylindrische Kern-Schale-Polymerbürsten mit Seitenketten aus poly(*t*-butylacrylat)-*b*-poly(*n*-butylacrylat) (PtBA-*b*-PnBA)-Zweiblockcopoly-meren synthetisiert. Die Hauptkette wurde durch anionische Polymerisation und die Seitenketten durch radikalische Atom-Transfer-Polymerisation (ATRP) hergestellt. Durch <sup>1</sup>H-NMR und GPC konnte die erfolgreiche Synthese wohldefinierter Polymerbürsten nachgewiesen werden. Die selektive Hydrolyse des PtBA-Blocks der Seitenketten führte zur Bildung von neuartigen zylindrischen Kern-Schale-Polymerbürsten mit Poly(acrylsäure)-*b*-Poly(*n*-butylacrylat) (PAA-*b*-PnBA)-Seitenketten mit amphiphilen Eigenschaften. Die charakteristische zylindrische Kern-Schale-Struktur der Bürsten konnte auf Mica direkt durch Rasterkraftmikroskopie (SFM) beobachtet werden. Es wurden amphiphile Bürsten mit 1500 Blockcopolymer-Seitenketten mit einer Längenverteilung von  $l_w/l_n = 1.04$  und einer Konturlänge von  $l_n = 179$  nm erhalten. Aufgrund der Kern-Schale-Struktur und der amphiphilen Eigenschaften der Seitenketten können diese Polymerbürsten als unimolekulare zylindrische Micellen angesehen werden.

Da die Säuregruppen (oder nach Neutralisation die Carboxylat-Gruppen) eine Vielzahl von Metallionen binden können, können die Polymerbürsten als unimolekulare Template für die Synthese von anorganischen Nanoteilchen benutzt werden.

Nach Neutralisation der Polyacrylsäure, dem hydrophilen Kern der Polymerbürste, wurde dieser mit Eisenkationen ( $\text{Fe}^{3+}$  und  $\text{Fe}^{2+}$ ) durch Ionenaustausch beladen. Die Bildung von Polychelaten zwischen der Polymerbürste und Eisenkationen konnte durch verschiedene analytische Methoden, wie Fourier-Transform-Infrarotspektroskopie (FTIR), UV-VIS-Spektroskopie, Transmissionselektronenmikroskopie (TEM) und SFM bestätigt und charakterisiert werden. Insbesondere wurde eine „Perlenketten-Struktur“ in den Polychelaten beobachtet, die durch die physikalische Verknüpfung von Seitenketten durch multivalente Eisenkationen erklärt werden kann. Während der Bestrahlung mit einem He-Ne-Laser in der konfokalen Raman-Mikroskopie konnte die Bildung von  $\alpha\text{-Fe}_2\text{O}_3$  (Hämatit) beobachtet werden.

Die in den Polymerbürsten gebundenen Eisenkationen konnten erfolgreich zur Synthese von magnetischen Nanoteilchen verwendet werden. Die Polymerbürste diente dabei als unimolekulares Templat. Dies wurde durch SFM, TEM und UV-VIS-Spektroskopie bestätigt. Der Superparamagnetismus der Hybrid-Nanozylinder bei Zimmertemperatur

konnte durch Messungen der Magnetisierung mit einem supraleitenden Quanteninterferenz-Gerät (SQUID) gemessen werden. Die Polymerschale sorgt nicht nur für die Stabilität der Nanoteilchen, sondern auch für die Löslichkeit der Hybrid-Nanozylinder. Da nach der Bildung der magnetischen Nanoteilchen die Carboxylatgruppen in der Polymerbürste wieder frei sind, können erneut Eisenionen koordiniert werden. Damit kann die Anzahl und/oder die Teilchengröße der Nanoteilchen durch wiederholtes Beladen mit Eisenionen und nachfolgender Teilchenbildung erhöht werden. Die so dargestellten Hybridmaterialien vereinigen die vorteilhaften Eigenschaften von Polymeren und superparamagnetischen Nanoteilchen und können zum Beispiel Anwendung in Ferrofluiden finden.

Auf ähnliche Weise wurden mit amphiphilen Kern-Schale-Zylinderbürsten mit PAA-Kern und *PnBA*-Schale als Templat erfolgreich leitungsartige Anordnungen von CdS-Nanoteilchen unter milden Bedingungen dargestellt und durch verschiedene analytische Techniken charakterisiert. Die beobachtete Blauverschiebung an der Absorptionskante im UV-VIS-Spektrum weist auf eine Quanteneinschränkung in den CdS-Nanoteilchen hin.

Die Darstellung von anorganischen Nanoteilchen durch templatgesteuerte Synthese mittels einer einzelnen Zylinderbürste, die in dieser Arbeit beschrieben wird, ist nicht auf magnetische oder halbleitende Nanoteilchen beschränkt, sondern kann auch auf eine Vielzahl anderer Metall-, Metalloxid- und Metallchalkogenid-Nanoteilchen ausgeweitet werden.

## Chapter 8 List of publications

During the course of this thesis the following papers have been published (or accepted/submitted):

- “Superparamagnetic hybrid nanocylinders”  
Mingfu Zhang, Claude Estournes, Werner Bietsch, Axel H. E. Müller\*  
*Advanced Functional Materials*, **2004**, accepted
- “Template-controlled synthesis of wire-like cadmium sulfide nanoparticle assemblies within core-shell cylindrical polymer brushes”  
Mingfu Zhang, Markus Drechsler, Axel H. E. Müller\*  
*Chemistry of Materials*, **2004**, 16, 537
- “Light scattering and small-angle neutron scattering of cylindrical polymer brushes”  
Mingfu Zhang, Henrich Frielinghaus,\* Markus Drechsler, Axel H. E. Müller,\*  
Dieter Richter  
*Langmuir*, **2004**, submitted
- “Amphiphilic cylindrical brushes with poly(acrylic acid) core and poly(*n*-butyl acrylate) shell and narrow length distribution”  
Mingfu Zhang, Thomas Breiner, Hideharu Mori, Axel H. E. Müller\*  
*Polymer*, **2003**, 44, 1449
- “Polychelates of amphiphilic cylindrical core-shell polymer brushes with iron cations”  
Mingfu Zhang, Pierre Teissier, Marina Krekhova, Valérie Cabuil, Axel H. E. Müller\*  
*Progress in Colloid and Polymer Science*, **2004**, 126, in press
- “Magnetic/semiconducting nanocylinders via polychelates of cylindrical core-shell polymer brushes”  
Mingfu Zhang, Markus Drechsler, Axel H. E. Müller\*  
*Polymer Preprint*, **2004**, 45(1), 454
- “*In situ* laser-induced formation of  $\alpha$ -Fe<sub>2</sub>O<sub>3</sub> from Fe<sup>3+</sup> ions in a cylindrical core-shell polymer brush”  
Carmen Pérez León,\* Lothar Kador, Mingfu Zhang, Axel H. E. Müller  
*Journal of Raman Spectroscopy*, **2004**, 35, 165

- “Thermoassociative block copolymers of poly(N-isopropylacrylamide) and poly(propylene oxide)”  
Erol Hasan, Mingfu Zhang, Axel H. E. Müller, Christo B. Tsvetanov\*  
*Journal of Macromolecular Science, Pure and Applied Chemistry*, **2004**, *A41(5)*, 467
- “Hybrid silica nanoparticles with hyperbranched polymer and polyelectrolyte shells”  
Hideharu Mori, Delphine Chan Seng, Mingfu Zhang, Axel H. E. Müller\*  
*Progress in Colloid and Polymer Science*, **2004**, *126*, in press
- “Synthesis of highly branched polyelectrolytes and silica/polyelectrolyte hybrid nanoparticles”  
Axel H. E. Müller, Adreas Walther, Mingfu Zhang, Hideharu Mori  
*Polymer materials: Science and Engineering*, **2004**, *90*, 262
- “A new double-responsive block copolymer synthesized via RAFT polymerization: poly(N-isopropylacrylamide)-*block*-poly(acrylic acid)”  
Christine M. Schilli, Mingfu Zhang, Axel H. E. Müller,\* Ezio Rizzardo, San H. Tang, Bill Y. K. Chong, Katarina Edwards, Göran Karlsson  
*Macromolecules*, **2004**, submitted
- “Effect of topology on the solution behavior of amphiphilic copolymers of *n*-butyl acrylate and acrylic acid. 2. characterization of block and graft copolymers in aqueous solution ”  
Yuanli Cai, Markus Hartenstein, Michael Gradzielski, Mingfu Zhang, Hideharu Mori, Oleg Borisov, Dmitry V. Pergushov, Johannes Zipfel, Peter Lindner, Axel H. E. Müller\*  
*Macromolecules*, **2004**, submitted
- “Micellar aggregates of amylose-*b*-polystyrene rod-coil block copolymers in water and THF”  
Katja Loos, Alexander Böker, Heiko Zettl, Mingfu Zhang, Georg Krausch, Axel H. E. Müller\*  
*Macromolecules*, **2004**, submitted
- “Amphiphilic Janus micelles with polystyrene and poly(methacrylic acid) hemispheres”  
Rainer Erhardt, Mingfu Zhang, Alexander Böker, Heiko Zettl, Clarissa Abetz, Peter Frederik, Georg Krausch, Volker Abetz,\* Axel H. E. Müller\*  
*Journal of the American Chemical Society*, **2003**, *125*, 3260

- “Hybrid nanoparticles with hyperbranched polymer shells via self-condensing atom transfer radical polymerization from silica surfaces”  
Hideharu Mori, Delphine Chan Seng, Mingfu Zhang, Axel H. E. Müller\*  
*Langmuir*, **2002**, *18*, 3682
- “Synthesis and characterization of branched polyelectrolytes 1. preparation of highly branched poly(acrylic acid) via self-condensing atom transfer radical copolymerization”  
Hideharu Mori, Delphine Chan Seng, Hans Lechner, Mingfu Zhang, Axel H. E. Müller\*  
*Macromolecules* **2002**, *35*, 9270
- “Allylation of esters promoted by metallic dysprosium in the presence of mercuric chloride”  
Y. Jia, M. Zhang, F. Tao,\* J. Zhou  
*Synthetic Communications*, **2002**, *32*, 2829.
- “Amphiphilic cylindrical core-shell brushes via a ‘grafting from’ process using ATRP”  
Guanglou Cheng, Alexander Böker, Mingfu Zhang, Georg Krausch, Axel H. E. Müller\*  
*Macromolecules* **2001**, *34*, 6883

## Acknowledgements

At this point I would like to thank all the people who helped me during the course of my Ph.D. study.

First I would like to thank Prof. Dr. Axel H. E. Müller for providing me a very interesting topic and a nice working atmosphere. I appreciate his great supervision, constructive suggestions, fruitful discussions and patience. With time I realize that I am very lucky to have a "Doktorvater" like him. With his help life is much easier for a foreign student like me.

Prof. Dr. Volker Abetz is acknowledged for his fruitful suggestions and friendly discussions.

Dr. Hideharu Mori is acknowledged for his great help. I benefit a lot from the daily talkings and discussions and close collaborations with him.

I am grateful to many colleagues in the group MCII for their helps in not only chemistry but also many other things. Thanks to Dr. Guanglou Cheng and Dr. Markus Hartenstein for introducing me the ATRP technique. Many thanks to Dr. Alexander Böker, Xavier Andre, and Sabine Wunder for the GPC measurements, Dr. Rainer Erhardt for introducing me the light scattering techniques, Dr. Mabel Graf for the help in NMR measurements, and Annette Krökel for the osmometry measurements. Thanks to Dr. Holger Schmalz and Chih-Cheng Peng for the helps concerning computer and network. Thank Harald Becker a lot for his many helps in my daily life. His helps seem to be small but actually very important for me. Thank Günther Jutz for the try of improving my German.

Thanks the people in our microscope-team: Artrid Göpfert and Dr. Markus Drechsler for their great patience in searching single molecules on the grid. For me the measurements were boring but *sometimes* really exciting. Clarissa Abetz is acknowledged for her great helps in the SEM and EDX measurements.

I also want to thank all the other colleagues – Gabi Cantea, Dr. Shimei Jiang, Dr. Yanfei Liu, Nemesio Martinez Castro, Markus Burkhardt, Sharmila Mutukrishnan, Flex Plamper, Adriana Boschetti, Evis Penott, Kerstin

Matussek, Cornelia Lauble and Dr. Olivier Colombani for the nice Zusammenarbeit.

I would like to thank Prof. Dr. Georg Krausch for offering me the access to SFM, which is so important for my research.

During my study, I benefit a lot from the close collaborations between chemists and physicists in Bayreuth. Because of my research topic, I have chances to collaborate with many physicists.

Polymer chemists may be not so happy when their nice polymers are burned, but I am happy that Carmen Pérez León and Prof. Dr. Lothar Kador (Experimental Physics IV) got  $\alpha$ -Fe<sub>2</sub>O<sub>3</sub> nanocrystalline when they burned my polymer brush containing Fe<sup>3+</sup> ions by laser. As many successful experiments in science are more or less accidental, this experiment provides a new example. Thanks them a lot for the nice measurements of confocal Raman microscopy.

Dr. Werner Bietsch (Experimental Physics II) initiated the magnetization measurements for my samples. Thanks him a lot for explaining me the ABCs of magnetization with great patience. The time we spent together with both families was very nice.

I am grateful to Dr. Claude Estournès (University of Strasbourg, France) for his great help in the SQUID and Mössbauer measurements. He did the nice measurements so quickly, although we don't have official collaborations and we even never meet each other. It is clear to me that people from different countries can work together very well.

I have to thank Gaby Oliver for her great help in so many things. Without her help, at least the sophisticated German documents would become big problems to me, specially at the beginning of my stay in Bayreuth.

The research shown in this thesis will never be possible without financial support from Deutschen Forschungsgemeinschaft.

At the end I want to give my special thanks to my wife, Wen Wu, for her support, encouragement and love.

# Erklärung

Die vorliegende Arbeit wurde von mir selbstständig verfasst und ich habe dabei keine anderen als die angegebenen Hilfsmittel und Quellen benutzt.

- Kapitel 3: Die Synthese von PHEMA durch anionische Polymerisation wurde von Dr. Thomas Breiner durchgeführt. Dr. Hideharu Mori unterwies mich in der SFM-Technik. Dr. Markus Drechsler machte die Cryo-TEM-Aufnahmen.
- Kapitel 4: Pierre Teissier, Dr. Marina Krekhova und Prof. Valérie Cabuil waren durch Diskussionen beteiligt. Carmen Pérez León und Prof. Lothar Kador führten die konfokalen Raman-Mikroskopie-Untersuchungen durch.
- Kapitel 5: Dr. Claude Estournès führte die SQUID- und Mössbauer-Messungen durch; Dr. Werner Bietsch machte erste Messungen der magnetischen Suszeptibilität.
- Kapitel 6: Dr. Markus Drechsler machte die TEM-Aufnahmen.

Ferner habe ich nicht versucht, anderweitig mit oder ohne Erfolg eine Dissertation einzureichen oder mich der Doktorprüfung zu unterziehen.

Bayreuth, den 10.02.2004

Mingfu Zhang